Imperial College of Science, Technology and Medicine
Department of Bioengineering

Impact of Aortic Root Acceleration on Haemodynamics

Mazen Mohamed Abou Gamrah

Submitted in part fulfilment of the requirements for the degree of
Doctor of Philosophy in Bioengineering and the Diploma of Imperial College, March 2022

Abstract

The aortic valve apparatus (AVA) is a complicated structure continuously moving throughout the cardiac cycle such that it may be regarded as a live organ. Different studies previously focused on analysing the dynamism or local deformations of the AVA; however, the effect of the axial movement of the AVA on blood flow or aortic valve loading remains uncharted. In this study we propose analysing the axial acceleration of the AVA and its effect on blood flow.

After mathematically decomposing the deformations of healthy AVA's from CT image tracking, it was deduced that the dominant component is the axial movement towards and away from the left ventricle. Using the 1D water hammer approximation we hypothesised a theory tying the previously inexplicable dicrotic notch seen on the arterial pressure waveform to the AVA acceleration during valve closure.

The next intermediate step was to use an idealised model replicating the anatomy of the AVA in order to study the effect of axial acceleration on blood flow combined with steady inflow conditions. A series of non-dimensional parameters describing the underlying physics were derived in order to enable an appropriate comparison with a patient specific anatomy.

The final step was to analyse a stationary and an accelerating patient specific AVA using high fidelity Fluid-Structure Interaction (FSI) simulations. The results showed qualitative and quantitative differences between both cases especially in valvular dynamics and loading.

Moreover, the FSI simulation results confirmed the presence of a sudden reactive force on the aortic valve in the accelerating AVA case at the time of peak acceleration during valve closure; where the same phenomenon was not present in the stationary AVA case. The calculated force of 0.6 N along with the aortic valve wetted area of 0.0013 m^2 yield $\approx 3.5\ mmHg$ which is in the same ball park as previously measured dicrotic notch pressure rises.

As a result, we propose that the axial acceleration of the AVA may be a crucial parameter in diagnosing aortic or ventricular disease since it has a significant effect on aortic valve function. We also propose a future plan of investigation in order to strengthen our hypothesis and enable the use of the acceleration of the AVA as a non-invasive diagnostic parameter.

Acknowledgements

I would like to express my extreme gratitude to my supervisors Professor Emeritus Kim Parker and Professor Sir Magdi Yacoub for their continuous help, supervision and guidance throughout the duration of this PhD.

I would also like to thank my family especially my parents for their endless moral and educational support.

In addition to this, I would like to thank my colleague and friend Mr.Yehia Raef for always offering to help and for engaging with me in interesting discussions about parts of the work in this thesis.

Contents

Abstract **i**

Acknowledgements **iii**

Nomenclature **x**

I **1**

1 Introduction **2**

1.1 Motivation 2

1.2 Statement of Originality 2

1.3 Copyright Declaration 3

1.4 Publications 3

2 Literature Review **4**

2.1 Clinical Background 4

2.1.1 Varied Functions of The Aortic Root 6

2.1.2 Aortic Root Structure & Function Interaction 20

2.1.3 Aortic Root Dynamism 29

2.2 Current Methods for Assessing Haemodynamics 38

2.2.1 Multi-modality Imaging 38

2.2.2 0D Numerical Models 45

2.2.3 1D Numerical Models 48

2.2.4 Higher Order Computational Models 51

2.2.5 Experimental Techniques 58

2.3 The Aortic Valve Apparatus (AVA) 60

II **63**

3 Plan of Investigation **64**

3.1 Aims 67

4 Aortic Root Kinematics **68**

4.1 Fiducial Point Tracking 71

4.2 Resultant Deformations 80

4.2.1 Axial Segments 80

4.2.2 Longitudinal Segments 86

4.3 Dicrotic Notch Hypothesis 89

4.3.1 History of the Dicrotic Notch 89

4.3.2 Previous Dicrotic Notch Theories 90

4.3.3 Acceleration-based Model 92

4.3.4 Mechanics of The Dicrotic Notch 97

5 Tube Orifice Idealised Model **101**

5.1 Problem Introduction 101

5.1.1 Parametric Model 102

5.1.2 Navier-Stokes Equations 103

5.1.3 Computational Mesh 103

5.2 Analysis Scenarios 106

5.3 Buckingham **Π** Theorem 108

5.4 Steady Orifice 113

5.5 Closing Orifice 118

5.6 Axially Accelerating Orifice 123

6 Patient Specific Root Model **139**

6.1 Fluid−Structure Interaction (FSI) Methodology 139

6.1.1 FSI Physics 139

6.1.2 Boundary Conditions 141

6.2 Stationary AVA 144

6.2.1 Valve Opening & Closure 144

6.2.2 Vortex Coherent Structures 146

6.3 Accelerating AVA 150

6.3.1 Valve Opening & Closure . . . 151

6.3.2 Axial Movement of The AVA . . . 153

6.4 Valve Force Response . . . 156

7 Conclusion **159**

7.1 Summary of Investigation . . . 159

7.1.1 Applications . . . 162

7.2 Suggestions for Future Work . . . 164

7.3 Limitations . . . 166

7.3.1 Chapter 4 . . . 166

7.3.2 Chapter 5 . . . 167

7.3.3 Chapter 6 . . . 168

A **169**

A.1 Chapter 4 . . . 169

A.2 Chapter 5 . . . 171

A.2.1 Non-dimensional parameters derivation . . . 171

A.2.2 Simulation parameters . . . 173

A.2.3 Modelling Blood as a Newtonian Fluid . . . 173

A.2.4 Grid Dependence . . . 176

A.3 Chapter 6 . . . 177

A.3.1 Simulation Parameters . . . 177

Bibliography **178**

Nomenclature

AVA Aortic Valve Apparatus. i

BAV Bicuspid Aortic Valve. 8

CFD Computational Fluid Dynamics. 7

COM Centre of Mass. 71

ESS Endothelial Shear Stress. 6

FFR Fractional Flow Reserve. 15

FFT Fast Fourier Transform. 95

FSI Fluid-Structure Interaction. i

GOA Geometric Orifice Area. 23

HOCM Hypertrophic Obstructive Cardio Myopathy. 15

ILT Interleaflet Triangles. 60

IVC Iso-volumic Contraction. 31

IVR Iso-volumic Relaxation. 31, 142

LA Left Atrium. 11

LAD Left Anterior Descending. 14

LCA Left Coronary Artery. 14

LCS Left Coronary Sinus. 14

LCX Left Circumflex. 14

LV Left Ventricle. 11

LVOT Left Ventircular Outflow Tract. 15

OSI Oscillatory Shear Index. 53

pchip Piece-wise Cubic Hermite Interpolating Polynomial. 142

PIV Particle Image Velocimetry. 59

RA Right Atrium. 14

RCA Right Coronary Artery. 14

RCS Right Coronary Sinus. 14

RV Right Ventricle. 14

STJ Sinotubular Junction. 60

SVD Singular Value Decomposition. 73

TAV Tricuspid Aortic Valve. 9

UDF User Defined Function. 118

WIA Wave Intensity Analysis. 12

WSS Wall Shear Stress. 54

List of Figures

2.1 The aortic root 4

2.2 Flow field in a hypoplastic aortic arch. 6

2.3 4D flow in a stenosed aortic valve. 8

2.4 ESS distribution on valve leaflets in TAV vs. BAV. 9

2.5 Temporal blood flow patterns in TAV vs. BAV. 10

2.6 Depiction of the reservoir function owing to arterial compliance. 11

2.7 Pressure waves' movement in the elastic artery. 13

2.8 Coronary artery anatomy. 14

2.9 WIA in a control vs. diseased patient. 16

2.10 Aortic Root vortices. 17

2.11 Bellhouse experimental apparatus and velocity quantification. 18

2.12 Aortic Root vortices post valve sparing surgery. 19

2.13 Aortic Root reconstruction using sonomicrometric crystals. 21

2.14 CFD results after applying the temporal motion to the aortic root. 22

2.15 Aortic root valve sparing techniques. 23

2.16 CFD results post-operative corrective surgery of the aortic root showing ESS. . . 24

2.17 Yacoub I and Yacoub II surgical procedures. 25

2.18 CFD results of the Yacoub I procedure. 26

2.19 CFD results of the Yacoub II procedure. 27

2.20 Depiction of the cardiac anatomy. 29

2.21 Longitudinal section of the aortic root. 30

2.22 Temporal dynamic behaviour of the aortic root in sheep. 31

2.23 Aortic root force response. 32

2.24 Coronary artery acceleration. 33

2.25 Aortic root acceleration. 34

2.26 Aortic motion. 36

2.27 Velocity vectors in the aorta at late systole. 39

2.28 Schematic of the temporal 3D blood flow in the healthy aorta. 40

2.29 Flow in an obstructed pulmonary homograft. 41

2.30 Flow field in a healthy LV obtained from 4D flow. 42

2.31 Velocity traces from 4D flow at mid systole. 44

2.32 A depiction of the Windkessel model showing the arterial system. 45

2.33 0D Windkessel model of the arterial system. 46

2.34 Different numerical models. 47

2.35 Non-invasive WIA results. 49

2.36 1D coronary FFR. 50

2.37 3D CFD simulation results in a simplified geometry mimicking the aorta. 52

2.38 3D CFD simulation results in a healthy aorta. 52

2.39 3D CFD simulation results with the moving wall method in a healthy aorta. . . 54

2.40 A schematic outlining the FSI technique. 55

2.41 FSI results in a normal aortic root. 57

2.42 A picture of the pulse duplicator modelling the left heart. 58

2.43 Velocity contours and streamlines from the pulse duplicator after post-processing. 59

2.44 AVA longitudinal section. 60

2.45 Cardiac fibrous skeletal body. 61

3.1 Flow chart outlining the plan of investigation 64

4.1 Formalised definition of the AVA. 68

4.2 Fiducial point selection on a reconstructed AVA. 70

4.3 Absolute position of the AVA fiducial points for two frames in the measured cycle. 72

4.4 AVA axis of best fit temporal movement. 73

4.5 Temporal movement of the AVA after alignment with the z axis. 74

4.6 Temporal movement of the AVA after decomposing the bending motion. 76

4.7 Temporal movement of the AVA after decomposing the axial stretching motion. 77

4.8 Temporal movement of the AVA after decomposing the segmental radial dilatations. 77

4.9 Temporal movement of the AVA after decomposing the torisonal movement. . . 79

4.10 Temporal percentage radial change in each segment of the AVA. 80

4.11 Sketch showing shape changes of the AVA from peak ejection to valve closure. . 82

4.12 Quantification of the *accordion* effect of the AVA. 83

4.13 Torsional movement of the AVA. 84

4.14 Sketch showing the interleaflet triangles of the AVA. 86

4.15 ILT's represented by the fiducial points. 87

4.16 Temporal changes in the areas of the ILT's. 87

4.17 Dicrotic notch in an arterial pressure waveform. 89

4.18 Experimental results of the dicrotic notch in open chest dogs. 90

4.19 Different interpolation functions that can fit the discrete data. 93

4.20 A plot showing the acceleration in global coordinates and the AVA axis. 96

4.21 Displacement and acceleration of the AVA. 97

4.22 CT images of a patient around the time of valve closure. 98

5.1 Idealisation of the AVA anatomy. 102

5.2 Computational mesh of the idealised model. 104

5.3 ICEM CFD quality metrics histogram for the computational mesh. 105

5.4 Flow chart summarising the scenarios to be analysed using the idealised model with a steady inflow. 106

5.5 Variation of the non-dimensional force response of the orifice with orifice Reynolds Number. 113

5.6 CFD results from scenario 1. 114

5.7 Difference between a laminar solver and a turbulence model solver. 116

5.8 Depiction of the shutter mechanism of the orifice and linear rates of closure. . . 118

5.9 Effect of Re_o on $\widetilde{F}$ for a closing orifice 119

5.10 Effect of linear rate of closure on $\widetilde{F}$. 120

5.11 Effect of nonlinear rate of closure on $\widetilde{F}$. 121

5.12 Axial motion of the orifice with a constant GOA. 123

5.13 Orifice wall motion boundary condition. 124

5.14 Flow field for an orifice moving with a frequency of 1 Hz. 125

5.15 Relative velocity between the inflow condition and the velocity of the orifice moving at a frequency of 1 Hz. 126

5.16 Orifice force response at 1 Hz. 127

5.17 Flow field for an orifice moving with a frequency of 2 Hz. 128

5.18 Relative velocity between the inflow condition and the velocity of the orifice moving at a frequency of 2 Hz. 129

5.19 Orifice force response at 2 Hz. 130

5.20 Flow field for an orifice moving with a frequency of 10 Hz. 131

5.21 Relative velocity between the inflow condition and the velocity of the orifice moving at a frequency of 10 Hz. 131

5.22 Orifice force response at 10 Hz. 132

5.23 Physiological wall motion boundary condition for the orifice. 134

5.24 Flow field for an orifice moving with a physiological displacement. 135

5.25 Orifice force response at a physiological frequency. 137

5.26 Orifice force time response focused at the time of valve closure. 138

6.1 FSI flowchart. 140

6.2 CT derived inflow boundary condition. 142

6.3 Temporal valvular motion for the stationary AVA. 144

6.4 Temporal changes in the stationary AVA valve GOA. 146

6.5 Vortex coherent structures in the AVA. 148

6.6 Velocity streamlines in the AVA at late systole. 149

6.7 Prescribed AVA acceleration as a boundary condition. 150

6.8 Temporal valvular motion for the accelerating AVA. 151

6.9 Temporal changes in the accelerating vs. stationary AVA valve GOA. 152

6.10 Temporal axial movement of the AVA. 153

6.11 Temporal axial movement of the annulus of the AVA. 155

6.12 Valve force time response for the stationary and accelerating AVA's. 156

6.13 Valve force frequency response for the stationary and accelerating AVA's. 157

A.1 Quantification of the AVA modes of deformation by R.M.S mean. 170

A.2 Relationship between viscosity and shear strain rate. 174

A.3 CFD testing of Newtonian vs. Non-Newtonian blood models. 175

A.4 Grid Dependence 177

Part I

Chapter 1

Introduction

1.1 Motivation

This thesis is a study of the effect of the acceleration of the aortic root on adjacent blood flow. The concept of the acceleration of the aortic root has not been quantitatively discussed in the literature with regards to its impact on blood flow. We present a theory that the acceleration of the root at the time of valve closure may be the cause of the dicrotic notch and may be used as a non-invasive diagnostic parameter for a wide range of cardiac diseases.

Four patients used in this study were admitted to Aswan Heart Centre for chest pain and were discharged for being normal after undergoing CT imaging. All patients signed consent forms declaring that their imaging data may be used for research purposes.

1.2 Statement of Originality

I hereby declare as the primary author of this thesis that all the hypotheses, results and discussions are original as a result of my own independent research and work unless otherwise referenced.

I also declare that Imperial College London is the only entity with full rights to this work which

has not been submitted to any other academic or non-academic institution in fulfilment of any form of education or academic award.

1.3 Copyright Declaration

The copyright of this thesis rests with the author. Unless otherwise indicated, its contents are licensed under a Creative Commons Attribution 4.0 International Licence (CC BY 4.0).

Under this licence, you may copy and redistribute the material in any medium or format. You may also create and distribute modified versions of the work. This is on the condition that: you credit the author.

When reusing or sharing this work, ensure you make the licence terms clear to others by naming the licence and linking the licence text. Where a work has been adapted, you should indicate that the work has been changed and describe those changes.

Please seek permission from the copyright holder for uses of this work that are not included in this licence or permitted under UK Copyright Law.

1.4 Publications

Partial work from Chapter 4 has been published in affiliation with Imperial College Bioengineering Department in May 2020 in the Proceedings of the IMechE Part H under the title:
"Mechanics of the dicrotic notch: An acceleration hypothesis."
Although the publication is the original work of the author, it was referenced appropriately throughout the thesis.

Chapter 2

Literature Review

2.1 Clinical Background

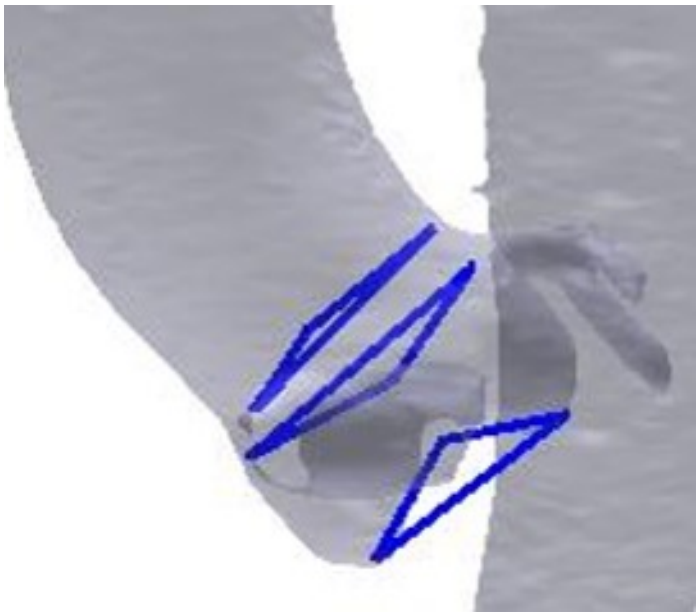


Figure 2.1: The aortic root reconstructed from CT imaging.

The aortic root is a moving structure working under pulsatile pressures and cyclic loading. It has a primary role of maintaining unidirectional oxygenated blood flow to the aorta during the cardiac cycle via its unique structure, flexible walls and dynamic valve [1]. Figure 2.1 shows a zoomed image of an aortic root reconstructed from CT imaging. The blue triangles in the figure bottom up show a representation of the annulus, commissures and STJ which is explained in

further detail in Chapter 4. The aortic valve sits in between the bottom and middle triangles in the figure.

Different functions of the aortic root are necessary to perform its varied vital roles [2],[3]. These functions are the conduit function, the valve function, the reservoir function and the coronary function [2]. Since the aortic root is dynamic, coupling between its temporal movement and blood flow is a challenging area of research.

In the coming sections of this review, the varied functions of the aortic root will be discussed in more detail to show the strong coupling between them. Moreover, a description of the interaction between the structure and function of the aortic root will be outlined based on previous state-of-the-art research. It will be revealed that some of the research about this complex interaction revolves around implications for clinical intervention while others revolve around normal physiology of the aortic root.

In addition to this, a review on previous research focused on the dynamic deformations of the aortic root will be discussed with the purpose of highlighting how such deformations may play a key role in controlling the flow distribution in the aortic root and thus affecting the aortic valve along with the other functions.

Finally, a review on the current state-of-the-art computational methods will be presented as this will be the main tool to carry out the aim of this thesis to investigate the interaction between the movement of the aortic root and blood flow. Also, the concept of aortic root acceleration will be introduced to show how the close relationship between the acceleration and force in Newtonian mechanics suggests that ignoring acceleration a priori could be disadvantageous.

2.1.1 Varied Functions of The Aortic Root

Conduit Function

The conduit function is a general property of arteries which guarantees continuous unobstructed passage of blood flow to the peripheral organs and tissues. It depends primarily on arterial morphology (changes in cross-section) during the different phases of the cardiac cycle [2]. The conduit function which is offered by low local resistance in major arteries e.g. the aorta, may be negatively affected by anatomical changes as a result of arterial disease [2]. The main quantities used to investigate or assess the conduit function are arterial compliance and distensibility. Compliance is the relationship between fractional changes in volume due to changes in pressure while distensibility is a fractional change in area due to changes in pressure [2].

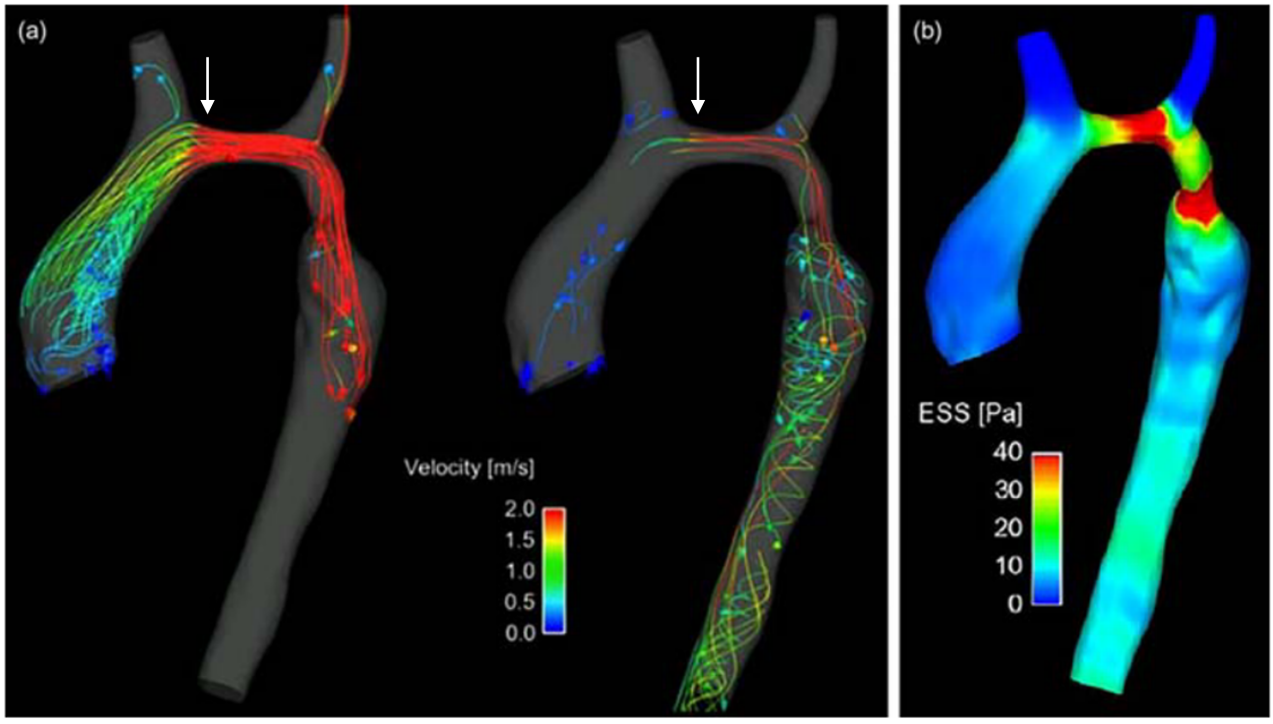


Figure 2.2: (a) Systolic (left) and diastolic (right) flow streamlines in patient with a hypoplastic aortic arch. (b) ESS for the same patient. (Reproduced from [4])

Although investigating compliance and distensibility may be challenging non-invasively, in Section 2.2 we will highlight some non-invasive methods depending on modelling and multi-modality imaging that provide state-of-the-art approximations and aid in clinical diagnoses. Other methods include quantifying velocity patterns and stresses on the conduit vessel wall in

the event of altered morphology.

Figure 2.2 shows preoperative flow patterns in a patient suffering from a hypoplastic aortic arch derived from Computational Fluid Dynamics (CFD). MRI images from the patient were used to provide inflow and outflow boundary conditions to augment the computational model. It is evident that the degraded conduit function of the aorta is manifested as a sudden rise in velocity present in both systole and diastole as indicated by the arrows in the figure. Moreover, the elevated values of Endothelial Shear Stress (ESS) present indicate danger of arterial rupture in the vicinity of the constriction [4]. Clinically speaking, atherosclerosis manifested by the presence of plaques or arterial stenosis (narrowing) is the main antagonist for a healthy conduit function [2].

Valve Function

Valve function is mainly concerned with the dynamic behaviour of the aortic valve to ensure unidirectional flow with the required cardiac output across the cardiac cycle [5]. The different paths followed by the valve leaflets during opening and closure have a direct effect on the flow upstream and downstream of the valve [6]. Additionally, the stress distribution over the surfaces of the valve leaflets determines their mobility [6]. Since conduit function is dependent on normal valve function, normal valvular motion is always needed to ensure continuous blood flow from the heart upstream of the aortic root to the rest of the body downstream.

Multiple methods exist for assessing valve function ranging from clinical tools to computational methods. Each method involves studying valve function from different perspectives. One of these perspectives involves studying the blood flow immediately downstream of the aortic valve when morphological changes in the aortic root walls are not dominant.

Such a scenario is possible on many occasions especially in middle-aged and older-aged patients [7]. In their study, Barker et al. investigated multiple scenarios of diseased aortic roots; however, one of the scenarios where aortic root morphological changes were not dominant was in the event of aortic valve stenosis.

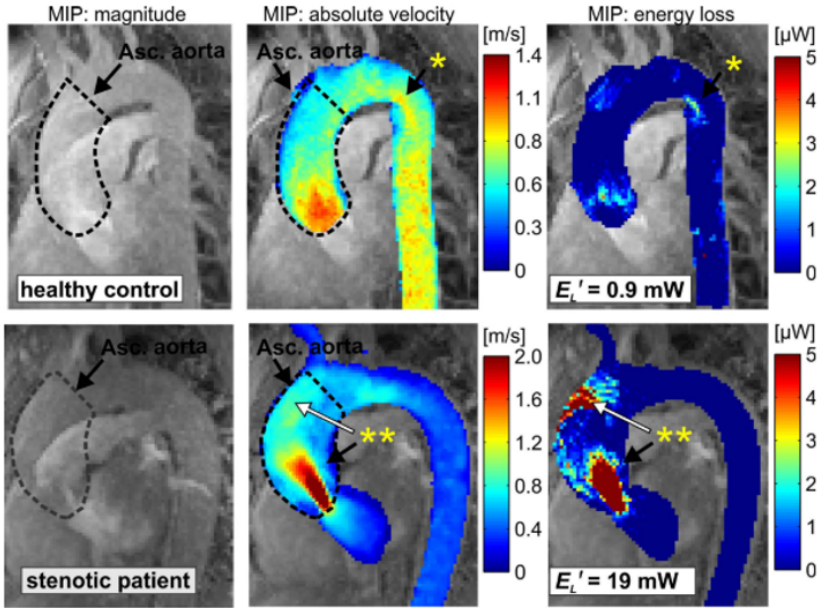


Figure 2.3: 4D flow deduced flow patterns in a control (top) vs. stenosed (bottom) aortic valve. (left) Anatomy from MRI image, (middle) magnitude of velocity from 4D flow, (right) calculated energy loss from 4D flow field. Energy loss was calculated from the viscous dissipation terms in the Navier-Stokes equations. (Reproduced from [7])

In this case, blood flow velocities immediately downstream of the aortic valve were a sufficient indicator of impaired valve function when compared to their values at the same spatial location in a control. Moreover, another parameter was included to assess adverse flow alterations in the aortic root i.e. viscous energy loss.

Figure 2.3 shows blood flow patterns in a healthy control compared to a patient with aortic valve stenosis. Extreme increases in flow velocity amounting to double the control value and altered flow patterns and increased viscous energy loss all point to a diseased aortic valve with impaired function [7]. As a result, the stenosed valve with impaired function is hindering the conduit function of the root.

Another example of impaired valve function tied with degraded conduit function is in Bicuspid Aortic Valve (BAV) disease. BAV disease is a highly common congenital defect affecting the aortic valve [8]. In BAV disease, two of the aortic valve leaflets are fused together causing the valve to have two leaflets instead of three.

The anatomical changes in the aortic valve in the event of BAV disease cause adverse flow patterns in the ascending aorta downstream of the valve. Not only do these flow patterns cause

dangers of negative remodelling to the aortic wall, they could be a potential cause of calcified aortic valves resulting in a higher degree of stenosis to the valve [8].

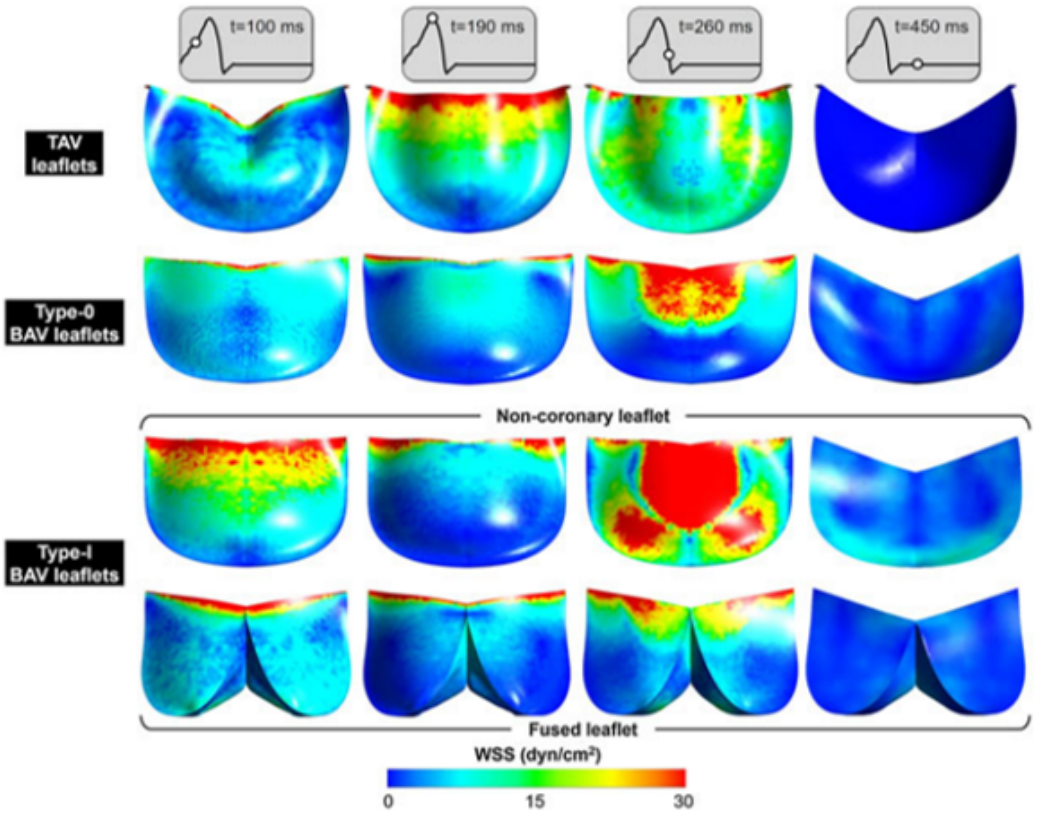


Figure 2.4: Temporal ESS distribution on the aortic valve leaflets. (Row 1) TAV leaflets (ventricular side). (Row 2) Type-0 BAV leaflets without leaflet fusion (ventricular side). (Row 3) Type-1 BAV non-coronary leaflet (ventricular side). (Row 4) Type-1 BAV fused leaflets (aortic side). (Reproduced from [8])

Figure 2.4 shows the temporal ESS distribution on the aortic valve leaflets in a normal Tricuspid Aortic Valve (TAV) versus two different types of BAV fusion anatomies. 3D FSI simulations were used as a method to evaluate the haemodynamics in these cases. The different ESS distribution showing elevated values in certain regions and lower values in others is a major indication of altered blood flow patterns [8].

In another study, Chandra et al. used 2D FSI simulations to look at the same problem. The main aim of the study was to see how the changes in flow patterns in the event of BAV impact the different layers of the impaired valve leaflets [9]. A byproduct of the study was to capture how the blood flow downstream of the valve becomes skewed in a way that limits the continuous flow rate and thus hinders the conduit function. This is possible since the rise

in pressure upstream of the malfunctioning valve as a consequence of its massively reduced orifice area in conjunction with recirculating flow regions downstream of the valve will result in reduced flow rate to the descending aorta.

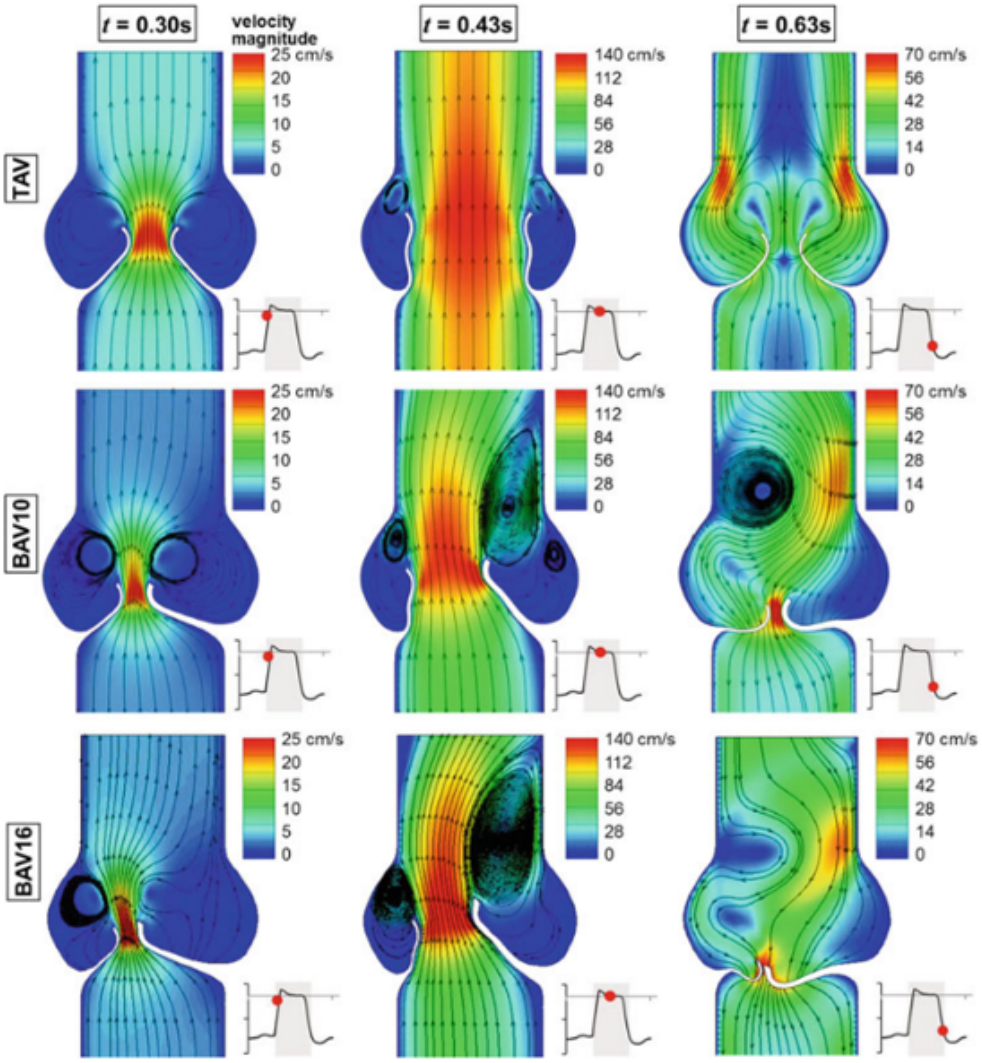


Figure 2.5: Temporal blood flow patterns in TAV vs. BAV. (Row 1) TAV model. (Row 2) Type-0 BAV leaflets without leaflet fusion. (Row 3) Type-1 BAV leaflets with leaflet fusion. (Reproduced from [9]

In Figure 2.5, the skewed jet downstream of the aortic valve is clearly evident in both types of BAV disease unlike in the normal TAV. The abnormal leaflet structure caused an adverse flow pattern that resulted in diminished cardiac output. Although CFD studies in different areas of research showed various differences between 2D and 3D velocity and vorticity fields, reduced order models like the 2D simulations presented by Chandra could still be useful in assessing the overall function of an impaired aortic valve.

Reservoir Function

The reservoir function is an inherent property of elastic tubes also known as compliant vessels. Similar to what was explained in the valve function section, the arterial system reservoir function always acts in conjunction with the conduit function [2]. With normal conduit function, the arteries manage to deliver unobstructed blood flow with direct support from the compliant nature of the elastic walls. The compliant vessels generally behave as a windkessel chamber which dampens pulsatility effects due to intermittent Left Ventricle (LV) ejection [2]. The LV which may be regarded as the heart pump ejects blood in the systolic phase of the cardiac cycle and relaxes in the diastolic phase where it fills with blood from the Left Atrium (LA) upstream [2].

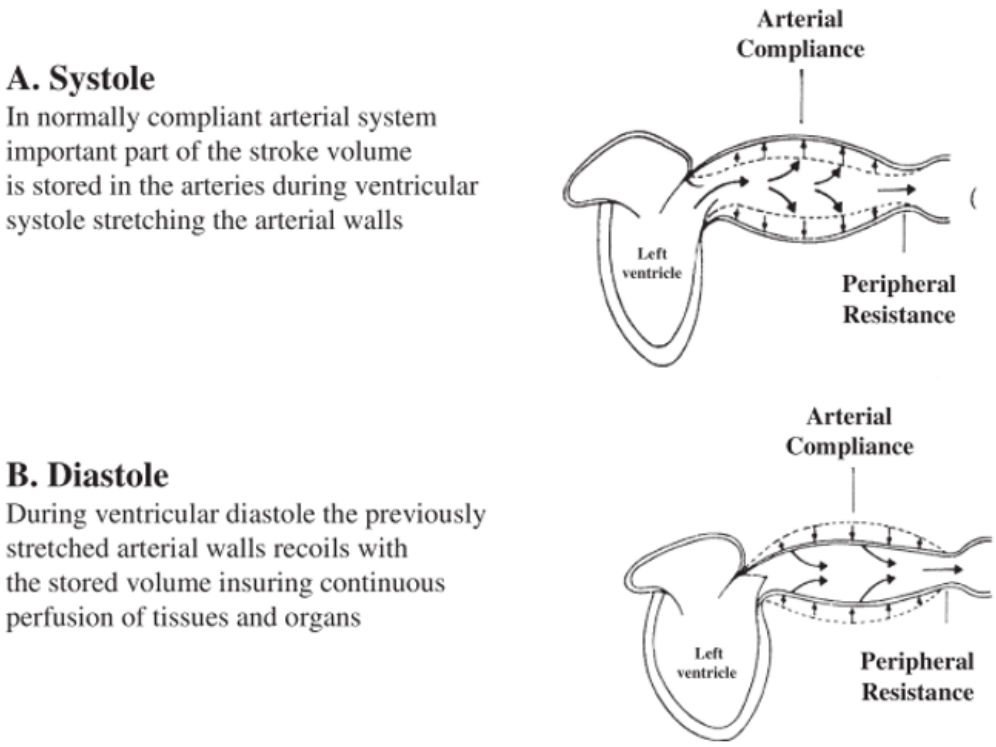


Figure 2.6: Depiction of the reservoir function owing to arterial compliance. (Reproduced from [2])

Figure 2.6 shows a simplified schematic of the aortic reservoir function. Initially during the systolic phase of the cardiac cycle, a significant fraction of blood flow gets stored in the volume created by the expanding arterial walls as shown in the top panel by the direction of the arrow heads. The amount of blood to be stored is dependent upon both the artery's peripheral

resistance and compliance [2]. This is because higher compliance will result in easier movement of the arterial wall in the outward direction to store blood while peripheral resistance regulates the flow rate to the periphery. On the other hand, during the diastolic phase of the cardiac cycle when the LV relaxes, the elastic walls recoil and maintain blood flow downstream in the absence of the LV pumping action after aortic valve closure [2].

The depiction in Figure 2.6 was described by Otto Frank in the 1890's through the windkessel model [10]. The windkessel model describes the arterial system as a closed hydraulic system with specific analogies. The LV is modelled as a pulsatile pump and the compliant arteries are modelled as a windkessel chamber with a volume of compressible air to mimic the elastic recoil effect of the elastic walls [10]. In mathematical terms, each property of the arterial system such as peripheral resistance, compliance and inertance are modelled as electrical circuit components. In later sections, we will see that due to uncertainties related to material modelling to simulate tissue response for computational methods to assess blood flow, the windkessel model may be coupled with 3D CFD to replicate the reservoir function [11],[12].

Another definition of the reservoir function is based on the reservoir-wave hypothesis explained by Parker [3]. The reservoir-wave hypothesis dictates that the exponential decay seen in the aortic pressure wave form is a resultant of the compliant nature of the artery in tandem with the pressure waves travelling in the elastic tube domain [3]. Separating each constituent of the reservoir-wave hypothesis depends on Wave Intensity Analysis (WIA) first derived by Parker from the 1D gas dynamics equations [3]. Unlike the windkessel model which is only a group of time dependent ordinary differential equations, WIA considered to be a 1D blood flow modelling method has been used in studies relating to coronaries and heart failure [13],[14].

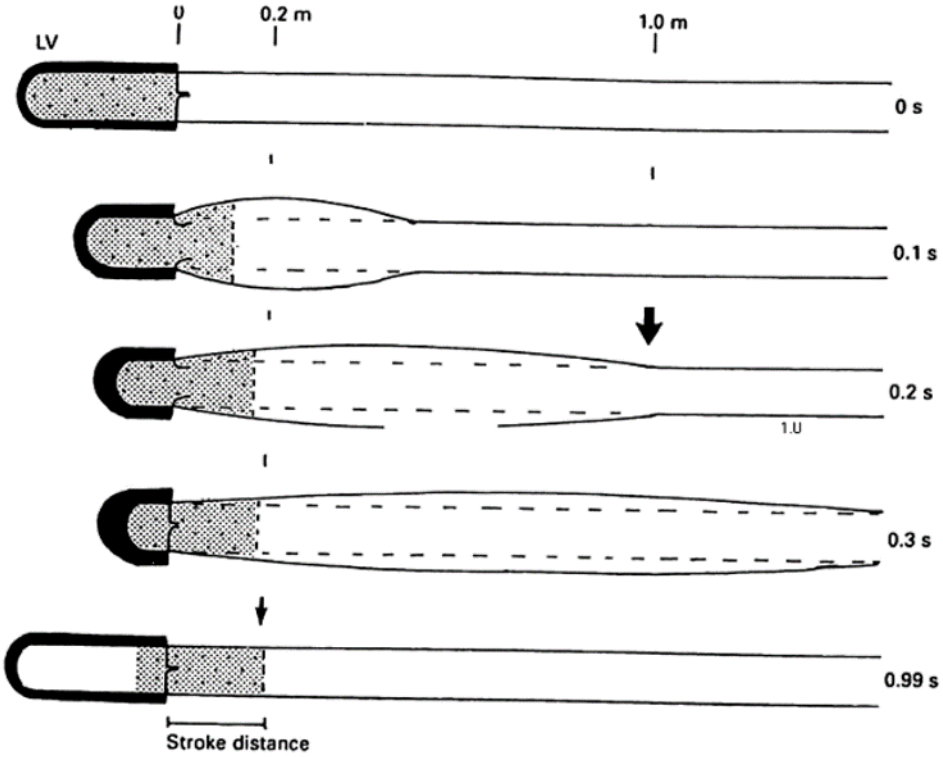


Figure 2.7: Pressure waves' movement in the elastic artery. The thick black arrow at 0.2 *s* shows the pressure wavefront of the forward compression wave. (Reproduced from [2])

Figure 2.7 combines both constituents of the reservoir-wave hypothesis in the simplified depiction. The pressure gradient between the LV and the aorta opens the aortic valve and propels blood forward. Simultaneously, the compliant walls begin storing potential energy while a pressure wave begins travelling forward. The pressure wave front is indicated by the thick black arrow (at 0.2 s). In the presence of morphological changes in the event of arterial disease, the mechanism of pressure waves travelling may be different and thus the overall reservoir function may be negatively affected.

Coronary Function

The coronary function is the last component in the varied functions of the aortic root. The coronary arteries, which are the main conduit vessels responsible for the coronary function, have a very complex anatomy. Their primary role is to perfuse the heart muscle and the myocardium throughout the cardiac cycle [15]. Each segment in the coronary arteries supplies a different area in the myocardium.

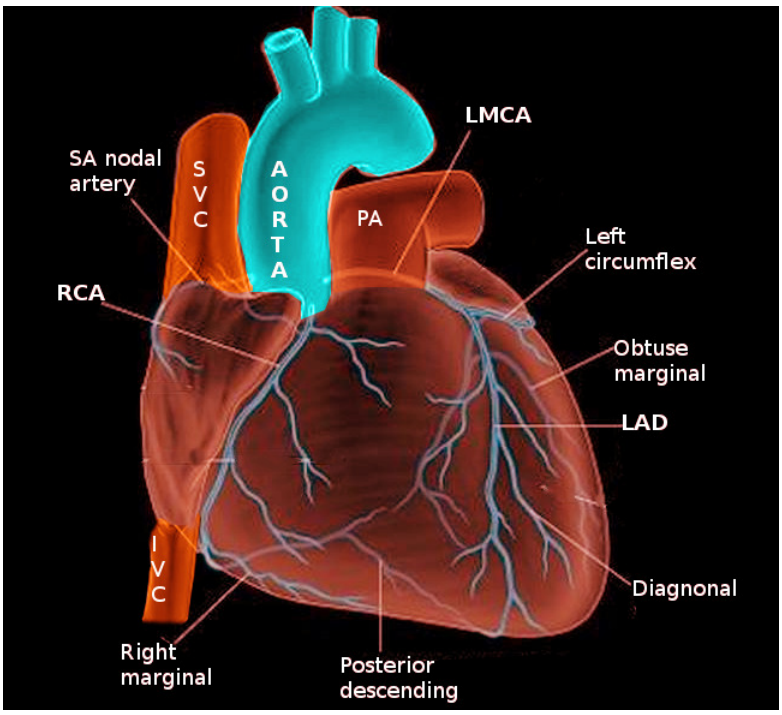


Figure 2.8: Coronary artery anatomy. The RCA originates in the RCS and the LCA originates in the LCS. The LCA bifurcates into the LAD and Left Circumflex branches. Each coronary artery perfuses a different area in the myocardium. (Reproduced from [15])

Figure 2.8 shows a graphic depiction of the coronary artery anatomy. The two coronary arteries named the Right Coronary Artery (RCA) and the Left Coronary Artery (LCA) originate in the aortic root at the Right Coronary Sinus (RCS) and the Left Coronary Sinus (LCS) respectively. The RCA supplies blood to the Right Atrium (RA) and Right Ventricle (RV) while the LCA supplies blood to the LA and LV [15]. The LCA bifurcates into two major arteries which are the Left Anterior Descending (LAD) and the Left Circumflex (LCX). The LAD is primarily responsible to supply the septum along with a large portion of the heart muscle.

In the event of any occlusive or obstructive disease to the coronary arteries known as Coronary Artery Disease, the myocardium malfunctions and thus the pumping ability of the LV is diminished [15],[16]. Since coronary structure and function are always coupled, methods to assess coronary function must offer an inclusive assessment that links both. With that said, it is worth noting that the LCA gives a rare occasion where its flow is diastolic dominant thus linking it to the intramyocardial pressure of the LV [17].

The gold standard to assess Coronary Artery Disease is a parameter called Fractional Flow

Reserve (FFR). FFR is the ability of a Coronary Artery to perfuse the myocardium under hyperaemia or exercise [12]. FFR provides a ratio between the proximal and distal pressures of a coronary artery during the diastolic phase of the cardiac cycle. Ideally, the ratio should be close to 1 to indicate no pressure losses; however, with certain severity in coronary artery disease the ratio may be much less thus indicating severe impairment of function. The cut-off value of FFR requiring medical intervention is below a value of 0.8 [12]. While it is invasively deduced by means of a catheter intervention, FFR is regarded as the gold standard in assessing coronary function since it eliminates possible subjectivity relating to the visual judgement of the clinician [18].

There have been recent developments in computational modelling giving rise to non-invasive methods to obtain the FFR parameter. Lo et al. managed to combine windkessel models explained in the Reservoir Function section coupled with CFD to deduce FFR [12].

Another popular method to diagnose coronary artery disease is WIA mentioned in Section 2.1.1 page 12. WIA separates the pressure waves transmitted through the arteries as a result of energy transfer between the elastic walls and blood flow into successive wavefronts [3]. Each pressure wave which may be characterised by its function and direction of travel, has a clinical significance tied to a physiological event.

In a study by Raphael et al., ischemia, a symptom of coronary artery disease, was captured using WIA [13]. The study focused on assessing patients with a hypertrophic obstruction in the Left Ventricular Outflow Tract (LVOT) known as Hypertrophic Obstructive Cardio Myopathy (HOCM). As seen in Figure 2.9, in this disease where the conduit function of the aortic root is impaired, the pressure wave separation is completely different from a control and the pressure and velocity waveforms in the coronary are thus adversely altered [13]. In other words as explained in the previous sections, the degraded conduit function in the aortic root led to a degraded coronary function which in turn led to impaired LV pumping.

Another vital factor affecting coronary function is the flow distribution in the aortic root. This also suggests that the aortic root structure and function may have an effect on coronary function. The aortic root flow vortices or recirculation regions which develop in the aortic sinuses during

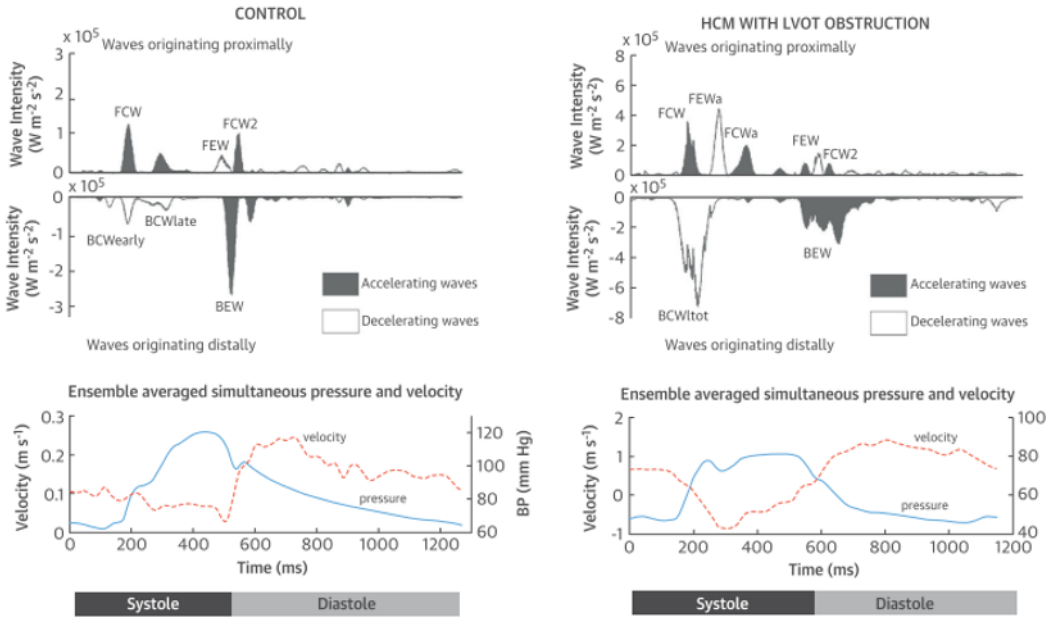


Figure 2.9: WIA in a control vs. diseased patient. (top) Wave separation in the left coronary of a control vs. HOCM patient. Impairment in the waves in the HOCM patient suggests the presence of myocardial ischemia. (bottom) Pressure and velocity waveforms which yield the wave separation. (Reproduced from [13])

late systole were always thought of as an inciter to valve closure [16]. Nonetheless, many studies from experimental to computational techniques started hypothesising that such flow behaviour in the aortic sinuses may play a critical role in serving coronary function. These studies state that the retarding flow within the bulging sinuses will rotate thus changing direction to fill the coronaries through their ostia which are located in the bulging sinuses [19], [20].

Mention of the flow vortices in the aortic root dates back to the 15th century through depictions by Leonardo Da Vinci [21]. Figure 2.10 shows the result of Da Vinci's experiment with the geometric layout of the aortic sinuses thought to be causing the formation of the flow vortices. Da Vinci used a glass model of an ox's aortic root through which he pumped grass seeds immersed in water as a rudimentary flow visualisation technique [21]. The vortices developing right above the aortic valve close to the coronary ostia may have a strong impact on coronary perfusion along with LV intramyocardial pressure previously mentioned.

Another experimental study carried out by Bellhouse et al. in the 1960's used a similar methodology to investigate flow vortices in the aortic root [19]. Using a rigid model of the aortic root, Bellhouse et al. managed to quantify average coronary velocities as a ratio of average aortic

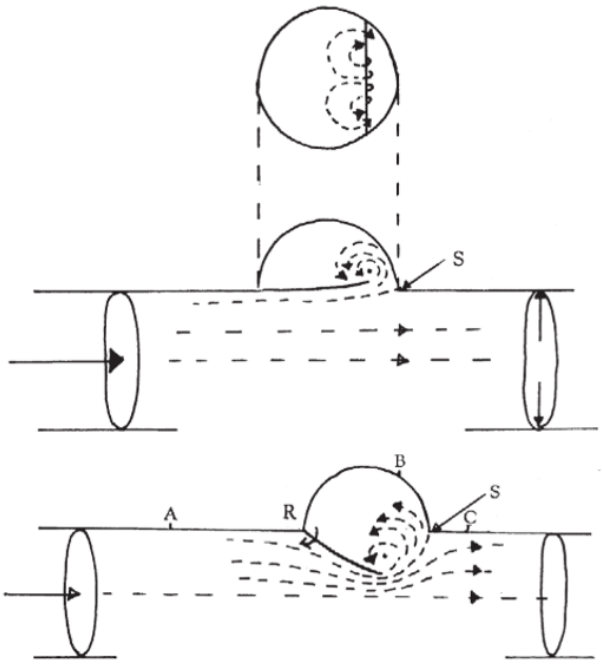


Figure 2.10: Aortic Root vortices as depicted by Leonardo Da Vinci. (Reproduced from [21])

velocities in four different phases of the cardiac cycle [19].

Figure 2.11 is an overview of the experiment conducted by Bellhouse. Figure 2.11a shows the flow distribution in the rigid tube with sinuses replicating the aortic root anatomy. The top panel in the figure shows the quasi-steady phase of the cardiac cycle which is also known as the peak systolic phase. In this phase the aortic valve leaflets are aligned with the aortic wall longitudinally and a small vortex forms at the tip of the leaflet [19]. The bottom panel shows the deceleration or late systolic phase where the valve leaflets are in the process of closing. The small vortex initially formed at peak systole begins expanding and filling the coronary sinus along with the coronary artery [19].

In Figure 2.11b, Bellhouse's temporal quantification of coronary velocities relative to aortic velocities is presented for three different anatomical scenarios. The scenarios include a stenosed valve with a coronary ostium located in the sinus, a normal valve with a coronary ostium located



(a) Experimental Apparatus

Pulsatile flow	Average coronary velocity / Average aortic velocity: Stenosed valve Sinus ostium (*B*)	Normal valve Aortic ostium (*C*)	Normal valve Sinus ostium (*B*)
(1) Non-reversing	−2·164	−0·253	−0·111
(2) Valve just closing	−1·273	+0·179	+0·357
(3) Valve closing firmly	−0·239	+1·208	+1·417

(b) Velocity Quantification

Figure 2.11: Bellhouse experimental apparatus and velocity quantification. The experiment shows the development of the aortic vortices in the sinus while the quantification shows the average coronary velocities as a fraction of the average aortic velocities. (Reproduced from [19])

upstream in the aorta and a normal valve with an ostium in the sinus. From the ratios presented, the location of the coronary ostium in conjunction with valve function may have a direct effect on coronary function [19].

Basic experiments like the works of Da Vinci and Bellhouse laid down the groundwork for the use of modern day multi-modality imaging or computational methods to investigate the structure-function interaction between the aortic root and the coronaries. In a study by Bissell et al., the authors claimed to confirm the presence of aortic root vortices initially predicted by Da Vinci using 4D flow [16]. Other studies were built on this research with implications for corrective valve sparing surgeries in the aortic root. In Section 2.1.2 we explain how surgical techniques like the Yacoub I and Yacoub II techniques to treat ascending aortic aneurysms

focus on maintaining sinus flow vortices post-operative.

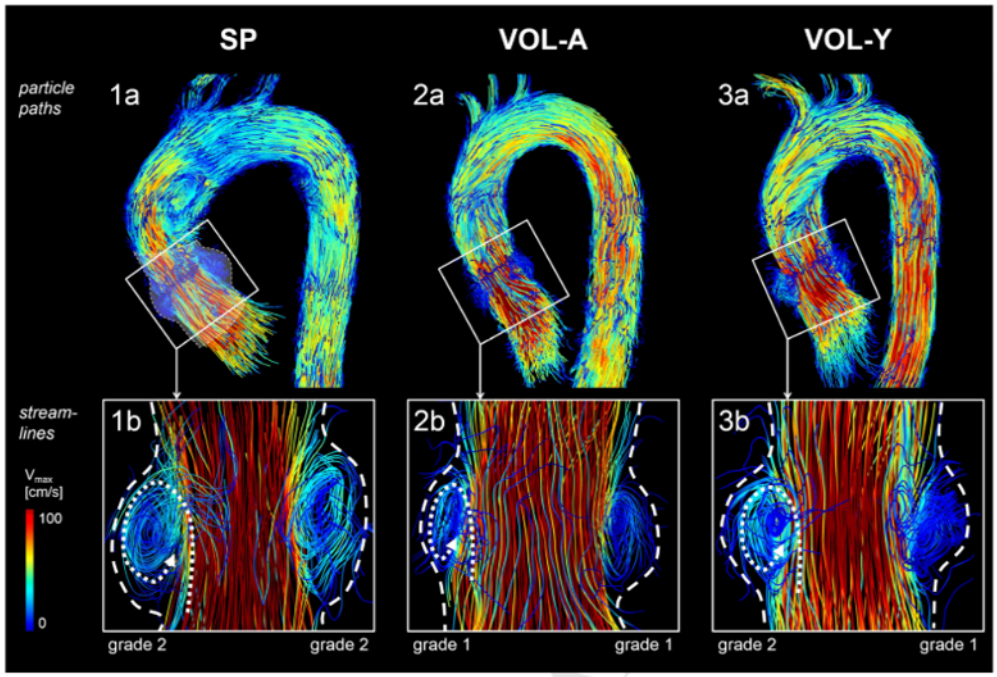


Figure 2.12: Aortic Root vortices post valve sparing surgery. Streamlines in the sinuses are shown in a sinus prosthesis vs. an aged and young healthy volunteers. (Reproduced from [20])

Oechtering et al. used 4D flow to visualise and assess the vortices in a sinus shaped prosthesis post valve sparing surgery compared to aged and young normal controls [20]. They graded the formation of sinus vortices based on average velocities and used it as a metric to evaluate the conduit and thus coronary function post valve sparing surgery. Figure 2.12 shows the results post-operative versus aged and young controls. This highlights the importance of linking structure and function of the aortic root in clinical decisions such as complicated corrective surgery [20],[22].

In conclusion, the varied functions of the aortic root are strongly coupled and assessing them requires extensive knowledge of the normal physiology of the aortic root before investigating different scenarios of cardiac disease.

2.1.2 Aortic Root Structure & Function Interaction

As explained in Section 2.1.1, the aortic root as a complex dynamic structure is greatly affected by morphological changes that directly impact on blood flow. In this section, studies attempting to investigate this complicated interaction will be discussed.

Many of the studies aimed at assessing aortic root morphological changes or structure to blood flow or function were focused on the clinical relevance of certain corrective surgical techniques. Other studies were focused on providing an understanding of normal aortic root physiology. Presenting an inclusive review of a wide range of studies with different objectives will be beneficial in highlighting the importance of the interaction of the structure and function in the aortic root.

One extensive study by Berdajs et al. used different *in vivo* and *in silico* techniques to investigate the temporal aortic root morphology linked to blood flow [6]. The study used surgically implanted sonomicrometric crystals in porcine aortic roots to track the dynamic movement of the aortic root during the cardiac cycle. The tracked movement of the crystals implanted at the valve commissures and annulus was used to provide a temporal reconstruction of the aortic root [6]. Invasive probes were also used during the implantation surgery to obtain temporal pressure and velocity readings. The obtained readings were then used in a dynamic CFD simulation to investigate the effect of aortic root bending and torsion on blood flow distribution in the aortic root [6].

Figure 2.13 shows Berdajs' reconstruction of the aortic root using the implanted sonomicrometric crystals. The Berdajs triangles presented a geometrical definition of the aortic root that enables dynamic tracking of its motion. A similar technique adopted in this study will be presented within the scope of this thesis. The tilt or bending angle is the angle between the solid and dashed arrows in Figure 2.13 (A) while the torsion angle is between the solid and dashed lines in Figure 2.13 (B). The tracked motion of the root showed a decrease in the tilt angle and the torsion angle during systole with a trough at the peak systolic phase. This suggests that there was a constant reduction in size for the triangle between the RCS and LCS [6]. It will be

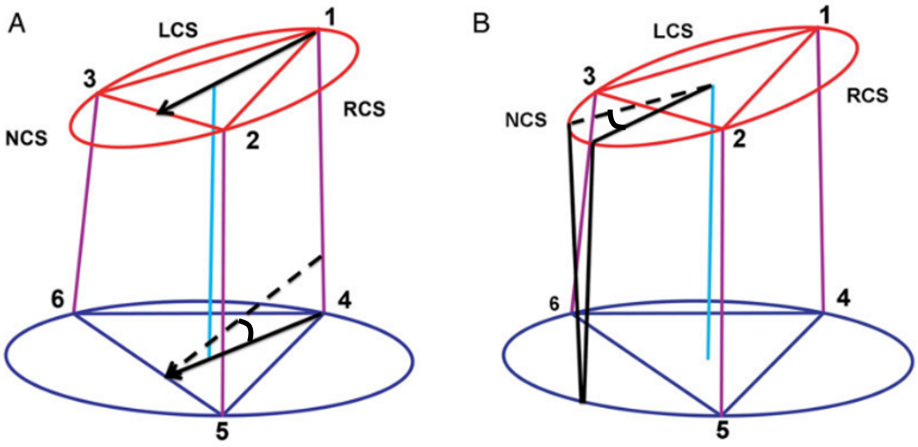


Figure 2.13: Aortic Root reconstruction using sonomicrometric crystals. (A) Tilt angle. (B) Torsion angle. The angles are between the dashed and solid arrows. (Reproduced from [6])

shown in the coming sections that we obtained similar results in the human aortic root.

The CFD results of applying the temporal motion tracking of the aortic root to the 3D reconstructed images are shown in Figure 2.14. The main parameters used to assess the interaction between the morphological changes of the root and blood flow are ESS and Pressure. The main conclusion from their study was that the dynamic motion of the aortic root changed its shape from a straight cylinder in peak systole to a frustum cone in diastole. The CFD results further showed that these changes in shape lowered the ESS and pressure gradient during peak systole which may facilitate ejection while being able to withstand the valve loading during diastole [6]. It is also worthy to note that the elevated values of ESS were usually present around the leaflet free edges or commissures thus corresponding to areas of low pressures throughout the cardiac cycle. This study by Berdajs is considered to fall under the category of investigating normal physiology and was later extended to assess corrective surgical techniques [6].

Berdajs et al. managed to use the methodology and results from the physiological study to assess two different corrective surgical techniques. Studies of this sort may have an impact on the benefit to the patients when it comes to choosing the appropriate surgical technique to restore optimal function.

Aortic aneurysm is a disease that requires corrective surgery. While it may or may not have negatively impacted the aortic root, aortic root replacement using synthetic material is nec-

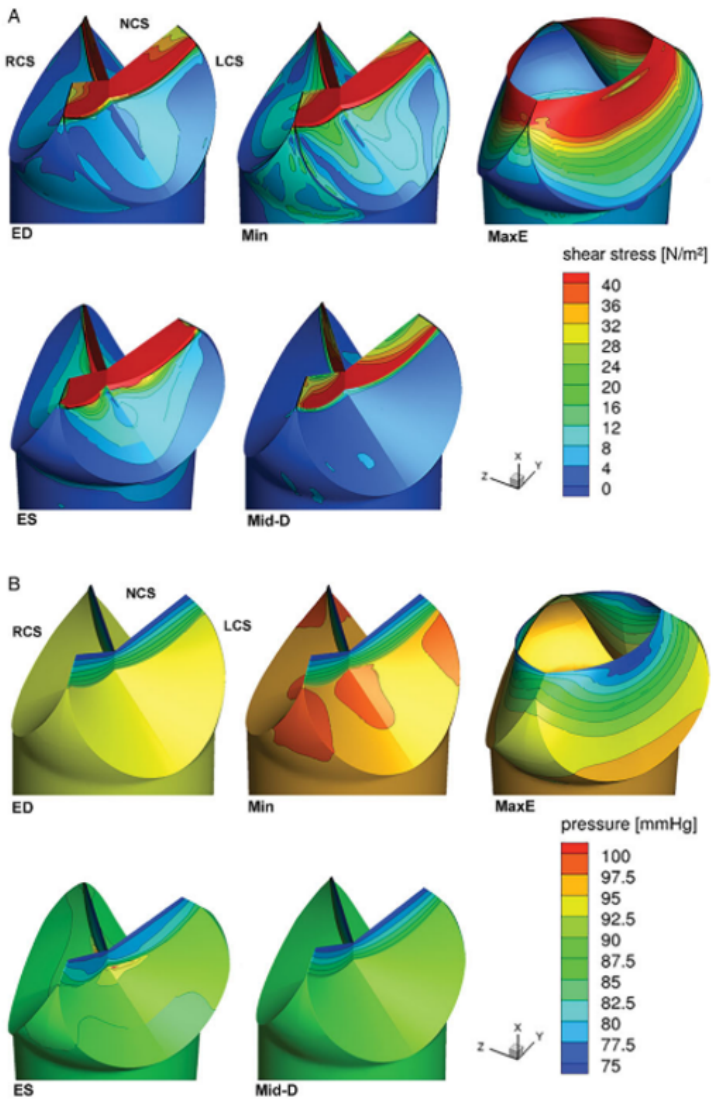


Figure 2.14: CFD results after applying the temporal motion to the aortic root. (A) ESS. (B) Pressure. (Reproduced from [6])

essary [23]. Figure 2.15 shows a depiction of two widely used corrective surgical techniques. Both techniques have been implemented to spare the aortic valve with the intent to maintain optimal valve function post-operative. The main difference is that in the Yacoub operation, the aortic root is remodelled for every patient based on their aortic root sizing unlike the David operation which re-implants the valve in a new synthetic aortic root [23].

Berdajs et al. managed to assess the aortic root function post the Yacoub and David operations comparing the results from CFD to the native porcine root analysed in the physiological study. The results showed that the David operation did not deliver the optimal flow patterns in the aortic root compared to the Yaocub operation post-operative where optimality is defined

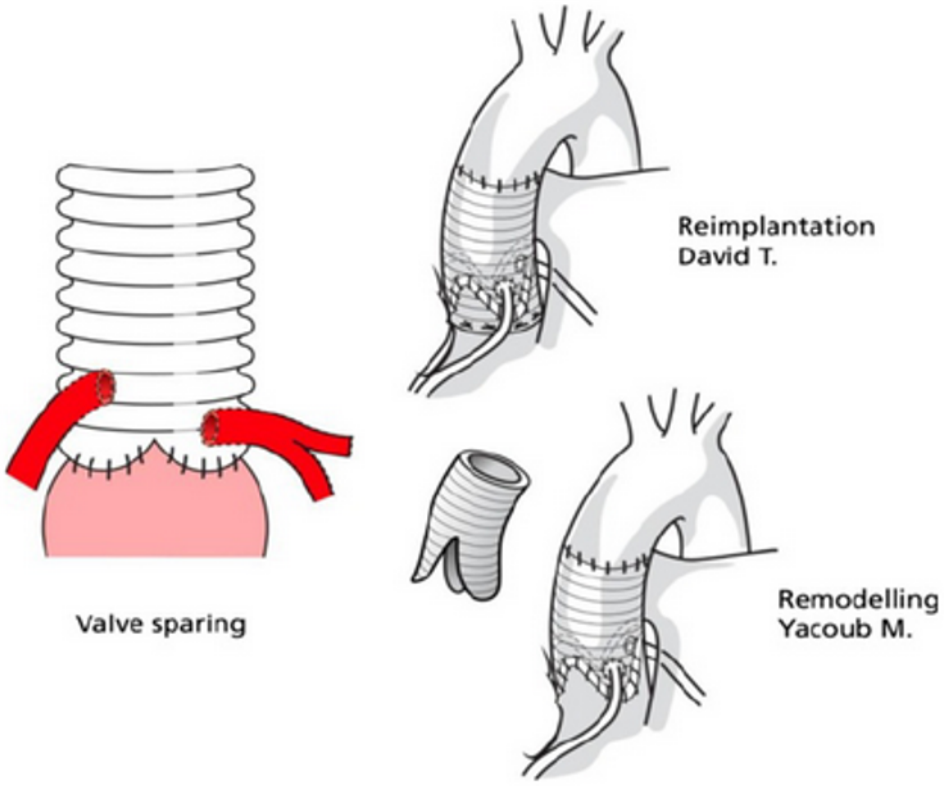


Figure 2.15: Aortic root valve sparing techniques. The diseased segment of the aorta is replaced with a graft while sparing the native valve of the patient. (Reproduced from [23])

as closest to the pre-pathological conditions [24]. The latter statement was concluded after comparing both techniques to the native porcine root in the physiological study. The summary of these results is shown in Figure 2.16.

Berdajs stated that the David operation resulted in high pressure gradients and low ESS for 2/3 of the cardiac cycle unlike the Yacoub operation [24]. The unfavourable function in the aortic root after the David procedure may be seen clearly in Figure 2.16 (A) and (B) panels labelled Max referring to the peak ejection phase. The area of the open valve also known as the Geometric Orifice Area (GOA) was visibly larger in the Yacoub operation thus showing better ejection and overall function of the spared valve and aortic root [24].

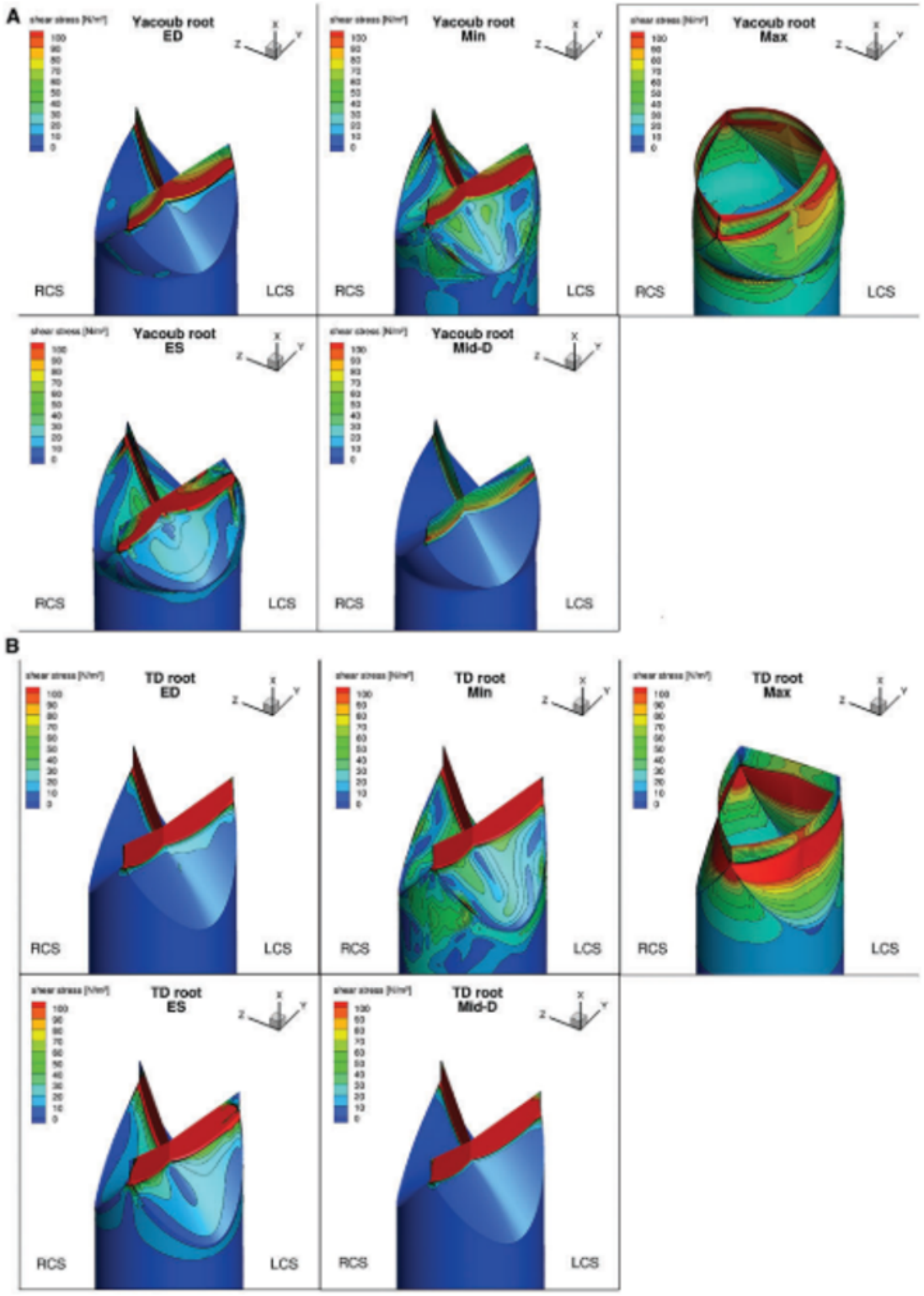


Figure 2.16: CFD results post-operative corrective surgery of the aortic root showing ESS. (A) Yacoub. (B) David. (Reproduced from [24])

Another extensive study conducted by Yacoub et al. resulted in the development of a new surgical technique i.e Yacoub II, to restore the function of the aortic root post valve sparing surgery. Their study contained comparison to controls from the same ethnic background, age, gender and physique thus including normal physiology in conjunction with surgical techniques to have a broad perspective in assessing the interaction between the structure and function of the aortic root [25],[26].

The first half of their study was focused on assessing the function of the aortic root by comparing post-operative Yacoub I patients to controls. The second half demonstrated a new surgical technique, namely Yacoub II, and was assessed using the same methods as the Yacoub I. Both studies relied on multimodality imaging and CFD to deliver a quantitative investigation of both surgical procedures.

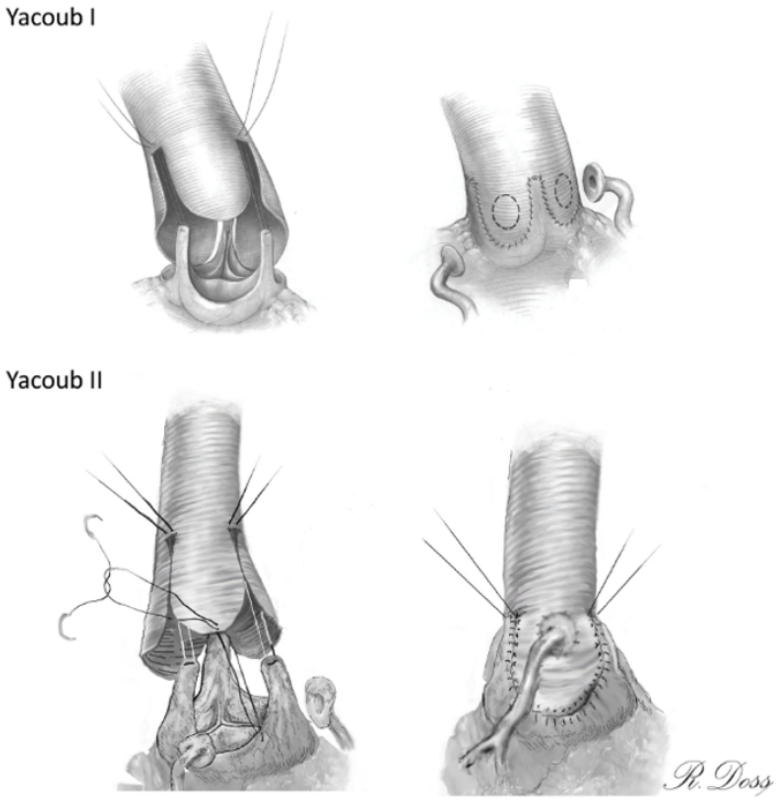


Figure 2.17: Yacoub I and Yacoub II surgical procedures. Please see following text for detailed description of the procedures. (Reproduced from [26])

Based on the drawings in Figure 2.17, the Yacoub I and Yacoub II techniques are very similar with only one main difference. As explained in Figure 2.15, the Yacoub I procedure is a valve

sparing technique that involves remodelling of the aortic root using a sinus graft to replace the diseased or aneurysm segment of the ascending aorta. The Yacoub II technique shares the same objective as the Yacoub I to spare the valve post corrective surgery; however, with a morphological modification at the commissures. The Yacoub II technique involves cutting three small inverted triangles at the commissure points along with remodelling of the graft [26]. This modification to the Yacoub I operation results in a tighter sinotubular junction and larger sinus bulges. Not only is the idea to restore the function of the aortic root, but also to make the technique usable on sinusless grafts as was performed in their study [26]. In other words, the Yacoub II technique gives the opportunity to create anatomical aortic root sinuses from a sinusless graft. This is considered an advantage based on the discussion in Section 2.1.1 about the role of the sinuses in fulfilling multiple functions in the aortic root.

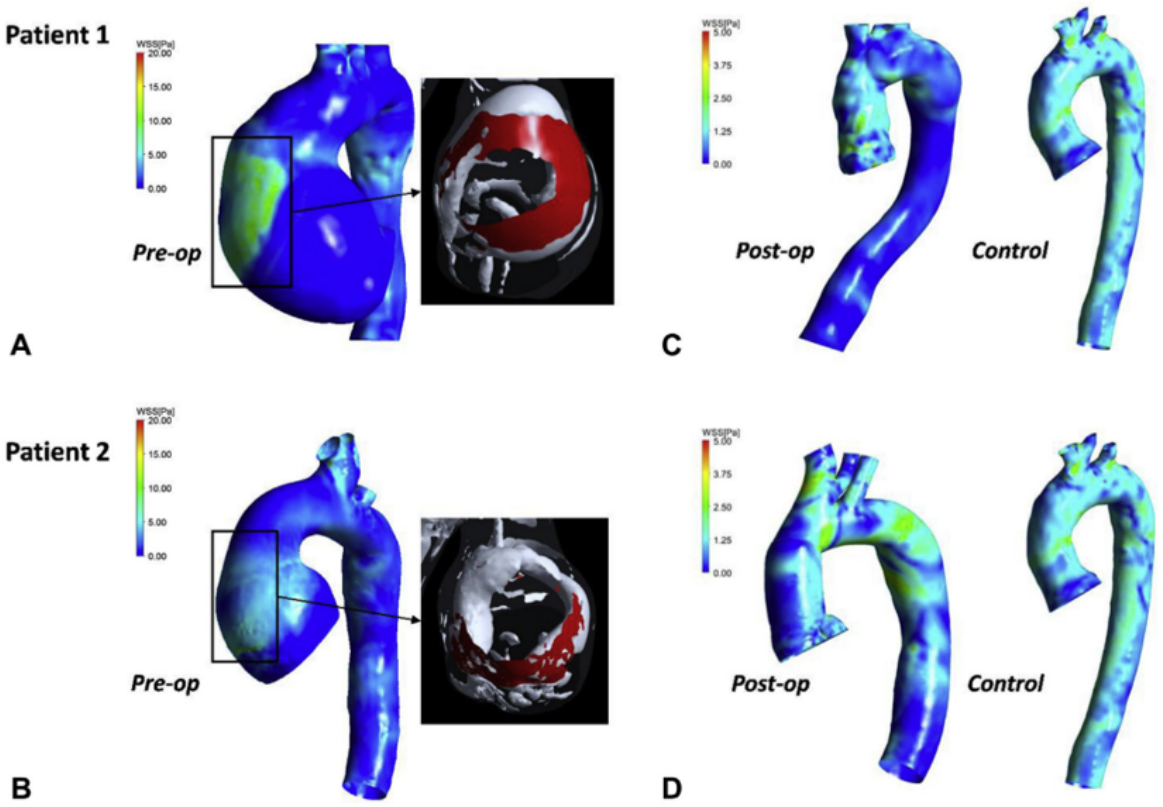


Figure 2.18: CFD results of the Yacoub I procedure. (A&B) Pre-operative ESS distribution on the anterior wall of the aorta with the corresponding vortex structures showing flow impairment. (C&D) ESS distribution post-operative showing similarities with age-matched controls. ESS values in A&B capped at 20 Pa and 5 Pa in C&D. (Reproduced from [25])

The results of the post-operative Yacoub I technique are represented in Figure 2.18 in terms

of the ESS. Panels A and B show the two diseased patients pre-operative while panels C and D show their results post-operative with their controls respectively. Both patients showed an abnormal distribution of ESS with elevated values concentrated in the anterior wall of the ascending aorta and near zero values in the rest of the aorta. The abnormal distribution of ESS owes to an adverse velocity distribution during the peak ejection or peak systolic phase of the cardiac cycle where a velocity jet impinges on the anterior wall of the ascending aorta. In both cases post-operatively, the distribution of ESS returned to a more favourable distribution as compared to controls thus implying restoration of structure and function in the aortic root. In addition to this, the insufficiency in the valve function was eliminated with an absence in aortic valve regurge (back flow through the aortic valve) post-operative [25].

Another crucial outcome of this study was the changes in the shape of the aortic annulus over the cardiac cycle. The annulus changed shape from near circular to a more elliptical shape from systole to diastole thus agreeing with the results presented by Berdajs et al. in their physiological study [25].

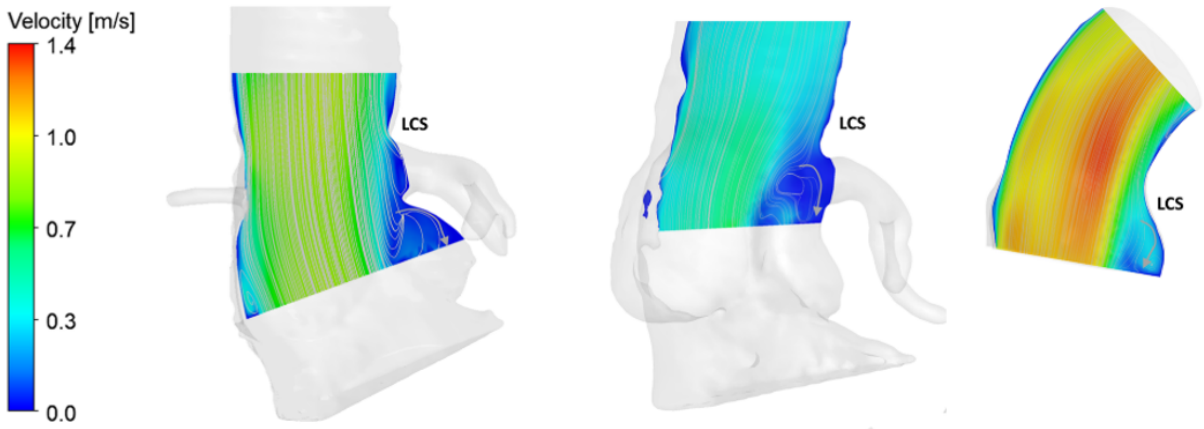


Figure 2.19: CFD results of the Yacoub II procedure. Two patients compared to an age-matched control show similar flow distribution in the LCS. Grey arrows show direction of flow rotation. (Reproduced from [26])

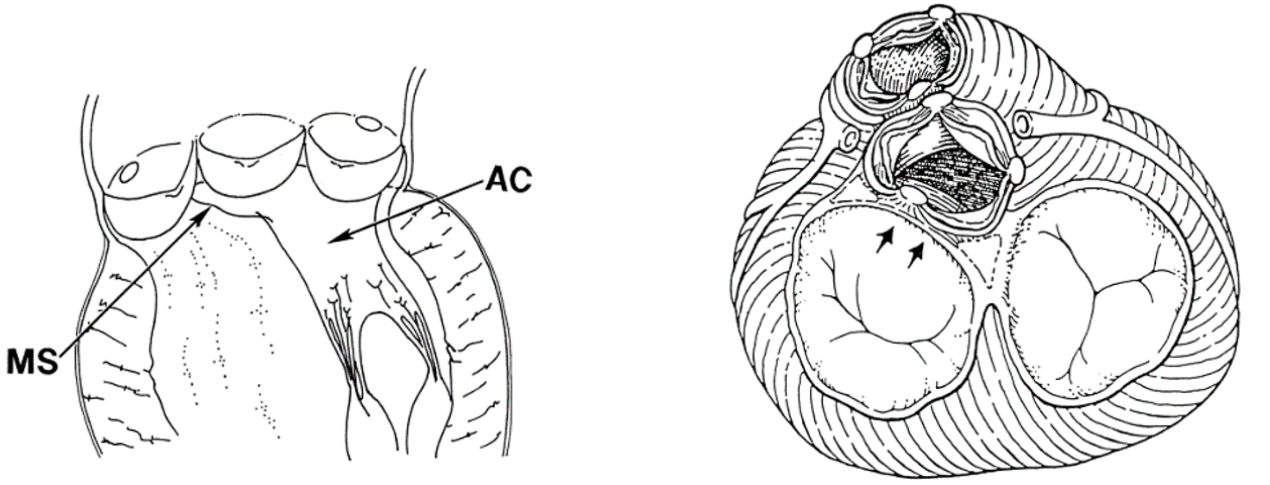
The second phase of the study where the novel Yacoub II technique was assessed showed similar outcomes to the Yacoub I technique. Figure 2.19 shows the CFD results of two patients compared to a matched control representing velocity and streamlines in the aortic root. Although there was a slight reduction in velocity values at the peak ejection phase shown, the

velocities and flow direction in the LCS (grey arrows) were similar to the control and agrees quantitatively with values deduced by Bellhouse's experiment mentioned in Section 2.1.1 [26].

Studies with an inclusive investigation like Berdajs' and Yacoub's providing clinical insights on the structure and function interaction of the aortic root with a relevance to optimum surgical treatment of aortic root disease are important [24],[25],[26]. However, both extended studies did not investigate the concept of aortic root acceleration or the movement of the aortic root towards and away from the LV. The concept of a moving or even accelerating fluid medium remains under-investigated especially in physiological fluid dynamics due to its complexity. There may be crucial effects on the aortic root function more than its interaction with its structure as a result of a moving fluid medium. In other words, it may not be necessarily that the interaction between the valve leaflets and the surrounding fluid medium having a dominant effect on the flow distribution in the root; but the movement of the fluid medium itself may have an effect of comparable magnitude. In the coming sections, studies concerned with the translational movement of the aortic root will be reviewed and the importance of its potential to affect aortic root function will be introduced.

2.1.3 Aortic Root Dynamism

The concept of aortic root dynamism initially appeared in Yacoub's description of the aortic root as a *tale of dynamism and cross-talk*. Yacoub et al. described the dynamic behaviour and interaction between the LVOT and surrounding structures as a coordinated orchestra hence the title of the study [5]. Yacoub further explained that planning surgical treatment of different aortic disease should take into account restoration of such coordinated movement or *dynamism*.



(a) Aortic root anatomy unwrapped

(b) Heart cross-section showing complex structures

Figure 2.20: Depiction of the cardiac anatomy. (a) MS is the membranous septum and AC is the subaortic curtain. (b) The arrows indicate the effect of the movement of the anterior leaflet of the mitral valve. (Reproduced from [5])

Figure 2.20 shows depictions of the cardiac anatomy and how complex it is. Figure 2.20a is focused on the anatomy of the aortic root with a view from an opening between the left and right coronary cusps while Figure 2.20b shows a cross-sectional view with all the heart valves visible [5]. The letters **AC** in Figure 2.20a refer to a structure called the *Aortic Curtain* that may have an important contribution to the dynamism of the aortic root along with the *Fibrous Trigones* which can be seen as a small triangle just below the open aortic valve in Figure 2.20b. The Fibrous Trigones are connective tissue that support the cardiac valves. In addition to the Fibrous Trigones acting as a hinge mechanism interacting with the aortic orifice or valve, the anterior leaflet of the mitral valve also plays a role in the dynamism of the aortic root as shown

by the small arrows in Figure 2.20b. When the anterior leaflet of the mitral valve opens, it pulls the commissures of the aortic valve along the black arrows shown in the figure and vice versa. This causes temporal changes in the shape of the aortic valve across the cardiac cycle.

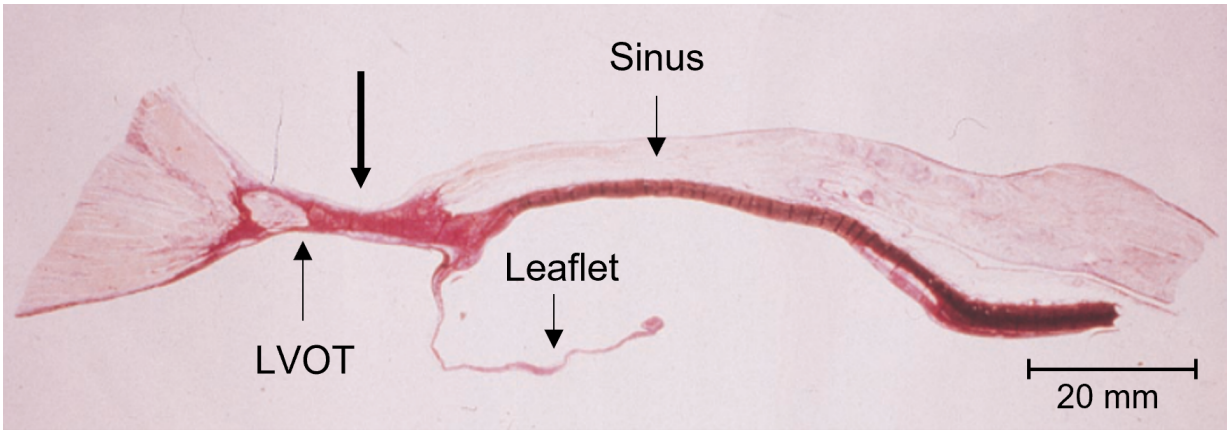


Figure 2.21: Longitudinal section of the aortic root. The far left of the figure shows the subaortic curtain. A section through one of the valve leaflets can be seen hanging from the thick hinge at the annulus. The subaortic section is indicated by the black arrow. The bulging section of the sinus is adjacent to the right of the subaortic section. (Reproduced from [5])

Figure 2.21 serves to sum up the complexity of the coordinated interaction and dynamism of the different structures in the aortic root described in the previous paragraph. The longitudinal stained section of the aortic root shows how the thickness varies along the root from the subaortic curtain to the sinotubular junction (left to right) with the thickest point at the hinge that coincides with the annulus [5]. The varying thickness between the different structures within the aortic root strongly correlates to different roles of each with implications on blood flow [5]. This is because of the non-uniform load distribution across the root [5].

Moreover, the subaortic section just to the left of the bulging section in Figure 2.21 has always been considered to be naturally dynamic, i.e. exhibiting *active dynamism*, due to the presence of myocardial tissue in segments of its wall. Furthermore, different histological studies confirmed the presence of nerve endings in the aortic cusps surrounding the valve thus enabling them to dynamically change size and shape across the cardiac cycle. This suggests that certain structures within the aortic root have the ability to exhibit *active dynamism* by contracting in response to certain pharmacological agents [5].

Above all, whether the dynamic behaviour of the aortic root is *active* by nature or *passive* due

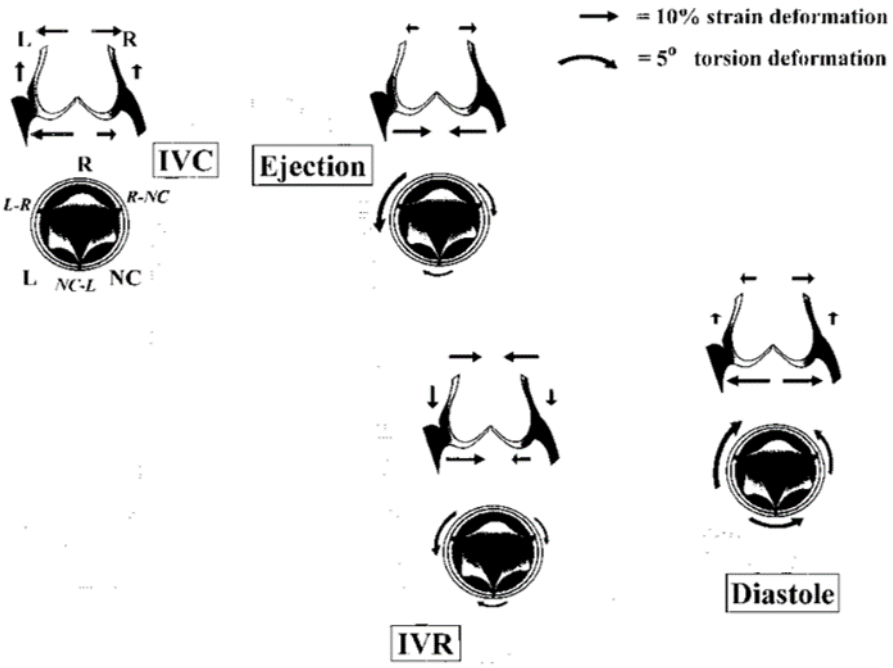


Figure 2.22: Temporal dynamic behaviour of the aortic root in sheep. The variable arrow lengths in torsion and strain indicate the asymmetric deformations of the aortic root from the ejection phase to the diastolic phase. (Reproduced from [27])

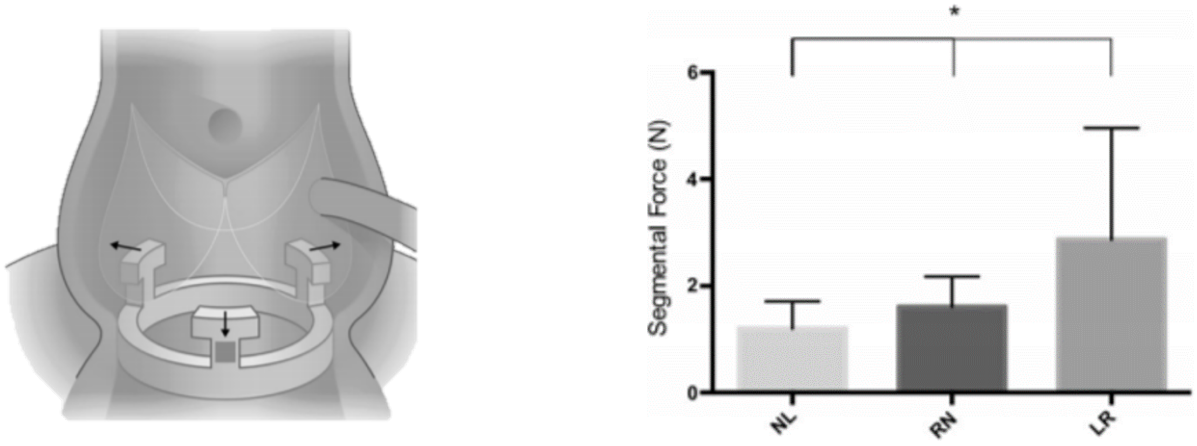
to induced motion from the surrounding structures in the heart, it is worthy of investigation when studying the interaction between the structure and function of the aortic root.

Another study further supporting the concept of *dynamism* in the aortic root was conducted by Dagum et al. with a technique using implanted sonomicrometric crystals similar to those used by Berdajs et al. as described in Section 2.1.2. Dagum et al. managed to track the dynamic movement of the aortic root at key time points in the cardiac cycle in six adult sheep [27].

Figure 2.22 shows a summary of the key findings from the study. The motion of the aortic root was deduced at the *isovolumic contraction* **(IVC)** phase which directly precedes the ejection phase, the *peak ejection* phase, the *isovolumic relaxation* **(IVR)** phase which directly precedes the diastolic phase and finally the *mid-diastolic* phase.

In the perspective of a cylindrical coordinate system, although the aortic root annulus is known to deform more in the radial direction rather than in the tangential direction which results in temporal changes in shape from circular to elliptical according to the previously mentioned dynamism study by Yacoub et al.; Dagum et al. deduced asymmetric deformation of the aortic

root annulus and STJ in the tangential direction across the cardiac cycle [25],[27]. Dagum's findings support previous findings by Berdajs that the aortic root takes a cylindrical shape in systole and a cone shape in diastole. In addition to this, asymmetric shortening and lengthening of the aortic root sinuses suggests that bending in the aortic root is present [27]. Although the results presented by Dagum et al. agree with Berdajs' results mentioned in Sections 2.1.1, 2.1.2 and augment the hypotheses discussed in Yacoub et al's study of the aortic root dynamism, the concept of aortic root acceleration or translational movement along the axial direction was not investigated. A few more studies will be presented to show why this concept should not be overlooked and how it will be presented within the scope of our study.



(a) Force transducers implanted in the aortic root

(b) Maximum forces endured by the interleaflet triangles in the aortic root

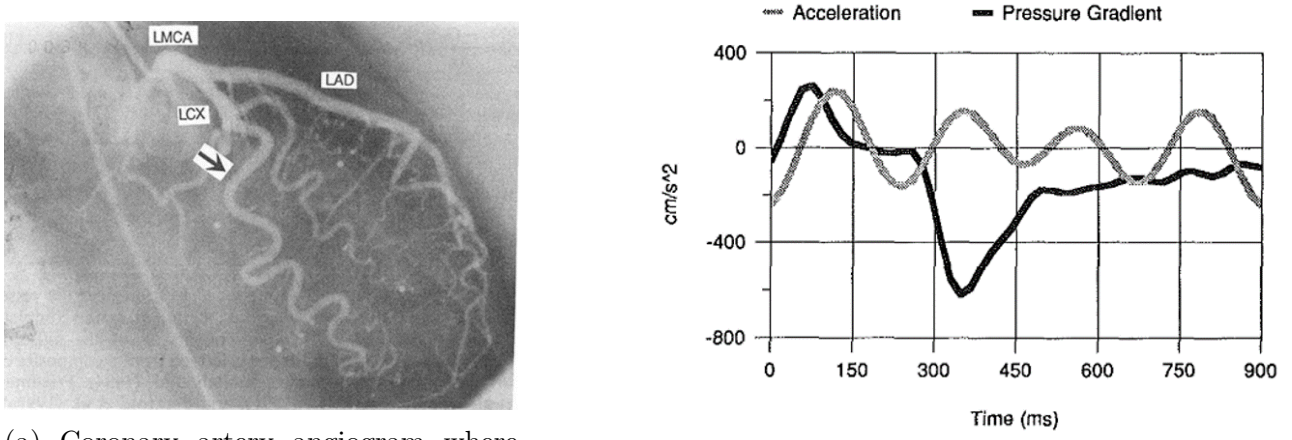
Figure 2.23: Aortic root force response. Location of implantation of the transducers are shown in the annulus ring and the measured forces show the higher values in the left-right interleaflet triangle. (Reproduced from [28])

A study by Benhassen et al. used the same methodology of implanted sonomicrometric crystals described previously in porcine aortic roots. However, they also implanted force transducers in the aortic root annulus in order to measure the force or loading experienced by the three interleaflet triangles [28]. The vertex of each interleaflet triangle corresponds to the commissure points of the aortic root while their base consists of a segment of the annulus.

Figure 2.23a shows the location of the implanted force transducers in the aortic root. Each transducer was used to represent the load incurred by each interleaflet triangle. The results

shown in Figure 2.23b reflect a consistent greatest force experienced by the left-right (**LR**) interleaflet triangle [28].

We believe this is a crucial result for two reasons. Firstly, our unpublished work in aortic root histology showed the greatest presence of smooth muscle cells in the LR triangle versus the other two triangles. This may correlate to findings by Berdajs et al. suggesting that the aortic root always bends towards its LR side. Secondly, although Benhassen et al. did not investigate the reason behind the highest forces being endured by the LR triangle, this could relate to the effects of aortic root acceleration.



(a) Coronary artery angiogram where vessel acceleration was deduced

(b) Temporal pressure gradient normalised with fluid density and vessel acceleration

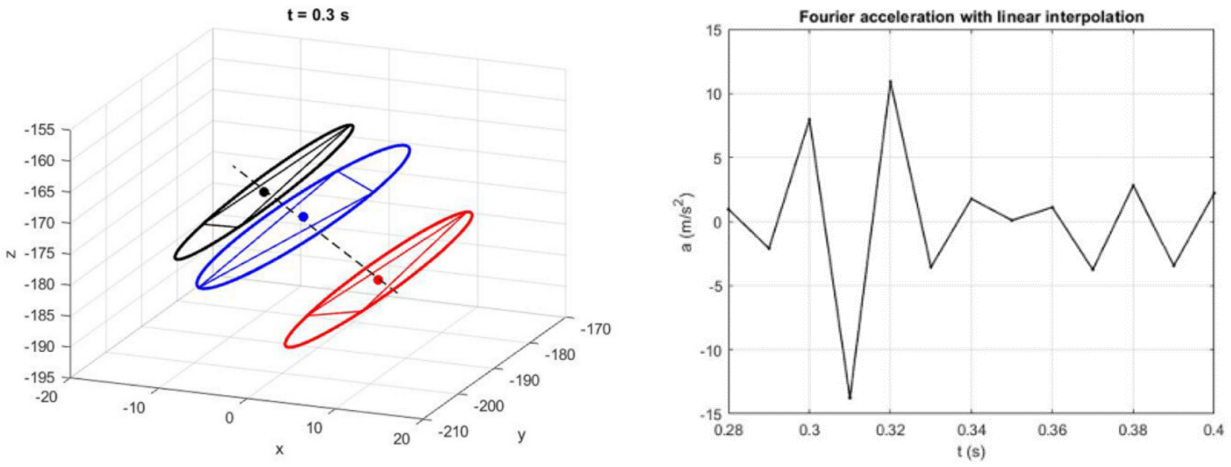
Figure 2.24: Coronary artery acceleration. The angiogram film shown was used to track the acceleration of the LCX branch of the coronary artery. The tracked acceleration is of comparable magnitude to the pressure gradient driving the flow. (Reproduced from [29])

Accordingly, it is vital to introduce the following study by Moore et al. at this stage since it provides an important investigation tackling the problem of a fluid medium in an accelerating blood vessel. Moore et al. focused the study on one of the main coronary branches described in Section 2.1.1 i.e. the LCX branch. Despite the fact that the coronaries are outside the vicinity of the aortic root, they still originate from the root; consequently, the vessel acceleration may be due to accelerations from the root or from the myocardium or from a combination of both. In all cases, their study serves the purpose in quantitatively demonstrating the importance of investigating a fluid medium in an accelerating blood vessel.

The outline of Moore et al.'s study is presented in Figure 2.24. Figure 2.24a shows a single

frame from an angiogram film of a coronary artery from which the vessel displacement and acceleration were obtained. Next, Moore et al. derived an analytical solution to the Navier-Stokes equations where the flow field inside the accelerating vessel was deduced [29]. Figure 2.24b shows how the vessel acceleration and pressure gradient normalised with respect to the fluid density are of a comparable order of magnitude; hence, highlighting the importance of including the vessel acceleration when studying the interaction between structure and function.

After comparing the flow fields in a stationary versus an accelerating artery, Moore et al. deduced that the temporal variation in certain flow parameters representing blood flow stability produced a **100 %** difference between both scenarios [29]. That being the case, including the motion or acceleration of the aortic root is necessary when assessing the relationship between its structure and function regardless whether its *dynamism* is *passive* or *active*.



(a) Geometrical representation of the aortic root (b) Temporal acceleration of the aortic root

Figure 2.25: Aortic root acceleration. Reconstruction of the root using fiducial point tracking is shown. The red, blue and black sections in (a) represent the annulus, commissures and sinotubular junction respectively. In (b), the quantified acceleration shows a peak value of 10 m/s^2 at the time of valve closure. (Reproduced from [30])

In a similar fashion Abou Gamrah et al. managed to quantify the temporal accelerations of the aortic root and study their impact on blood flow. Since this is our original published work, a quick review will be presented in this section but a detailed explanation of the work will be provided in the coming sections of this thesis.

A similar technique in image tracking such as that used in the studies by Berdajs et al. was

adopted; however in our case, four normal aortic roots were used without any surgical implantation of sonomicrometric crystals. CT scans from these normal patients were reconstructed over different phases in the cardiac cycle and the anatomical landmark points were tracked emulating the implanted crystals [30].

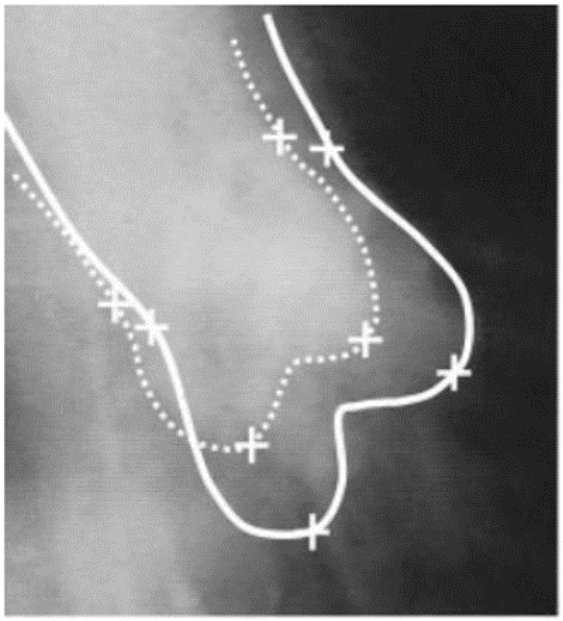
The four cases always showed a peak acceleration of the aortic root of approximately **10** m/s^2 at the time of aortic valve closure. In other words, the aortic root moves towards the LV during the ejection phase of the cardiac cycle and accelerates away from the LV at the time of valve closure [30].

Figure 2.25a shows the geometrical representation of the landmark points or different segments in the aortic root at a single time frame. Figure 2.25b shows the temporal acceleration of one aortic root with a peak positive value at the time of valve closure. In consequence, using a 1D approximation through the water-hammer equations, it was found that hypothetically the aortic root positive acceleration at the time of valve closure may account for the dicrotic notch arterial pressure rise usually coinciding with valve closure [30].

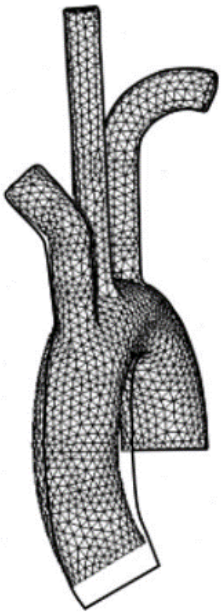
If the concept of the dicrotic notch or the inexplicable pressure rise at the time of aortic valve closure when the fluid is decelerating is due to the acceleration of the aortic root, this suggests that a higher order study investigating this effect on blood flow is necessary. In the coming sections of this study we will present how we achieved the transition from a 1D approximation to a higher fidelity simulation of an accelerating aortic root.

To conclude the argument about the importance of investigating the acceleration of the aortic root, the study by Beller et al. is presented. The focus of their study was on the pathogenesis of aortic dissection and its correlation to the acceleration of the aortic root. To do this they incorporated the motion of the aortic root deduced from MRI imaging in a finite element simulation studying only the stress distribution on the aortic wall due to the effects of acceleration of the aortic root [31].

Figure 2.26a shows the outline of the aortic root from MRI imaging at different time frames. The root moves downwards towards the LV in systole and away from the LV in diastole. Figure



(a) Downward motion of the aortic root at peak systole



(b) Reconstruction showing maximum aortic motion

Figure 2.26: Aortic motion. The maximum downward position of the root is shown at peak systole. The 3D mesh of the numerical model shows the maximum displacement of the aorta by the black frame. (Reproduced from [31])

2.26b shows a 3D reconstruction of the aorta at the beginning of the cardiac cycle and the black outline of the aorta at the peak systolic or ejection phase.

Although the study involved neither a comparison with non-accelerating aortas nor involved an assessment of blood flow, the results still shed light on the possible clinical impact of the acceleration phenomenon. The key finding in their study was that the downward motion of the aortic root strongly correlates to age and LV function and at the same time caused regions of high stresses in the ascending aorta where intimal dissection tear of the wall usually originates [31].

In conclusion, the studies discussed in this section mentioned the importance of the *dynamism* or temporal deformation of the aortic root. On the contrary, the effect of the acceleration of the aortic root on blood flow was unavailable. Therefore, the motive behind our work is to extend low order approximations to higher order blood flow simulations in an attempt to delve into the potential impact of the acceleration of the aortic root. We believe the effects of the acceleration of the aortic root may emerge to be a useful parameter in diagnosing aortic disease or aid in

surgical intervention to restore favourable interaction between the structure and function of the root.

Moreover, the concept of active dynamism mentioned in the literature touches on the anatomy of the aortic root and surrounding structures of the heart without discussing the relation with physiology. The main explanation provided behind the active mechanism relates to the presence of contractile elements in certain segments of the aortic root. We believe that the complex nature of testing this concept is the reason why active mechanisms are under discussed in the literature since such testing would require electrical stimulation of certain segments in the aortic root. This is also the reason we decided not refer to the kinematics of the aortic root discussed in Chapter 4 as passive or active.

In the next section, different techniques for assessing blood flow in the aortic root will be introduced with a focus on techniques that have been used in our study to help achieve its main aim of integrating a higher fidelity computational model to investigate the effects of the acceleration of the aortic root.

2.2 Current Methods for Assessing Haemodynamics

Different techniques have been used to study and assess haemodynamics of the aorta or aortic root for different motives or scenarios. Some of these scenarios include studying the flow patterns in healthy aortas, pre-operative planning and post-operative assessment of corrective surgeries for aortic pathologies, the optimisation of aortic root or valve prosthesis design and tissue-engineered valve design. The methods used in the aforementioned scenarios may be categorised into the following:

- Multi-modality imaging
- 0D numerical models
- 1D numerical models
- Higher order computational models
- Experimental techniques

2.2.1 Multi-modality Imaging

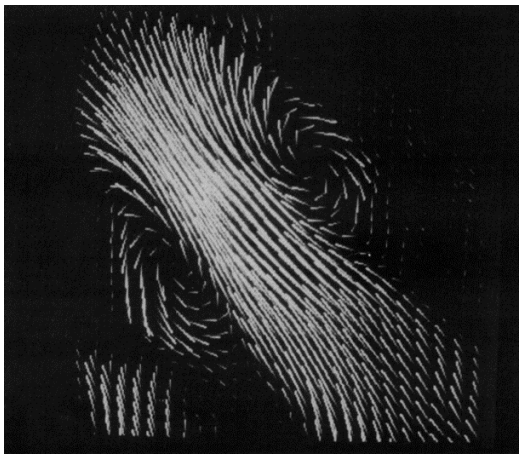
Multi-modality imaging which has become a convention in the field of Radiology involves the use of two or more imaging techniques within the scope of a single examination or assessment [32]. While on many occasions multi-modality imaging has been used to derive physiological boundary conditions for high order computational models, it is still used as a solo tool to assess blood flow or arterial function.

2D Cardiac Magnetic Resonance (CMR)

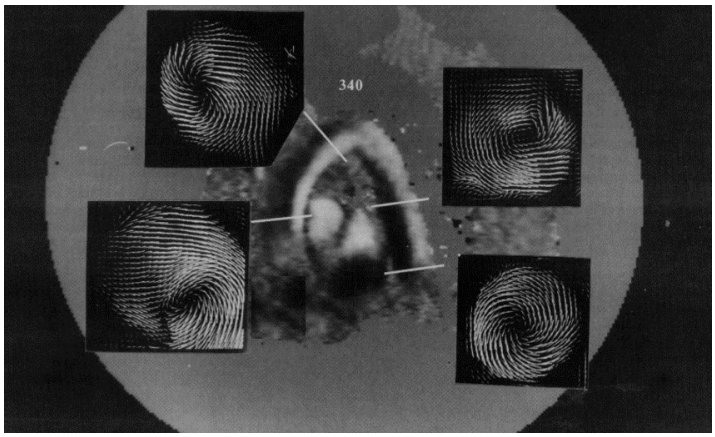
One of the earliest techniques used in visualising and assessing aortic blood flow was 2D CMR Velocity Encoded (Venc) Imaging. From its name, CMR is simply an MR imaging method that follows a protocol tailored to capture images of the heart. Although the technique relies

on a single mode of imaging i.e. CMR, it requires the use of velocity encoding as an additional modality. The Venc images contain velocity data within each pixel in the anatomical MR images.

Kilner et al. conducted a study focusing on the normal physiology of the aorta using 2D CMR. The novelty in the study was using different 2D flow planes at different angles to reconstruct a 3D flow field in healthy aortas. Each 2D flow plane with a built-in echo spin imaging technique was used to generate the encoded 3D velocity field values [33].



(a) Velocity vectors after post-processing in the aortic root



(b) 2D velocity vectors at different sections in the aorta

Figure 2.27: Velocity vectors in the aorta at late systole. The vectors in the aortic confirm the presence of the aortic root vortices and the cross-sectional planes show the helical flow development at late systole. (Reproduced from [33])

Figure 2.27 shows some of the results from Kilner et al.'s study. Figure 2.27a shows a longitudinal MR image through the LVOT and aortic root after post-processing to plot the velocity vector flow field at the late systole phase of the cardiac cycle. The vector field agrees with predictions by Bellhouse et al. where the vectors form a recirculating region in the sinuses of the aortic root at slower velocities compared to the flow downstream of the sinuses; hence, the different vector sizes [19],[33].

Figure 2.27b shows the cross-sectional vectors at different locations along the aorta. The swirling patterns in each of the planes suggests the presence of a helical flow pattern changing from a right-handed rotation in the ascending aorta to a left-handed rotation in the descending

aorta. Kilner et al. stated that such flow pattern at late systole may correlate to the acute angle of the aortic arch in this particular healthy volunteer [33].

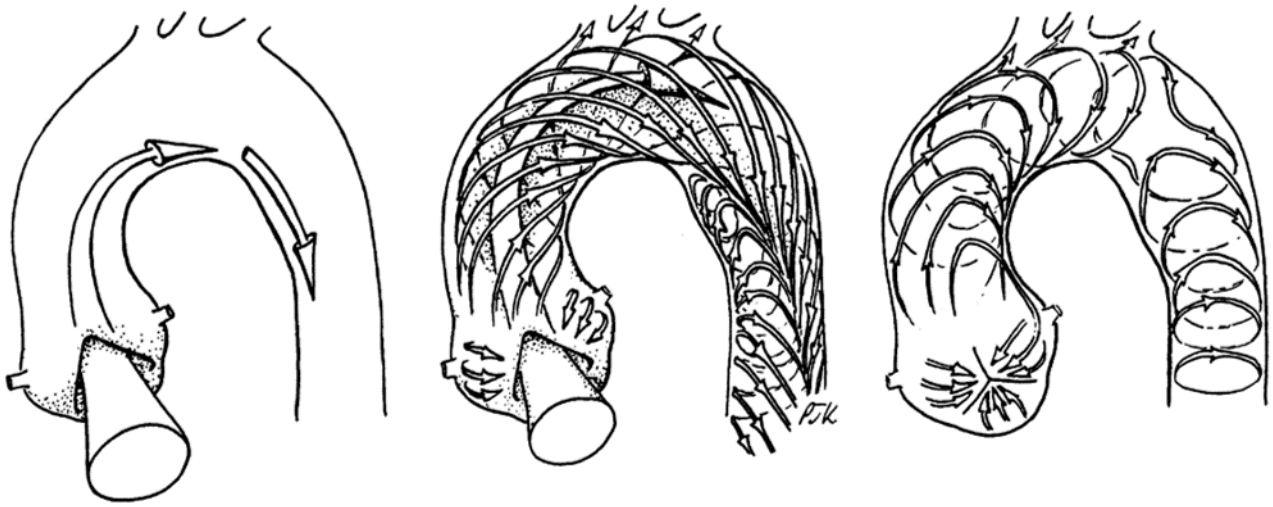
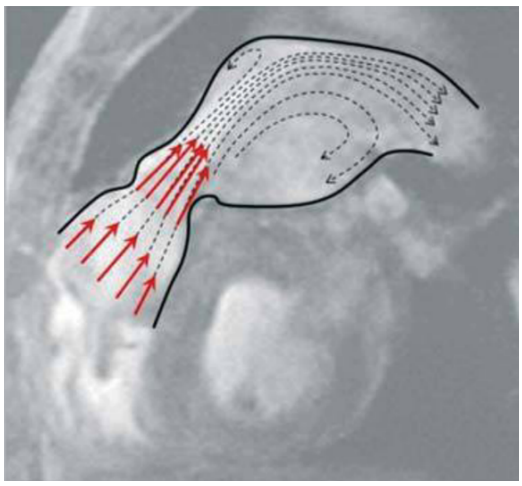
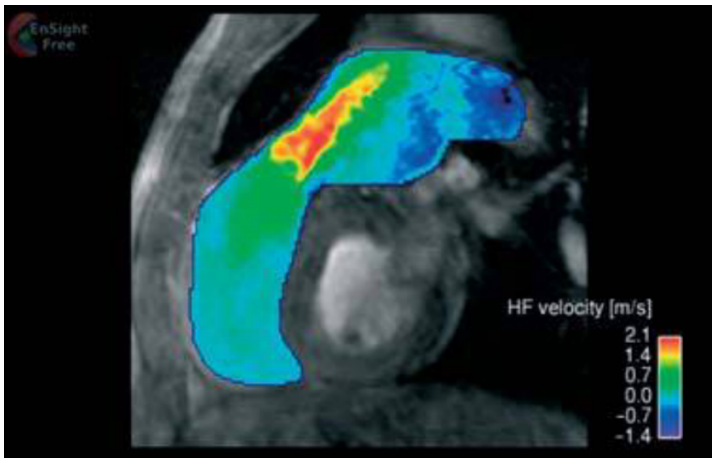


Figure 2.28: Schematic of the 3D blood flow in the healthy aorta at early systole, late systole and end systole. The arrows at late systole show the helical flow development predicted by Kilner. (Reproduced from [33])

Figure 2.28 shows a depiciton representing the final product from Kilner et al.'s 3D reconstruction of the velocity flow field in the healthy aorta from the 2D CMR venc images. At the early systole phase, the blood flow in the aorta follows the aortic centreline with the highest blood velocities occuring close to the inner wall of the aorta. At late systole, the vortices in the sinuses of the root are drawn on the figure as small curved arrows and the higher velocities begin migrating towards the outer wall of the aorta. As a result, a right-handed helix begins to take shape extending from the ascending to the descending aorta. Finally, at end systole after the flow has decelerated in the aorta, the aortic valve closes and axial recirculating patterns form along the centreline of the aorta [33]. Although more recent studies using more advanced techniques showed partial disagreement with the flow patterns obtained by Kilner et al. which showed a single helix rather than a dual rotating helix during late systole, 2D CMR still remains a powerful tool in assessing blood flow in the heart.



(a) Depiction of the flow pattern at peak systole in the main pulmonary artery



(b) Velocity values from 2D CMR at peak systole

Figure 2.29: Flow in an obstructed pulmonary homograft. Vectors show abnormal recirculation regions downstream in the main pulmonary artery and the velocity contours show elevated values due to the obstruction. (Reproduced from [34])

Figure 2.29 shows the results from a more recent study by Chapron et al. investigating flow patterns at peak sysole in pulmonary artery homograft. Inserting a pulmonary homograft is a surgical treatment in patients suffering from severe pulmonary valve stenosis [34]. Since the treatment may regress due to morphological changes surrounding the inserted homograft or due to other clinical reasons, follow up is usually necessary for the patients.

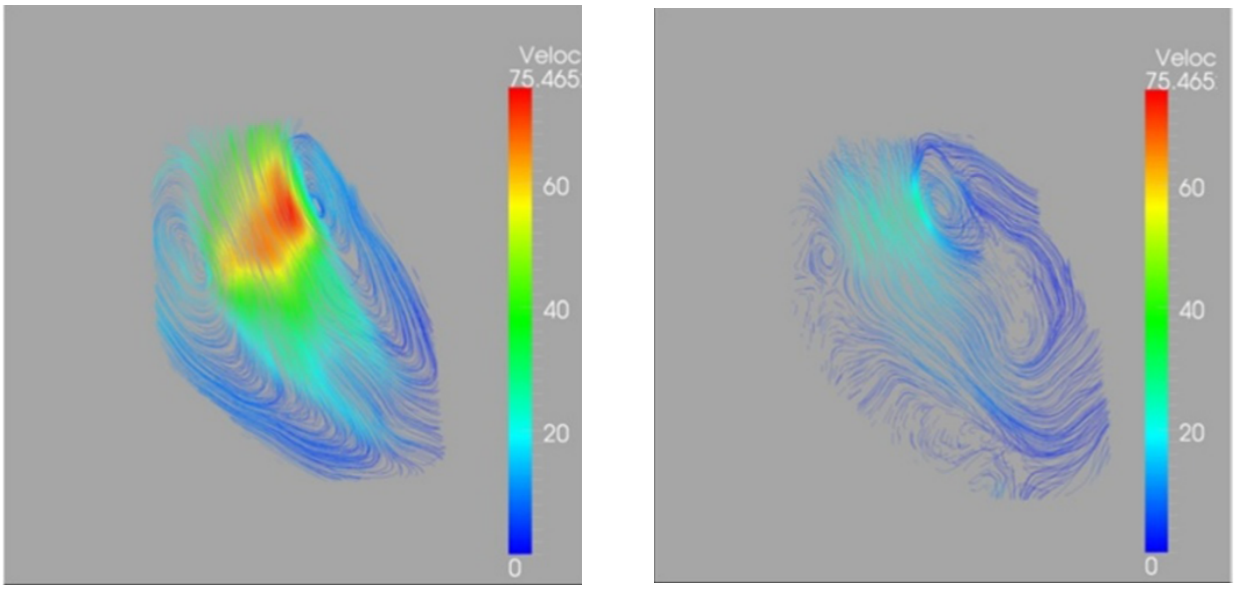
Chapron et al. used phase contrast 2D CMR images of the pulmonary artery to assess the flow patterns at peak systole for a patient with a pulmonary homograft. At peak systole where the flow should be aligned with the centreline of the main pulmonary artery, the obstruction induced choking of the blood flow with skewed high velocities and a big recirculating region downstream of the obstruction [34].

Figure 2.29a shows the depiction of the flow pattern in the region of interest. The large red arrows in the obstructed region represent the skewed flow jet while the dashed arrows downstream represent the large recirculating region downstream. Figure 2.29b shows the quantitative flow pattern of the region of interest. Elevated velocities in the obstructed region peak to twice the normal values and negative velocities downstream confirm the presence of a recirculating region [34].

Despite the fact that the 2D images may not fully represent the real flow field, they still provide a fast non-invasive mode of assessment that may be used for clinical diagnosis.

4D Flow

While the use of 2D CMR for assessing blood flow still holds until today, it started evolving into more advanced techniques such as 4D flow. From its name, 4D flow gives the time-resolved 3D spatial flow pattern within a volume of interest. 4D flow alleviates the uncertainties behind using 2D images to assess a flow field by providing the ability to study the 3D field directly in any volume of interest. Similar to 2D CMR, this is done by phase contrast MRI showing velocity values at 3D voxels instead of 2D pixels. This procedure when repeated across different time points in the cardiac cycle results in a time-resolved 3D flow field [35].



(a) LV peak early filling (b) LV peak late filling

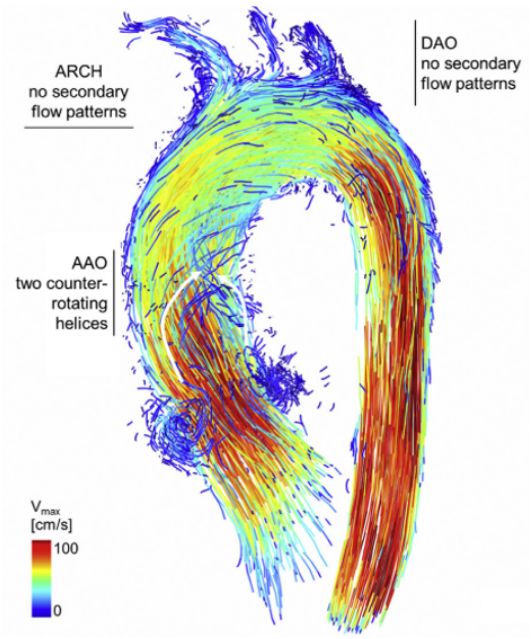
Figure 2.30: Flow field in a healthy LV obtained from 4D flow showing velocity streamlines. The temporal patterns show the development of the recirculation regions present in the LV from the early filling to the late filling stage. (Reproduced from [36])

Figure 2.30 shows the results from a study conducted by Elbaz et al. using 4D flow. The main aim of the study was to look at the distinctive flow distribution in a healthy LV as it may correlate to healthy LV function [36]. Figure 2.30a shows the velocity streamlines obtained at the peak of the early filling stage of the LV while Figure 2.30b shows the streamlines at the

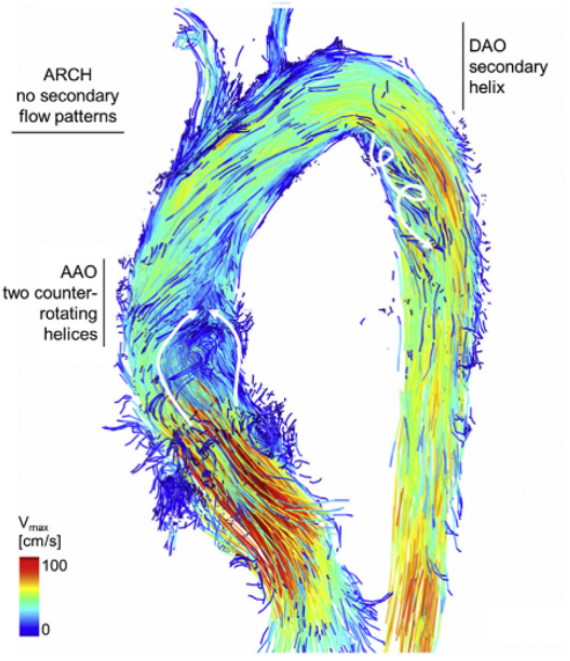
peak of the late filling stage. Two large recirculating regions form at the early filling stage on either side of a centralised bulk of flow coming out of the mitral valve. At the late filling stage, the bulk flow decelerates with the recirculating region on the right expanding while the recirculating region on the left towards the aortic side diminishes in size [36].

Another study by Oechtring et al. used 4D flow in order to assess the function of the aorta post-operative valve conserving operation [37]. Figure 2.31 shows the flow streamline traces in the aorta of a healthy young volunteer, aged volunteer and a patient post-operative valve conserving surgery. While the main aim of the study was to assess the function of the aorta post-operative, the results from 4D flow showed disagreement with the results obtained using 2D CMR imaging by Kilner et al.. Oechtring et al. showed the presence of a dual rotating helix in young and aged healthy aortas unlike the single right-handed helix obtained by Kilner et al. [33],[37]. In addition to this, Oechtring et al. concluded that the flow patterns in the aorta post-operative valve conserving surgery were closer to an aged healthy volunteer with altered flow patterns in the ascending aorta that may have certain clinical implications [37].

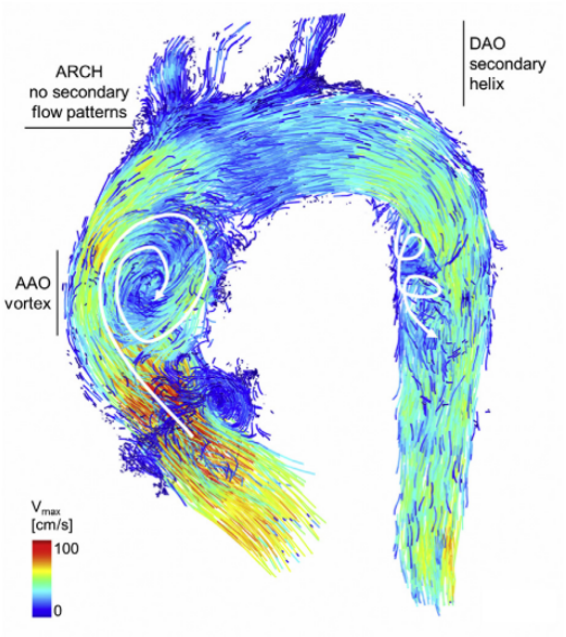
In all cases, disagreement between results obtained from 2D CMR imaging and 4D flow does not indicate which technique is more accurate. Above all, both techniques may be used to facilitate assessment of blood flow in the arteries of the heart and if used with other techniques may provide an conclusive assessment.



(a) Velocity traces from 4D flow in a healthy aorta from a young volunteer



(b) Velocity traces from 4D flow in a healthy aorta from an aged volunteer



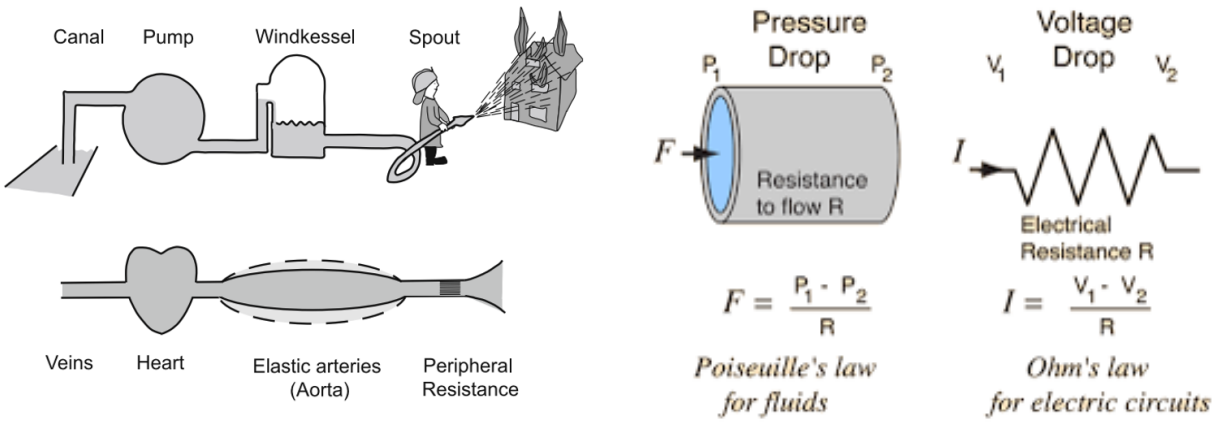
(c) Velocity traces from 4D flow in an aorta post-operative valve conserving operation

Figure 2.31: Velocity traces from 4D flow at mid-systole. Velocity patterns in the patient post-operative show a pattern different from a young and an aged healthy volunteers. (Reproduced from [37])

2.2.2 0D Numerical Models

The multi-modality imaging techniques described rely on direct scans of the patient or subject whose arteries are to be assessed in terms of function. On the other hand, there exists numerical models that rely on input parameters deduced from clinical data to assess blood flow behaviour in the arteries without the need to scan patients. Such input data may be the brachial blood pressure, the heart rate and the stroke volume of the heart deduced from echo measurements. The most basic of these numerical methods which falls under the category of 0D numerical models is the Windkessel model.

While fluid flow analysis requires spatial dimensions for its investigation, it may be inferred from its name that 0D models represent an overall analysis of the system behaviour without the inclusion of any spatial dimension. The zeroth dimension may be time as in temporal variation or any other non-spatial variable [38].



(a) Depiction of the Windkessel model (b) Fluid flow - Electrical circuit analogy

Figure 2.32: A depiction of the Windkessel model showing the arterial system. The governing 0D model is derived from electrical circuits' analogy to fluid flow where F stands for volume flow rate. (Reproduced from [38]),(From hyperphysics.phy-astr.gsu.edu, 2009)

Figure 2.32 explains the concept of the Windkessel model as a 0D numerical model to assess blood flow. Figure 2.32a shows how the arterial system behaves as a firefighting pumping station. The Windkessel effect is due to the reservoir filled with compliant air and water downstream of the pump which draws flow from a water source. In the arterial system, the veins coming from the lungs with oxygenated blood serve as the fluid source which supplies the

heart that acts as a pump. The heart then pumps blood to the elastic arteries that play the role of the Windkessel chamber. The elastic arteries have the compliant nature giving them the reservoir ability to act as a Windkessel chamber maintaining continuous blood flow to the rest of the body throughout the cardiac cycle. Moreover, the elastic arteries supply the peripheral system which has resistance [38].

Figure 2.32b shows the analogy between an elastic artery and a basic electrical circuit component. The pressure across an artery is analogous to the voltage drop across a resistor while the arterial resistance is analogous to the resistor component in a circuit. The current passing through the resistor is analogous to the flow rate of blood passing through an artery. Other circuit components such as capacitors and inductors can be used to represent arterial compliance and blood inertia respectively. From such analogy, time-dependent 0D equations may be used to model the entire arterial system as an electric circuit [38].

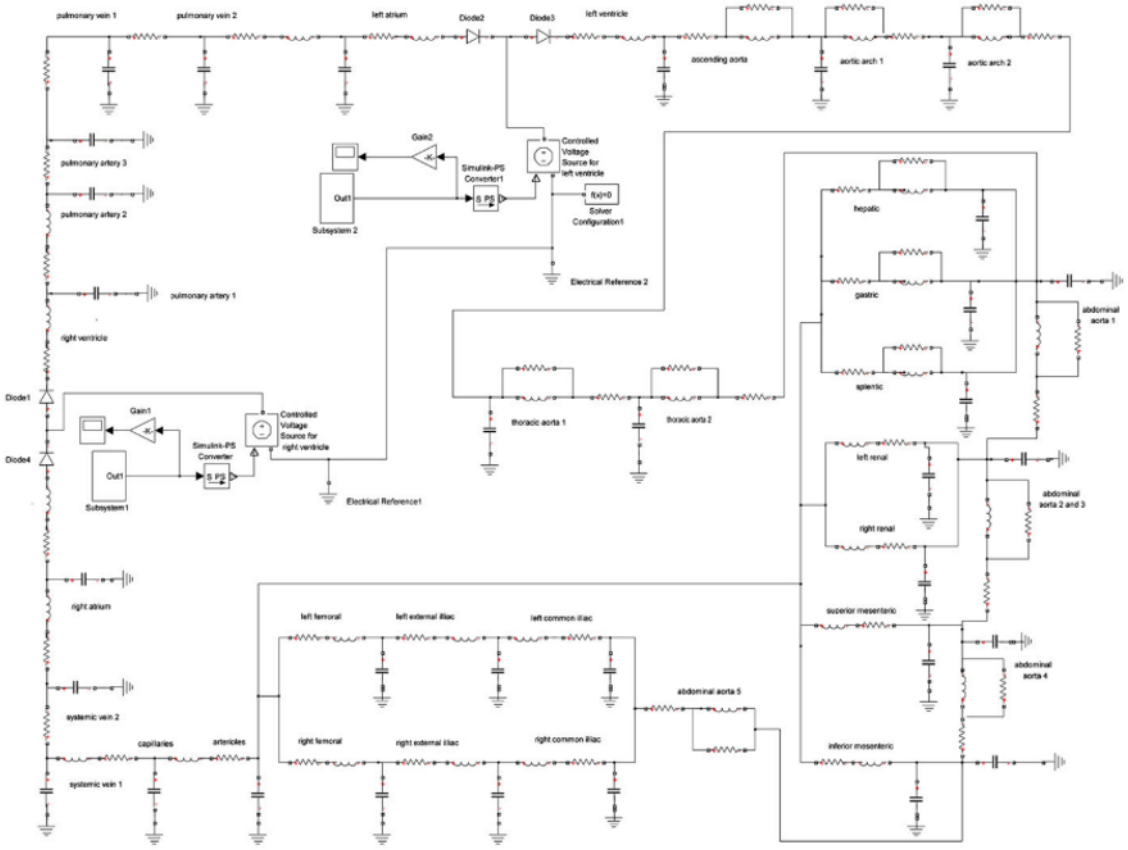


Figure 2.33: 0D Windkessel model of the arterial system. The behaviour of the arterial system is simulated using a simulink model where each circuit component represents a segment of the arterial system. The values for each component were derived based on subject-specific clinical data. (Reproduced from [39])

While the use of standalone 0D models is not very common to assess blood flow, they are still useful as they provide an assessment of the arterial function as a lumped system eliminating expensive modelling time costs. Figure 2.33 shows a 0D Windkessel model of the entire arterial system used in a recent study by Abdi et al.. The main aim of the study was to provide a quick tool to investigate the effects of tachycardia on arterial blood flow [39]. Tachycardia is a cardiac abnormality which involves an irregular, rapid heart rate. Although the entire 0D model in Figure 2.33 may seem complicated, it is only a closed system of simple electrical circuit components. The electrical components result in a system of ordinary differential equations (time-dependent) which may be solved using a simple computer software. After using simple clinical inputs known a priori like blood pressure and heart rate, Abdi et al. deduced that tachycardia results in an overall decreased blood flow to the capillaries. This may provide a quick tool to diagnose the effect of irregular heart rates if they are clinically suspected to be significant [39].

As stated, the use of models similar to that used by Abdi et al. is not very common; however, Windkessel models are more commonly used to provide physiological boundary conditions in 3D CFD models for assessing blood flow.

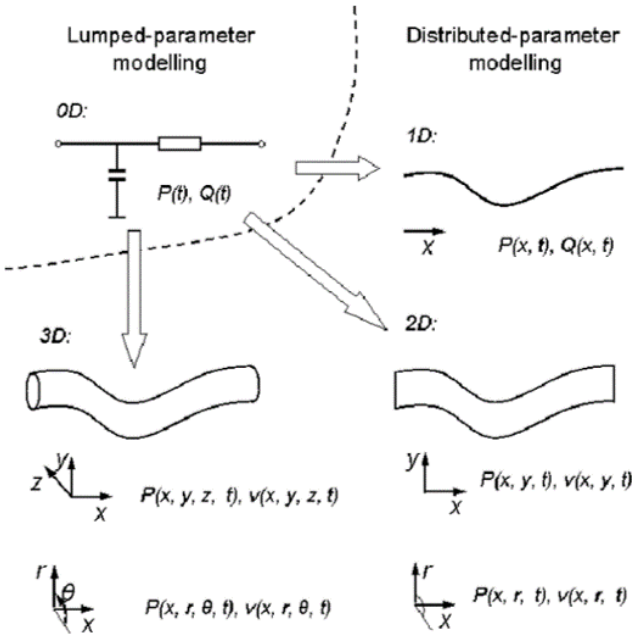


Figure 2.34: Different numerical models. (Reproduced from [40])

Figure 2.34 shows how different numerical models of different order of complexity may be

used with 0D models. 0D models also known as lumped parameter models which are simply analogous to electrical circuits may be used to derive boundary conditions that can augment 1D, 2D and 3D higher order models to yield useful information about arterial function to assess blood flow [40].

2.2.3 1D Numerical Models

1D numerical models stem from a similar theoretical basis as the 0D numerical models, however with a single spatial dimension in addition to the time dependency in the equations. As seen in Figure 2.34, the spatial dimension integrated into the equations is usually the centreline of the artery under investigation. In other words, the artery under investigation is represented geometrically in terms of its centreline in the 1D numerical model.

While 1D models are a useful tool in terms of reducing time costs compared to 3D CFD models, they have certain limitations with regards to the parameters of assessment they can provide a means to investigate arterial function. With that said, 1D models are always focused on assessing arterial function in terms of the propagation of pressure and velocity waves in the elastic arteries. They are used in problems concerned with pulse wave transmission or reflection. As with 0D models, 1D models may still be used to derive physiological boundary conditions for higher order CFD models [40].

Wave Intensity Analysis

Since this study is concerned with the function of the aortic root or its surrounding structures, we will focus this section on the most famous 1D numerical model at use in the field of cardiology, i.e. WIA. WIA is a 1D numerical model first introduced by Parker [3]. It is derived from the 1D conservation laws governing fluid flow in an elastic tube. As explained in Section 2.1.1 page 15, it assesses the propagation of the pressure and flow waves across time along one spatial dimension. WIA gives wave propagation results that have been used clinically to diagnose certain cardiac diseases [3]. Figure 2.9 shows the results from a study by Nijjer et al. that

proposed an explanation for the mechanism behind ischemia in the event of heart disease [13]. After obtaining the pressure and velocity waveforms in the coronaries using an invasive catheter procedure, the wave separation derived using WIA showed a major difference between a control and a diseased patient. The patient disease with obstructive cardiomyopathy had an extra deceleration wave during diastole which is an indication of impaired coronary function due to the obstruction [13].

Although WIA is a powerful tool in assessing arterial function, its dependency on an invasive intervention to derive the pressure and flow waveforms may be a limitation.

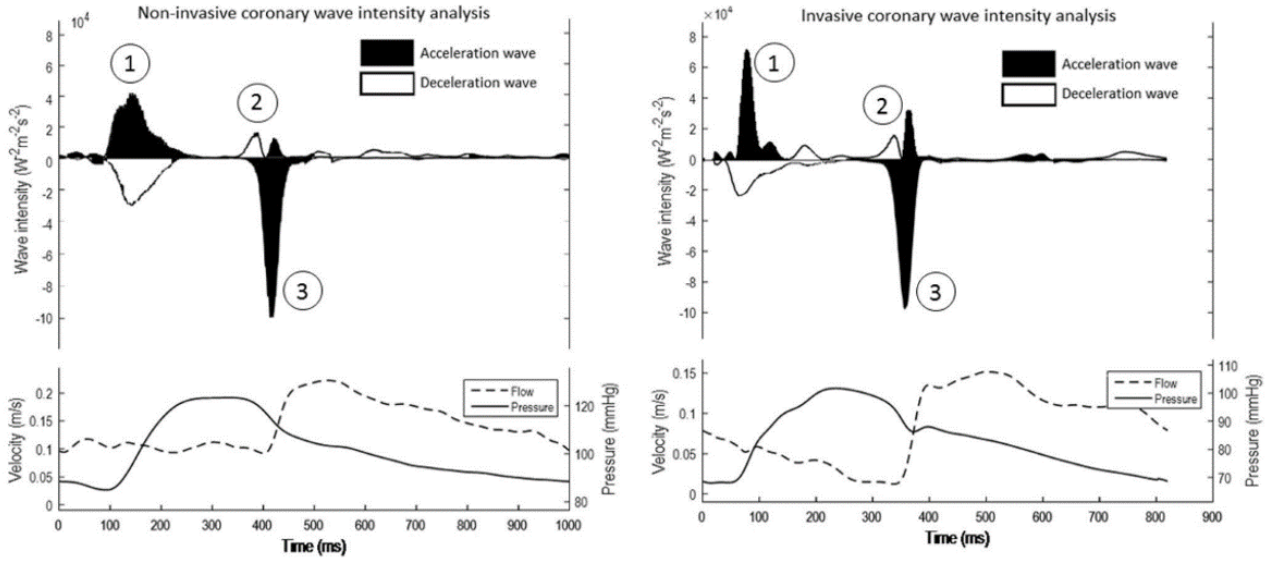


Figure 2.35: Non-invasive WIA results compared to invasive WIA results from the same patient. Both techniques show similar wave separation from similar velocity and pressure measurements. (Reproduced from [41])

Broyd et al. proposed a non-invasive method to carry out WIA in a recent study. Instead of using an invasive catheter procedure to obtain the pressure and velocity waveforms in the coronary, an echo machine was used to obtain the velocity waveform while a Pulsecor device was used for non-invasive pressure measurements [41].

Figure 2.35 shows the results using the non-invasive method of WIA in the coronary LAD branch of a patient versus the invasive results of WIA in the same coronary branch of the same patient. The decomposed waves labelled from 2 to 3 in the figure along with the waveforms obtained suggest a quantitative similarity in the results deduced using both methods with

acceptable error margins with the non-invasive technique [41]. However, the forward wave labelled 1 is different since the non-invasive method is currently under development. With its non-invasive nature, this method proposed by Broyd et al. is expected to gain popularity as a clinical diagnostic tool to assess cardiac function.

1D Computational Fluid Dynamics

Another recent state-of-the-art use of 1D models is in CFD simulations. Blanco et al. proposed a non-invasive 1D CFD method relying solely on a patient's CT scan to calculate coronary FFR which is used to assess coronary function in the event of disease suspecting the need for clinical intervention [42].

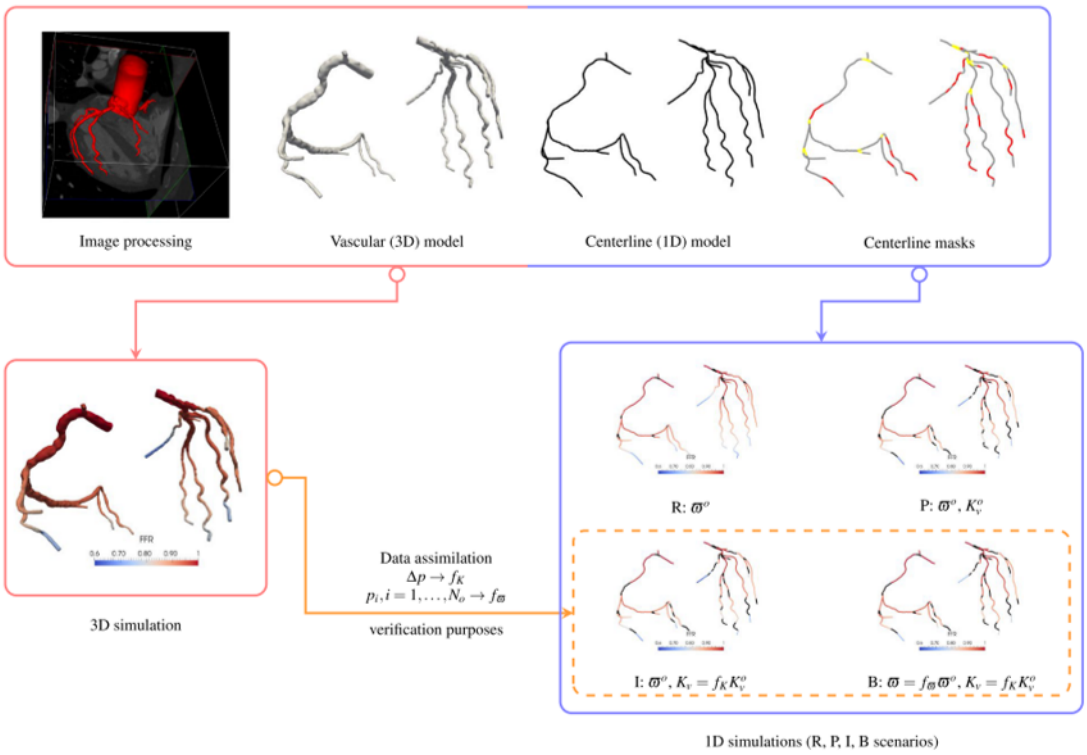


Figure 2.36: Flow chart describing the process of 1D CFD simulation for coronary FFR calculations. The anatomy of the coronary vasculature is modelled using the centreline model of the artery. (Reproduced from [42])

Figure 2.36 shows a flow chart describing the process carried out by Blanco et al. [42]. The CT scan of the patient is reconstructed to create the 3D anatomy of the aortic root and coronaries. Next, a centreline for the coronaries is extracted from the 3D anatomy which constitutes the

1D region of interest for the simulation. Finally, a CFD simulation is carried out on the centreline regions shown to deduce the pressure losses in the coronaries to be assessed for clinical significance [42].

Although the proposed method marginally reduced the time cost of the simulation compared to the conventional 3D CFD model, it only showed high accuracy in patients with non-functionally significant obstructive lesions in the coronaries. This result suggests that the use of 1D CFD still needs further research in how to represent lesions mathematically in a 1D model [42].

With recent advances in deep learning techniques and research in the field of morphometrics, 1D CFD may emerge to be a powerful tool in certain clinical scenarios as they do not require the same computational power constraints that higher order models do.

2.2.4 Higher Order Computational Models

As shown in Figure 2.34, higher order computational models are an extension of the 0D and 1D models that have been mentioned. Higher order models include more spatial dimensions hence their name. 2D CFD models will not be mentioned as they are used in certain cases where the region of interest is axisymmetric for example and have limitations as far as assessing a flow field is concerned. Due to this, we will focus the coming discussion on higher order 3D CFD models.

3D Computational Fluid Dynamics

The use of 3D CFD simulations to assess flow behaviour has been existent since the 1970's. Although their use started with simulating simple flow scenarios, they have continuously evolved along with advances in computational resources. Nevertheless, we believe investigating flow scenarios using simplified geometrical models in CFD can help give a fundamental understanding on more complex scenarios.

In a study by Doorly et al., their aim was to understand flow behaviour in simple arched

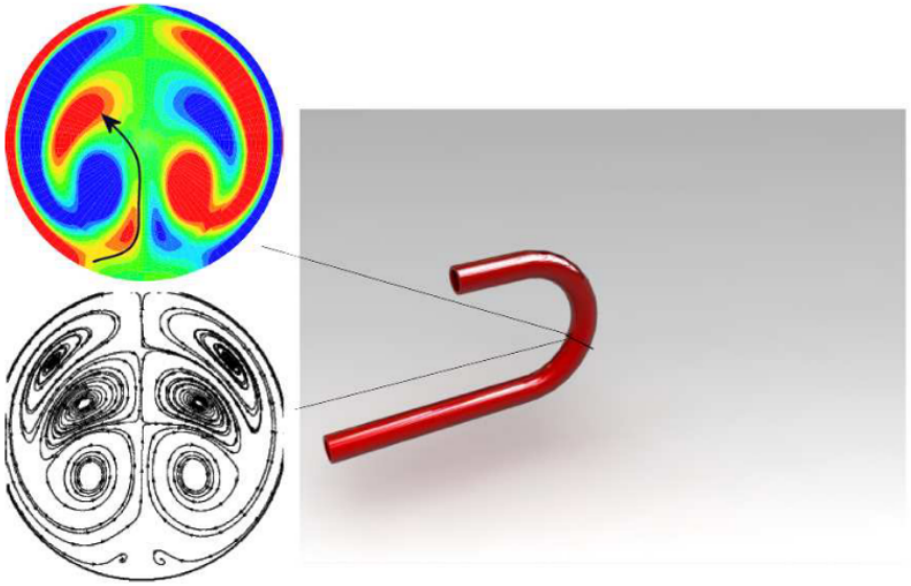


Figure 2.37: 3D CFD simulation results in a simplified geometry mimicking the aorta. The coloured map shows vorticity at the selected plane. (Reproduced from [43])

geometries. The knowledge acquired under such scenario may further help in understanding more complex flows in the aortic arch [43].

Figure 2.37 shows a key finding from the study conducted by Doorly et al.. A simple *U-bend* was used to mimic the anatomy of the aorta while excluding the bifurcations and flow pulsatility to simplify the model. After running a 3D CFD simulation, a plane within the vicinity of the aortic arch was used to assess flow behaviour. The chosen plane coloured by values of vorticity, the curl of a flow field, and the velocity streamlines show how a dual rotation of opposite directions occurring in the flow. This key finding suggests that the arched anatomy of the aorta may be responsible for inducing a dual rotating helix from peak to late systole in the cardiac cycle [43].

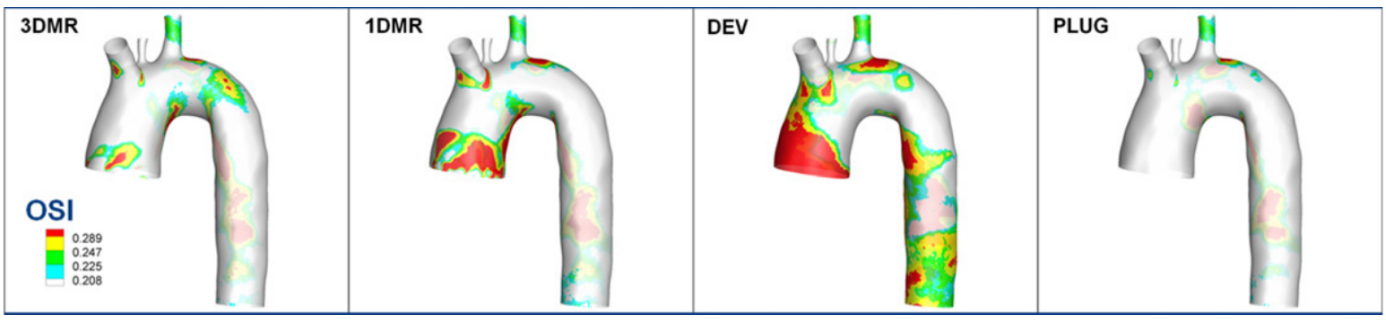


Figure 2.38: 3D CFD simulation results in a healthy aorta investigating different boundary conditions. Results show OSI. (Reproduced from [44])

Another study by Morbiducci et al. investigated the effect of different inflow boundary conditions on flow in a healthy aorta [44]. In their study, they prescribed different inflow boundary conditions to the aorta and investigated certain flow parameters to monitor the differences between the results. Four different boundary conditions were used; 3D CMR (**3DMR**) Venc, 1D CMR Venc (**1DMR**) in the through plane direction, a generic fully developed Poiseuille flow profile (**DEV**) and a generic time dependent spatially constant flow profile (**PLUG**). The location of the inflow was at a plane in the middle of the aortic root right above the aortic sinuses [44].

Figure 2.38 shows one of the key results in their study. Oscillatory Shear Index (OSI) which is a parameter representing flow disturbance over the cardiac cycle was used to assess the impact of using different inflow boundary conditions. It was concluded that the 1DMR or PLUG may be sufficient in capturing bulk flow behaviour and temporal flow disturbances without the need of using a complicated **3DMR** model which was used as the base case [44]. Moreover, using simplified inflow boundary models like the **DEV** model may obscure complete modelling and assessment of disturbed flow behaviour in the aorta especially in the proximal aortic region.

Moving Wall Method

Studies like those by Doorly et al. and Morbiducci et al. led to the ability of using more advanced CFD models with the comfort of knowing which appropriate boundary conditions to be used for the simulations in addition to expecting certain flow behaviour under different clinical scenarios a priori.

One of these advanced CFD models is the moving wall method where the walls of the artery under investigation are not modelled as rigid walls but instead prescribed some form of wall motion in the simulation. This serves the purpose to investigate certain clinical scenarios where the movement of the fluid medium is important as in the scope of this work.

The study by Berdajs et al. investigating the differences between the Yacoub and David valve conserving operations in porcine aortic roots used the moving wall method [24]. Figure 2.16

shows the results of the moving wall simulations. In these simulations, the motion of the boundaries of the domain of interest is tracked using an imaging technique then implemented in the CFD solver to capture the boundary movement along with spatio-temporal blood flow. In that scenario, such simulation technique was helpful in order to assess the aortic valve dynamic behaviour in different clinical scenarios.

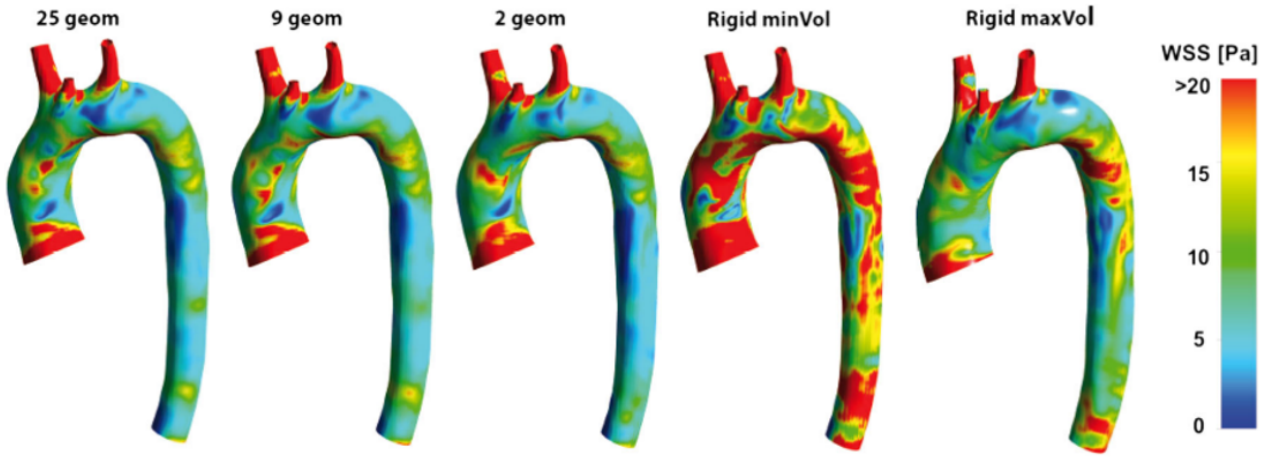


Figure 2.39: 3D CFD simulation results with the moving wall method in a healthy aorta. Results show WSS at peak systole in different scenarios of interpolating geometries and rigid models. 'geom' models refer to the moving wall models with 25,9 and 2 temporal geometries with interpolation to represent the motion of the aorta. (Rigid minVol) and (Rigid maxVol) represent the rigid wall models at end diastole and peak systole respectively. (Reproduced from [45])

The moving wall technique was also used in a study by Lantz et al. to investigate the effect of aortic wall motion on blood flow across the cardiac cycle. In their study, Lantz et al. used MR images of a healthy aorta to reconstruct the vessel at 2, 9, and 25 different time points across the cardiac cycle. Next, they deduced the motion of each section in the aorta from these reconstructions and prescribed them to the CFD solver. The results were compared to two different rigid wall models where the aorta was reconstructed at the peak systolic phase (**Rigid maxVol**) and at the end diastolic phase (**Rigid minVol**) [45].

Figure 2.39 shows the Wall Shear Stress (WSS) distribution on the wall of the aorta at the peak systolic phase of the cardiac cycle. It is visible from the colour map that incorporating the motion of the aorta in the CFD simulation gives a different distribution compared to the rigid wall cases which show areas of elevated WSS in the ascending aorta [45]. On the other

hand, the differences between the moving wall cases using 9 and 25 geometries reconstructed at different phases were minute suggesting that 9 geometries or time points were sufficient [45].

These results suggest that prescribing the motion of the aorta in a CFD solver may yield a different flow distribution; hence, a different assessment of the flow field. In certain scenarios where the wall motion is comparable to the size of the domain of interest as in the aortic root, such wall motion may be worthy of including in the simulation.

Fluid-Structure Interaction

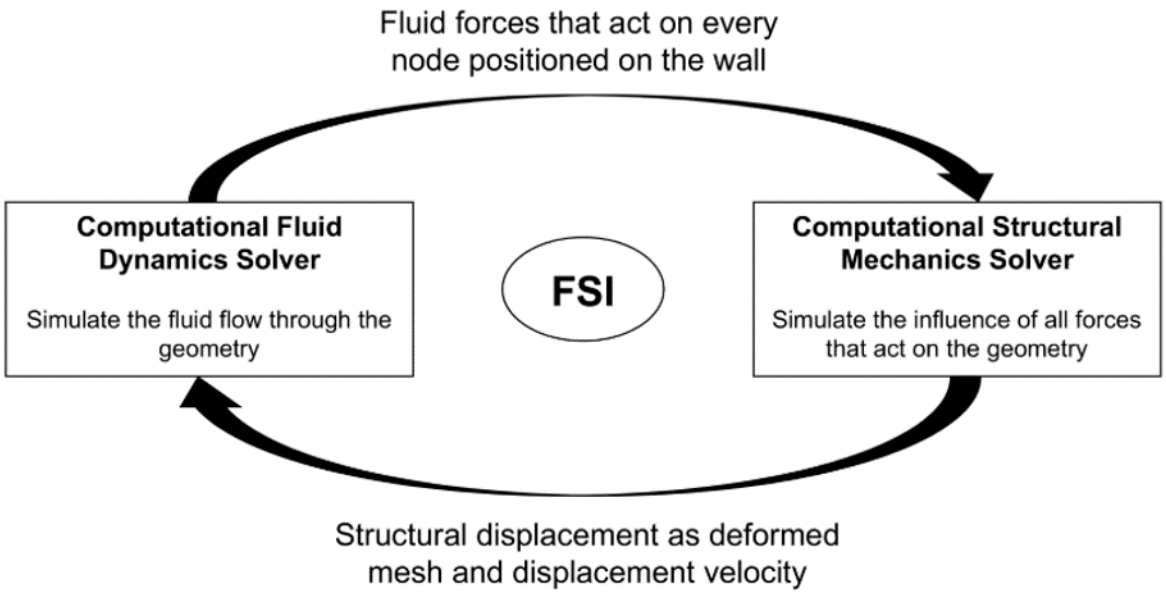


Figure 2.40: A schematic outlining the FSI technique. (Reproduced from [46])

Another higher order computational model is FSI. FSI simulations have become popular in the field of physiological fluid dynamics due to their ability to model the interaction between the fluid and surrounding structures. In this model, a CFD solver for capturing the flow field is used along with a solid solver to capture the structural behaviour also known as a finite element solver owing to its numerical technique. When the two solvers interact, the fluid dynamics equations are solved and the pressures are used as forces impacting the surrounding structures. However, the major problem in using FSI methods in physiology problems is the uncertainty behind choosing a material model to represent the behaviour of the structure for the finite

element solver [11],[45],[46]. In addition to this, rigid body movement such as accelerations of the aortic root will have an effect on the fluid flow.

Figure 2.40 summarises the FSI method. The arrows signify that coupling between both solvers is the main method behind the technique. FSI is useful when the purpose of the analysis is to model the dynamic behaviour of the aortic valve leaflets.

Sturla et al. used *in vivo* and *ex vivo* imaging data from literature to reconstruct a normal aortic root and run an FSI simulation to assess the dynamic behaviour of the valve leaflets [47]. Figure 2.41 shows the temporal stresses on each leaflet along a curve running down their middle as shown. This is one of the benefits of using FSI as obtaining stresses due to haemodynamic forces is not possible computationally without this method.

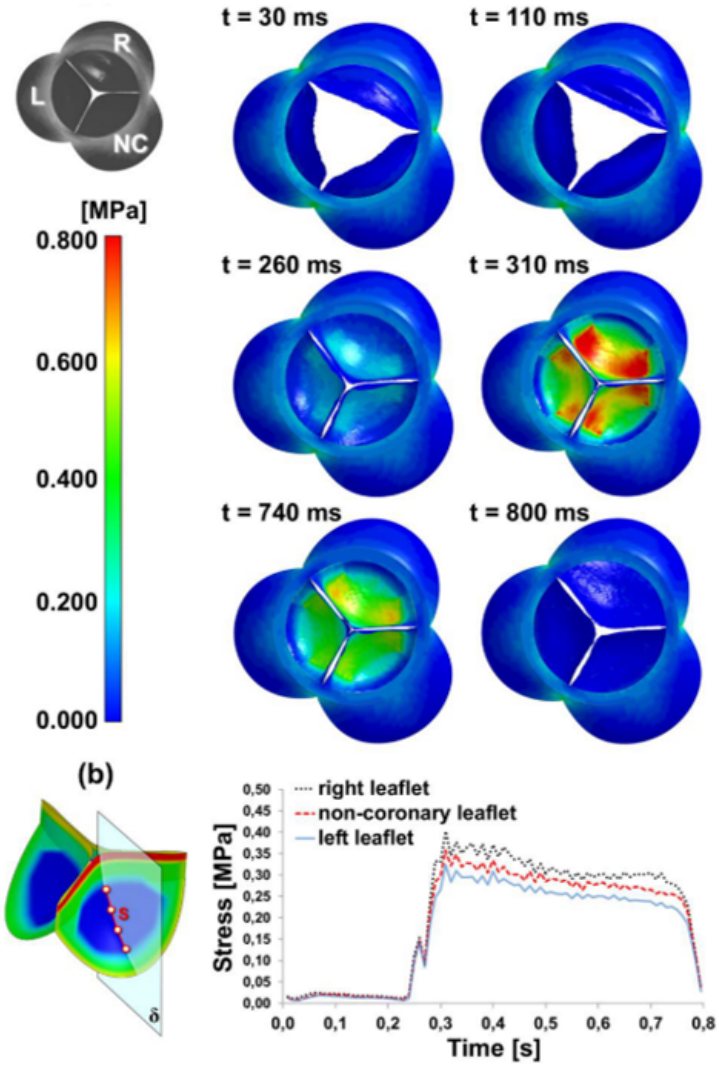


Figure 2.41: FSI results in a normal aortic root. Results show temporal stresses along a curve in the middle of the valve leaflets. (Reproduced from [47])

The results show that the stresses on all leaflets are almost identical with the stresses peaking at the time of valve closure then decreasing again towards the end of diastole [47]. In addition to this, Sturla et al. used the results from the CFD solver to support the concept of the vortices in the aortic sinuses forming in late systole in the cardiac cycle [47].

It is worthy to mention at this stage that the different methods in assessing haemodynamics outlined are versatile and incorporate different technicalities. Since the perfect model does not exist, it is advisable to use whichever method or mix multiple methods depending on the problem under investigation. We will further discuss in this thesis how using different methods to assess haemodynamics may be beneficial to tackle a specific clinical question.

2.2.5 Experimental Techniques

Although using experimental apparatuses to assess cardiac blood flow is beyond the scope of this thesis, they are still useful in certain cases to assess blood flow in complex clinical scenarios. Toninato et al. conducted a study using a popular experimental apparatus, i.e. pulse duplicator, in order to investigate different surgical configurations of aortic valve bio-prosthesis and their effect on aortic root flow [48].

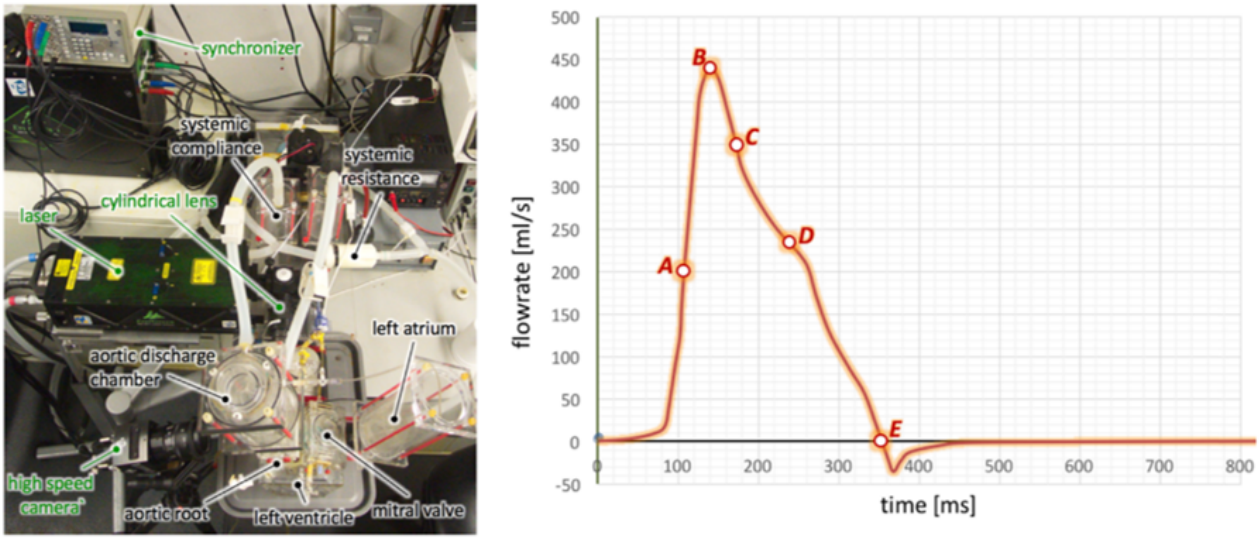


Figure 2.42: A picture of the pulse duplicator modelling the left heart and the physiological flow condition used to conduct the experiment. The analysed region for the flow field is labelled as the aortic root. (Reproduced from [48])

Figure 2.42 shows the pulse duplicator used by Toninato et al. to conduct the experiment. The pulse duplicator contains chambers which can model the atrium, ventricle and artery either on the left or right side of the heart. The valve placed in the artery section along with the flow and pressure conditions set before the experiment dictate whether the pulse duplicator is modelling the left or right side of the heart [48]. The figure also shows the physiological flow waveform used just upstream of the aortic valve to conduct the experiment.

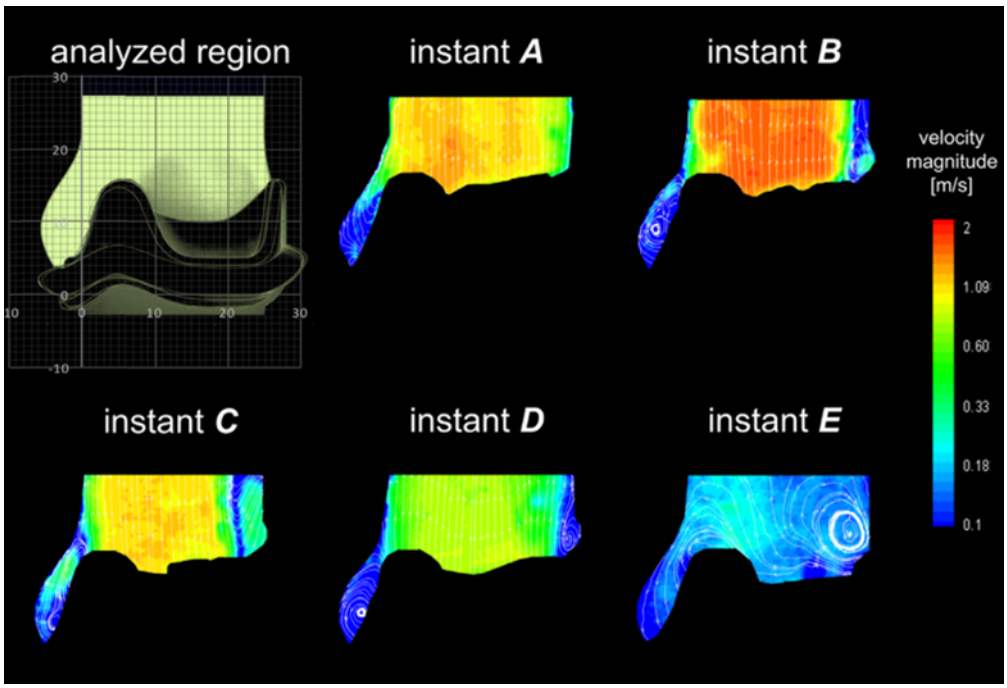


Figure 2.43: Velocity contours and streamlines from the pulse duplicator after post-processing. (Reproduced from [48])

The results from the pulse duplicator experiment were analysed using Particle Image Velocimetry (PIV) which is an experimental flow visualisation technique. Figure 2.43 shows the velocity contours and streamlines at the chosen five time points shown in the flow waveform in Figure 2.42. In this surgical configuration where the porcine valve was implanted according to physiological anatomy of the aortic root, Toninato et al.'s results are in agreement with Bellhouse et al.'s where the vortices in the aortic sinuses exist from peak to late systole [48],[19].

Using experimental techniques as in the study by Toninato et al. is beneficial as it may help in assessing optimum surgical configurations in valve replacement or valve sparing surgeries prior to the operation. Computational techniques have not yet demonstrated that ability; hence, experimental techniques cover a clinically important area of research.

With the variety of methods in assessing haemodynamics, we believe that computational methods relying on inputs from clinical imaging will be our best option to address the hypotheses behind this thesis. However, we must first provide a clear definition of our domain of interest in this study since the aortic root may be a source of confusion with different anatomical definitions present in the physiological literature.

2.3 The Aortic Valve Apparatus (AVA)

The aortic root contains different components with different functions; hence, it is preferable to be described on a macroscopic level dividing it into different components by function rather than on a microscopic level by histopathological content [49]. In addition to this, different complex physical interactions between the aortic root and surrounding blood flow are to be tackled in this study; thus, a unified definition of aortic root anatomy will be necessary.

Left Ventricular Outflow Tract

The first component in the AVA is the LVOT. This is the conduit passage between the LV and aortic root. Anatomically, it sits in between the aortic root sinuses forming the so called interleaflet triangles (ILT). These triangles are the extensions of the LVOT that coincide with the sinotubular junction (STJ). [49].

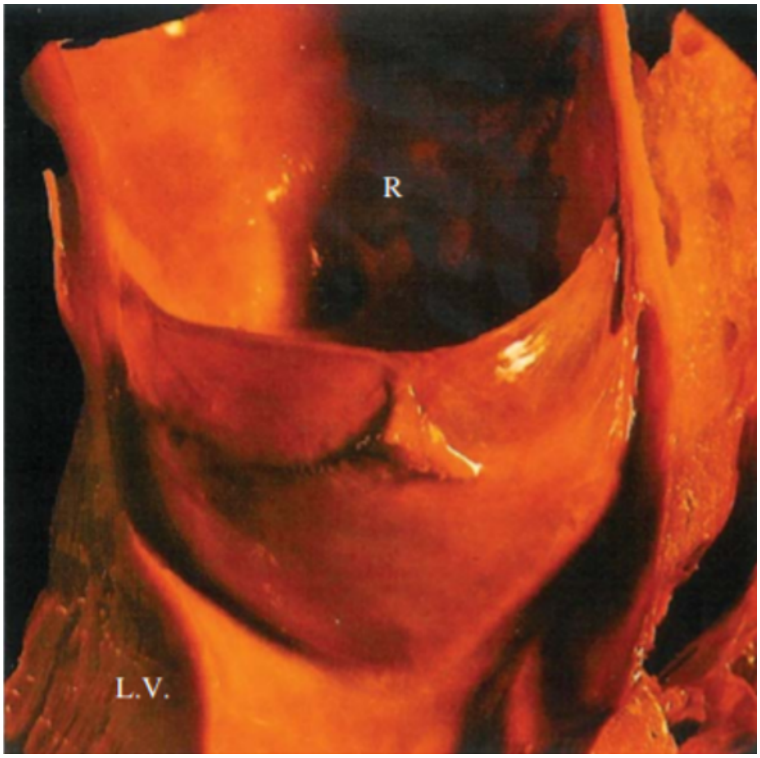


Figure 2.44: AVA longitudinal section. The LVOT is indicated by the letters LV and the letter R shows the RCS. (Reproduced from [49])

Bearing in mind the considerations of certain simulations to be conducted in this study, we

defined the base of the AVA i.e. the LVOT base to be 20 mm below the aortic annulus. This value is not critical in the sense that it was chosen only to consider leaving room for the movement of the AVA in the computational work in Chapter 6.
Figure 2.44 shows a longitudinal section of the AVA. The LVOT sits on top of the LV and coincides with the commissures.

Annulus

The second component is the annulus which may also be referred to as the ventriculo-arterial junction. The annulus is an imaginary ring, not necessarily circular, connecting 3 intersection points between the sinuses and LVOT.

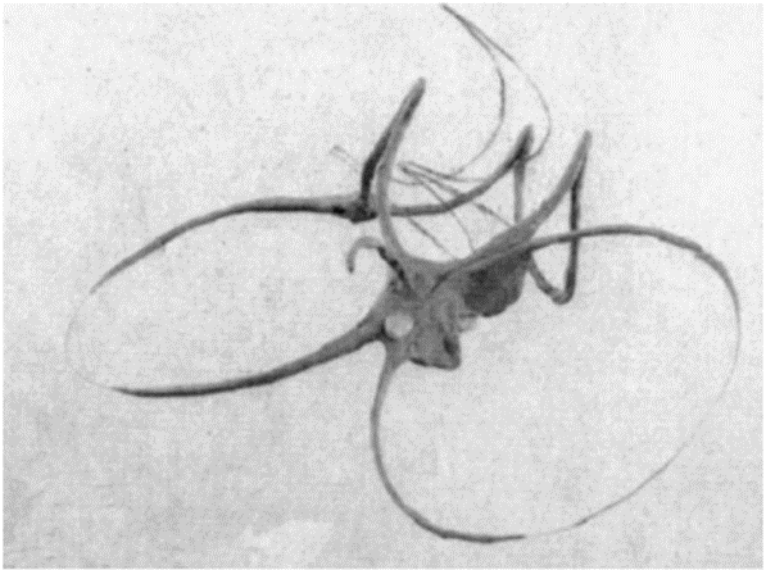


Figure 2.45: Cardiac fibrous skeletal body. (Reproduced from [49])

Figure 2.45 shows the fibrous skeleton of the heart. The mitral and tricuspid annuli may be seen with the aortic crown shaped structure sitting on top. The crown shaped structure contains 3 minima which are the 3 annulus points. The annulus points are also the intersection points between the aortic root and the LVOT.

Commissures

The peaks of the crown shaped strucutre are known as the commissures. They are the coaptation points of any two valve leaflets on the aortic wall [49]. The commissures also correspond with the STJ points.

Sinuses of Valsalva

The three sinuses of valsalva encompass the aortic valve leaflets and form the bounding walls of the aortic root. One sinus may be seen in Figure 2.44 as the bulging area opposite the visible leaflet. Each sinus along with its corresponding leaflet form a pocket like space which may redistribute blood flow in its vicinity [19]. The sinuses also contain the attachment to the coronary arteries via the coronary ostia [49].

AVA Top

The aortic wall at the top of the AVA merges smoothly into the wall of the ascending aorta without any visible anatomical markers. This makes the boundary between the AVA and the ascending aorta somewhat arbitrary.

As a result, the AVA Top is chosen to be the first section in the ascending aorta with a circular cross-section. This is always visible with a through plane imaging view and is usually located at approximately 7 mm above the commissures for adults.

Part II

Chapter 3

Plan of Investigation

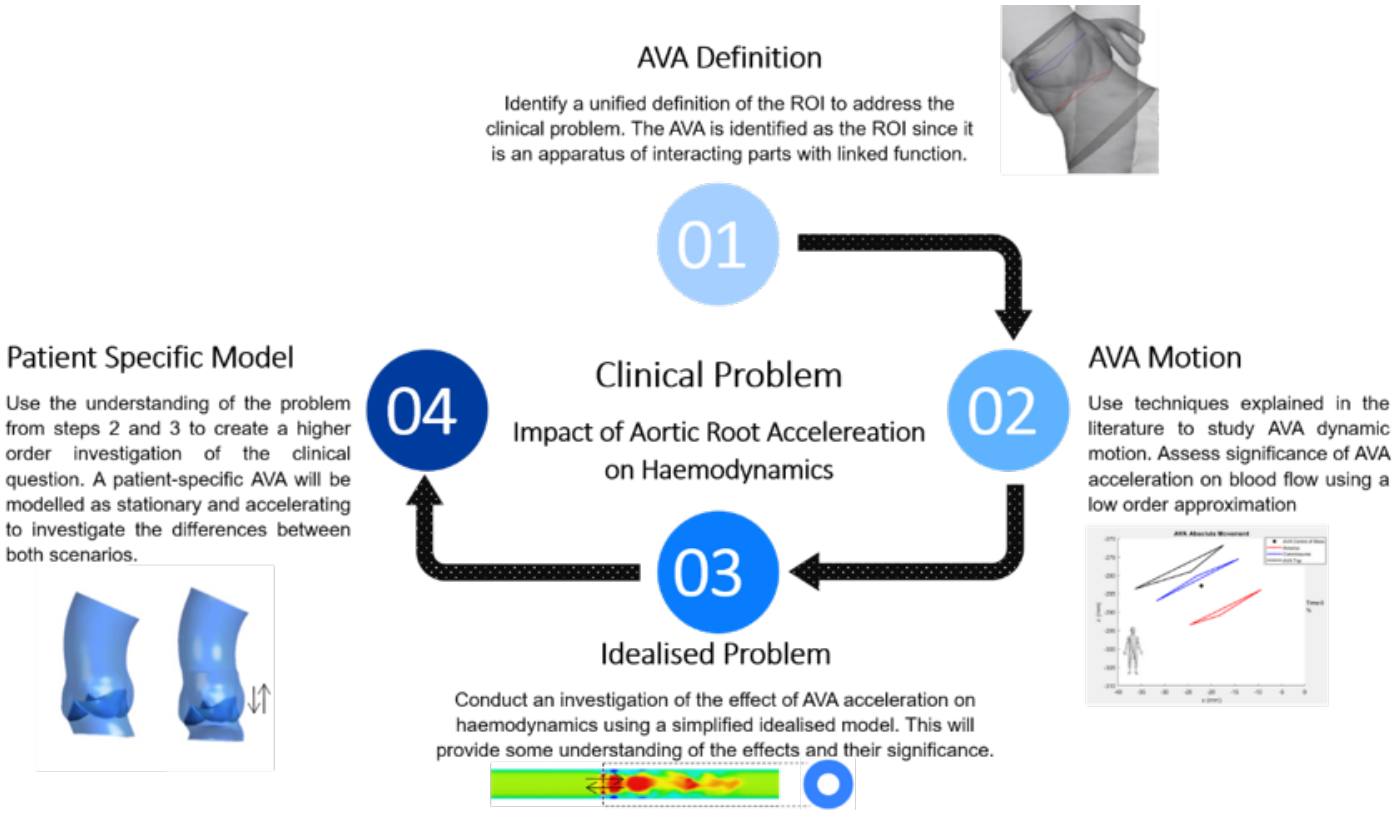


Figure 3.1: Flow chart outlining the plan of investigation

As seen in the literature review, the effect of aortic root acceleration on haemodynamics has generally been neglected. In addition to this, the varied functions of the aortic root are linked in a complex, orchestrated manner via the complicated dynamic motion of the root and its surrounding structures. Strong coupling also exists between the structures in the aortic root

and the blood flow in their vicinity.

A hypothesis suggesting that the aortic root is *actively* dynamic has been presented by Yacoub et al. [5]. This *active dynamism* hypothesis means that the aortic root may be considered a separate organ within the cardiovascular system and may contain elements that give it its dynamism abilities and not just a collection of tissues responding to haemodynamic forces. Other theories considered the motion of the aortic root to be cardiac induced meaning that the root exhibits *passive dynamism*.

We believe that whether or not the aortic root exhibits *active* or *passive* dynamism, the effect of its motion i.e. acceleration should be investigated as it may be of clinical significance. From that perspective, we aim to tackle the clinical question of investigating the impact of aortic root acceleration on blood flow distribution. Since we have seen while reviewing the literature that it is necessary to understand the physics behind this problem and its neglect in physiology, we will restrict the work of this thesis in investigating the clinical question for normal aortic roots rather than looking into scenarios of aortic disease.

Figure 3.1 is a summary of the tasks to be carried out in this thesis. Since the aortic root may be considered a cardiac organ performing vital functions, it may have different definitions in physiology. Firstly, we present a clear definition of the AVA which will be used throughout this thesis to carry out the plan of investigation. The AVA will be the region of interest (**ROI**) for investigating the impact of its acceleration on blood flow distribution.

Secondly, we study the motion of the AVA using techniques previously presented in the literature. We use a technique that shares similarities with the technique of sonomicrometry presented by Berdjas et al. and Benhassen et al. [6],[28]. Since our work is restricted to studying the normal AVA, surgical implantation of sonomicrometric crystals to track the motion of the AVA is not an option. As a result, we use CT images from four patients admitted to Aswan Heart Centre with chest pain suspecting coronary disease who were later discharged as normal. In order to emulate the sonomicrometry technique, we introduce the concept of landmark or *fiducial* point tracking to represent the motion of the AVA. From the CT images, the AVA was reconstructed and the motion was assessed using an in-house developed MATLAB code. In the

code we use the nine *fiducial* points to construct three triangular segments representing the AVA [6]. More details on the methods will be presented in Chapter 4.

We then deduce through a basic 1D approximation using the water-hammer equations that the acceleration of the AVA may be responsible for the dicrotic notch feature present in aortic pressure measurements at the time of valve closure where the AVA accelerates to its peak value away from the LV. The hypothesis of the AVA acceleration being responsible for the dicrotic notch pressure rise at the time of valve closure led us to believe that a higher order model is necessary to investigate this effect.

Thirdly, we resort to an idealised geometrical model as in the study by Doorly et al. in order to investigate the preliminary significance of the acceleration of the AVA on blood flow [43]. Hence, we came up with a simple geometrical model of a tube with a circular orifice simplifying the complex anatomy of the AVA as shown at the bottom of Figure 3.1. At this stage we realised that not only the motion of the AVA plays a role in the complexity of the clinical question to be addressed in this study, but also the fact that the flow is pulsatile in nature and that the aortic valve opens and closes during the cardiac cycle.

As a result, we outline simple scenarios to decompose the investigation of these complex features in the idealised geometrical model. We also deduce non-dimensional parameters using the Buckingham Π theorem to ensure an understandable mathematical representation of the physics involved. The analysis is carried out on the idealised geometry using a moving wall CFD technique. All the derivations and analytical outcomes will be explained in Chapter 5.

Finally to address the clinical problem in this thesis, we reconstructed a full AVA model using one of the four normal CT scans and used it in higher order simulations. The complexity of the higher order simulations made it unfeasible to investigate more the one normal in addition to the unavailability of CT images to capture the valve leaflets with acceptable resolution. The method presented in these simulations is novel as we deployed both the moving wall CFD method and the FSI method simultaneously in order to capture the dynamics of the AVA and valve. We use the reconstructed model to investigate two scenarios where the AVA is not accelerating and where it is accelerating. We then compare the results from both scenarios to

assess the impact of the acceleration on blood flow distribution. In Figure 3.1 we show a single time frame with the stationary AVA and the accelerating AVA at the time of valve closure where the accelerating AVA will suddenly move away from the LV. In Chapter 6 we will show how the results from these simulations correlate to the 1D approximation of the mechanics of the dicrotic notch suggesting that the acceleration of the AVA may have an impact in assessing aortic disease.

3.1 Aims

In summary, the main hypothesis under investigation in this thesis is the impact of aortic root acceleration on the surrounding blood flow. The main objectives in Chapters 4, 5 and 6 are set up to investigate the aforementioned hypothesis.

In Chapter 4, we start by quantifying the different asymmetric movements of the AVA using fiducial point tracking from CT images of four normal subjects to emulate the technique of sonomicrometry described in Chapter 2. This gave us insight on the kinematics of the AVA decoupled from blood flow effects.

In Chapter 5, we resort to a simplified geometrical model of a tube and orifice in order to apply the kinematics obtained from the analysis in Chapter 4 in an idealised model. This will serve to provide some insight on blood flow distribution coupled with the kinematics of the AVA in a model which shares some anatomical similarities with the physiological AVA.

Finally in Chapter 6, we upgrade the analysis by using a subject's physiological AVA reconstruction in order to investigate the hypothesis of this thesis. The higher order simulation used is complex as it employs both the FSI and wall motion techniques in order to capture valvular motion and the kinematics of the AVA respectively.

The motive behind this plan of investigation is to test the correlation between the dynamic behaviour of the AVA and the flow distribution. If such correlation exists, this work can provide the basis of a novel non-invasive technique to assess patients with cardiac disease.

Chapter 4

Aortic Root Kinematics

In Chapter 2 we mentioned how we need to formalise a unified definition of AVA to avoid confusion with different definitions of the aortic root in physiology. We also introduced the concept of *fiducial* point tracking in Chapter 3 in order to use a non-invasive technique to emulate the process of sonomicrometry used by Berdajs et al. [6].

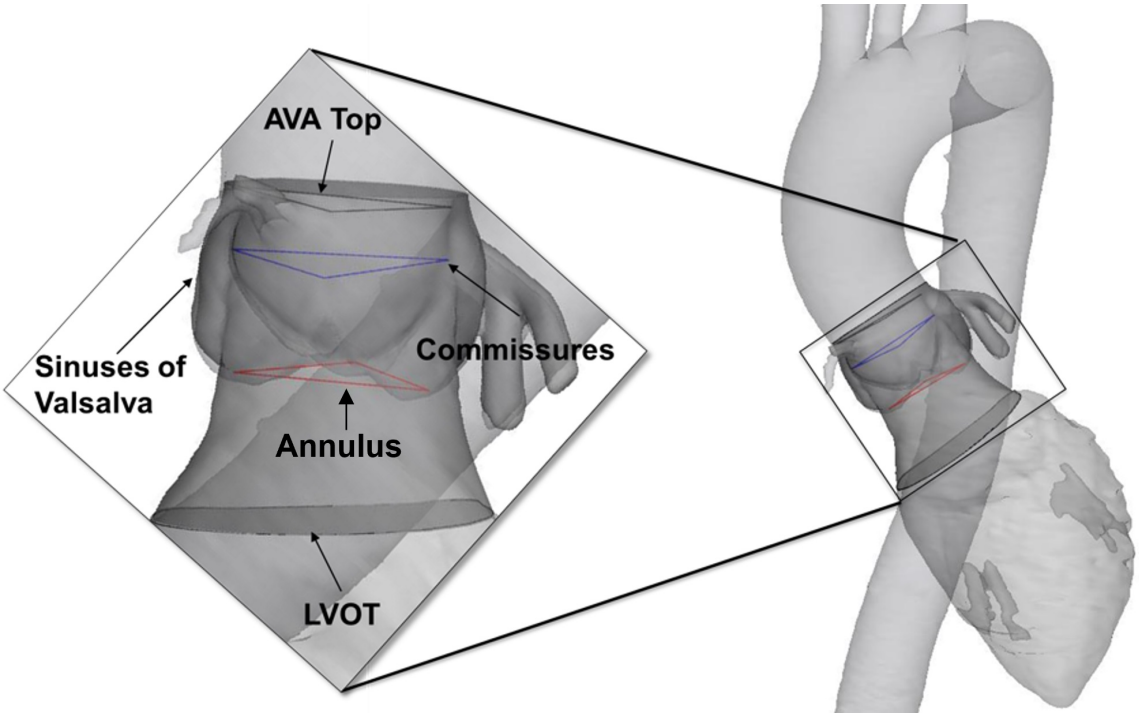


Figure 4.1: Formalised definition of the AVA. (right) Reconstruction from a CT scan showing the LV, the AVA and the thoracic aorta. (left) An expanded view of the AVA showing the three planes defined by the fiducial points. Red, blue and black show the annulus, commissures and AVA top sections respectively.

In this chapter we explain how our definition of the AVA is used in this thesis to study the motion, particularly the acceleration, of the AVA and its effect on blood flow distribution. We then use a geometrical representation of fiducial points to quantify the kinematics of the AVA. It is important to clarify at this stage that we believe the kinematics of the AVA needs quantification regardless of its relationship to surrounding haemodynamic forces or the forces that may be causing it [50].

Figure 4.1 shows our formalised definition of the AVA in one out of the four normal cases used in this thesis. The CT scan of each patient was reconstructed over ten equispaced times during the cardiac cycle. It is important to note that one of the disadvantages of CT which is discussed in detail in the Limitations Section is that each time point is acquired as the best in spatial resolution from many heartbeats. This means that CT images do not provide the ability to assess multiple cardiac cycles after reconstructing the AVA and hence why we only show temporal results throughout this chapter from one cardiac cycle. Next, the aorta and LV were reconstructed using a semi-automated image processing method of the left heart in Materialse MIMICS. On the right side of Figure 4.1, the aorta and LV of the patient can be seen. On the left side of the figure, a zoomed in image on the AVA which was extracted from the 3D reconstruction can be seen.

As stated in Chapter 2, we defined the AVA to contain a section in the LVOT 20 mm below the annulus to accommodate for the AVA motion during the higher order simulations, the sinuses of valsalva which play an important role in the blood flow distribution, the aortic valve and commissures, and the AVA top which is the section in the ascending aorta where the aortic cross-section starts to be circular. The coloured triangles connecting the three fiducial points at each level shown in Figure 4.1 show our geometrical representation of the AVA used to quantify its kinematics. Although multiple representations are available in the literature like Berdajs' representation of the AVA using two triangles at the annulus and STJ, we chose this representation in particular to account for the region of interest for blood flow assessment [6].

The vertices defining each segmental triangle have been deduced on an anatomical landmark basis. The annulus triangle in red is defined by the three vertices of the annulus points. The

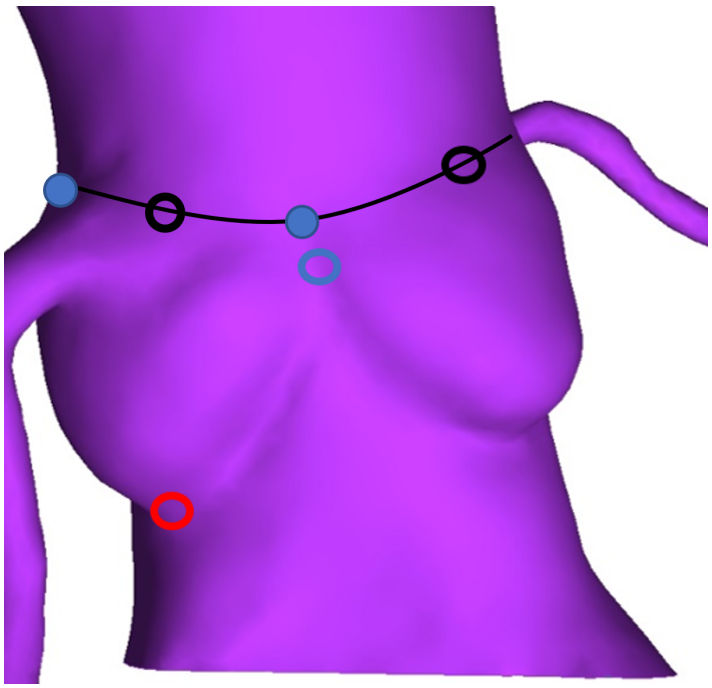


Figure 4.2: Fiducial point selection on a reconstructed AVA. The fiducial points have an anatomical significance. Red, blue and black circles denote an annulus point, commissure point and AVA Top point respectively. Solid blue circles show the projection of the commissure points on a plane at the chosen AVA top section. The projected points construct the black curve shown where the midpoints of each segment are the AVA top points in black.

annulus points are known to be the minima in the aortic root or the intersection between the sinuses of valsalva and the LVOT. The commissure triangle in blue is defined by the three intersection points between the valve leaflets and the AVA wall. Finally, the AVA top triangle in black is defined by the midpoints of the curve constructed by a projection of the three commissure points on a plane at the chosen AVA top section.

Figure 4.2 shows how the fiducial points were selected from each reconstruction of the AVA. Each point is shown in the same colour as the triangle it constitutes. The annulus point is at the intersection between the sinus and the LVOT. The commissure point is the intersection between the valve leaflet fixed edge and the AVA wall. After projecting the commissure points on a curve at the chosen circular section at the AVA top, the AVA top points were simply at the midpoints along the projected curves. The aforementioned circular section was chosen to be at the junction between the AVA and the ascending aorta where the cross-section appears to be circular from the CT axial images.

4.1 Fiducial Point Tracking

The process of selecting the fiducial points to be tracked, explained in pages 68-69, was repeated over ten equispaced time frames in the cardiac cycle for each one of the four patients in order to analyse the kinematics of the AVA. Since we seek a mathematical representation and quantification of the kinematics of the AVA, we decided to represent the temporal coordinates of the fiducial points in a multi-dimensional matrix using the following notation :

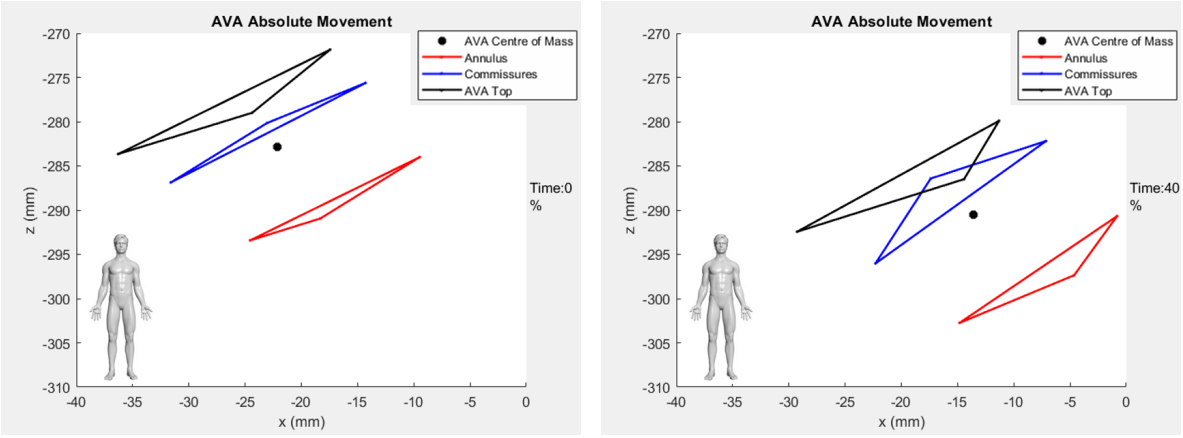
$$[X] = X_{ijn} \tag{4.1}$$

Equation 4.1 only states that the matrix of fiducial points is constructed by i rows which are the indeces of the chosen fiducial points ($i = 1-9$), j columns which represent the global spatial coordinate system [x,y,z] ($j = 1 - 3$), and a third dimension n which represents the temporal phases of the cardiac cycle ($n = 1 - 11$). For each case we constructed a three dimensional tensor in order to assess the kinematics of the AVA using the definition in equation 4.1. It is important to note that we have extended the number time frames to 11 so that we can treat the measurements as periodic with a periodicity of 10; i.e. $X_{ij1} = X_{ij11}$.

In order to simplify the notations further, we decided to use a common convention in statistics for expressing summations. This is necessary as we will be using summations to calculate the centre of mass (COM) of the AVA. The dot notation for summation is given by:

$$X_{\cdot jn} = \sum_{i=1}^{9} X_{ijn} \tag{4.2}$$

In other words, equation 4.2 shows that a summation over all the fiducial points indexed ($i = 1 - 9$) is represented by a dot in the subscript replacing the index of summation.



(a) Start of systolic phase (b) Start of diastolic phase

Figure 4.3: Absolute position of the AVA fiducial points for two frames in the measured cycle. The origin is not visible as the absolute position of the AVA is given initially in the CT machine coordinates.

Figure 4.3 shows the resultant motion tracking of the AVA at two distinct times in the cardiac cycle. We chose the cardiac cycle to be aligned with the RR interval since the CT scan was ECG gated. This means that the inital phase in the cardiac cycle shown in Figure 4.3a is at the R wave of the cardiac cycle representing the beginning of the ejection phase. The fiducial points were used to construct three segmental triangles along the axis of the AVA coloured according to the description in this chapter. We also used equation 4.3 to deduce the COM of the AVA at each phase in the cardiac cycle.

$$COM_{jn} = \frac{X_{.jn}}{9} \tag{4.3}$$

At the end of systole shown in Figure 4.3b, the AVA has moved the maximum distance towards the LV and is about to accelerate in the opposite direction along its axis. The COM of the AVA is shown along with the segmental triangles as a black dot at the chosen time frames.

It is visible that the AVA is rigidly translating towards and away from the LV across the cardiac cycle while deforming locally. As a result, we chose to decompose the general motion of the fiducial points into the motion of different averages of the points in order to in order to be able to assess and quantify the complex dynamic motion. The first step in the process of decomposing the motion of the AVA was to transform the motion to a local origin i.e. the AVA

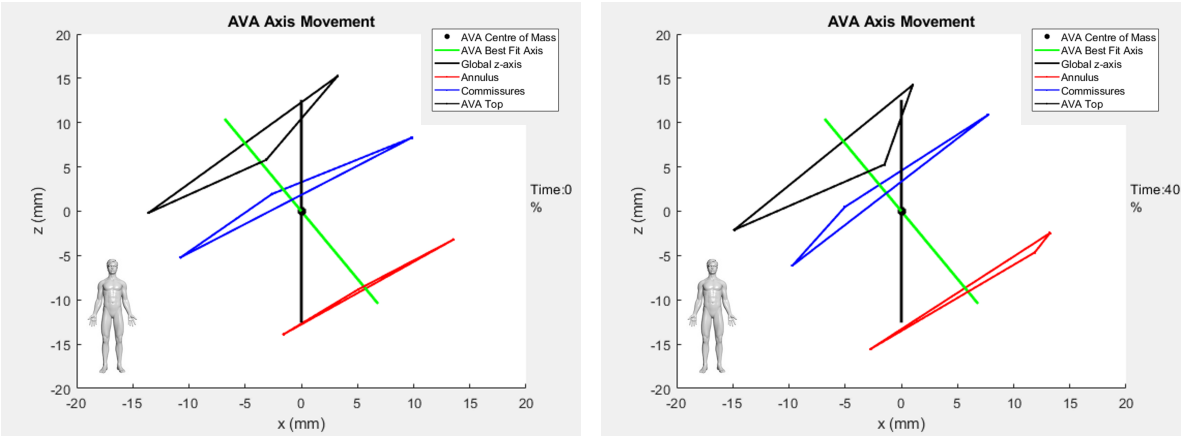
COM. This was simply done by equation 4.4.

$$[X]_{local,ijn} = X_{ijn} - COM_{jn} \tag{4.4}$$

The second step was to obtain a best fit axis of the AVA at all time frames in the cardiac cycle. This best fit axis would be a basic representation of the AVA centreline. The best fit axis should pass through the COM of each segmental triangle along with the COM of the AVA. This is ensured by using the local origin as given by equation 4.4. Therefore, the best fit axis noted by Y can be calculated using singular value decomposition (SVD) for each time frame. SVD has a wide range of uses in a variety of fields since it decomposes a matrix into three different matrices. This decomposition can yield interesting features about the initial matrix [51]. In our case, decomposing $[X]_{local,ijn}$ using SVD will return a matrix containing the best fit axis of the AVA at each time frame in the cardiac cycle.

$$U_{jn}S_{jn}V_{jn} = SVD([X]_{local,ijn}) \tag{4.5}$$

Equation 4.5 which may be executed by one line of code using the svd function in MATLAB yields the three matrices U_{jn}, S_{jn} and V_{jn} at each time point in the cardiac cycle. The matrix V_{jn} is a 3x3 matrix where the coordinates of the best fit axis of the AVA at each time point are given by the first column.



(a) Start of systolic phase (b) Start of diastolic phase

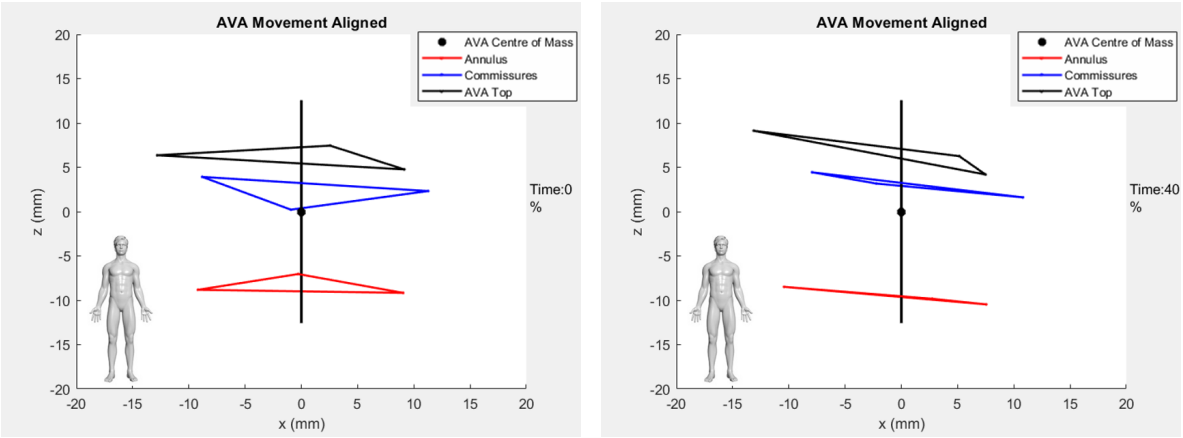
Figure 4.4: AVA axis of best fit temporal movement.

Figure 4.4 shows the deduced axis of best fit of the AVA at two time points in the cardiac cycle. The axis in green is plotted along with the global z axis in black. Both axes pass through the COM of the AVA which is shown by the black dot in the figure. The triangles of the AVA passing through the fiducial points are also shown. The angle between the axis of best fit of the AVA and the global z axis changed from 34° at the beginning of systole to 45° at the beginning of diastole which suggests the presence of rigid rotations of the AVA.

To further reduce the complexity of the kinematics problem, we aligned the best fit axis of the AVA along with the global z axis.

$$\{X'\}_{jn} = [R]_y[R]_x\{X\}_{local,jn} \tag{4.6}$$

Equation 4.6 shows how the alignment of the best fit axis of the AVA with the global z axis was performed. This was mathematically done by multiplying each fiducial point vector by two rotation matrices about the x and y axis. The rotation matrices were obtained by simple direction sines and cosines.



(a) Start of systolic phase (b) Start of diastolic phase

Figure 4.5: Temporal movement of the AVA after alignment with the z axis.

Figure 4.5 shows the temporal movement of the AVA after alignment with the global z axis which contains multiple local deformations that need to be quantified. We believe this alignment reduced the complexity of the problem due to the fact that the movement of each triangle will be reduced to a simple planar problem. At this stage, the aim was to quantify the following

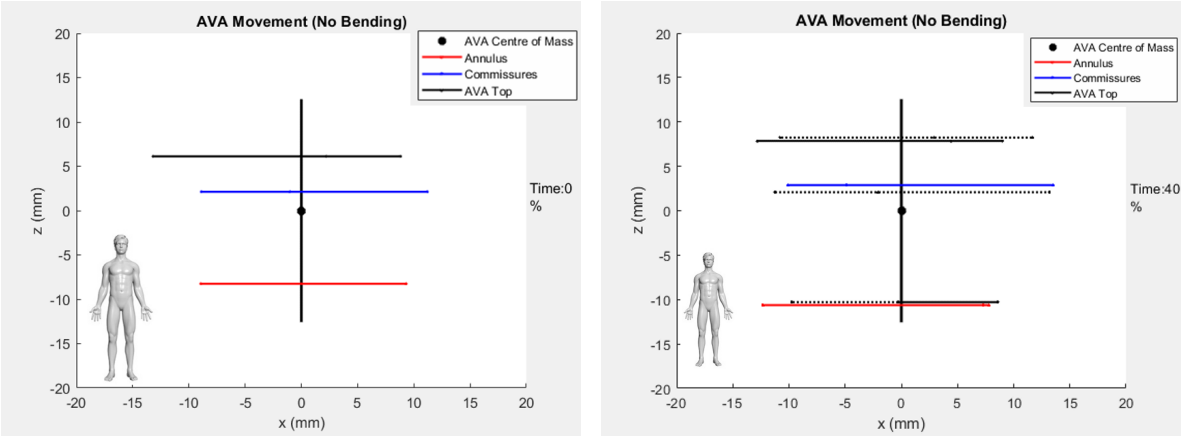
local deformations in the following order

1. Tilting or bending of the AVA
2. Axial stretching of the AVA
3. Radial dilatation of each segment in the AVA
4. Torsion of each segment in the AVA

Each one of the above local deformations of the segmental triangles in the AVA has a physiological significance. The tilting of the triangles represents the bending incurred by the AVA during the cardiac cycle. The axial stretching component which has not been mentioned in the literature to our knowledge demonstrates that the AVA may exhibit an *accordion* effect during the cardiac cycle. This means that the segmental sections in the AVA may be moving towards and away from each other locally. Next, the radial dilatation component is crucial to assess since it will quantify the temporal expansion and contraction of each segment in the AVA. Finally, torsion of the AVA will be also quantified to show whether the temporal twisting behaviour of the AVA is synchronised amongst all segments or not.

To calculate or decompose the tilting of the segmental triangles, first the outward normal of each triangle was obtained by the cross product of two sides in the triangle. Then, the triangles' tilting was decomposed by using equation 4.6. In this case, the rotation matrices used were derived based on aligning the triangle normals with the global z axis.

Figure 4.6 shows the resultant motion of the AVA after the bending component of motion was decomposed. From Figure 4.6b, it is visible that at the end systolic phase of the cardiac cycle the commissure segment of the AVA has moved closer towards the AVA top segment. In addition to this, the segmental triangles of the AVA are exhibiting in plane shearing while changing size simultaneously. This will lead to the other modes of deformation that still need to be analysed. These movements can be seen in Figure 4.6b where the dotted lines show the position of the triangles at the start of the systolic phase.



(a) Start of systolic phase (b) Start of diastolic phase

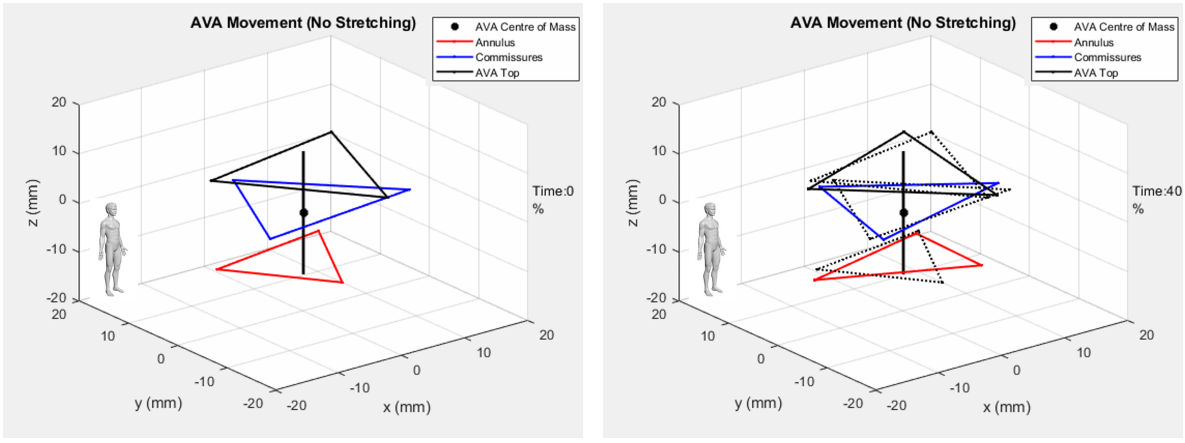
Figure 4.6: Temporal movement of the AVA after decomposing the bending motion. Black dotted lines in (b) show the position of the triangles at the start of the systolic phase.

The next mode of deformation to be analysed and decomposed is the axial stretching component which we will refer to as the accordion effect of the AVA. In order to analyse the accordion effect of the AVA, mathematical averaging is needed for each segment of the AVA. We will denote the vector for each triangular vertex after averaging the stretching component by $\{X'''\}_{jn}$.

$$\{X'''\}_{3n} = \frac{\{X''\}_{3\cdot}}{n} \tag{4.7}$$

Equation 4.7 shows how the mathematical averaging of the *accordion* effect was achieved. The new position along the z axis for each fiducial point is equal to the mean value of the temporal z position of the segmental triangle to which it belongs. $\{X''\}_{jn}$ in equation 4.7 denotes the fiducial point vectors before the decomposition of the *accordion* effect of the AVA.

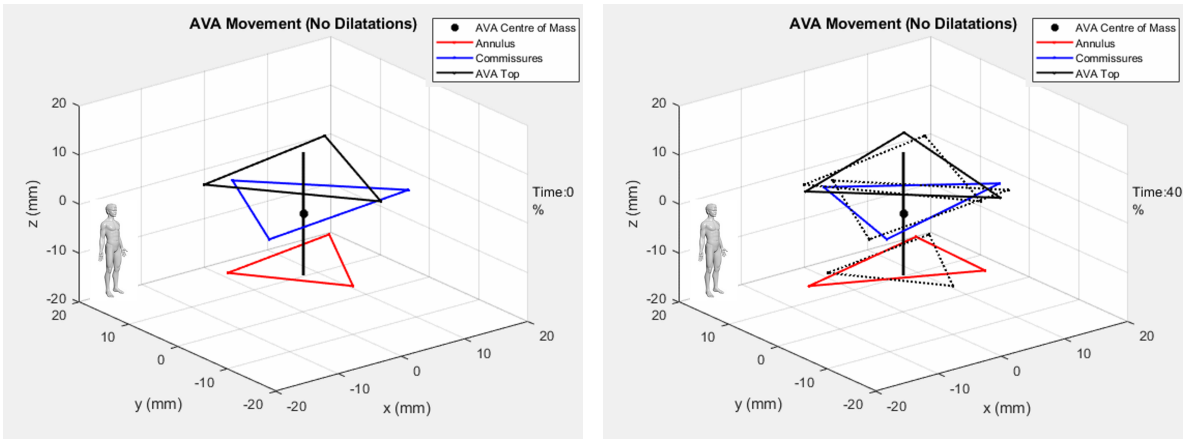
Figure 4.7 shows the temporal movement of the AVA after the averaging of the *accordion* effect. The viewing angle was changed by a 45° rotation around the global z axis in order to facilitate seeing the changes after decomposing the axial stretching component. Figure 4.7b shows that the annulus triangle has increased in area compared to the beginning of systole where the dotted black lines show the initial shape at the beginning of systole. Moreover, the segmental triangles are still twisting in addition to changing areas which led us to tackle the radial dilatation component of each axial segment in the AVA before assessing the twisting motion of the AVA.



(a) Start of systolic phase (b) Start of diastolic phase

Figure 4.7: Temporal movement of the AVA after decomposing the axial stretching motion. Black dotted lines in (b) show the position of the triangles at the start of the systolic phase.

To normalise or average the radial dilatation component of each segment of the AVA a very simple mathematical approach was used. Firstly, the distance between each triangular vertex and the z axis was calculated for each time frame. Next, the mean of the three distances between each of the three vertices constructing a triangle and the z axis at each time frame was calculated. Finally, each segmental triangle was normalised by the average radial distance its vertices at each time frame.



(a) Start of systolic phase (b) Start of diastolic phase

Figure 4.8: Temporal movement of the AVA after decomposing the segmental radial dilatations. Black dotted lines in (b) show the position of the triangles at the start of the systolic phase.

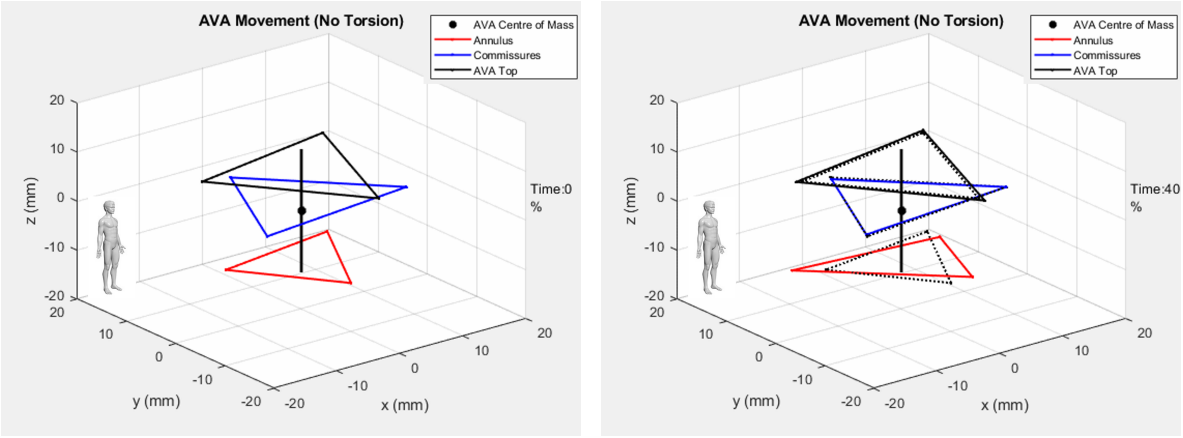
Although it may not be clearly visible from Figure 4.8 how the movement of the AVA was greatly reduced after the averaging of the radial dilatations component, it is mathematically deduced that the segmental triangles are no longer changing area. On the other hand, it is

visible from the figure that the triangles or their vertices are changing orientation with respect to the z axis which means that AVA is undergoing torsional movement during the cardiac cycle.

The final step in assessing the kinematics of the AVA is to decompose the torsional component of motion as previously mentioned in this chapter. In the same manner as the previous analyses, the idea is to calculate the mean position of each triangle from all the time frames. This is simply the mean x and y position of each triangular vertex across time. The next step is to average the position of each segmental triangle to the calculated time averaged position. This can be done using SVD. Having two different data sets of points or vertices as in our case, the optimal rotation angle between both data sets can be calculated using the following equations:

$$\begin{aligned} [H] &= [A][B]^T \\ [U, S, V] &= SVD([H]) \\ [R] &= [V][U]^T \end{aligned} \tag{4.8}$$

In our case, $[A]$ is the position of each fiducial point at each time frame. $[B]$ is the mean position of a segmental triangle across all time frames. The covariance matrix $[H]$ can then be easily calculated according to the above equations. After applying SVD to matrix $[H]$, the rotation matrix $[R]$ to decompose or average the torsional motion of each segment in the AVA is simply the product of two matrix outputs from the SVD of the covariance matrix.



(a) Start of systolic phase

(b) Start of diastolic phase

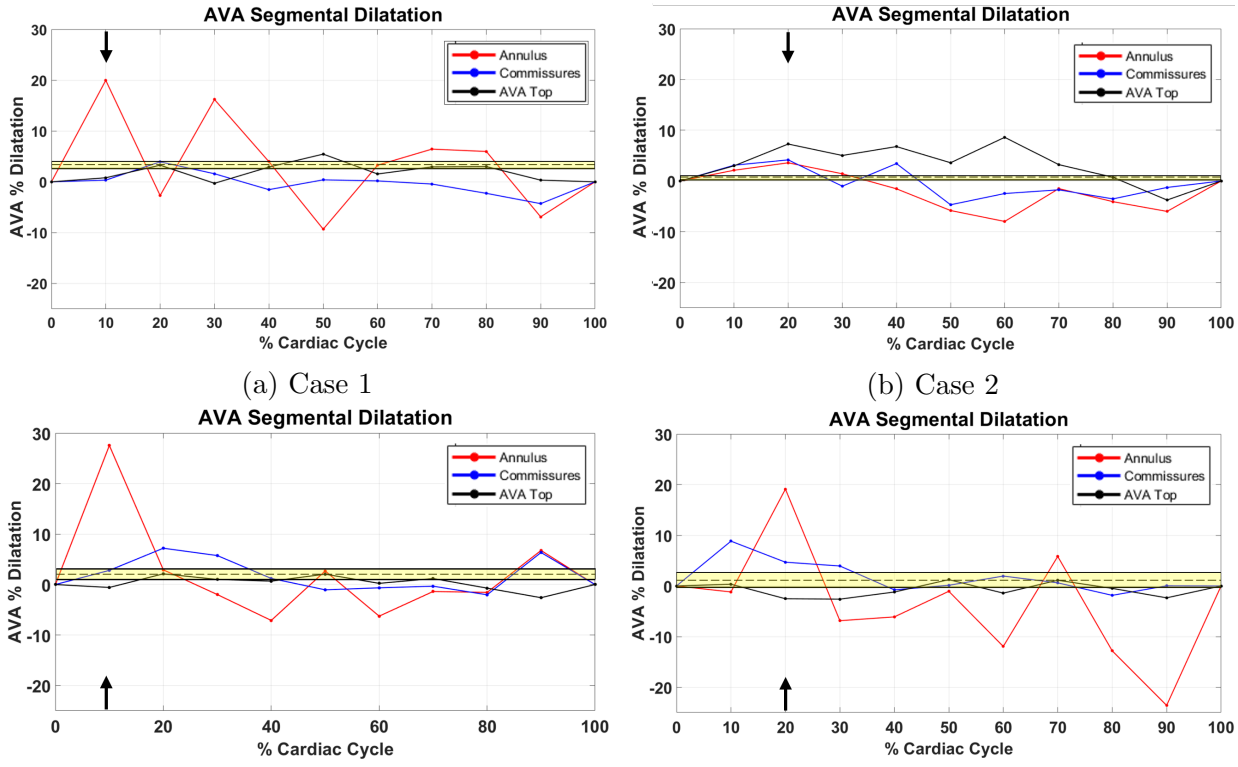
Figure 4.9: Temporal movement of the AVA after decomposing the torisonal movement. Black dotted lines in (b) show the position of the triangles at the start of the systolic phase.

Figure 4.9 shows the movement of the AVA segmental triangles at the same chosen phases in the cardiac cycle. It is visible that after decomposing or mathematically averaging what we thought of as the different modes of local deformation, the AVA exhibits almost no motion across the time frames. At each step in decomposing or averaging of each mode of local deformation, we recorded the temporal values as they may be of clinical relevance. Thus, the recorded values from each decomposition step need to be further analysed.

4.2 Resultant Deformations

At each step in decomposing the kinematics of the AVA, the local deformation was recorded for quantitative analysis. This was carried out using the axial segments at the annulus, commissures and AVA top in addition to using longitudinal or vertical segments in order to assess the deformation of the interleaflet triangles of the AVA. This was necessary since we are representing the motion of the AVA using finite fiducial points and triangles. As a result, its geometric representation needed to be done using both the axial and longitudinal segments.

4.2.1 Axial Segments



(a) Case 1 (b) Case 2

(c) Case 3 (d) Case 4

Figure 4.10: Temporal percentage radial change in each segment of the AVA for each case. The beginning of systole was used as the reference phase. Black arrows indicate the peak systole (peak ejection) phase for each case. Black dashed line shows the mean dilatation for all segments of the AVA per patient with the yellow area showing ± one standard deviation.

Figure 4.10 shows the resultant radial dilatations of each segment in the AVA quantified. The y axis shows the dilatation normalised by the area at the beginning of the cardiac cycle which

was used as the reference phase. The x axis shows the cardiac cycle time as percentages. As stated, the beginning of systole corresponds to the R-wave on the ECG.

Although the whole process of choosing the fiducial points and analysing the motion using averaging techniques as explained, the CT scans could not give images averaged over multiple cardiac cycles per case. The CT machine gives the images of each phase in the cardiac cycle based on the optimum spatial resolution from multiple cardiac cycles. This is a challenge when quantifying the amount of noise in the data. Alternatively, we calculated the mean and standard deviation of the dilatation of all segments of the AVA across the cardiac cycle as shown by the yellow area in Figure 4.10. This gives an estimate that the major peaks in each case observed at the peak systolic phase are not simply due to noise.

All cases showed a peak annulus radial dilatation occurring at the peak ejection (peak systolic) phase of the cardiac cycle. Cases 1,3 and 4 showed a peak annulus dilatation exceeding the commissure and AVA top segments reaching between 20 to 30 % dilatation of the original annulus radius. Although Case 2 showed an annulus dilatation of only 5 %, it still occurred at the peak ejection phase of the cardiac cycle. This agrees with results presented by Dagum et al. in the aortic root of sheep where they found that the annulus underwent a rapid circumferential expansion around the time of ejection [27].

Since the annulus begins the cardiac cycle with the smallest diameter compared to the other segments of the AVA including the LVOT segment which has an elliptical shape, the results support previous statements by Berdajs et al. that the AVA tends to a more cylindrical shape during the ejection phase of the cardiac cycle and as depicted in Figure 4.11 [6]. Berdajs et al. also stated that the AVA tends to a cone shape during the diastolic phase of the cardiac cycle. From the quantification of the segmental dilatations, we believe the AVA tends to a nozzle shape during the diastolic phases of the cardiac cycle around valve closure with the neck being at the annulus level. This can be seen on Figure 4.10 as the annulus always showed a contraction of up to 10 % of its undeformed diameter at the time around valve closure.

The change in shape of the AVA from cylindrical in systole to a more nozzle shape around valve closure may have an impact on fluid flow. Berdajs et al. suggested that in systole, the cylindrical

shape relieves the pressure gradients and facilitates ejection. Whether this movement of the annulus is *active* or *passive* in response to haemodynamic forces, we do believe it facilitates ejection [6]. Moreover, we believe the nozzle shape with a neck at the annulus around the time of valve closure may accelerate the flow just upstream of the valve which is already decelerating in order to aid in ejecting the last volume of blood before valve closure.

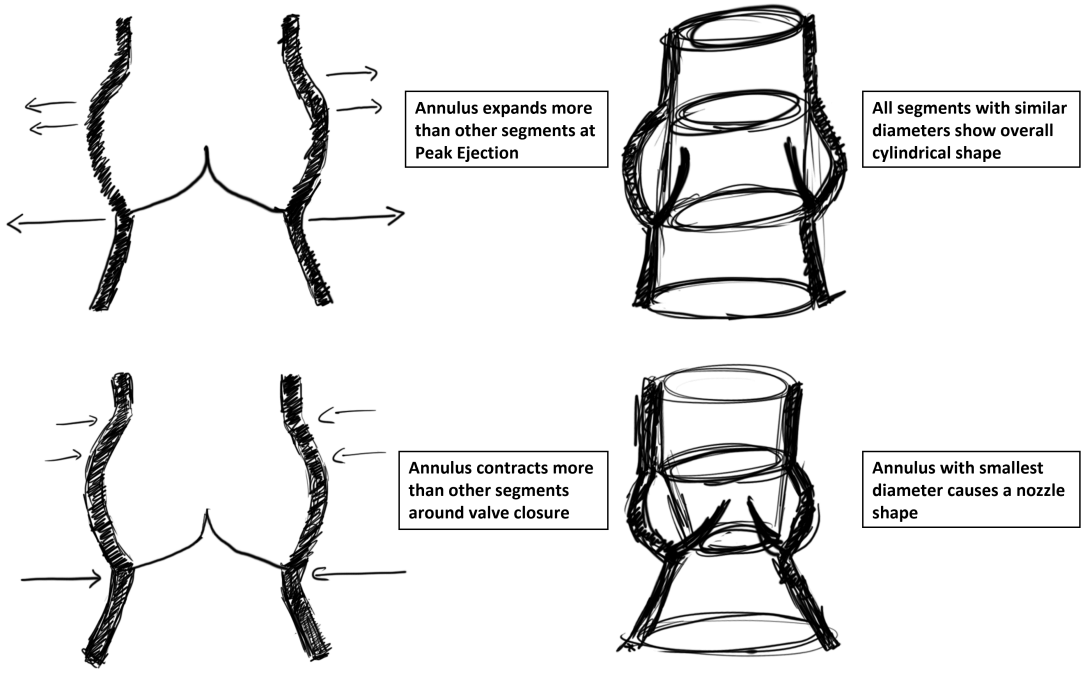
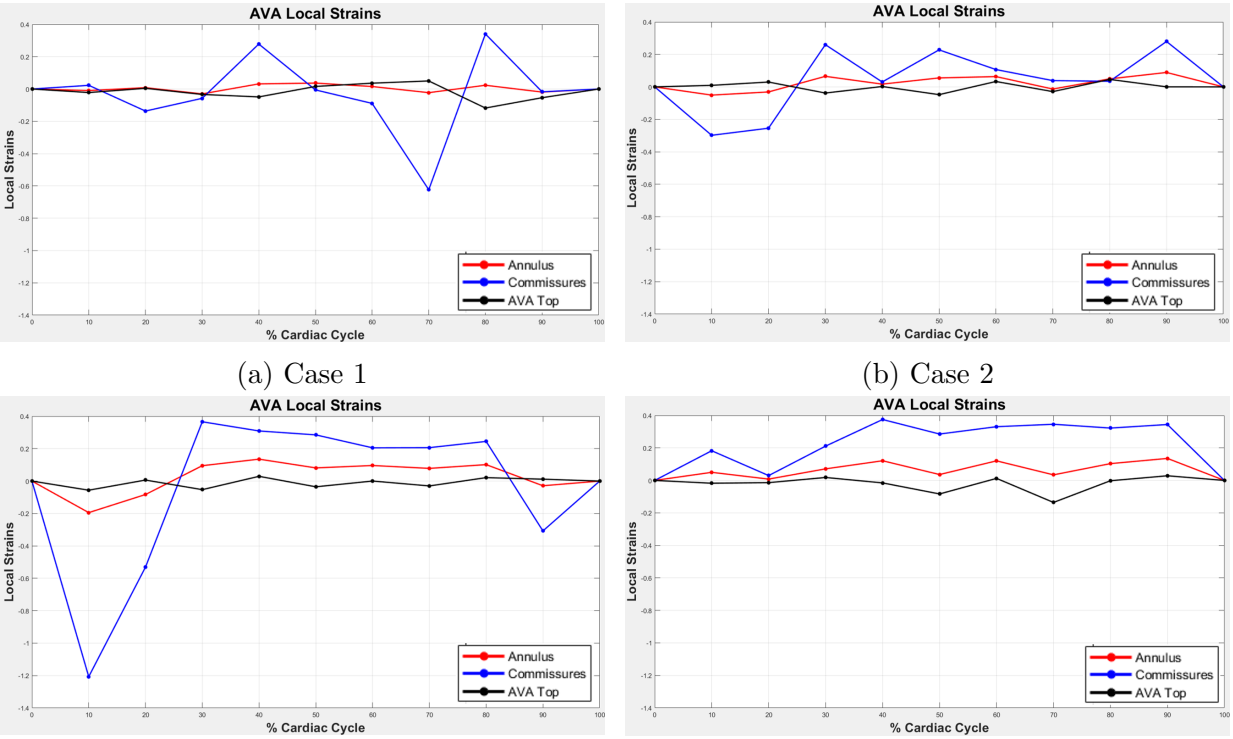


Figure 4.11: Sketch showing shape changes of the AVA from peak ejection to valve closure. Undeformed AVA (left) and deformed (right). Peak ejection phase (top) and valve closure (bottom).

Figure 4.11 shows a sketch summing up the key changes in area of the AVA during the cardiac cycle which are manifested by the segmental dilatations. At peak ejection, the annulus expands more than the other two segments as indicated by the outward arrow lengths thus tending to an overall cylindrical shape of the AVA. The long cylindrical shape of the AVA at peak ejection may serve to alleviate the elevated values of ESS experienced by the valve leaflets due to their angle in their open configuration with respect to the flow.

On the other hand, the annulus contracts around the time of valve closure forming a throat in an overall nozzle shape of the AVA. This shape change may facilitate ejection of the last volume of blood before the valve fully closes by accelerating the already retarding fluid just upstream of the valve.



(a) Case 1

(b) Case 2

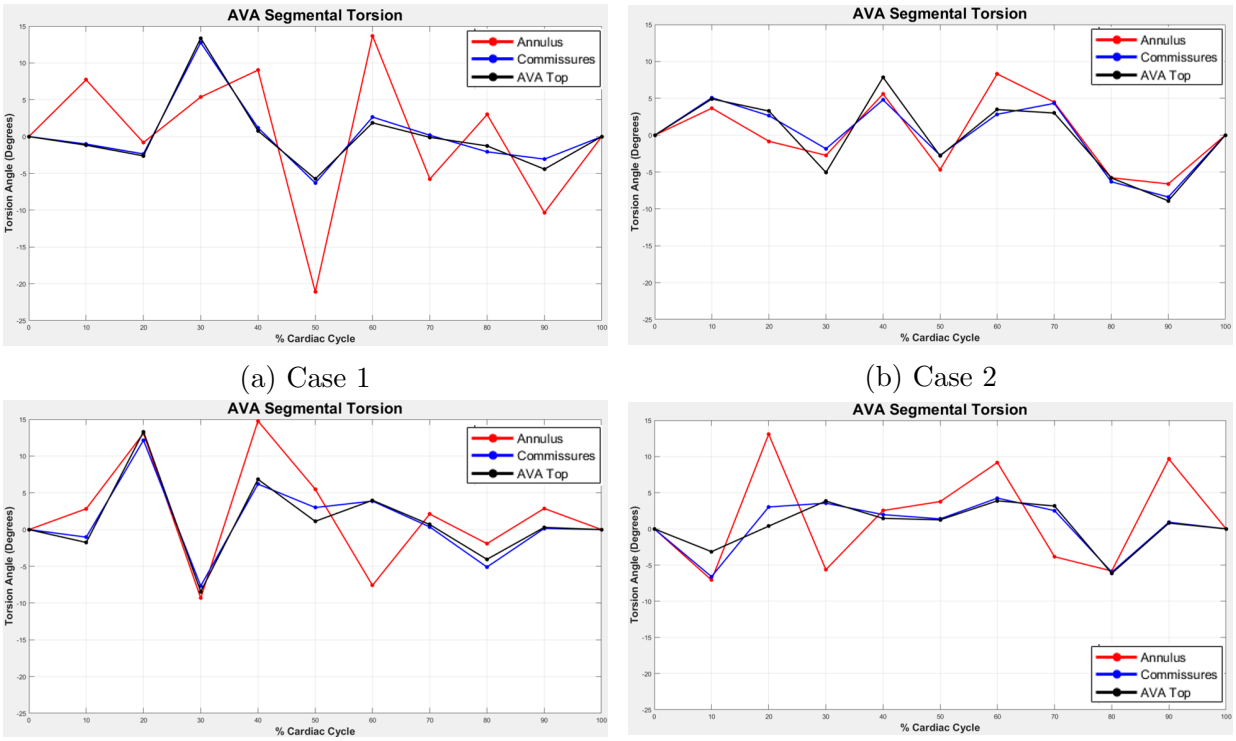
(c) Case 3

(d) Case 4

Figure 4.12: Quantification of the *accordion* effect of the AVA. The temporal strain of each segment was calculated with reference to the initial position of the AVA top.

Figure 4.12 shows another set of results from the axial segments which we believe may be of interest and uncharted according to our knowledge of the literature. The accordion effect of the AVA is an interesting feature reflected by the local axial strains exhibited by the AVA segments during the cardiac cycle. In order to follow convention, we tracked the axial motion of each segment of the AVA with reference to a fixed position along the z axis. We chose the fixed position of reference to be the location of the annulus segment at the initial phase in the cardiac cycle. From Figure 4.12, it may be seen that all cases showed correlated minimal axial movement of the annulus and AVA top segments compared to the commissure segment. On the other hand, the commissure segment moved towards and away from the AVA top and annulus segments across the cardiac cycle in a very complicated manner. However, a local strain of up to 40 % was evident at the commmissure level of all cases during the diastolic phases of the cardiac cycle. In other words, the commissures were moving towards the AVA top and away from the annulus at the time of valve closure. This may be of clinical relevance since the commissures are at the peaks of the fibrous crown shaped skeleton shown in Figure 2.45 which bears the loads on the AVA. As the maximum loads incurred by the AVA valve are

during diastole, we believe the local stretching of the AVA via the upward movement of the commissures may behave as a shock absorber mechanism in relieving the high loads incurred by the valve during diastole. We believe that the movement of the commissures tracked is highly unlikely to be due to noise in the data since the other two segments of the AVA did not exhibit movement of similar order of magnitude.



(a) Case 1 (b) Case 2

(c) Case 3 (d) Case 4

Figure 4.13: Torsional movement of the AVA. The temporal torsion of each segment was calculated with reference to the position at the previous time frame in the cardiac cycle.

Figure 4.13 shows a quantification of the torsional behaviour of the AVA across the cardiac cycle. For each axial segment, the torsion angle at each time frame was calculated with reference to the position at its previous time frame in the cardiac cycle to show torsional displacement. The torsion angles shown on the y axis of the figure are either positive or negative indicating a clock-wise or anti-clockwise rotation respectively looking from the ventricular side of the AVA.

All cases showed a synchronised torsional movement between the commissure and AVA top segments. Only Case 2 showed suppressed torsional movement of the annulus segment unlike the other three cases. The faster rates of torsion exhibited by the annulus segment suggest that the AVA undergoes continuous winding and unwinding across the cardiac cycle which may

have an impact on relieving ESS as explained by Berdajs et al. [24]. This is because the flow in the AVA evolves into helical flow with high speeds during ejection and a torsional movement in the same direction as the rotating flow would decrease the relative velocity between the flow and the wall and in turn relieve ESS.

The main observation we can draw from the quantification of the torsional behaviour of the AVA is that the asynchrony between the annulus and the other two segments in all cases, except Case 2 which showed much lesser torsion of the annulus segment, occurs during the ejection phase of the cardiac cycle. This could further support the hypothesis presented by Berdajs et al. since the elevated values of ESS occur during the systolic phase of the cardiac cycle where the blood flow velocities are high compared to the diastolic phase.

The common factor amongst the quantification of the different local deformations of the AVA is that the temporal deformations are asymmetric and as such must have an impact on blood flow distribution. As a result, the previous analysis merits an extension to looking at the AVA from the longitudinal view in order to dig deeper into the asymmetric kinematics of the AVA. This will also serve as the method to assess the bending behaviour of the AVA.

4.2.2 Longitudinal Segments

To our understanding, the best way to represent the AVA longitudinally according to methods previously adopted in the literature is to look at the ILT's of the AVA. These are the three vertical triangles around the AVA. Each triangle is composed from two annulus points as the base of the triangle and a commissure point as the top vertex [52].

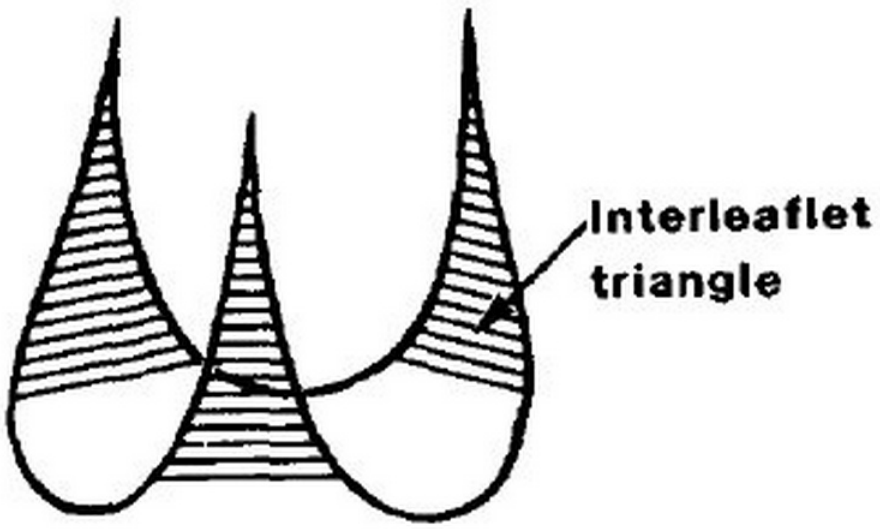
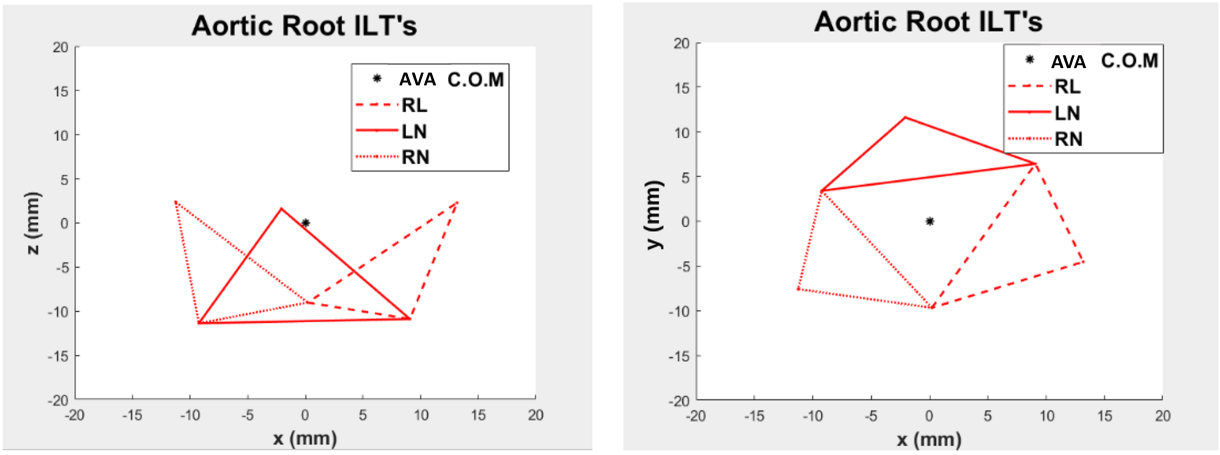


Figure 4.14: Sketch showing the interleaflet triangles of the AVA as the shaded regions. (Reproduced from [52])

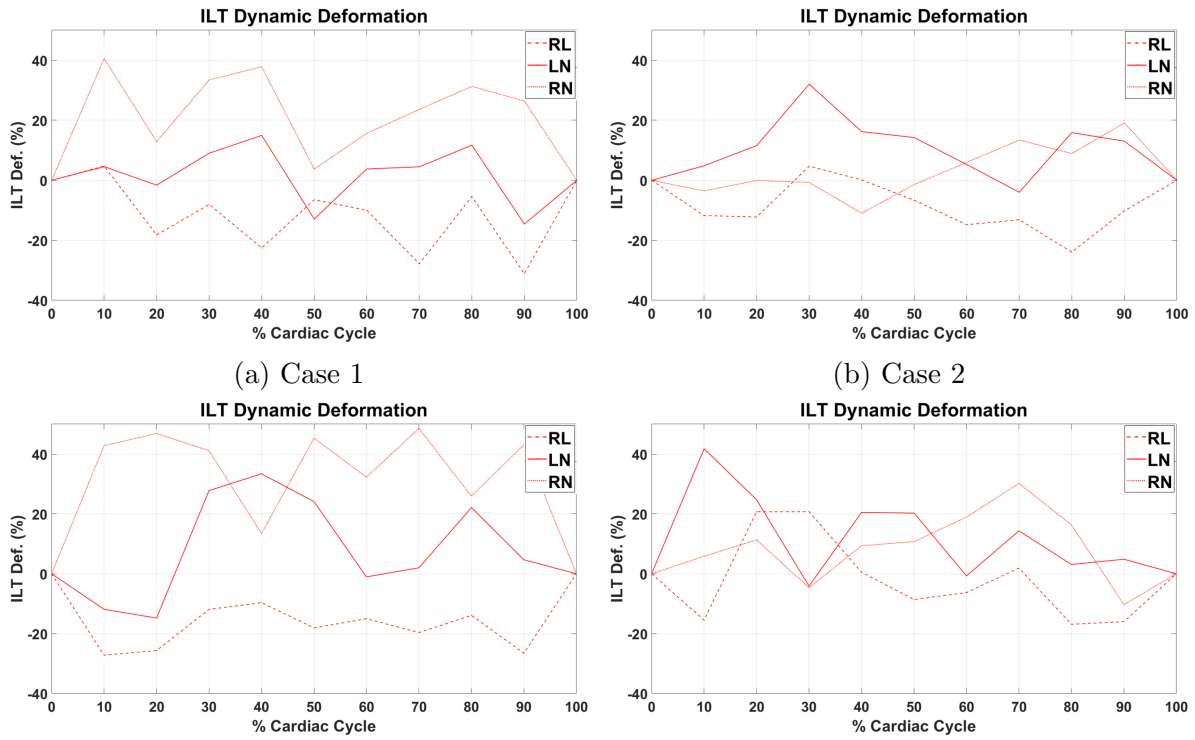
Figure 4.14 shows a sketch of the interleaflet triangles of the AVA. They have a crucial position as they contain a circumferential segment of the annulus in addition to one of the peaks of the crown shaped fibrous skeleton [52].



(a) ILT side view (b) ILT top view

Figure 4.15: ILT's represented by the fiducial points. RL, LN and RN denote the right-left, left-non and right-non ILT's.

Figure 4.15 shows the representation of the interleaflet triangles using the fiducial points that are tracked. The method we devised to assess the local deformations of the ILT's is similar to the method used in dealing with the axial segments. Equations 4.3 and 4.4 were used in order to calculate the AVA COM and transform the AVA into a system with a local origin. Next, the changes in area of each interleaflet triangle were quantified across the cardiac cycle.



(a) Case 1 (b) Case 2

(c) Case 3 (d) Case 4

Figure 4.16: Temporal changes in the areas of the ILT's.

Figure 4.16 shows the temporal changes in the area of the interleaflet triangles. Each triangle area was referenced to its area at the initial phase in the cardiac cycle to quantify its percentage change. All cases showed a similar behaviour with a continuous contraction of the RL interleaflet triangle across the systolic phase of the cardiac cycle and an expansion of the other two interleaflet triangles.

This result is in agreement with the data from the analysis by Berdajs et al. which shows a continuous tilt of the AVA across the systolic phase of the cardiac cycle contracting the RL interleaflet triangle [6]. We also believe this data may strongly correlate to previous unpublished data from our group at Magdi Yacoub Institute showing an abundance of smooth muscle cells in the RL interleaflet triangle compared to the other two triangles in porcine AVA's. It also agrees with the results presented by Benhassen et al. showing that the maximum segmental force incurred in the AVA is at the RL interleaflet triangle compared to the other two triangles [28].

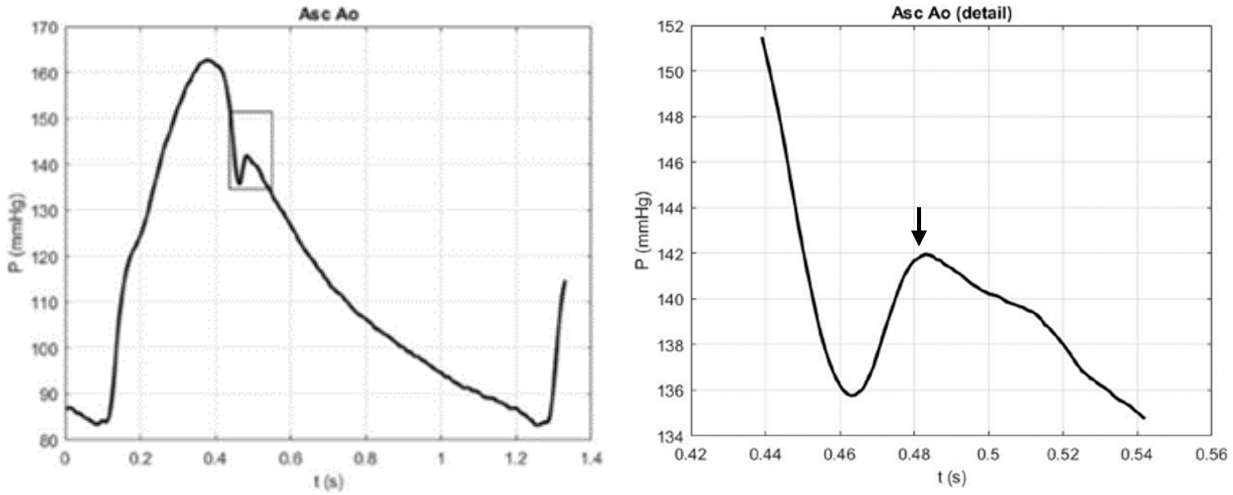
Whether or not the tilting behaviour of the AVA is *active* or *passive*, we believe it will affect the blood flow distribution in its vicinity. We also believe the data presented by Benhassen et al. correlates to our unpublished data due to the fact that the abundance of smooth muscle cells in the RL interleaflet triangle may be behind the elevated forces incurred by it across the cardiac cycle and hence its continuous contraction.

We have seen from our observations while quantifying the kinematics of the AVA that they are asymmetrical. In return, this will result in an asymmetrically deforming fluid medium in addition to its translational movement. The asymmetrical deformations of a moving fluid medium is a complicated process. In consequence, this explains the necessity to use a low order approximation in order to monitor the preliminary effects of the kinematics of the AVA on blood flow.

4.3 Dicrotic Notch Hypothesis

4.3.1 History of the Dicrotic Notch

The dicrotic notch is a unique feature visible in the pressure waveforms of the central arteries especially the aorta. It is usually used by clinicians to demarcate valve closure. Although most studies of the arterial system using 1D numerical modelling show a dicrotic notch in the resultant pressure waveforms of the central arteries, it is usually due to the dicrotic notch being present in one of the boundary conditions in the problem and not taking into account the fluid behaviour causing it. Other studies using Windkessel Models show the dicrotic notch by using inductors which represent the fluid inertia in the electric circuit analogy. These studies refer to the dicrotic notch as a high frequency component of pressure while not acknowledging the cause behind it [30].



(a) Ascending aortic pressure waveform

(b) Dicrotic notch

Figure 4.17: Dicrotic notch in an arterial pressure waveform. The square area in (a) is shown magnified in (b). The black inset arrow in (b) shows how we refer to the dicrotic notch as the peak following the drop in pressure. (Reproduced from [30])

Figure 4.17 shows the pressure in the ascending aorta measured invasively in a patient. The pressure of the decelerating fluid suddenly rises by 6 $mmHg$ over a time period of 20 ms then exponentially decays. To avoid confusion, we refer to the dicrotic notch in our study as the peak in pressure preceeding the exponential decay.

4.3.2 Previous Dicrotic Notch Theories

Although an explanation of the cause of the dicrotic notch is absent in studies of blood flow in the aorta, there have been previous theories explaining the mechanics of the dicrotic notch. The earliest mechanism proposed is related to the Bernoulli pressure. The theory states that the dicrotic notch is due to the recovery in dynamic pressure of the retrograde fluid in the AVA at the time of valve closure. As the flow is recirculating towards the valve, the sudden closure causes a halt in the fluid and thus reverses its direction. This theory could be refuted with a simple order of magnitude estimate.

The velocity of the retrograde flow at the time of valve closure U is generally in the range of $0.1 - 0.3\ m/s$. If the blood density ρ is taken to be 1060 kg/m^3, the recovery in dynamic pressure according to Bernoulli's equation ($\frac{1}{2}\rho U^2$) gives an estimate of pressure rise in the range of $0.04 - 0.36\ mmHg$ which does not fall in the typical range of pressure rises of the dicrotic notch ($3 - 10\ mmHg$) [30]. [30].

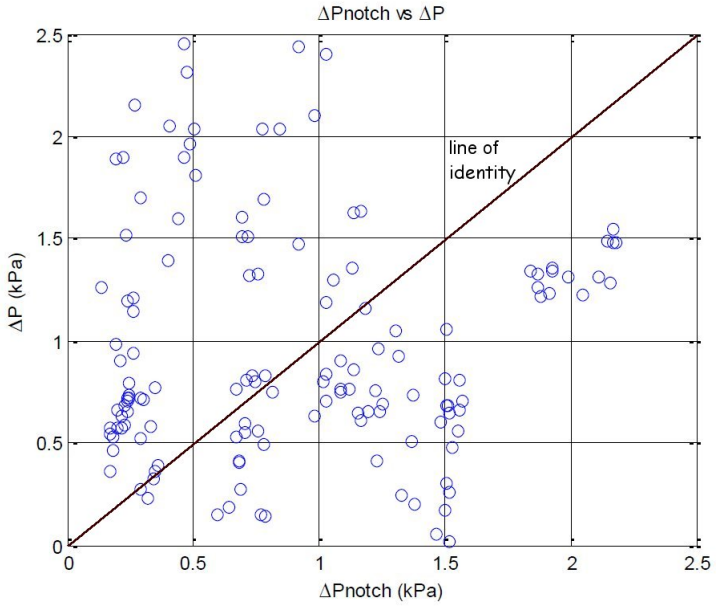


Figure 4.18: Experimental results of the dicrotic notch in open chest dogs. The measured $\Delta Pnotch$ and the calculated ΔP based on the wave reflection hypothesis do not fall on the line of identity. (Reproduced from [30])

An alternative theory popular in the literature states that the pressure rise in the dicrotic notch is due to wave reflection from the retrograde flow stopping by the aortic valve closure. This

theory was found to be unviable from experimental analysis in open chest dogs.

Figure 4.18 shows the results of the experimental analysis. The data on the x axis is simply an invasive measurement of the dicrotic notch rise in pressure in open chest dogs. The y axis shows the estimates of the dicrotic notch rise in pressure based on the wave reflection hypothesis. This was carried out using the water-hammer equation which will be explained in more detail in Section 4.3.4.

Taking the blood density ρ to be 1060 kg/m^3 and the wave speed c in the aortic root to be 5 m/s, the estimate of the dicrotic notch rise in pressure due to wave reflection can be obtained by multiplying ρ and c by the measured changed in velocity in the aortic root at the time of valve closure which was available from the invasive measurements in the open chest dogs. However, it is clear from the figure that the estimates and measured pressures do not fall on the identity line meaning that the theory is unviable [30].

Bearing in mind the absence of a feasible explanation behind the cause of the dicrotic notch rise in pressure in the literature and the possible link between fluid inertia and the high frequency change in pressure at the time of valve closure, we propose a novel hypothesis using an acceleration-based model analysing the sudden movement of the AVA away from the LV at the time of valve closure.

4.3.3 Acceleration-based Model

From our analysis of decomposing the kinematics of the AVA, we discovered that the rigid translation component produces the largest value of residual motion. This means that the rigid movement of the AVA is numerically dominant over the modes of local deformation of its axial or longitudinal segments. The rigid motion of the AVA which we observed involves moving along an axis towards and away from the LV while rigidly moving in the lateral directions. The observed motion may be due to contraction of the LV or induced by larger scale motion of the heart; however, relative motion between the AVA and the LVOT segment exists. The lateral translations which are an order of magnitude less than the axial translations may be of clinical relevance when analysing the interaction between the flow in the AVA and the coronaries; however, this hypothesis is beyond the scope of this thesis. As a result, we will attempt to quantify the dominant axial acceleration of the AVA and use a low order approximation to assess if it may have any impact on haemodynamics.

We consider the acceleration of the AVA to be given by the movement of its COM. From our analysis of the kinematics of the AVA, the positions of the COM of the AVA tracked in time can be found using equation 4.3. The global $[x,y,z]$ positions of the COM of the AVA were stored in a 11x3 matrix where the rows represent the time frames across the cardiac cycle. From there, equation 4.9 can be used to deduce the displacement of the COM of the AVA.

$$\{\Delta x\}_{COM} = \{COM\}_{jn} - \{COM\}_{jn-1} \tag{4.9}$$

Instantaneous Acceleration of the AVA

After obtaining the displacement of the COM of the AVA, we needed to mathematically obtain its second derivative in order to calculate its temporal acceleration. Looking into the options of obtaining the second derivative of a discrete function, the options lay between the second

order finite difference scheme and the Fourier transforms.

$$a_n = \frac{\partial^2 x_n}{\partial t^2} = \frac{x_{n+1} - 2x_n + x_{n-1}}{(\Delta t)^2} \tag{4.10}$$

Equation 4.10 shows how the second derivative of a function is calculated using a finite difference central difference discretisation. The Fourier transform method was chosen over the finite difference method since we had a problem of under-sampled data.

The Problem of Under-sampled Data

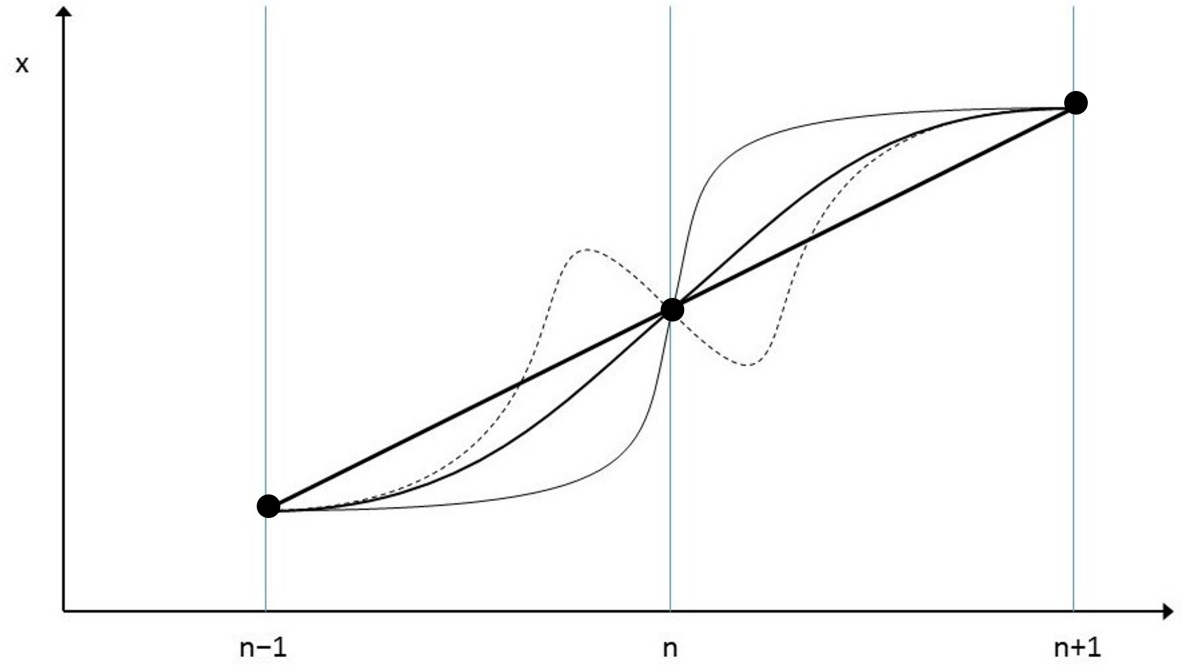


Figure 4.19: Different interpolation functions that can fit the discrete data indicated by the points.

Figure 4.19 is a sketch to explain why the finite difference method was not used. Suppose the discrete displacement of the AVA is represented by the points in the figure at times $n-1$, n and $n+1$. The finite difference scheme assumes a linear interpolation between the data points as shown by the thick black line in the figure. However, it is possible that the displacement of the AVA follows a different distribution in between the sampled data points as shown by the different curves in the figure. This means that the acceleration calculated using the finite

difference method with our Δt sampling of 100 ms (10 time points across the cardiac cycle of 1 s) may be underestimating the actual value of the acceleration of the AVA.

In order to mitigate these problems, we decided to use the Fourier transform method to calculate the instantaneous acceleration of the AVA. While this may solve the problem with linear interpolation, we still needed a solution for data under-sampling. Since we observed that the AVA undergoes a sudden axial movement away from the LV around the time of valve closure, this interesting process happens within approximately 20 ms in time. As a result, we looked into one of the four patients where it was feasible to sample the data around the time of valve closure at intervals of 10 ms. Along with using the Fourier transform method, the higher sampling of data around the time of valve closure should improve the accuracy of our low order approximation.

The Fourier Transform Method

Calculating the second derivative of periodic function using the Fourier transform method may be given by the following equations:

$$\mathfrak{F}\left(\frac{dx(t)}{dt}\right) = i\omega\mathfrak{F}(x(t)) \tag{4.11}$$

The fourier transform of the derivative of a function $x(t)$ may be calculated using equation 4.11. It immediately follows that the fourier transform of the second derivative of a function may be given by equation 4.12.

$$\mathfrak{F}\left(\frac{d^2x(t)}{dt^2}\right) = -\omega^2\mathfrak{F}(x(t)) \tag{4.12}$$

Hence, the acceleration of the function $x(t)$ may be calculated by taking the inverse fourier transform of equation 4.12.

$$a(t) = \frac{d^2x(t)}{dt^2} = \mathfrak{F}^{-1}\big(-\omega^2\mathfrak{F}(x(t))\big) \tag{4.13}$$

Equations 4.11-4.13 are easily implemented using the Fast Fourier Transform (FFT) function in MATLAB for discrete data. We know apriori that the inverse FFT will return complex numbers; however, they should be real values since the values of $x(t)$ are real. Using the REAL function in MATLAB, the real values of the acceleration of the AVA can be returned while ignoring the negligible imaginary parts that arise due to machine precision.

Acceleration Along AVA Axis

Since the displacement of the AVA that was tracked is given in the global $[x, y, z]$ coordinates, we are only interested in the acceleration along the axis of the AVA as it will reflect the movement towards and away from the LV. In order to do this, the FFT method is applied to the displacements in the three local directions or axes of the AVA then the acceleration vector at each time point in local coordinates is projected to the axis of the AVA. Since we already obtained the axis of best fit of the AVA at each time point using equation 4.5, the acceleration along the axis of the AVA may be given by equation 4.14 where AVA_{axis} is a unit vector of the axis of best fit from the svd and a is the acceleration vector in global coordinates.

$$a_{axial} = \vec{a} \cdot \overrightarrow{AVA}_{axis} \tag{4.14}$$

Since the axis of best fit of the AVA at each time point deduced is returned as a unit vector, the dot product in equation 4.14 will yield a projection of the acceleration calculated in the three local directions along the axis of the AVA.

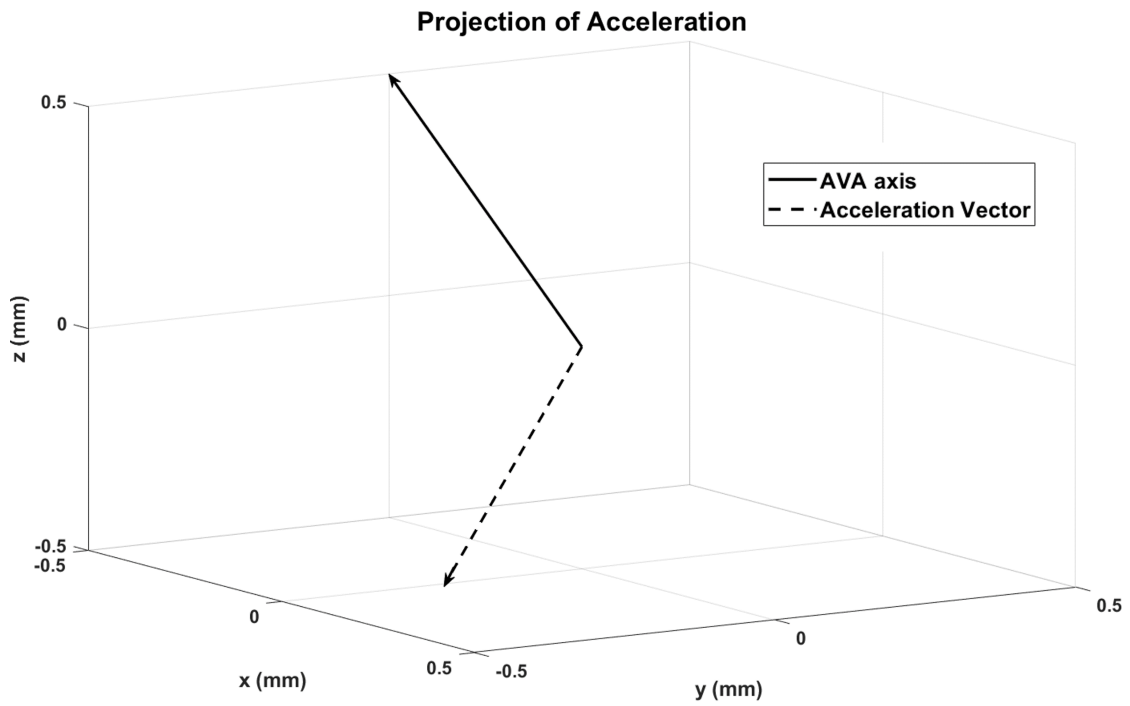
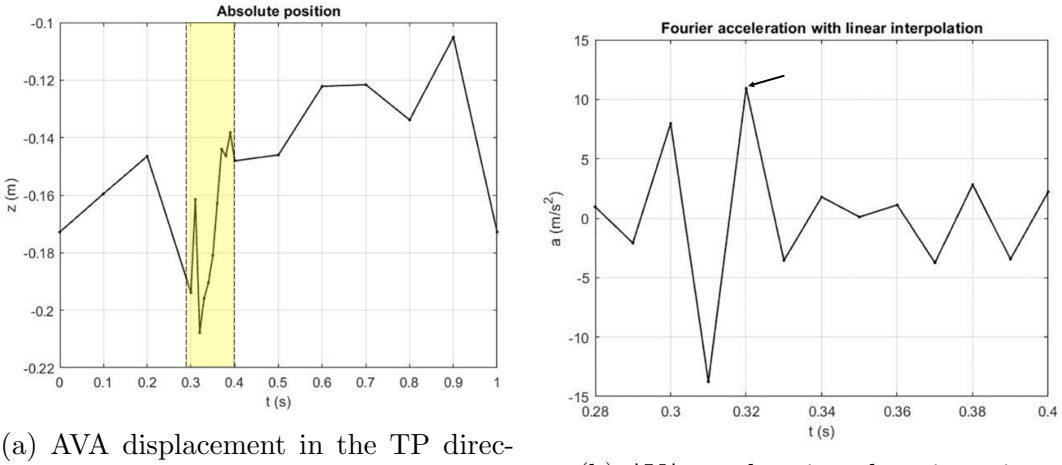


Figure 4.20: A plot showing the acceleration in global coordinates and the AVA axis.

Figure 4.20 shows how the transformation or projection of the acceleration of the AVA from global coordinates to the local AVA axis of best fit was carried out. The points tracked which were given in machine coordinates were in the global $[x, y, z]$ directions. Since we are concerned with a physiological problem, we need to transform the global axes into a set of axes representative of the problem in hand. Using svd, the resultant AVA axis of best fit is shown as the solid line in the figure. This axis is known to clinicians as the *through-plane* (TP) axis. This local axis of best fit is analogous to the global z axis. It is crucial to remember that the lateral movement of the AVA along the x and y directions also has a contribution towards the acceleration of interest in the TP direction. This is the reason behind applying a projection of the acceleration vector at each time point on the TP direction of the AVA. The acceleration vector in the global x, y and z directions shown as the dashed line in the figure can be projected to the AVA axis of best fit to yield the acceleration of the AVA along its axis.

4.3.4 Mechanics of The Dicrotic Notch



(a) AVA displacement in the TP direction

(b) AVA acceleration along its axis

Figure 4.21: Displacement and acceleration of the AVA. Highlighted area in (a) shows the time around valve closure covered in (b). The arrow in (b) shows the peak acceleration at the time of valve closure. (Reproduced from [30])

Figure 4.21 shows the results from one of the patients where we were able to sample the data at intervals of 10 ms around the time of valve closure. Figure 4.21a shows the displacement of the AVA along the TP direction and Figure 4.21b shows the acceleration of the AVA after applying the projection from equation 4.14 to the second derivative of the displacement data in all the local directions or axes of the AVA. It is visible that at a time of 0.32 s, the AVA attains a peak acceleration value of 10 m/s^2 as indicated by the black arrow. To put this into perspective, the AVA needs to move a distance of 2 mm away from the LV in the space of 20 ms in order to produce such positive acceleration [30].

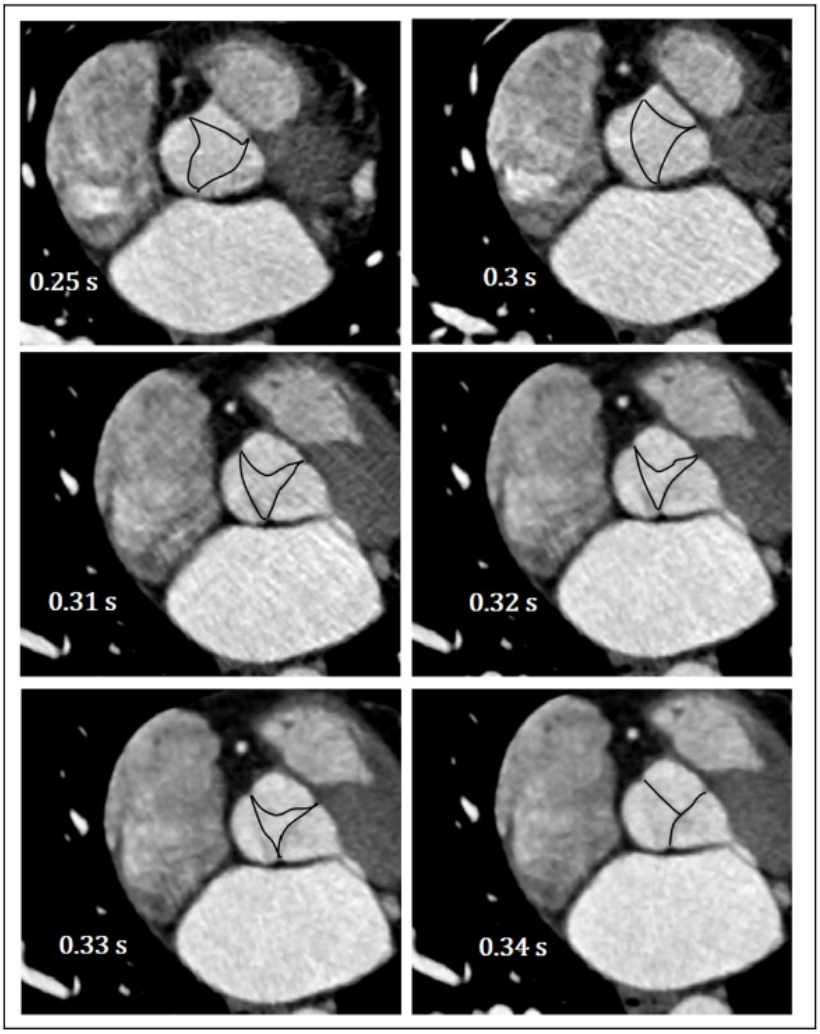


Figure 4.22: CT images of the same patient around the time of valve closure from an axial through plane showing the valve leaflets in the black lines. (Reproduced from [30])

Figure 4.22 shows CT images of the same patient from an axial through plane cutting through the AVA. The leaflet free edges have been highlighted using the black lines for ease of visibility. The valve is almost fully closed at the time of 0.32 s with a greatly reduced GOA compared to the GOA at 0.25 s and it fully closes 20 ms later. This corresponds to the time it takes the AVA to reach the peak acceleration value while moving away from the LV as shown in Figure 4.21b.

Taking into account the axial movement of the AVA away from the LV at the time of valve closure as it is the dominant movement, analysing the haemodynamics using a low order approximation becomes straightforward.

$$\Delta P_{\pm} = \pm \rho c \Delta u_{\pm} \tag{4.15}$$

Equation 4.15 is known as the *water-hammer* equation. It is derived from the 1D gas dynamics equations and hence a low order approximation [3]. The *water-hammer* equation is usually used to describe the relationship between the change in pressure and the change in velocity across a wave propagating in an elastic tube. The values are positive or negative depending on positive or negative changes in the values of ΔP and Δu respectively. The subscripts are positive or negative depending on whether the wave is proximally or distally originating respectively. $\Delta P_{+} = \rho c \Delta u_{+}$ would be for a forward wave and $\Delta P_{-} = -\rho c \Delta u_{-}$ would be for a backward wave.

When the valve is open, the AVA can be considered to be an elastic tube structure filled by a continuous column of blood. If the AVA is accelerated in the axial direction this only affects the blood in a boundary layer near the tube walls. When the valve is closed, however, any acceleration of the AVA in the axial direction must be matched by the acceleration of the blood contiguous with the newly closed valve; a consequence of the no-slip condition between the blood and the walls of the tube containing it in addition to conservation of mass. This will result in a sudden reversal of direction of the flow just downstream of the newly closed valve which may cause a wave to be transmitted through the walls of the aorta. In this case an acceleration of 10 m/s^2 over a time interval $\Delta t = 20\ ms$ will produce a change in velocity in the axial direction $\Delta u = a\Delta t$. This change in velocity becomes a boundary condition for the wave that is generated in the aortic root.

The relationship between the change in velocity and the change in pressure across the wave is given by the water hammer equation 4.15. The pressure change caused by the axial wave in the aorta caused by the acceleration of the closed valve is $\Delta P = \rho c a \Delta t$. For example, considering the blood density ρ to be 1060 kg/m^3, the wave speed c to be 5 m/s in healthy humans and $\Delta u = a\Delta t$; then equation 4.15 gives a positive ΔP value of 1060 Pa or approximately 8 $mmHg$. In other words, the positive acceleration of the AVA away from the LV during valve closure may account for the pressure rise in the adjacent fluid through the generation of a forward

compression wave [30],[3].

This led us to the hypothesis that a forward compression wave from the movement of the AVA at the time of valve closure to the surrounding fluid medium will cause a pressure rise that may explain the mechanism behind the dicrotic notch.

The dicrotic notch is a distinct feature present in the arterial pressure waveform of the aorta. It is usually used by clinicians to indicate aortic valve closure [30]. We thought it is counter-intuitive that a decelerating fluid medium at the time of valve closure could exhibit a rise in pressure seen as the dicrotic notch.

This is an interesting feature to investigate since the dicrotic notch pressure rises are typically within the range of $3 - 10\ mmHg$. Although previous theories to mathematically describe the dicrotic notch pressure rise did not yield a close approximation (unlike our hypothesis), we still believe that we need to improve the analysis by using a higher order model in order to assess the effect of the axial acceleration of the AVA on blood flow.

Chapter 5

Tube Orifice Idealised Model

5.1 Problem Introduction

In order to study the effect of the complex AVA kinematics on haemodynamics, it would be very difficult to start with a patient-specific or physiological geometry of an AVA and valve as isolating the effect of the complex interaction between the dynamic structures of the AVA and the surrounding blood flow will be challenging. Hence, taking an idealised problem as an initial iteration will make the analysis easier.

Since our analysis of the kinematics of the AVA has shown that the dominant motion is the axial translation or acceleration of the AVA, we will focus the computational higher order models to assess the effect of the axial acceleration component of motion on blood flow while excluding the local modes of deformation.

The 1D model using the water-hammer equation showed an observation that the acceleration of the AVA at the time of valve closure and the sudden dicrotic notch pressure rise while the flow around the valve is retarding occur at the same time. This is shown in Section 4.3 Figure 4.22 where valve closure occurred at the same time where the peak acceleration occurred as shown in Figure 4.21b. As a result, a transfer to a higher order computational model is necessary to test our hypothesis further.

In this chapter, we will use 3D CFD modelling in order upgrade the low order approximation. The moving wall method will also be incorporated in our computational model in order to test the effect of the axial acceleration of the AVA. In spite the fact that using a higher order model will provide a more in depth analysis of the acceleration of the AVA and its impact on haemodynamics, we will use a simplified geometrical model that shares some similarities with the physiological AVA as a stepping stone before probing into the full physiological model of the AVA.

5.1.1 Parametric Model

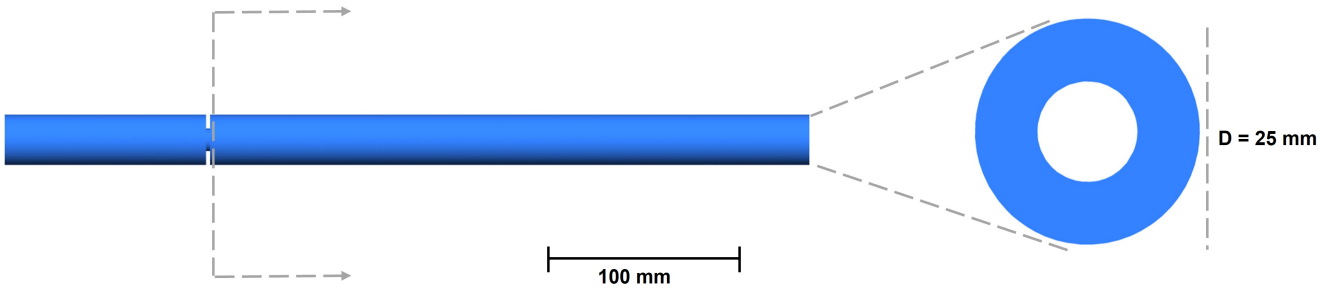


Figure 5.1: Idealisation of the AVA anatomy. The tube orifice model replicating the physiological AVA.

Figure 5.1 shows the tube orifice model which we used as an idealisation of the physiological anatomy of the AVA. As shown, the idealised model contains an axisymmetric tube replicating the anatomy of the aorta and an orifice replicating the aortic valve. The orifice plate shown on the right of the figure may be thought of as the projected area of the valve leaflets while the opening represents the Geometric Orifice Area (GOA) of the valve.

In addition to this, the idealised tube orifice model is parametric with a total length of 800 mm and a diameter of 25 mm. The diameter was chosen to replicate physiological diameters in the aorta [53]. The length of the tube was chosen to be 32 times larger than the diameter to allow for the flow to stabilise towards the tube outlet and mitigate numerical instabilities caused by recirculating flow due to ill-posed outlet boundaries [54].

5.1.2 Navier-Stokes Equations

Before applying a computational model to investigate a certain flow scenario, an understanding of the theory behind CFD is necessary.

$$\nabla \cdot \vec{\mathbf{v}} = 0 \tag{5.1}$$

$$\frac{\partial \vec{\mathbf{v}}}{\partial t} + (\vec{\mathbf{v}} \cdot \nabla)\vec{\mathbf{v}} = -\frac{1}{\rho}\nabla \mathbf{P} + \nu \nabla^2 \vec{\mathbf{v}} \tag{5.2}$$

Equations 5.1 and 5.2 given in vector notation will be used to mathematically represent our case studies using CFD. We know that physiological flow involves the movement of blood as a fluid which is effectively incompressible. As a result, the above equations suffice to describe the physics of the problem. Equation 5.1 is known as the continuity equation for incompressible flow. In simple language it states that the amount of incompressible fluid flowing into a volume of interest must equal the amount of fluid flowing out of the volume of interest.

Equation 5.2 which are the incompressible Navier-Stokes equations describe the momentum of a fluid in 3D space as in our case. The equation states that the local acceleration of a fluid from its change in velocity over time combined with its convective acceleration must equal the pressure force driving the flow minus the viscous dissipation or viscous drag retarding the flow. In simpler terms, the fluid acceleration must equal its net driving force divided by its mass.

While some analytical solutions exist for the above equations, we do not have an analytical solution to these equations for our scenario. As a result, the use of experimental or computational techniques is necessary. We assumed that blood is a Newtonian fluid with constant viscosity for simplicity since previous studies show no differences in numerical results between Newtonian and Non-Newtonian fluids for the major arteries [55].

5.1.3 Computational Mesh

Equations 5.1 and 5.2 can be solved numerically using commercially available computer software. At the moment, the standard method in solving these equations numerically is the finite

volume method. The theoretical details of this method is beyond the scope of this thesis; however, certain prerequisites are important to take into account in order to approach a realistic solution to our problem.

The first pre-processing step after the creation of the geometry in a CFD model is the meshing process. Meshing is the process of representing the geometrical domain of interest by a finite number of control volumes in order to apply the finite volume method [56]. From that, equations 5.1 and 5.2 can be applied on each one of these finite control volumes to give a solution for the velocity and pressure fields.

There is a trade-off between the number of finite volumes used as a mesh representing the geometry and the computational power needed to achieve a solution. From our previous experience, we managed to produce a mesh which contains finite volume sizes that are able to capture the interesting effects we need for our analysis while at the same time not incurring heavy computational and time costs.

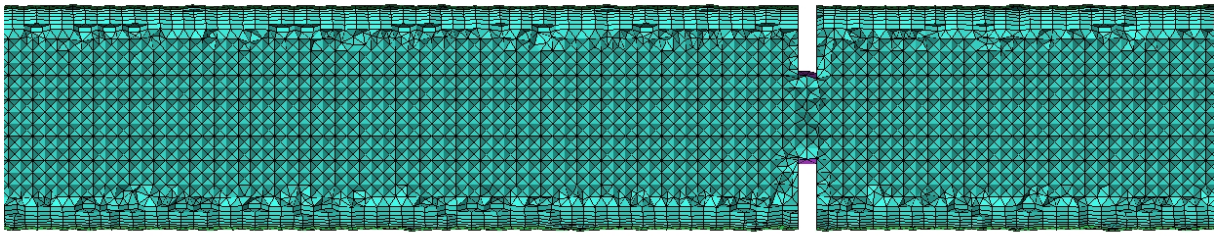


Figure 5.2: Computational mesh of the idealised model along a segmental length of the tube. Prism volumes are used near the walls with a smooth transition in size to the tetrahedral elements in the rest of the fluid domain.

The tube orifice model and its mesh were created using ICEM CFD. Figure 5.2 shows the finite volume mesh we used in our idealised model. The geometry was discretised into 2 million tetrahedral elements of similar sizes where the minimum element size was in the order of 500 μm. Similar sizes between elements is necessary to avoid artificial gradients when solving the Navier-Stokes equations. This is because the Navier-Stokes equations contain nonlinear terms. Having a mesh with extremely varying sizes may result in inaccurate flux calculations by the software at the faces of the finite volumes representing the geometry consequently affecting the accuracy of the flow field solution [57].

We also included 6 inflation layers, consisting of first order rectangular prism elements, from the tube wall inwards in order to capture the near wall effects of the boundary layer as seen in the figure. These layers were formed by specifying a near zero first layer height then a growth factor of 1.2. Smooth transition in the sizes of the finite volumes between the prism elements and the tetrahedral elements is necessary since the different shapes will pose a difficulty in flux calculations for the algorithm; hence, maintaining similar sizing or conformity will circumvent the problem.

It is always important to check the quality of the mesh before using it for a CFD simulation to avoid inaccuracies induced by poor quality elements. While different metrics exist to assess the quality of the finite volume elements, we opted for the ICEM CFD quality metric. This is because it contains a weighting for element skewness. It is always essential to not have heavily skewed elements with acute angles and that the angles between adjacent elements should be close to 90°. The ICEM CFD quality metric ensures a good quality mesh if the lowest element quality is 0.2. We ensured that our minimum mesh quality exceeds that value [57].

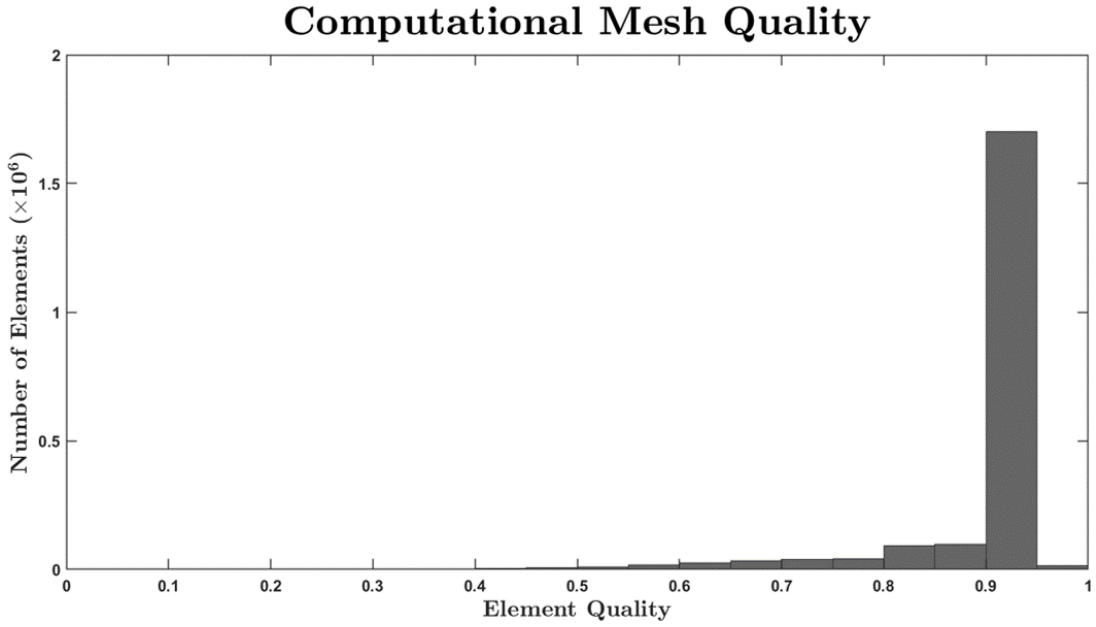


Figure 5.3: ICEM CFD quality metrics histogram for the computational mesh. 83 % of the mesh elements are of quality within the range $0.9 - 1$.

Figure 5.3 shows the resultant quality metrics of the computational mesh as a histogram deduced from ICEM CFD. The figure shows that the number of elements with a minimum quality

of $0.35-0.4$ is negligible while approximately 83 % of the elements fall within the $0.9-1$ range.

5.2 Analysis Scenarios

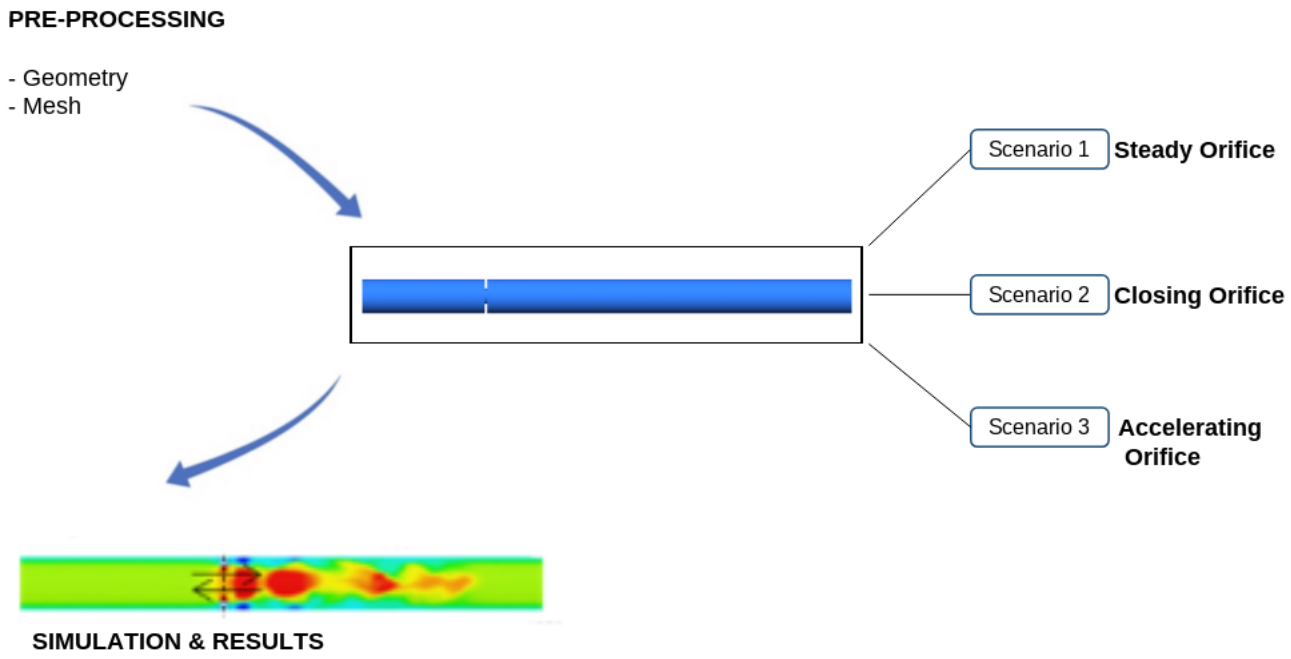


Figure 5.4: Flow chart summarising the scenarios to be analysed using the idealised model with a steady inflow.

We have chosen to focus the analysis of the idealised problem on the effects of the axial acceleration of the orifice, which will be referred to as the AVA in this analysis, on blood flow distribution. However, the axial acceleration of the AVA is coupled with complex physiological events during the cardiac cycle. These complex events include the pulsatile nature of the inflow to the AVA from the LV and the opening and closing of the aortic valve. As a result, we came up with different separate scenarios in an attempt to decouple the complex physiological events during the cardiac cycle.

Since the effects of flow pulsatility are known from the theoretical investigations by Womersley as the Womersley flow, we will focus the decoupling scenarios to investigate the other effects. Figure 5.4 shows a flow chart summarising the scenarios to be analysed. The tube orifice model will be used with a steady inflow boundary condition in three different scenarios to investigate

the effect of a stationary orifice with a fixed GOA, a stationary orifice with a closing shutter mechanism and an axially accelerating orifice with a fixed GOA. The analysis using the idealised model with a steady inflow will give us insights into the effect an orifice immersed in flow, the effect of orifice closure and the effect of orifice acceleration respectively.

Because the highest loads experienced by the valve are during the late systolic phases of the cardiac cycle, we will restrict the second scenario to assessing a closing orifice rather than an opening orifice. Another reason is that an orifice with GOA's lower than 50 % will experience significant loads. Accordingly, limiting the analysis to a closing orifice will yield helpful insight into understanding the problem.

A good representation of the analysis will be in terms of the force response of the valve or the orifice in the idealised problem. Not only is the force response of the orifice a representation of the pressure integrals on its wetted or projected area, but more importantly an indicator of valve wear and tear under different physiological or pathological conditions.

In addition to the three scenarios, the force response of the orifice may depend on different flow variables; hence, it is of best interest to narrow down the number of trials using CFD by combining the independent flow variables in non-dimensional groups. This will also provide a mathematical basis where results from the simplified idealised model can be used to investigate or assess the physiological model of the AVA.

5.3 Buckingham Π Theorem

The investigation using higher order CFD modelling aims to assess certain complex physiological events to ultimately test for the dicrotic notch hypothesis. There are uncertainties surrounding the problem in terms of the physical conditions since the investigation is directed towards a novel phenomena to our knowledge and the various scenarios behind the physics have not been fully connected.

This may result in numerous calculations to test the effect of all the independent variables in the problem thus dimensional analysis is necessary to economise the total number of calculations. This will involve forming non-dimensional groups of the independent variables. This is also advantageous since it will provide the scaling necessary to transfer the knowledge to the more advanced modelling scenarios using a physiological model of the AVA and valve [58].

We use the Buckingham Π theorem for the dimensional analysis. The Buckingham Π theorem states that in a problem if a certain quantity under investigation depends on a set of n independent variables, with k physical dimensions then the problem can be represented by $p = n - k$ non-dimensional groups [58].

Beginning with with the problem in the first scenario where we have a steady inflow boundary condition to the axisymmetric tube and a stationary orifice with a fixed GOA. The dependent variable under investigation is the axial force on the orifice F_o which has a physical significance. In this case, F_o will depend on the following independent variables:

- ρ - blood density
- D - characteristic/maximum tube diameter
- μ - blood dynamic viscosity
- Q - volume flow rate

where F_o may be calculated using equation 5.3.

$$F_o = \int_A \Delta P_o \, dA \tag{5.3}$$

In equation 5.3, ΔP_o is the pressure load on the orifice plate and when integrated over its projected or wetted area will yield the loading F_o. This integral can be deduced from a built-in function in the CFD post-processing software we used which is ANSYS CFD post.

Each of the above variables may be expressed as a product of three dimensions which are M, L and T meaning mass, length and time respectively regardless of their absolute units. For example, the blood density ρ is of units mass per volume and volume is length cubed; hence, it translates to ML^{-3}. Any non-dimensional group must have its physical dimensions M, L and T all raised to a power of zero ($M^0L^0T^0$).

Following the Buckingham Π theorem, having a total of five variables and three dimensions, the problem of the first scenario may be represented in terms of a total of two non-dimensional groups. From that, we choose three of the independent variables which also have no dependency between them in order to obtain the non-dimensional groups. The three independent variables chosen are known as the repeating variables and they are three to be equal to the number of physical dimensions in the problem. As a result, the first non-dimensional group Π_1 can be given by:

$$\begin{aligned}
\Pi_1 &= f(\rho, D, Q, F_o) \\
\Pi_1 &= \rho^a D^b Q^c F_o \\
\Pi_1 &= (ML^{-3})^a (L)^b (L^3T^{-1})^c (MLT^{-2}) \\
\Rightarrow (M^0L^0T^0) &= (ML^{-3})^a (L)^b (L^3T^{-1})^c (MLT^{-2}) \\
\Rightarrow (M^0L^0T^0) &= \left(M^{a+1}L^{-3a+b+3c+1}T^{-c-2}\right)
\end{aligned}$$

where a, b and c are the unknown integer powers of the dimensional variables.

In the above equations, the three repeating variables along with one of the remaining two variables together form a non-dimensional group.

Subsequently, we can obtain three linear equations to solve for the unknown powers a, b and c:

$$a + 1 = 0$$

$$-3a + b + 3c + 1 = 0$$

$$-c - 2 = 0$$

$$\Rightarrow a = -1, b = 2, c = -2$$

$$\mapsto \Pi_1 \equiv \widetilde{F} = \frac{F_o D^2}{\rho Q^2}$$

The first non-dimensional group Π_1 is simply the non-dimensional axial force acting on the orifice plate which is the non-dimensional load experienced by the valve. We will denote the non-dimensional axial force on the orifice by $\widetilde{F}$.

Applying the same dimensional analysis described using the three repeating variables together with the remaining variable μ we obtain the second non-dimensional group,

$$\Pi_2 \equiv Re = \frac{\rho Q}{\mu D}$$

Π_2 is commonly known as the Reynolds Number Re representing the ratio of the inertial forces to viscous forces. In the special case of Poiseuille flow, the Reynolds Number is multiplied by a factor of $4/\pi$. This is important to note since non-dimensional parameters may be multiplied by non-dimensional constants in certain scenarios. In our analysis, this parameter will be helpful as it will reduce the number of computations necessary to test the effect of velocity into one lumped parameter. Since we assume the flow in the AVA to be incompressible, Q should be conserved through any given cross-section in the flow domain and from that, a scaling exists from the domain inlet to the orifice using the following relationship:

$$Re_o = Re_i \frac{D_i}{D_o} \tag{5.4}$$

where the subscripts i and o denote inlet and orifice locations respectively.

The dimensional analysis using the Buckingham Π theorem may be repeated for the different physical scenarios under investigation to yield the following non-dimensional parameters:

$$\alpha = \frac{D}{2}\sqrt{\frac{\omega\rho}{\mu}}$$
$$\xi = \frac{\dot{A}_{max}D}{Q}$$
$$\beta = \frac{\dot{A}_{max}}{\overline{\dot{A}}}$$
$$St = \frac{\omega_a D^3}{Q}$$
$$\tilde{t} = \frac{tQ}{D^3}$$

Each one of the above non-dimensional parameters has a physical meaning describing a different effect of the behaviour of the AVA on its force $\widetilde{F}$. The parameter α is known as the Womersley Number which is a measure of flow pulsatility where ω is the fundamental frequency of the inlet flow. This parameter is simply a ratio between the transient inertial forces of the fluid to its viscous forces. In other words, the bigger the parameter α the more pulsatile the flow is.

The second parameter ξ is a parameter describing the opening or closure of the orifice. $\dot{A}_{max}$ is the maximum rate of opening or closure of the orifice. For example, suppose the orifice closes from a 90 % GOA to a 20 % GOA following a linear rate of closure over the course of 0.5 s, then $\dot{A}_{max}$ can be calculated using:

$$\dot{A}_{max} = \frac{0.2GOA - 0.9GOA}{0.5}$$

If the orifice closure follows a nonlinear change of area, then $\dot{A}_{max}$ may be calculated using:

$$\dot{A}_{max} = max\left(\dot{A}\right)$$

Another parameter describing the closure behaviour of the orifice is β which is a ratio between the local maximum rate of orifice closure and the average rate of orifice closure $\overline{\dot{A}}$. If the orifice

closure is following a linear rate of change of area then the parameter β will be equal to 1.

It will be seen in Section 5.5 that from ξ and β a more significant parameter ξ/β will be deduced. ξ/β is analogous to ξ with the only difference that it is the non-dimensional average rate of opening or closure of the orifice rather than the non-dimensional maximum rate of opening or closure of the orifice. ξ/β assumes that the opening or closing of the orifice whether linear or non-linear does not matter and that the non-dimensional average rate of opening or closure over a certain time period is more significant.

The following parameter to describe the underlying physics of the accelerating orifice problem St is known as the Strouhal Number where ω_a is the fundamental frequency of the orifice acceleration. This number is usually used to describe unsteady oscillating flows in terms of the vortex shedding frequencies in the wake of the oscillating body. We will use it in our case analogously where the orifice acceleration frequency will determine the vortex shedding frequency and thereby its force response.

Finally, the parameter $\tilde{t}$ is a non-dimensional time which will be used to describe any transient simulations in our study where $\tilde{t} = \pi$ is one full oscillation analogous to one cardiac cycle. A more detailed analysis showing the derivation of the aforementioned non-dimensional parameters using the Buckingham Π theorem may be found in the appendix section A.2.1.

5.4 Steady Orifice

The first scenario we outlined is a steady inflow boundary condition with a stationary orifice at a fixed GOA. In this analysis we used a steady uniform inflow boundary condition with velocity 0.1 m/s or Q equals to 4.91×10^{-5} m^3/s while varying the orifice GOA in a series of steady simulations with no transient dependency. The blood was modelled as a Newtonian incompressible fluid with ρ equals to 1060 kg/m^3 and μ equals to 0.0034 $Pa \cdot s$.

Since the inflow boundary condition was the same for all trials and the volumetric flow rate must be conserved through any cross-section in the domain due to fluid incompressibility, varying Re_o was simply done by varying the orifice GOA.

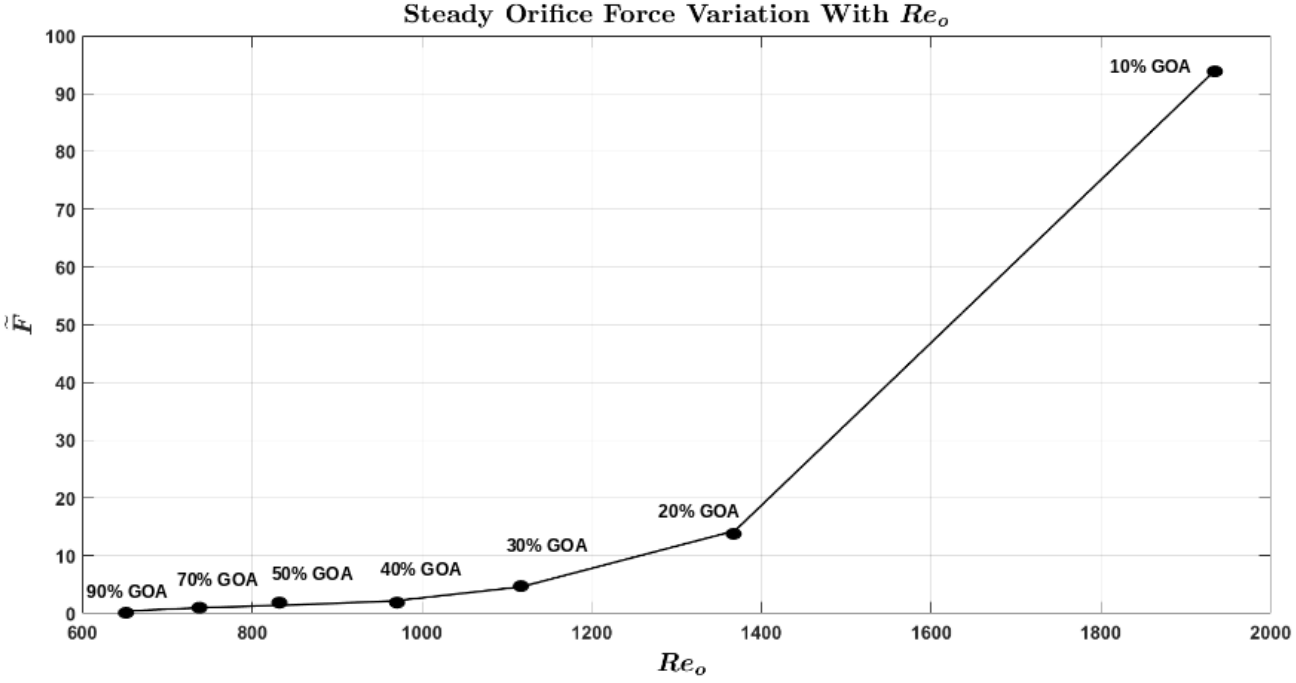
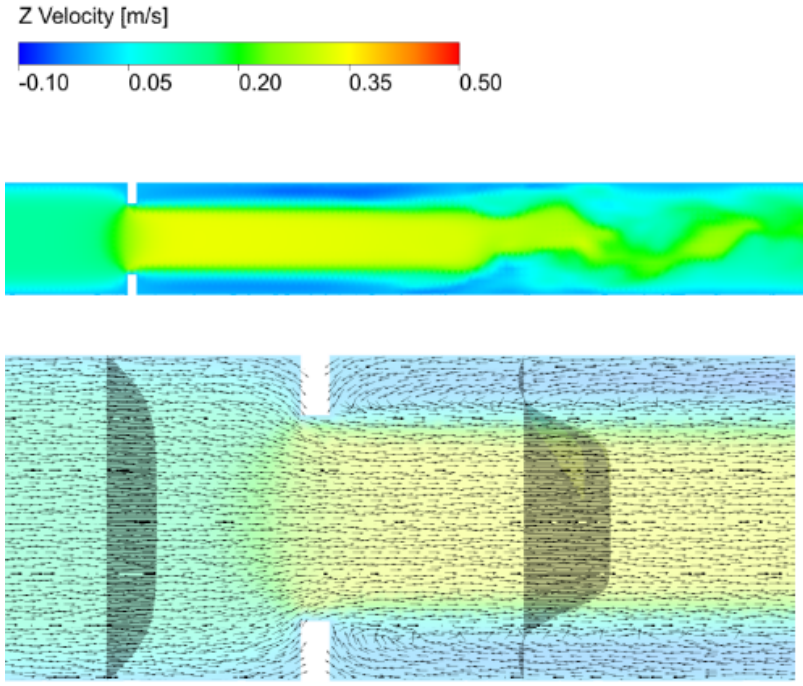


Figure 5.5: Variation of the non-dimensional force response of the orifice with orifice Reynolds Number.

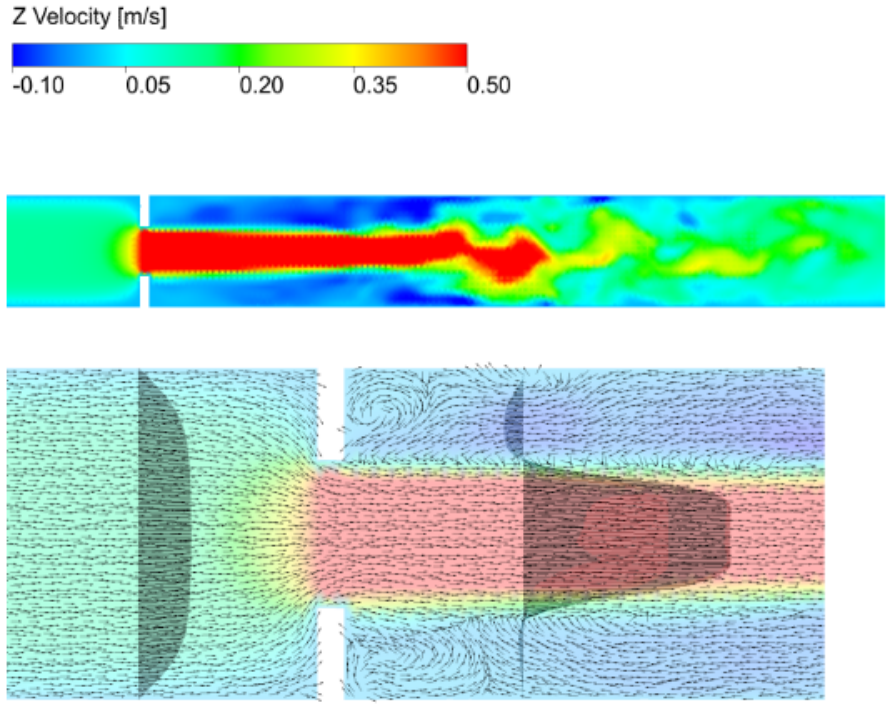
Figure 5.5 shows the response of $\widetilde{F}$ with varying Re_o. The different GOA's producing different values of Re_o tested in this analysis are shown in the figure. From equation 5.4, decreasing the orifice GOA resulted in a higher value of Re_o.

The rise in the value of $\widetilde{F}$ is small with lower values of Re_o as the orifice GOA was varied from 90 % to 40 %; however, decreasing the orifice GOA from 40 % (5.6a) to 20 % (5.6b) resulted

in approximately a 3-fold increase in $\widetilde{F}$. Furthermore, decreasing the GOA to 10 % resulted in a sudden 6-fold increase in $\widetilde{F}$.



(a) 40 % GOA flow distribution. (top) z velocity contour map. (bottom) Velocity vectors showing direction.



(b) 20 % GOA flow distribution. (top) z velocity contour map. (bottom) Velocity vectors showing direction.

Figure 5.6: CFD results from scenario 1.

Since $\widetilde{F}$ depends on F_o given by equation 5.3, elevated values of $\widetilde{F}$ with smaller orifice GOA's suggests the existence of higher pressure gradients across the orifice. Figure 5.6 shows why this is the case. Decreasing the orifice GOA from 90 % to 40 % does not produce a large pressure gradient or a higher velocity across the orifice compared to the inflow. However, when the orifice GOA is decreased to 20 %, the larger pressure gradient or higher velocity across the orifice requires a compensation of backflow at the orifice plate in order to ensure mass conservation. The vortices or recirculating flow at the orifice plate cause a rise in the value of $\widetilde{F}$. In other words, we believe that the stronger the retrograde flow downstream of the orifice due to higher pressure gradients and higher backward flow velocity, the higher the loads incurred by the orifice.

Figure 5.6a shows the flow distribution in the orifice with a 40 % GOA. In the top panel, the contour map of velocity shows that the orifice did accelerate the steady inflow by three times; however, the light black vectors in the bottom panel show that recirculation regions forming just downstream of the orifice are relatively small. The dark black vectors show the velocity profiles upstream and downstream of the orifice. The flow upstream of the orifice maintains a plug profile with a boundary layer while the accelerated flow downstream of the orifice results in minimal backflow above and below the bulk flow layer (yellow colour) due to conservation of mass.

Figure 5.6b on the other hand shows a velocity increase downstream of the orifice by more than five times. Retrograde flow forms downstream impinging back on the orifice plate with speeds of comparable magnitude to the inflow velocity. In the bottom panel of the figure, the light black vectors show strong recirculation regions forming unlike the orifice with 40 % GOA. The bulk flow downstream of the orifice has a thinner width (red colour) with higher velocities which is why strong retrograde flow exists due to conservation of mass. It is such flow distribution that is responsible for the sudden rise in $\widetilde{F}$ seen in Figure 5.5 between the 40 % and 20 % GOA. It follows from our simulations that for the vortices around the orifice to start having the effect of exponentially increasing its incurred load, the orifice diameter needs to be less than half of the maximum tube diameter which corresponds to a GOA of 30 %.

Flow Field Asymmetry

It is important to mention that although both computations with a 40 % GOA and a 20 % GOA had a symmetrical geometry and boundary conditions, some asymmetry is present in the results. This is because rather than imposing a symmetry boundary condition in the middle of the tube model, we ran the simulation for the full 3D geometry using a full Navier-Stokes solver.

For the orifice with 40 % GOA, the results are symmetrical adjacent to the orifice and continue to be symmetrical downstream until some flow instabilities occur due to convection. On the other hand, the orifice with a 20 % GOA showed asymmetries in the results beginning just adjacent to the orifice. This is due to the higher Re_o for the 20 % GOA case being close to transitional flow. Such flow regime is known to exhibit instabilities in the flow which can cause asymmetry in the flow field inspite being in a symmetrical geometry.

The results in this CFD simulation are reproducible meaning they will be the same if the computation is carried out each time with the same geometry, initial conditions and boundary conditions. However, due to the chosen solver, instabilities in the flow exhibiting the asymmetry in the results will be captured depending on how fine the computational mesh is.

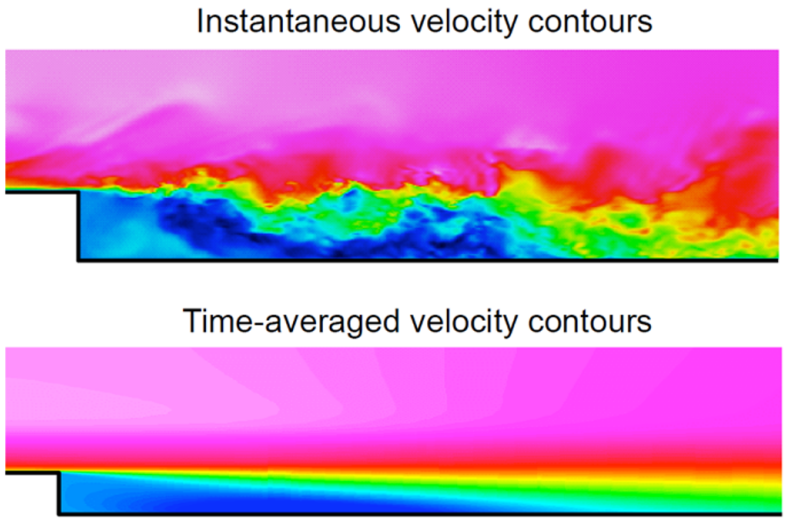


Figure 5.7: Difference between a laminar solver and a turbulence model solver. (top) A resolved flow field using a Direct Numerical Simulation. (bottom) the same flow field averaged using a turbulence model with only the mean quantities resolved. (From www.worksaero.com)

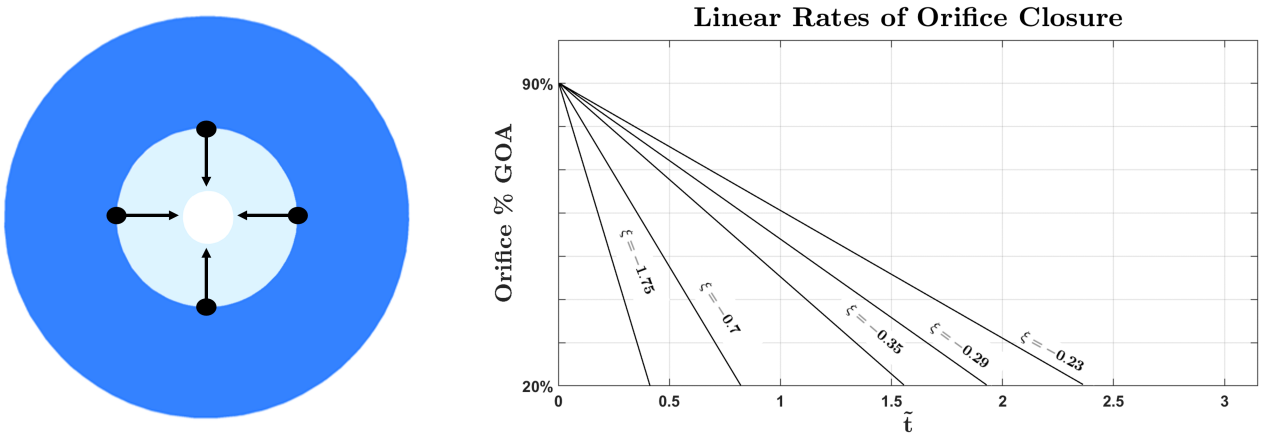
Figure 5.7 highlights the difference between CFD solvers. We refrained from using turbulence models since they usually depend on empirical constants which may add inaccuracy to the results. Instead, we opted for the laminar solver in fluent which approaches the results by a Direct Numerical Simulation as the finite volumes of the mesh tend to infinitesimally small sizes. Due to the limit in computational resources we only refined the mesh to the level necessary to capture certain flow effects that we need to monitor such as the force on the orifice. Using the laminar flow solver at transitional values of Re will result in asymmetric flow fields due to the instabilities captured. The laminar flow solver was used throughout the computations in this thesis since it avoids the uncertainties introduced by using turbulence models. Although we believe this may be a limitation in our computations as stated in Section 7.3, we showed that from our grid dependence study in Section A.2.4 that refining the mesh to a certain level resulted in convergence of the parameter $\widetilde{F}$.

We also believe the graphical representation of the relationship between $\widetilde{F}$ and Re_o will be beneficial in the physiological model of the AVA since calculating the GOA in that case is notoriously complex while knowing the value of $\widetilde{F}$ and therefore Re_o can yield an approximation of the value of the GOA of the AVA valve.

5.5 Closing Orifice

The second scenario in the investigation using the idealised model is the quasi-steady response of the orifice during closure. We chose to focus the analysis on the closure phase of the orifice since we have seen that the open orifice with a GOA higher than 50% incurs minimal loads compared to smaller GOA's. Studying the response of the orifice to closure requires using the non-dimensional parameters ξ and β. Since the response will not be steady as the orifice closure is a transient process with a steady inflow boundary condition, using the parameter $\tilde{t}$ is necessary.

Using the same inflow boundary condition from the previous scenario, each idealised model was tested with the orifice closing in a camera lens *shutter-like* mechanism to monitor the effect of ξ and β on $\widetilde{F}$.



(a) Orifice Shutter Mechanism

(b) Orifice linear rates of closure

Figure 5.8: Depiction of the shutter mechanism of the orifice. Final closing position is shown with higher transparency corresponding to a reduction in the GOA and an increase in the orifice plate area. The linear rates of closure to be analysed are shown in the graph with varying values of ξ while β is kept equal to 1.

Figure 5.8a shows a depiction of how the *shutter* mechanism closing the orifice was achieved. Using the moving wall method in the CFD model, the nodes on the orifice edge denoted by the black circles were displaced radially inward in the direction of the black arrows by means of a compiled user defined function (UDF) plugged into ANSYS Fluent [54]. This will increase the orifice plate area in blue and decrease the orifice GOA in the middle. The movement of

the nodes was applied as a displacement boundary condition on all the nodes on the orifice edge. Since the mesh sizing was refined in the vicinity of the orifice, mesh distortion due to the nodal movement was not a problem in this analysis [54]. In all the simulations in this analysis, the initial state of the orifice was at a 90 % GOA which was closed at different rates while the response of the axial force $\widetilde{F}$ was monitored. Figure 5.8b shows the different rates of closure of the orifice to be analysed. The rates of closure are linear in terms of area changes over time. This is achieved by varying the value of the parameter ξ while maintaining the value of β equal to 1.

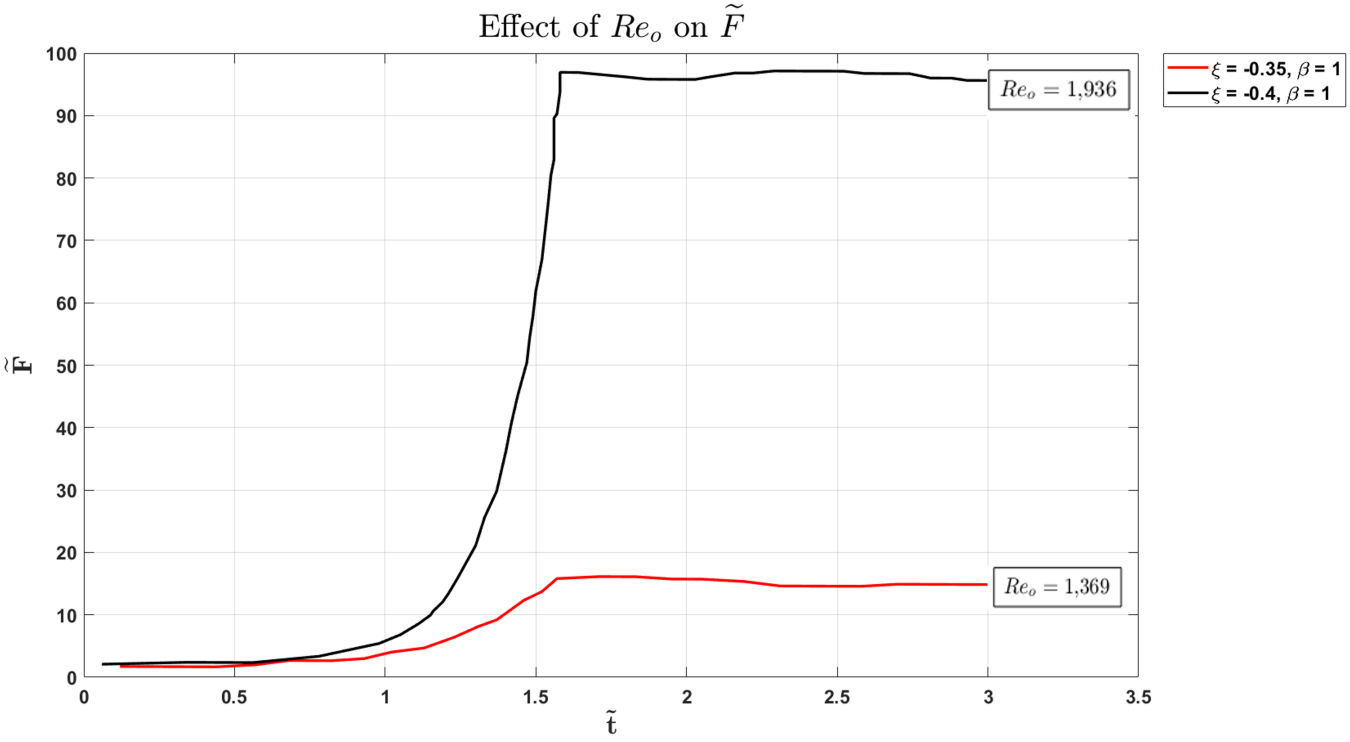


Figure 5.9: Effect of Re_o on $\widetilde{F}$ for a closing orifice. The red curve is for a final orifice GOA of 20 % while the black curve is for a GOA of 10 %.

Figure 5.9 shows the effect of increasing Re_o on $\widetilde{F}$ during orifice closure. Closing the orifice to a 20 % and 10 % GOA in the same time interval $\tilde{t} = 1.57$ resulted in the red and black curves shown respectively. With a steady inflow both scenarios showed an unsteady response with different steady state values of $\widetilde{F}$ attained. The steady state values of $\widetilde{F}$ are the same as the values shown in Figure 5.5 according to the variation of $\widetilde{F}$ with Re_o. An increase in the value of Re_o by a factor of 1.4 resulted in a 6-fold increase in the value of $\widetilde{F}$. This supports the analysis using an orifice with a fixed GOA where an increase in Re_o through a reduction in

GOA results in an increase in $\widetilde{F}$.

The second part of the analysis is to investigate the effect of different linear rates of closure on $\widetilde{F}$. This is done by changing the parameter ξ while keeping the parameter $\beta = 1$ in order to ensure a linear rate of closure.

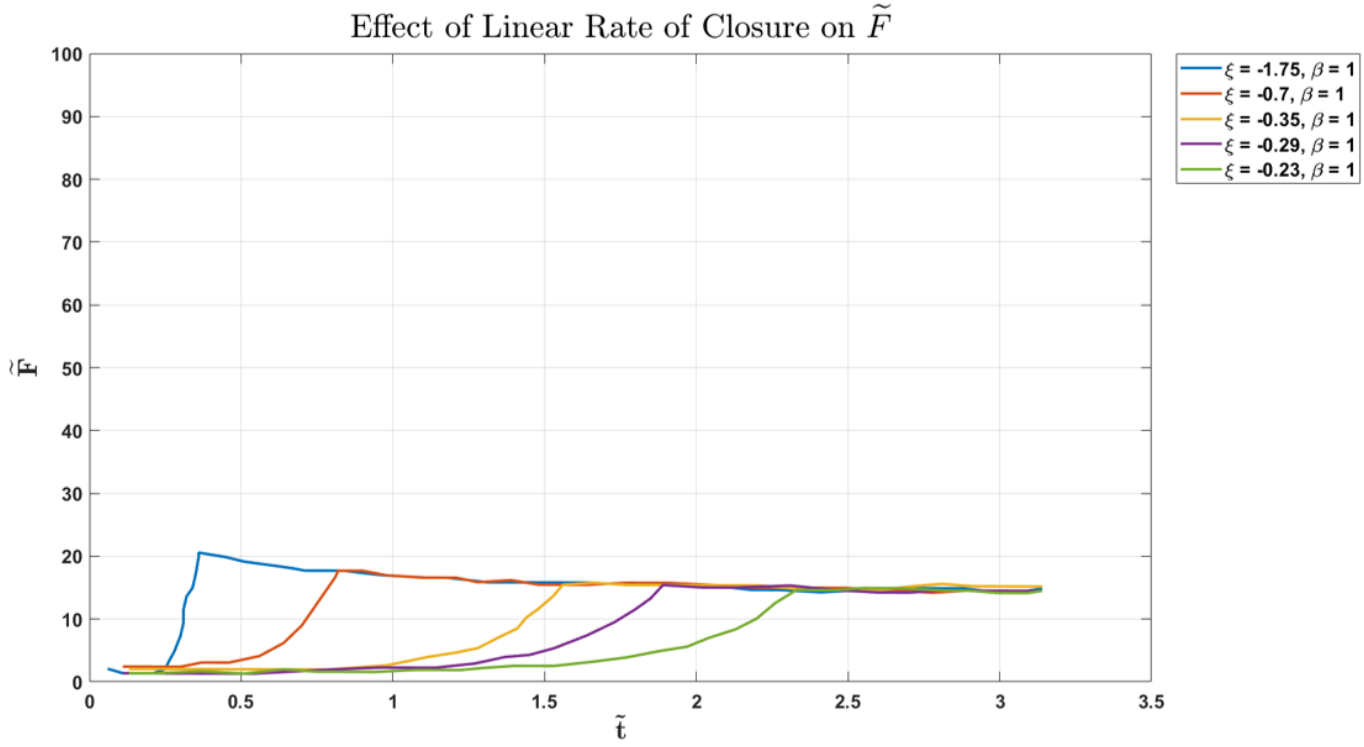


Figure 5.10: Effect of linear rate of closure on $\widetilde{F}$.

Figure 5.10 shows the response of $\widetilde{F}$ with varying linear rates of closure (linear changes in GOA) by varying ξ and keeping β equal to 1. Varying the rate of closure did not make a difference in the steady-state value of $\widetilde{F}$ attained by the orifice as expected from the previous analysis shown in Figure 5.5. The fact that all the resultant curves from all the trials have the same shape further confirms the results from the previous analysis. This is because when the orifice is initially at 90% GOA the value of $\widetilde{F}$ is negligible but when the orifice starts closing, the value of $\widetilde{F}$ non-linearly rises to the steady-state value when the GOA of the orifice reaches approximately a GOA of 30 %.

Accordingly, varying the parameter ξ had a specific effect on the response of $\widetilde{F}$. Firstly, since all the simulations had a value of β equals to 1, the orifice closure was linear where the GOA was linearly decreased from 90% to 20%. In consequence, increasing the magnitude of ξ which

is the local maximum rate of closure of the orifice resulted in a faster time $\tilde{t}$ to reach the steady-state load as expected. It is important to note that ξ is negative since the orifice is closing. We believe this has a clinical significance as in some aortic root disease, a rapid rate of valve closure accompanied by a non-decreasing flow rate will result in high valve loading. Moreover, slow or insufficient valve opening accompanied by an upstream high flow rate will also result in high valve loading.

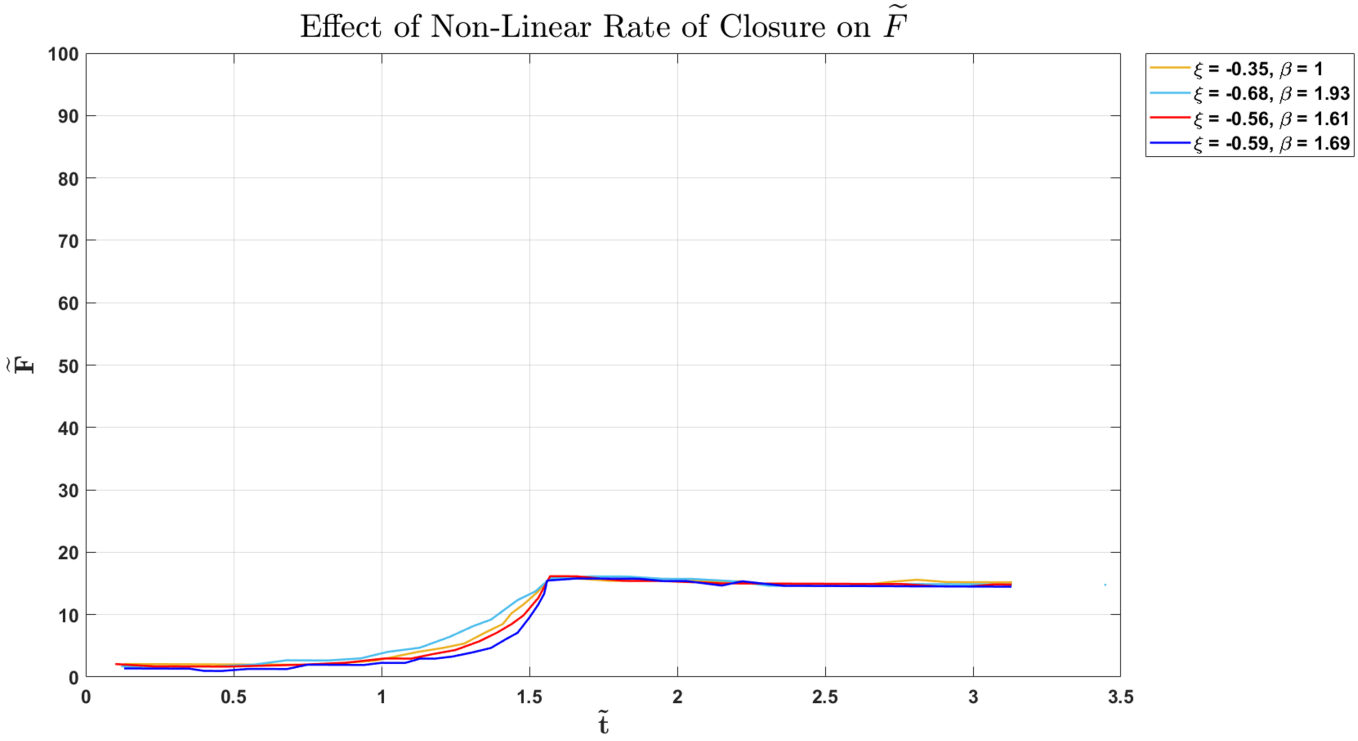


Figure 5.11: Effect of nonlinear rate of closure on $\widetilde{F}$. This was achieved by varying ξ and β.

Figure 5.11 shows the effect of varying nonlinear rates of closure on $\widetilde{F}$. This can be simply achieved by varying both ξ and β simultaneously while ensuring the orifice closes to 20 % GOA at $\tilde{t} = 1.57$. In this analysis, the trials included an orifice closing with an exponential decay function ($\xi = -0.68$, $\beta = 1.93$), an inverse exponential decay function ($\xi = -0.59$, $\beta = 1.69$) and an orifice closing following a cosine function ($\xi = -0.56$, $\beta = 1.61$).

From the figure, the three curves and their control with $\beta = 1$ shown in yellow show no difference in their behaviour with the steady-state value of $\widetilde{F}$ attained at $\tilde{t} = 1.57$. This is an important result since it shows that more important than ξ and β, their ratio ξ/β which is simply the non-dimensional form of the average rate of closure $\overline{\dot{A}}$ should be investigated. In

other words, the main parameter which makes a difference in how fast the steady-state value of $\widetilde{F}$ will be attained is the average rate of closure $\overline{\dot{A}}$. It is also worth noting that the four curves were not coincident which means they reached the steady-state force at slightly different rates. We believe this correlates to the initial local rate of orifice closure which is beyond the scope of our work in this thesis.

In summary, higher values of ξ/β or the average rate of orifice or valve closure will result in higher loads to be experienced by the orifice or valve if not accompanied by a decay in flow rate. This may be of clinical relevance as in cases of disease where the valve is incompetent or the LV function is impaired this may lead to higher valve loading which will result in wear and tear of the valve leaflets.

5.6 Axially Accelerating Orifice

The third scenario involves assessing the effect of an accelerating orifice under different acceleration frequencies on the force on the orifice. Based on our analysis of the kinematics of the AVA which revealed the dominance of the axial motion of the valve over all modes of local deformation and the hypothesis of the link between the valve acceleration and the dicrotic notch pressure rise at the time of valve closure; we believe the third scenario (Figure 5.4) will be pivotal in simplifying the analysis of the effects of the acceleration of the AVA on the surrounding flow therefore augmenting our ability to understand these effects in the physiological problem of the accelerating AVA.

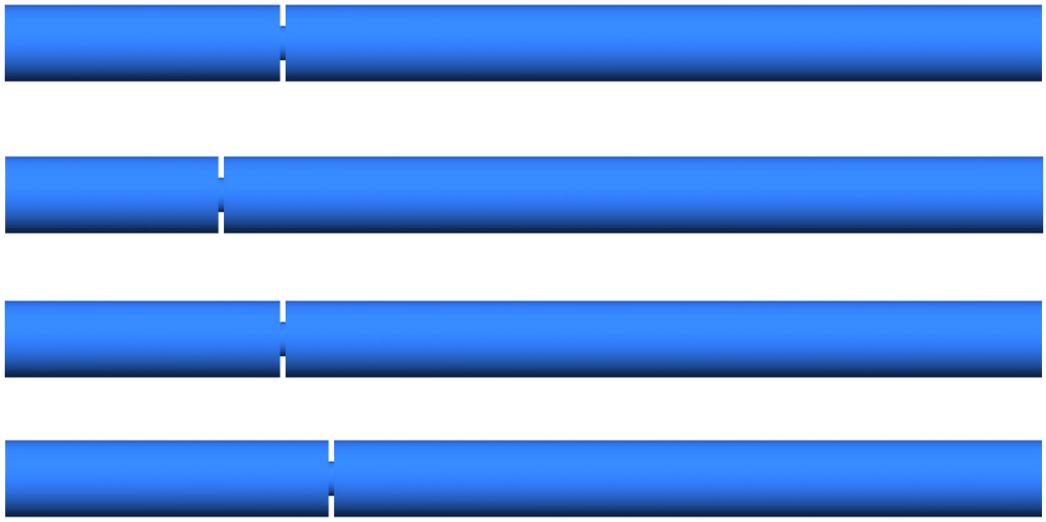


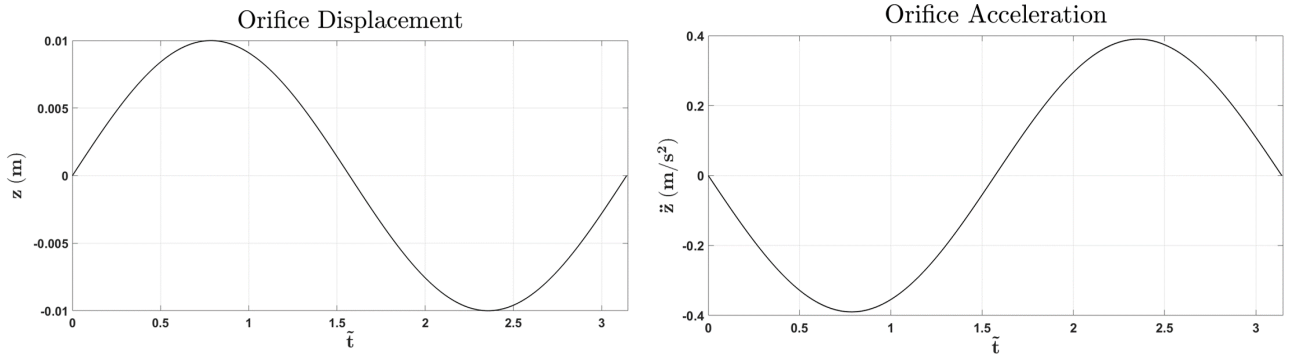
Figure 5.12: Axial motion of the orifice with a constant GOA. The motion shown follows a sinusoidal displacement function. The orifice can move in the positive or negative axial direction with varying frequencies of the displacement.

Using an orifice with 20% GOA for this analysis, the same meshing technique was used as in the previous scenarios explained in section 5.1.3. However, in this scenario the axial movement of the orifice is expected to cause problems in the mesh. Figure 5.12 shows the expected movement of the orifice along the axis of the tube. It is known a priori that the motion depicted in the figure will cause excessive mesh distortion during the simulation especially for high frequency displacements relative to small time increments and may result in poor quality finite volumes

which will cause failure of the numerical method. This is because the axial motion of the orifice will result in axial deformation of the mesh elements in its vicinity. When the orifice is moving towards a set of finite volumes they will be excessively compressed and similarly the volumes behind the orifice will be stretched. The mesh deformation will result in a change in element sizes and therefore quality. In order to bypass this issue, we used the remeshing algorithm in ANSYS fluent [54].

The remeshing algorithm in ANSYS fluent is automated in the sense that it analyses the mesh quality at every timestep in the simulation. When the mesh quality deteriorates beyond a certain threshold, the remeshing algorithm is invoked and produces a new mesh replacing the distorted one. Since the remeshing algorithm results in a higher computational cost, setting the invoking parameters must be done economically. In order to invoke the remeshing algorithm we set the remeshing criteria to maintain the original element sizes as we know the initial undeformed mesh was of good quality needed to maintain a converging simulation [54].

Using the UDF feature in ANSYS fluent, we prescribed the movement of the orifice as a sine wave with frequencies of 1 Hz, 2 Hz and 10 Hz with an amplitude of 10 mm. Furthermore, we tried one simulation with an orifice moving with a function as deduced in our analysis of the kinematics of the AVA in order to mimic the axial movement of the physiological AVA. Figure 5.13a shows the prescribed motion for the 1 Hz case which corresponded to $St = 2$ while Figure 5.13b shows the acceleration of the orifice derived from the displacement function.



(a) Prescribed temporal orifice displacement

(b) Orifice acceleration

Figure 5.13: Orifice wall motion boundary condition.

Figure 5.14 shows the transient results for the orifice moving at a frequency of 1 Hz. The

contour maps show the velocity values in the z direction at different times in the simulation.

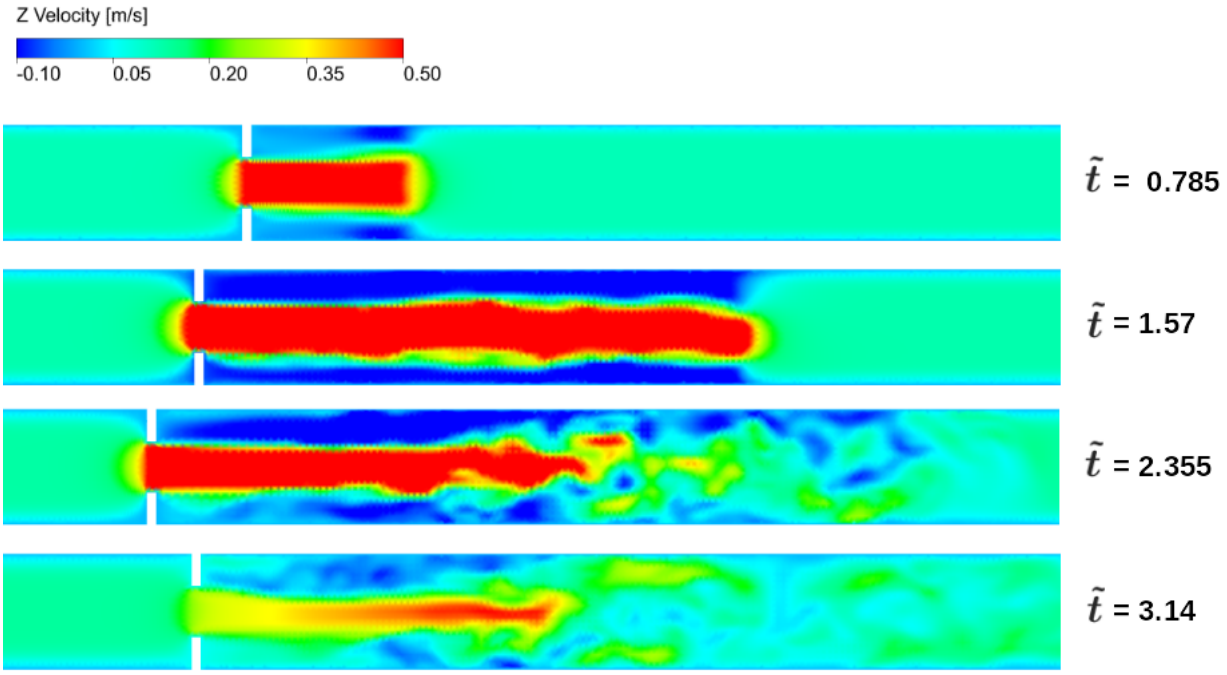


Figure 5.14: Flow field for an orifice moving with a frequency of 1 Hz.

As seen from the figure, the movement of the orifice in the $-z$ direction resulted in accelerating the bulk flow or vena contracta through the orifice. In comparison to the same case using a stationary orifice shown in Figure 5.6b, the velocity through the orifice reached a value more than ten times larger than the inflow velocity at $\tilde{t} = 1.57$, which corresponds to half of the complete oscillation, when the orifice was at its maximum speed in the $-z$ direction unlike the steady case where the velocity through the orifice was approximately five times larger than the inflow velocity (not clearly visible in the figure).

From the steady orifice analysis, the higher acceleration of the flow through the orifice will result in intensifying the retrograde regions adjacent to the orifice plate through increasing their backward velocity by conservation of mass.

On the other hand, when the orifice accelerates back in the $+z$ direction to its initial position, the bulk flow through the orifice is decelerated compared to the steady orifice case. As a result, the retrograde regions which were present have reversed direction with positive velocity values meaning no longer recirculating. This is because the orifice, now moving in the $+z$ direction,

reverses the direction of the retrograde regions.

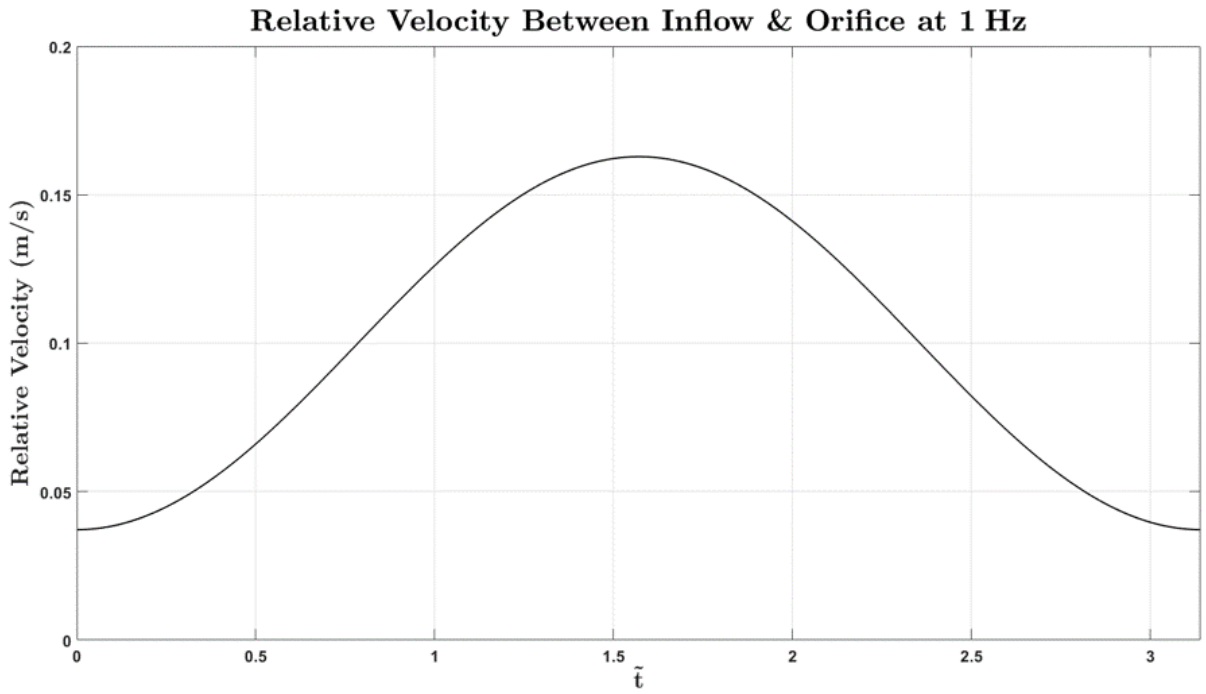
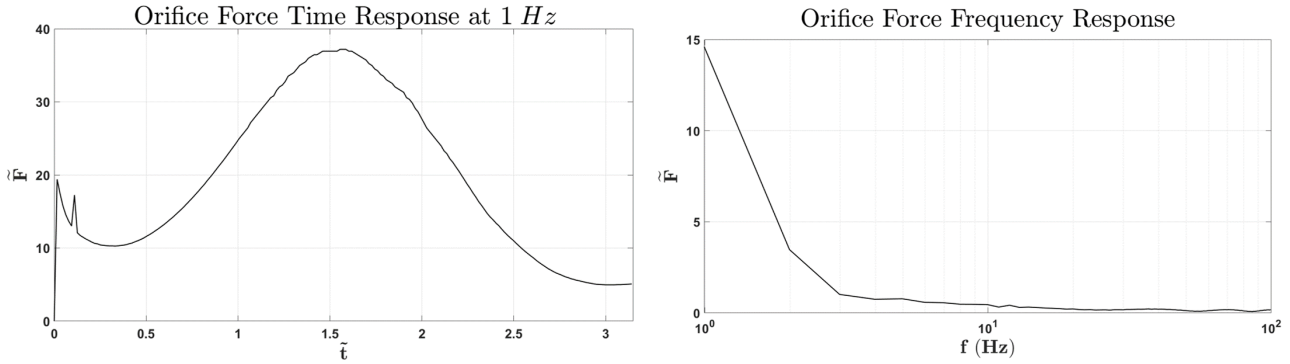


Figure 5.15: Relative velocity between the inflow condition and the velocity of the orifice moving at a frequency of 1 Hz. The sign of the relative velocity will determine the direction of flow through the orifice.

Figure 5.15 shows the relative velocity between the steady inflow velocity and the velocity of the orifice. An orifice moving in the $-z$ direction will increase the relative velocity and vice versa. It is clear from the figure that the relative velocity was always positive in sign meaning the flow was always moving in the $+z$ direction through the orifice as shown in the CFD results. Due to the low frequency of motion, the orifice movement slightly altered the velocities of the flow field without changing its direction. Since the relative velocity was always positive in this scenario it means that the orifice velocity was always slower than the inflow velocity. At $\tilde{t} = 1.57$ where the relative velocity reached its maximum, the flow through the orifice was accelerated to ten times the value of the inflow.

Figure 5.16 shows the time and frequency response of $\widetilde{F}$. In the time response, initial condition effects resulting from a single cycle can be seen in the beginning but it is an inverted cosine response overall. This is also observed in the 2 Hz case. More explanation on the limitation of initial condition effects is available in Section 7.3.2. One would expect the time response of



(a) Orifice force time response

(b) Orifice force frequency response

Figure 5.16: Orifice force response at 1 Hz.

$\widetilde{F}$ to be of the same shape as the orifice acceleration which is an inverted sine wave; however, the inertia of the fluid coupled with the movement of the orifice at a fundamental frequency of 1 Hz introduced a phase shift in the response of $\widetilde{F}$ in relation to the acceleration of the orifice. The frequency response on a semi-log scale shows that the dominant frequency is at the fundamental frequency of 1 Hz with a magnitude of $\widetilde{F}$ approximately 15 which is equal to the value approached by the steady orifice.

This means that the acceleration of the orifice disturbed the flow downstream causing a disturbance with the same frequency as the orifice motion. However, since the motion was over a large time period compared to the period of the dicrotic notch event for example, the fluid inertia resulted in a phase shift in the response of $\widetilde{F}$. We expect that increasing the frequency of the orifice movement may result in decreasing the phase shift seen in the response of $\widetilde{F}$ and overcoming the inertia of the fluid.

Figure 5.17 shows the transient results for the orifice moving at a frequency of 2 Hz. Since the frequency was doubled, the results were presented at the analogous time frames to the ones used in the simulation with a movement of 1 Hz. This is because the cycle of the movement of the orifice is covered in half the time after doubling the frequency. The resultant flow field follows the same events as in the 1 Hz case; however, the 2-fold increase in frequency slightly altered the velocity distribution. At $\tilde{t} = 0.39$ when the orifice is at its maximum displacement in the $+z$ direction, the bulk flow through the orifice had a much shorter length compared to its conjugate in the 1 Hz case at $\tilde{t} = 0.785$. This means that increasing the acceleration of the

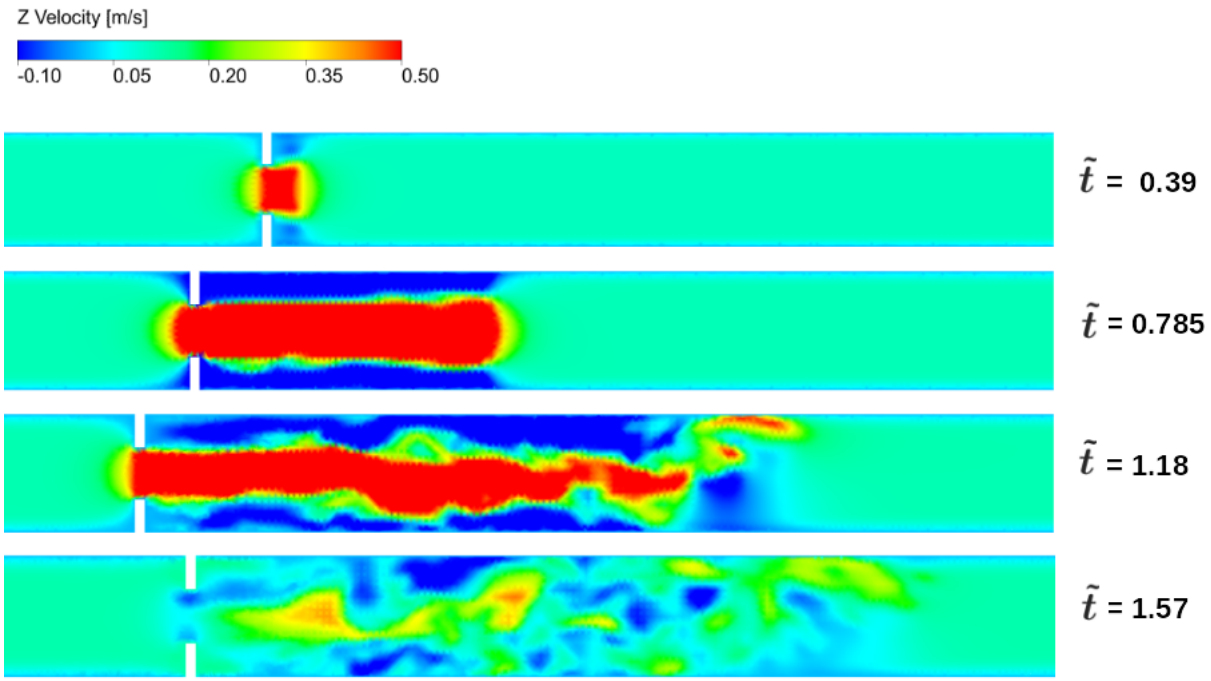


Figure 5.17: Flow field for an orifice moving with a frequency of 2 Hz.

orifice four times changed the flow field around the orifice by delaying the bulk flow formation seen by its shorter length. This also means that the retrograde regions around the orifice were diminished in terms of size and backward flow velocity.

When the orifice movement at 2 Hz has completed a cycle and returns to its initial position at $\tilde{t} = 1.57$, the flow field is completely disturbed with disorganised vortex shedding compared to its conjugate at $\tilde{t} = 3.14$ in the 1 Hz case. Moreover, the retrograde regions around the orifice plate have completely reversed direction with higher velocities in the $+z$ direction compared to the 1 Hz case. The velocities downstream of the orifice are retarded with small scale recirculation regions seen as small blue circles being convected downstream with length scales an order of magnitude less than the characteristic diameter of the tube. We believe the movement of the orifice at double the frequency or four times the acceleration decreased the phase lag between the flow field response and the displacement function by overcoming the inertia of the fluid unlike the 1 Hz case.

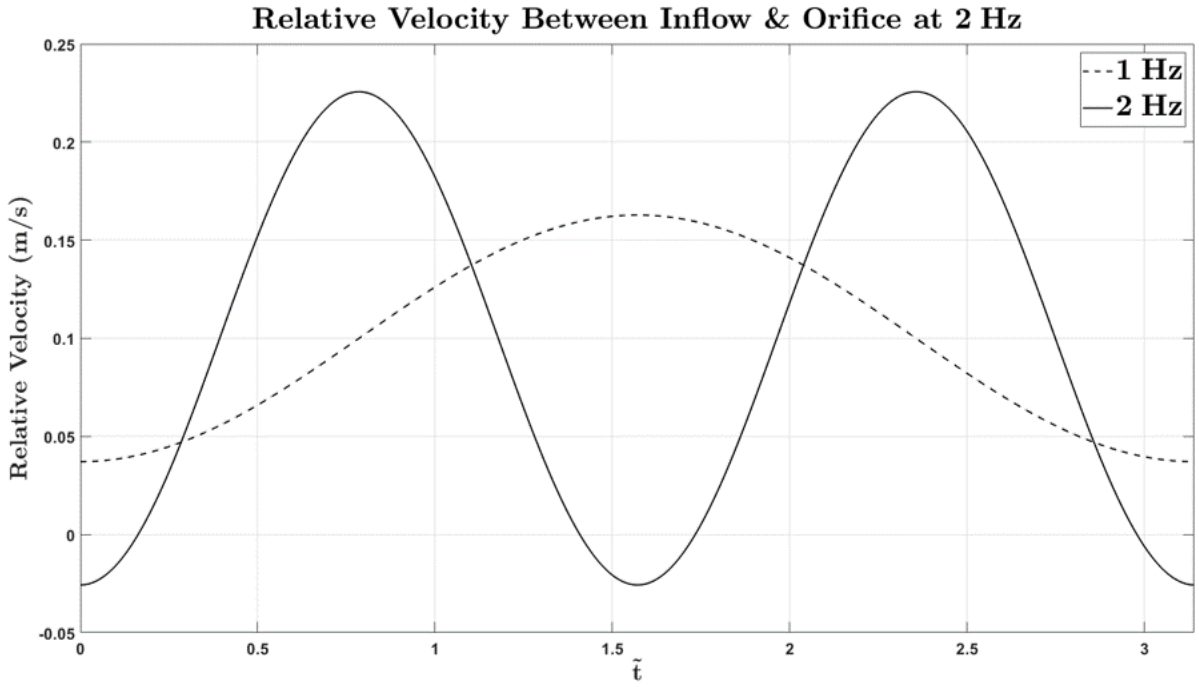
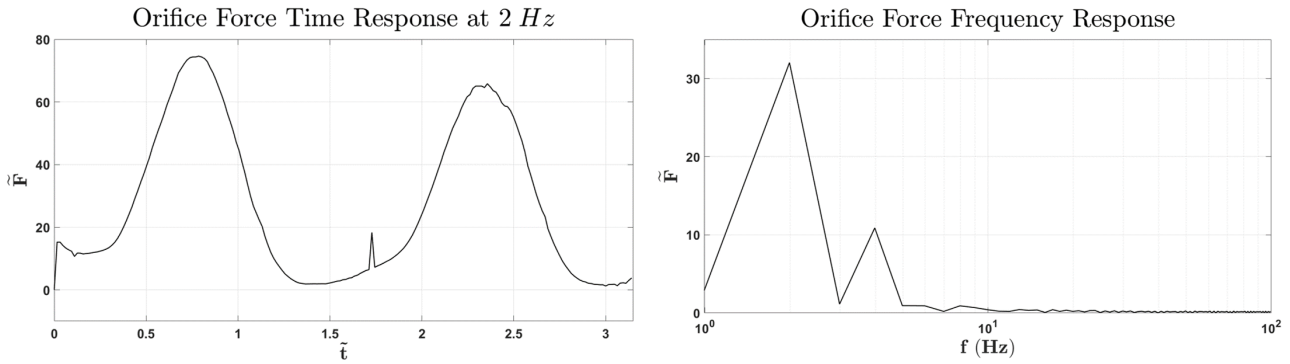


Figure 5.18: Relative velocity between the inflow condition and the velocity of the orifice moving at a frequency of 2 Hz. Negative relative velocities suggests a change in direction of the flow through the orifice.

The relative velocity for the 2 Hz case shown in Figure 5.18 shows some negative values and higher positive values compared to the curve in Figure 5.15. At $\tilde{t} = 0.785$ when the orifice is at its peak velocity in the $-z$ direction, the relative velocity with the inflow reaches a value of $0.23\ m/s$ which resulted in higher velocities through the orifice at this time point compared to the 1 Hz case.

At $\tilde{t} = 1.57$ when the orifice returns to its initial position by moving in the $+z$ direction with a velocity higher than the inflow velocity, the relative velocity becomes negative meaning the flow will be moving in the $-z$ direction through the orifice but with a small velocity of $-0.03\ m/s$. Although this is the average velocity of the orifice relative to the inflow there will be local changes across the orifice which we have seen to be small in magnitude in correlation with the small relative velocity. This explains why the resultant flow field in the 2 Hz case at $\tilde{t} = 1.57$ is different than its conjugate for the 1 Hz case. The higher velocities of the orifice due to the higher frequency was able to overcome the fluid inertia from the inflow. This is visible in Figure 5.17 in the bottom panel.



(a) Orifice force time response

(b) Orifice force frequency response

Figure 5.19: Orifice force response at 2 Hz.

Figure 5.19 shows the time and frequency response of $\widetilde{F}$ at 2 Hz. As anticipated, the time response shows a decrease in phase shift with the acceleration function prescribed to move the orifice where one and a half inverted sine waves can be seen. The frequency response shows that the dominant shedding frequency is at 2 Hz which corresponds to the frequency of the movement of the orifice. Nonetheless, the magnitude of $\widetilde{F}$ shows that the value at the fundamental frequency is double the value attained by the response of the steady case. This is expected since increasing the acceleration of the orifice by four times and therefore the value of St by two times would double the steady state value of $\widetilde{F}$ incurred by the orifice. In other words, this shows that the higher the frequency of orifice acceleration, the higher the value of the load incurred by the valve as predicted by the non-dimensional relationship.

Figure 5.20 shows the flow field for the orifice moving at a frequency of 10 Hz. At $\tilde{t} = 0.08$ when the orifice reached its maximum displacement in the $+z$ direction, the vena contracta is not present downstream of the orifice and the flow is completely retarded to a value approximately equal to the inflow condition. The flow upstream of the orifice on the contrary shows elevated values in the $-z$ direction approximately equal to the speed of movement of the orifice. At $\tilde{t} = 0.24$ when the orifice reached its maximum displacement in the $-z$ direction, the flow downstream shows a vena contracta present with high $+z$ velocities due to the rapid acceleration of the orifice. The flow upstream of the orifice is permanently disturbed due to the process of convection.

Finally, at $\tilde{t} = 0.31$ when the orifice finishes the cycle of motion and moves back to its initial

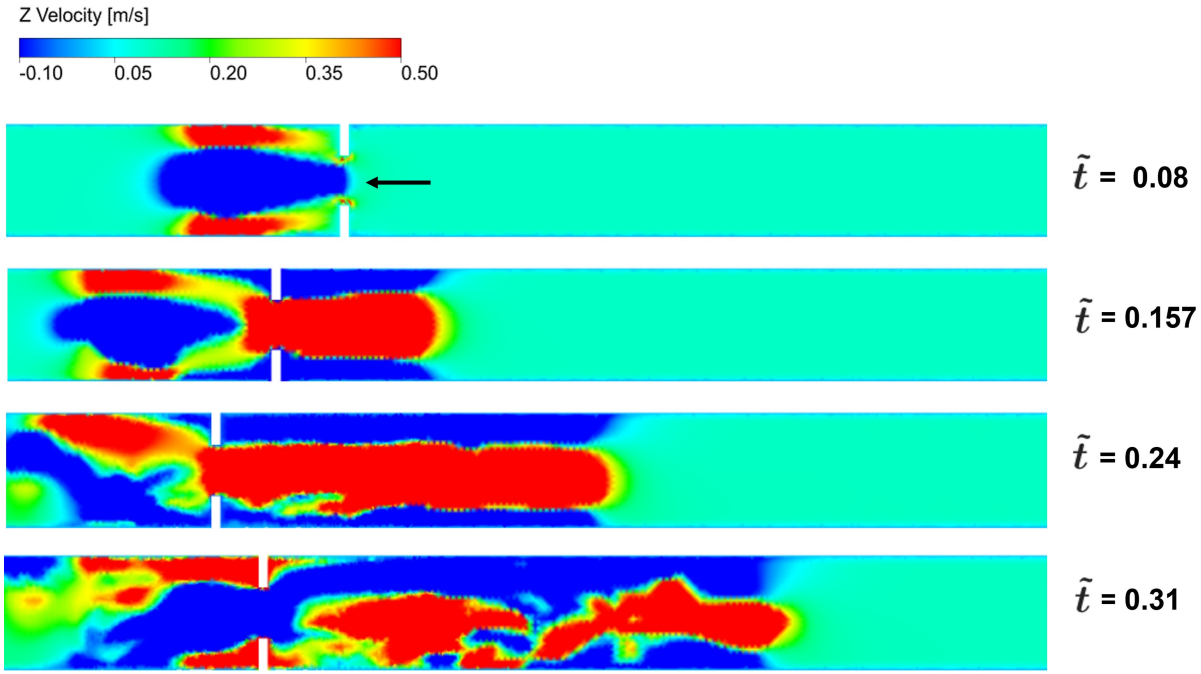


Figure 5.20: Flow field for an orifice moving with a frequency of 10 Hz.

position, the flow is disturbed upstream and downstream of the orifice showing shedding regions of variable length scales.

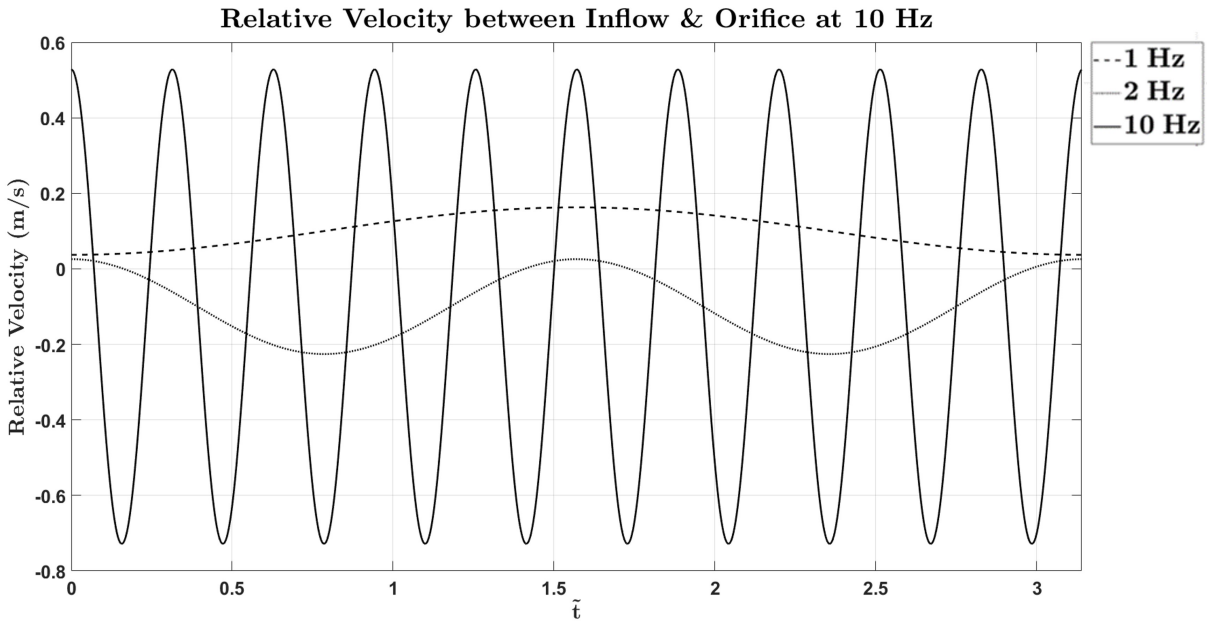
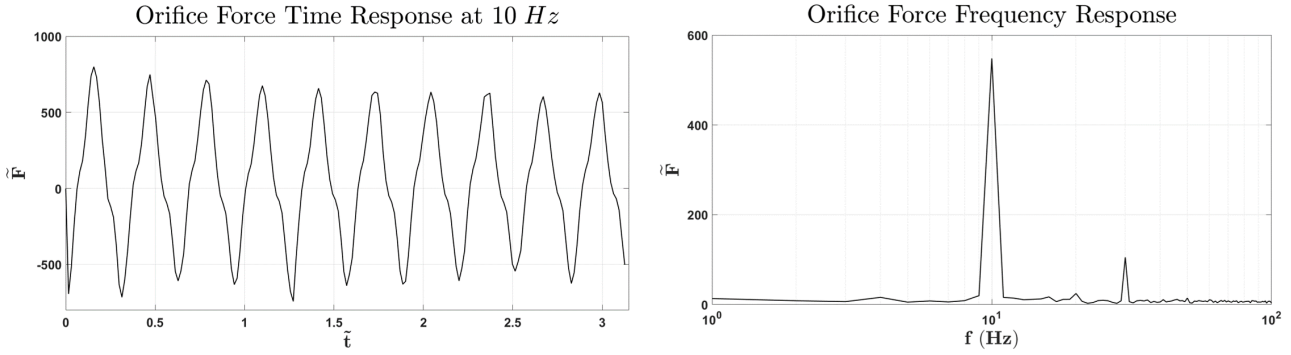


Figure 5.21: Relative velocity between the inflow condition and the velocity of the orifice moving at a frequency of 10 Hz. Higher magnitudes of the relative velocities seen due to higher velocities of the orifice suggests more alterations and disturbances to the flow field.

The motion of the orifice at a frequency of 10 Hz resulted in the relative velocity curve seen

in Figure 5.21. The higher peaks of relative velocity due to higher velocities of the movement of the orifice in the $-z$ direction resulted in higher velocities in the $+z$ direction through the orifice which in turn caused elevated values of $\widetilde{F}$. The troughs of the relative velocity showing values twice the inflow velocity resulted in complete reversal in direction of the vena contracta seen in the resultant flow field as indicated by the black arrow in Figure 5.20. As expected, the high frequency of motion causing velocities of the movement of the orifice marginally exceeding the inflow velocity at certain time points resulted in a flow field completely different than that of the 1 Hz and 2 Hz cases.

It is important to mention that the value of Re_i of 612 was the same as all the other computations in this chapter in order to decouple the effect of changing Re_i while adding complex motions of the orifice. However, we believe that changing the value of Re_i will result in different relative velocities between the orifice and the inflow which will change the values of the force incurred by the valve.



(a) Orifice force time response

(b) Orifice force frequency response

Figure 5.22: Orifice force response at 10 Hz.

Figure 5.22 shows the time and frequency response of $\widetilde{F}$ at 10 Hz. From Figure 5.22a it can be seen that the time response of $\widetilde{F}$ is in phase with the acceleration of the orifice showing 10 inverted sine waves. The frequency response in Figure 5.22b shows the dominant shedding frequency equal to 10 Hz. What was not expected in this scenario was that increasing the frequency of acceleration of the orifice by ten times and therefore St to a value equals 20 would result in a 16-fold increase in the value $\widetilde{F}$. This can imply that a high acceleration in the movement of the orifice may also contribute to increased load.

The sudden acceleration in the $+z$ direction should accelerate the fluid downstream of the orifice with the same value which would result in a negative change in $\widetilde{F}$ since it is a reaction force to the direction of movement.

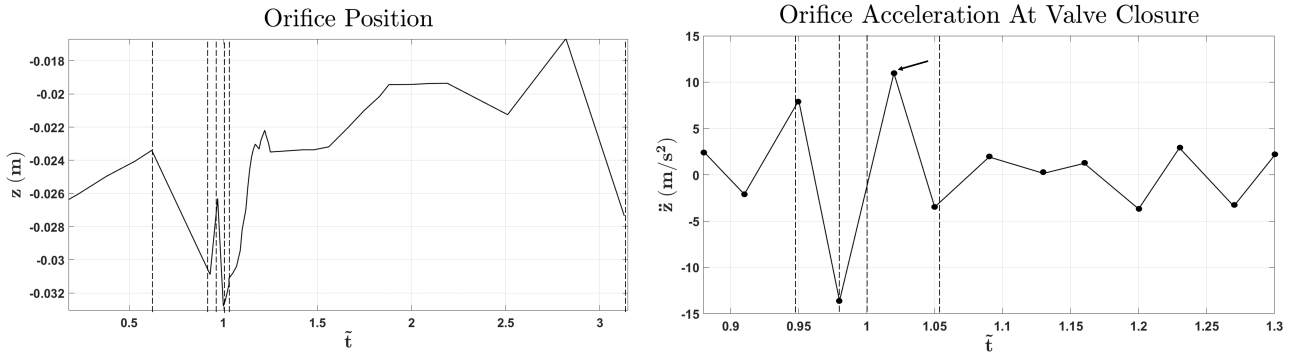
Increasing the acceleration of the orifice or the frequency of its displacement resulted in decreasing the phase lag and the orifice acceleration was able to overcome the inertia of the fluid. The time response of the force on the orifice should always be in phase with the acceleration (inverted sine wave); however, this was only seen in the 10 Hz case in comparison to the 1 Hz case for example where the force response was an inverted cosine wave.

Before investigating the more complicated scenario of an orifice moving with a physiological displacement or acceleration rather than simple sinusoidal displacements, we must restate a summary of the main observation from the above three cases. When a stationary orifice with a certain GOA is immersed in internal flow in a tube, the flow passing through the orifice is accelerated forming what is known as the vena contracta. The vena contracta is a bulk flow region with velocities higher than the flow velocities upstream of the orifice. Since the flow is treated as incompressible, the volume flow rate of fluid must be conserved at any given cross-section in the tube. Taking a cross-section just downstream of the orifice, retrograde regions or back flow regions must form in order to compensate for the vena contracta accelerated flow by the governing laws of conservation as mentioned in section 5.4.

Intuitively speaking, when an orifice starts accelerating in the positive axial direction away from the flow inlet, it should retard the flow in the vena contracta and and therefore the backflow regions which were impinging on the orifice plate will change direction. This will induce a force on the orifice which must be negative or decreasing as it is a reaction force to the orifice direction of movement. When the orifice moves in the negative axial direction, the exact opposite events happen and the orifice should incur a positive force opposing its negative direction of movement.

As seen in this section, the above intuition did not hold for an orifice moving at a frequency of 1 Hz or 2 Hz. This is because the lower the frequency meaning the lower the acceleration results in a phase lag and the orifice movement can not overcome the inertia of the fluid changing its

direction. For example for an orifice moving at a frequency of 1 Hz, the maximum acceleration was 0.39 m/s^2 which was not enough to overcome the inertia of the fluid and a phase lag of approximately 90° was present and the above intuition was completely reversed. Figure



(a) Orifice physiological displacement

(b) Orifice physiological acceleration

Figure 5.23: Physiological wall motion boundary condition for the orifice. Dashed lines in (a) and (b) show key time points for the flow field analysis. Arrow in (b) shows peak acceleration suspected to cause dicrotic notch pressure rise.

5.23 shows the physiological position and acceleration implemented as a moving wall boundary condition. The displacement to be deduced from the positions in Figure 5.23a is complex in the sense that it is a combination of multiple frequencies unlike the simple sinusoidal displacements we implemented in the previous simulations. The displacement boundary condition was deduced from our analysis of the kinematics of the AVA presented in chapter 4; however, it was projected on to the axis of best fit of the AVA (centreline) using equation 4.14 and scaled in order to obtain a realistic $+z$ movement at the time of valve closure equal to 1.6 mm. This was explained in chapter 4 section 4.3 as we hypothesised that an AVA moving a distance of 1.6 mm over 20 ms during valve closure at an acceleration of 10 m/s^2 is sufficient to generate a pressure rise in the retrograde flow surrounding the aortic valve or orifice [30].

Since the purpose of this analysis is to test our hypothesis behind the cause of the pressure rise in the dicrotic notch, Figure 5.23b shows the acceleration of the orifice during the time around valve closure at $\tilde{t}$ from 0.87 to 1.3. Valve closure or the event of the dicrotic notch occurs in the interval of $\tilde{t}$ from 1 to 1.07 which is a period of 20 ms. Since a minute phase lag between the displacement and acceleration still exists, at $\tilde{t} = 1$ when the orifice suddenly accelerates in the $+z$ direction, the acceleration changes from approximately 10 m/s^2 to 0 m/s^2 as stated in Chapter 4.

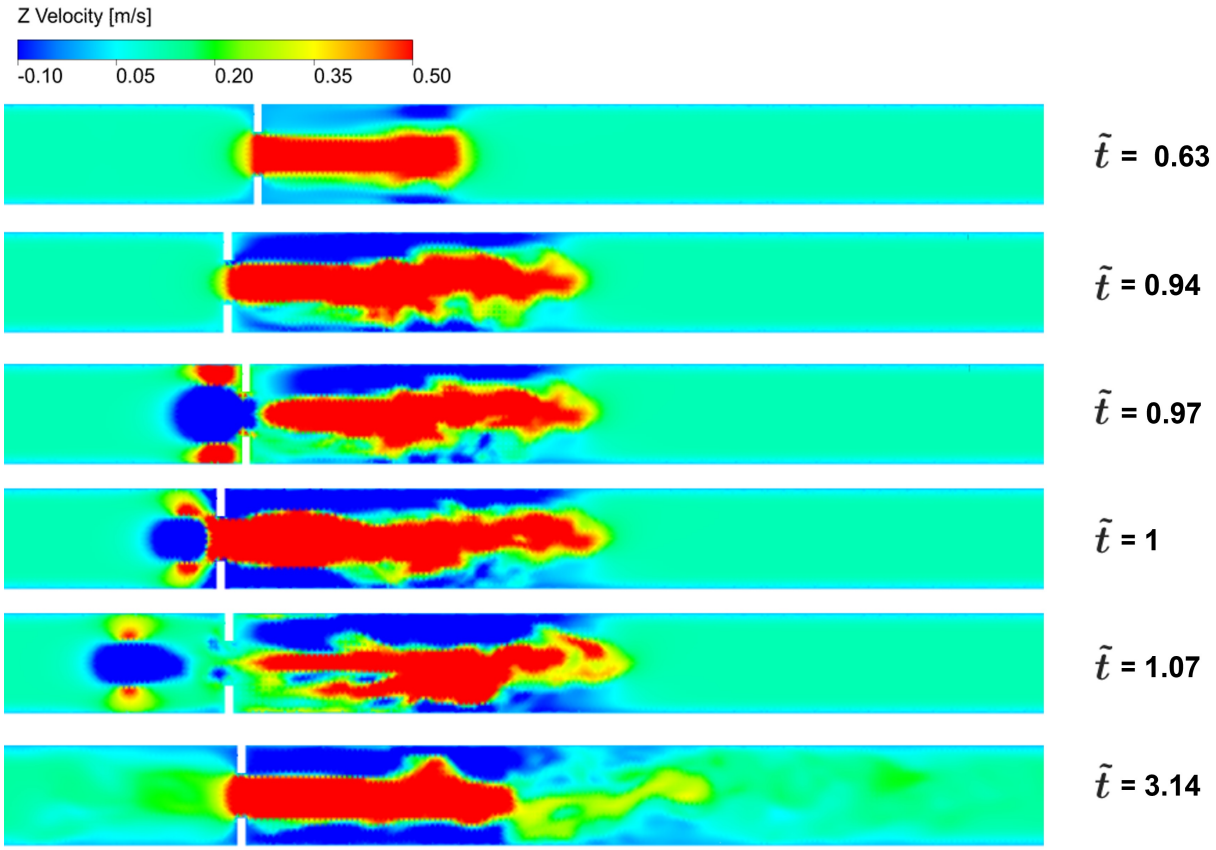


Figure 5.24: Flow field for an orifice moving with a physiological displacement.

Figure 5.24 shows the flow field for the orifice moving with the prescribed physiological displacement function. At $\tilde{t} = 0.63$, the orifice has moved from its initial position a total distance of 4 mm in the $+z$ direction but with an acceleration approximately close to 0 m/s^2. As a result, the flow field is only affected by the geometry of the orifice forming the vena contracta region and two retrograde regions with low $-z$ velocities adjacent to the orifice plate.

At $\tilde{t} = 0.94$, the orifice moved a distance of 4 mm in the $-z$ direction with an acceleration of approximately 5 m/s^2. This accelerates the flow through the orifice which results in two asymmetric retrograde regions impinging on the orifice plate.

At $\tilde{t} = 0.97$ the orifice accelerates in the $+z$ direction a distance of 4 mm with an acceleration of 7 m/s^2. This sudden movement over a period of 10 ms accelerates the flow upstream of the orifice in the opposite direction as a reaction while in the same time reversing the flow direction of the retrograde regions which were present at $\tilde{t} = 0.94$. In addition to this, the vena contracta has detached from the orifice but maintains the same length and velocity due

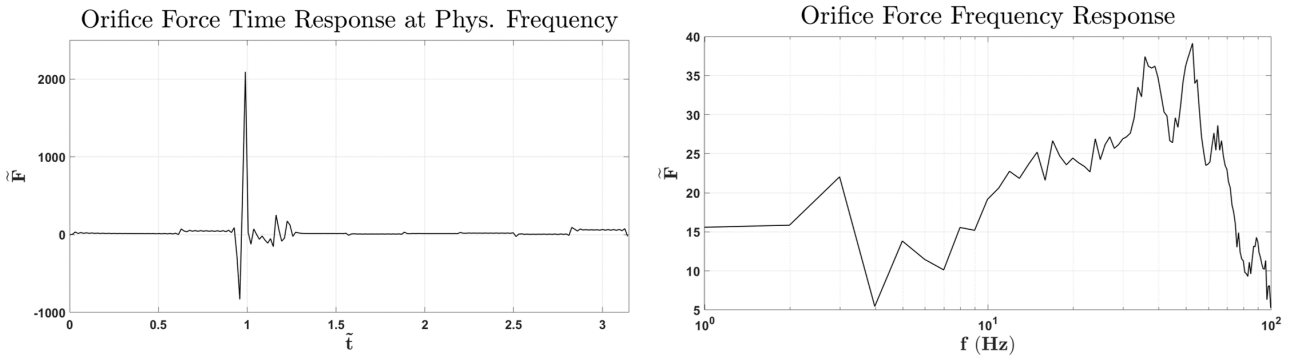
to being convected downstream. Moreover, a vena contracta starts forming upstream of the orifice with flow accelerating in the $-z$ direction at a velocity twice the inflow velocity. Two retrograde regions also form upstream of the orifice impinging on the orifice plate from the back. The back of the orifice plate is analogous in this case to the ventricular side of the aortic valve.

At $\tilde{t} = 1$ the orifice accelerates back in the $-z$ direction at 15 m/s^2. The flow in the vena contracta is accelerated thus forming two retrograde regions again adjacent to the orifice plate from the front side which is analogous to the aortic side of the aortic valve. The vena contracta which was present upstream of the orifice now slows down as seen by its shorter length and the retrograde regions upstream of the orifice are now reversing direction.

At $\tilde{t} = 1.07$ which is approximately the time of valve closure, the orifice accelerates at 10 m/s^2 a distance of 1.6 mm in the $+z$ direction. The retrograde regions downstream of the orifice change direction while the vena contracta upstream of the orifice is detached and moves upstream by convection since it has a velocity twice the inflow velocity. Due to conservation of mass, two small vortices still exist around the flow convected upstream with a local velocity five times the inflow velocity (0.5 m/s). We believe that the sudden movement of the orifice in the $+z$ direction at the time of valve closure is responsible for the pressure rise in the flow downstream and consequently will result in a negative change in force on the orifice plate as a reaction to changing the direction of the downstream retrograde regions.

Finally at the end of the cycle at $\tilde{t} = 3.14$, the orifice has already moved back to its initial position and is no longer accelerating. The flow is no longer affected by any acceleration of the orifice and simply accelerates due to the orifice GOA forming a vena contracta and two retrograde regions downstream of the orifice.

Figure 5.25 which shows the time and frequency response of the orifice supports our previous analysis of the flow field. In Figure 5.25a, we can see that the values of $\widetilde{F}$ are constantly close to zero since the orifice or AVA is not accelerating on average across the cardiac cycle; however, the main disturbances in the orifice force happen around $\tilde{t} = 1$ which is the time of peak acceleration of the orifice or valve closure.



(a) Orifice force time response

(b) Orifice force frequency response

Figure 5.25: Orifice force response at a physiological frequency. The dominant shedding frequency in (b) is at 50 Hz on the semi-log scale which corresponds to the dicrotic notch period of 20 ms.

As seen from Figure 5.24, at $\tilde{t} = 0.97$, the orifice moved forward in the $+z$ direction. This corresponds to a drop in $\widetilde{F}$ to a value of approximately -800. At $\tilde{t} = 1$, the orifice accelerated in the $-z$ direction so $\widetilde{F}$ undergoes a sharp rise to a value of 2000. Since the orifice needs to come to a complete halt before reversing its direction of acceleration, the value of $\widetilde{F}$ drops to almost 0. At $\tilde{t} = 1.07$ which is the time of valve closure, the orifice accelerated in the $+z$ direction yielding a value of $\widetilde{F} \simeq -150$. This is an important result since it yields a change in pressure in the fluid surrounding the orifice approximately equal to 6 $mmHg$ which was initially predicted using the *water-hammer* equation and is commensurate with the typical values of the pressure rise in the dicrotic notch (at $\tilde{t} = 1.05$).

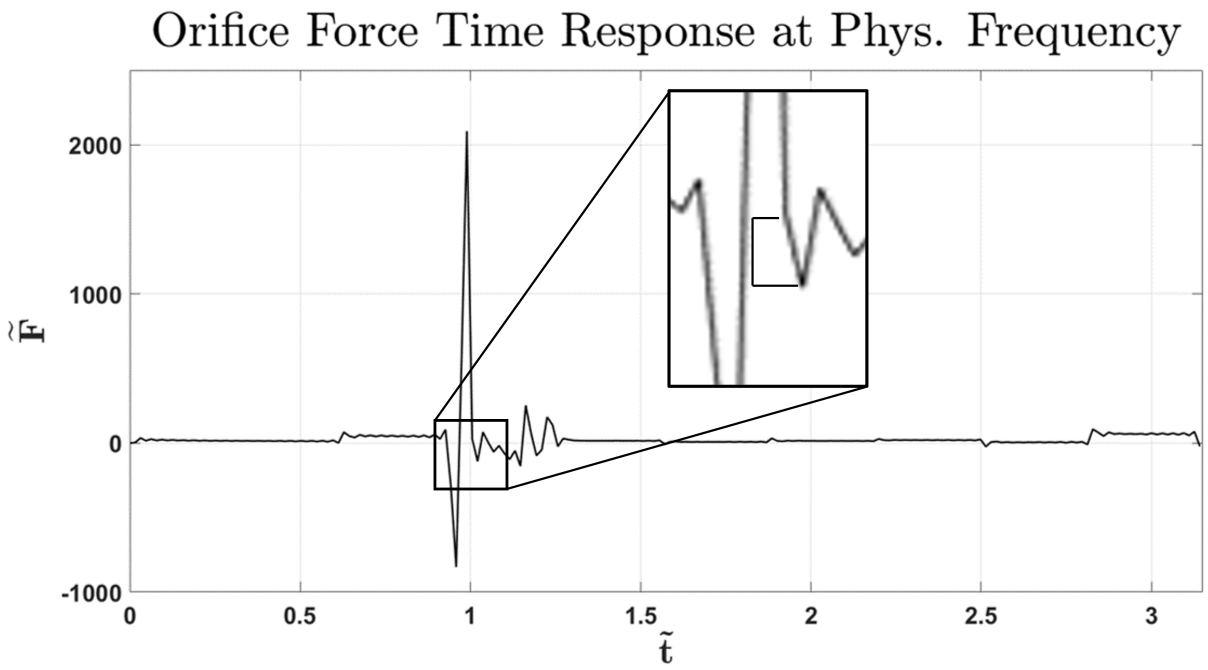


Figure 5.26: Orifice force time response focused at the time of valve closure. The marked drop in $\widetilde{F}$ in the zoomed panel over a period of 20 ms coincides with the sudden positive acceleration of the orifice.

Figure 5.26 shows a zoomed in version of Figure 5.25a at the time of valve closure. The whole of event of the orifice accelerating in the $+z$ direction over a period of 20 ms is also confirmed by Figure 5.25b which shows that the dominant shedding frequency is precisely at 50 Hz.

In conclusion, we believe our hypothesis behind the mechanics of the dicrotic notch still holds as seen from the results of the accelerating orifice idealised model. Moreover, the low order approximation using the *water-hammer* equation gave a result which was close to the result predicted by a higher order CFD model. In order to test the hypothesis further, we will improve the analysis by involving a physiological geometry of the AVA including the motion of the aortic valve which highly interacts with the surrounding flow field as it opens and closes. Using the previous results from the analysis of the idealised model, we will be able to simplify the analysis of the physiological model of the AVA undergoing acceleration at the time of valve closure. We will also compare an accelerating AVA to a non-accelerating AVA to confirm if the sudden pressure rise in the decelerating flow in the vicinity of the valve is due to the sudden acceleration away from the LV at the time of valve closure.

Chapter 6

Patient Specific Root Model

6.1 Fluid−Structure Interaction (FSI) Methodology

One would think from the analysis in Chapter 5 that a higher order CFD model of the physiological AVA along with the moving wall method to mimic the acceleration of the AVA would be sufficient to analyse the problem. However, the need for FSI in this scenario is pivotal since we need to model the opening and closing behaviour of the aortic valve.

The motion of the valve may be prescribed using the moving wall method as a displacement boundary condition if and only if geometric reconstruction of the valve at a high frequency across the cardiac cycle is available. This is known to be a tedious task and primarily depends on the CT images having a good resolution across all time points in the cardiac cycle. Since CT images have a low temporal resolution compared to other imaging techniques, not all temporal images of the AVA have a sufficient resolution. As a result, we need a different technique to model the highly dynamic behaviour of the valve opening and closure.

6.1.1 FSI Physics

Figure 2.40 shows the coupling between the fluid and structure solvers in FSI. Figure 6.1 shows a simplified verions tailored to our FSI plan. The basic idea in an FSI simulation is to have a

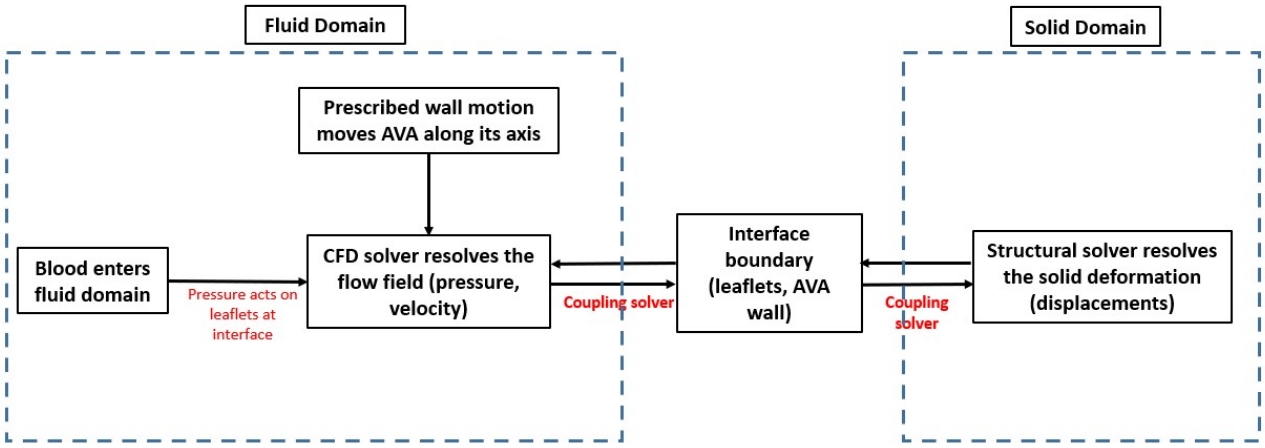


Figure 6.1: Flowchart showing the sequence of events in the planned FSI scenario. The presence of data exchange across the interface via the coupling solver suggests that it is a partitioned approach.

solid entity interacting with a surrounding fluid domain. The equations describing the motion of the fluid are the Navier-Stokes equations. The equations describing the motion of the solid entity are the Cauchy equations of motion for a deformable solid. The fact that the interaction is two-way means that the fluid domain will affect the solid domain and simultaneously the solid domain will affect the surrounding fluid domain as shown by the closed loop in the figure. The interaction between both domains only takes place at the boundary or *interface*. This yields an important boundary condition to complete the FSI loop which states that the force from the fluid pressure at the interface must equal the force acting on the solid domain and thus deforming the solid entity [59],[60].

FSI simulations require solving the fluid equations using a CFD solver which employs the finite volume method coupled with a structural solver which employs the finite element method. Since both types of solvers have different formulations, a separate algorithm for coupling both of them is also needed.

FSI coupling algorithms follow one of two strategies; either a monolithic approach or a partitioned approach. The monolithic approach is the most robust since it combines all the governing equations of the fluid and solid blocks shown in Figure 6.1 in a single matrix so the fluid and solid equations are always solved simultaneously. While this approach is robust it may be very computationally expensive. A more relaxed approach which is how partitioned solvers work

is that both sets of equations are solved separately and the solutions are transferred between them in order to fulfil the interface boundary condition.

The frequency of the load transfer during a time step will determine how *strongly* coupled the partitioned approach is. While this approach is less computationally expensive it may suffer from stability issues during the iterative solution process [46].

The plan we devised to use an FSI technique in conjunction with the moving wall method is complex yet sequential. Taking our fluid domain to be the internal volume of the physiological model of the AVA, the solid domain to be the valve leaflets and walls of the AVA, and the interface where the fluid and solid loads will be transferred to be the surfaces of the valve leaflets and walls of the AVA; we can outline the whole scenario in the following steps:

1. Blood enters the fluid domain from the LVOT
2. The blood applies a pressure on the AVA walls and valve leaflets
3. The prescribed moving wall condition moves the AVA along its axis
4. The CFD solver resolves the flow field
5. The pressures from the resolved flow field apply a load at the interfaces
6. The loads are transferred to the solid domain via the coupling solver
7. The solid domain deforms
8. The displacements from the solid deformation apply a load on the flow field
9. The new altered flow field is updated

6.1.2 Boundary Conditions

In order to carry out the above steps, we must use a good quality mesh along with appropriate boundary conditions. Similar to the analysis in Chapter 5, blood will be treated as an incompressible Newtonian fluid with $\rho = 1060\ kg/m^3$ and $\mu = 0.0034\ Pa \cdot s$.

In order to apply a realistic inflow boundary condition, we needed a patient-specific inflow velocity waveform. Since we only had CT images for the patients used in this study which did not give direct information about the inflow, we had to analyse the temporal images of the LV to obtain a patient-specific inflow velocity waveform.

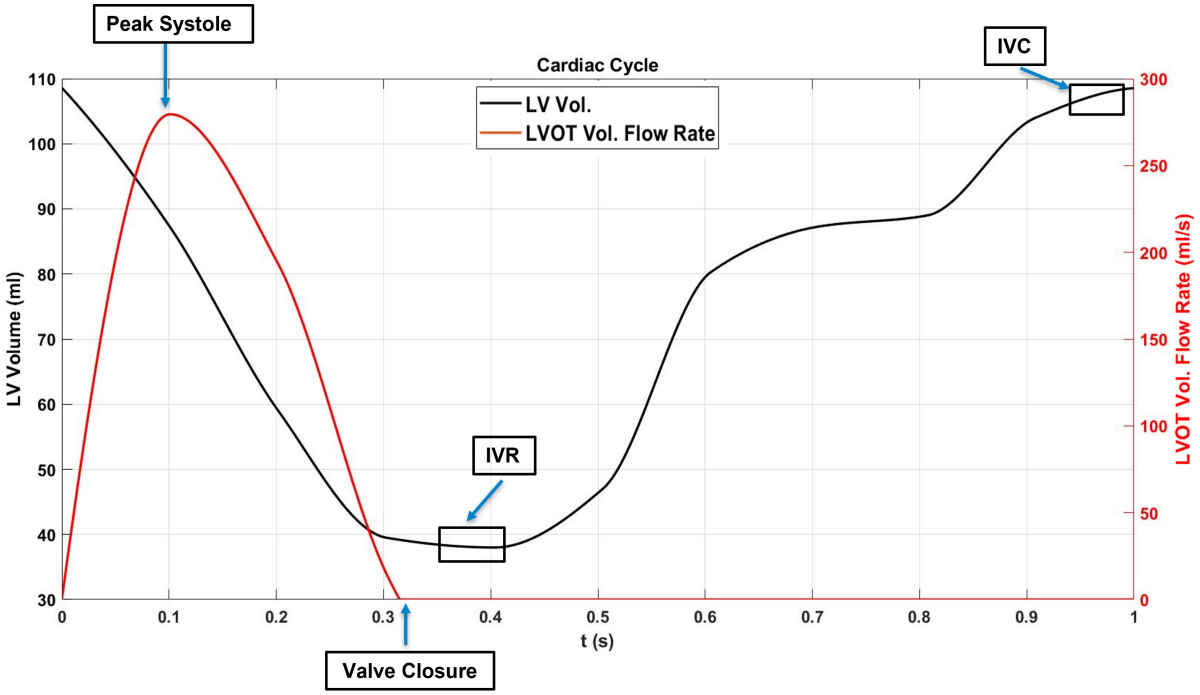


Figure 6.2: CT derived inflow boundary condition. The period of LV isovolumic relaxation and isovolumic contraction are marked by the black bloxes labelled IVR and IVC respectively.

Figure 6.2 shows the inflow boundary condition we derived from the CT images from one of the patients in this study. Firstly, we reconstructed the LV from the CT images over ten time points in the cardiac cycle then interpolated using a piece-wise cubic hermite interpolating polynomial (pchip) algorithm in MATLAB. The interpolated LV volume is shown by the black curve in the figure. In the IVC phase, the LV contracts without a change in the volume which raises its pressure above aortic pressure. The negative change in the black curve means that the LV is ejecting the blood through the LVOT to the aorta. This happens until the IVR phase where the LV pressure falls below aortic, the aortic valve closes and the LV relaxes. Taking the first derivative of the black curve from the end of the IVC phase to the beginning of the IVR phase should yield the volume flow rate Q into the LVOT shown by the red curve. To convert Q at the inflow to velocity, the value of Q was divided by the area of the inflow at each time point. The inflow is assumed to be zero during diastole as the aortic valve is closed

during that time and the flow through the mitral valve into the LV begins; hence, the rise in LV volume during diastole. It is important to mention that this method will not work in the event of mitral regurgitation as the negative change in LV volume will not be solely due to ejection through the LVOT into the aorta.

For the outflow condition, we used a constant 0 Pa pressure boundary condition at the aortic outflow. Along with the inflow condition, this will provide a robust set of boundary conditions for the CFD solver; however, will not provide realistic absolute pressure measurements. Instead, pressure gradients resolved from the simulation will suffice to be passed on to the solid domain at the interface. In order to improve the outflow condition one would need invasive pressure measurements or use of Windkessel models. In Section 7.3.3 we explained in detail how this was unfeasible in this work and why the aforementioned boundary condition was used instead.

After prescribing the CFD boundary conditions, we only need one more input to apply for the structural solver to complete the FSI setup. This input is the material model. The material model is analogous to the fluid model used in terms of density and compressibility. The material model numerically describes how a structure will respond to applied loads and therefore deform. Material modelling remains one of the most difficult challenges in FSI simulations since it plays a huge role in the solution of the structural equations and hence affects the surrounding fluid domain.

In order to obtain a reliable material model for an FSI simulation, one must go through the process of material testing using a biaxial testing technique to see how a material will strain under specific stress conditions. In this thesis our aim is to model a normal aortic valve in our FSI simulations so obtaining such material testing results will be a challenge. Consequently, we chose to rely on an isotropic hyperelastic material model for the valve leaflets obtained from porcine valve testing data and a linear elastic material model for the aortic wall [61].

Since the FSI simulations were computationally expensive due to the strong coupling between the structural and fluid solvers in addition to the dense mesh used to resolve the geometry and the smaller time steps in the simulation to avoid stability issues, both FSI simulations were run for a total time of 0.45 s which is 45 % of the cardiac cycle for this patient. We believe this is

enough run time to yield results that are sufficient to show the differences between a stationary and an accelerating AVA.

6.2 Stationary AVA

6.2.1 Valve Opening & Closure

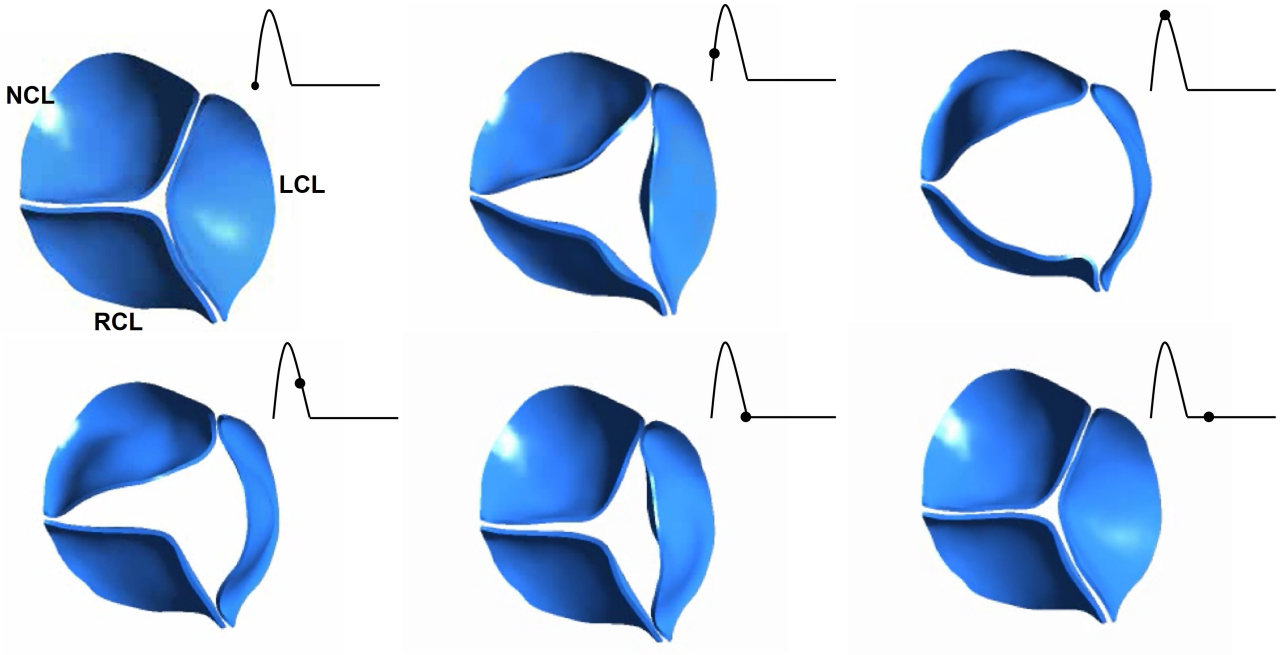


Figure 6.3: Temporal valvular motion for the stationary AVA. Black inset curves show the cardiac cycle in terms of the prescribed inflow. The black dot shows the current time frame for each panel. The positions of the left, right and non coronary valve leaflets are shown in the first panel.

Figure 6.3 shows the calculated temporal movement of the valve leaflets of the non-accelerating AVA at six distinct time points in the cardiac cycle. These are the beginning of the RR interval, the maximum flow acceleration phase, the peak systolic phase, the late systolic phase, the end systolic phase and the early diastolic phase. The valve which starts initially closed reaches a 28 % GOA at the time of peak acceleration of the inflow condition. The maximum acceleration of fluid entering through the LVOT plays a role in the rapid opening of the valve leaflets. At the time of peak systole, the valve has reached a maximum GOA of 93 %. During late systole, the valve leaflets begin the closure phase which is significantly slower than the opening phase.

At the end of systole, the right and non coronary valve leaflets are fully closed whereas the left coronary leaflet is still lagging. Finally in early diastole at approximately 0.35 s the valve becomes fully closed.

It is crucial to state that we refer to a fully closed valve in this analysis as a valve with a small gap of 500 μm between the leaflets as shown in the last panel of Figure 6.3. This is to circumvent the problem of a split domain in the CFD solver. Fully closing the valve with no gap will result in degraded mesh elements between the valve leaflets and the domain upstream and downstream of the valve will be split leading to divergence in the solution. Hence, we used a gap of 500 μm enough to accommodate at least one mesh element of high quality between the valve leaflets to avoid divergence of the solution.

In the previous analysis in Chapter 5, we observed that higher velocity at the inflow with a small GOA will result in higher loads on the valve leaflets. As a result, rapid valve opening is beneficial in decreasing the load on the valve leaflets during the systolic phase of the cardiac cycle where the blood flow is accelerating. On the other hand, slower closure serves to decrease the load on the valve leaflets during the closure phase.

To put this in context, the non-dimensional rate of valve opening or closure ξ/β was $+1.5$ during the opening phase and -1.35 during the closing phase. This suggests that the rate of opening of the valve is 10 % faster than the rate of closure. We believe that this correlates to the temporal behaviour of the fluid surrounding the valve. During the maximum acceleration phase succeeding the beginning of the RR interval, the leaflets of the valve are initially convex to the rapid inflow. In other words, the rapid inflow is almost normal to the surfaces of the leaflets thus causing rapid opening. When the valve leaflets change shape during closure to become concave to the flow upstream, this may cause a delay in closure combined with the decelerating flow surrounding the aortic valve.

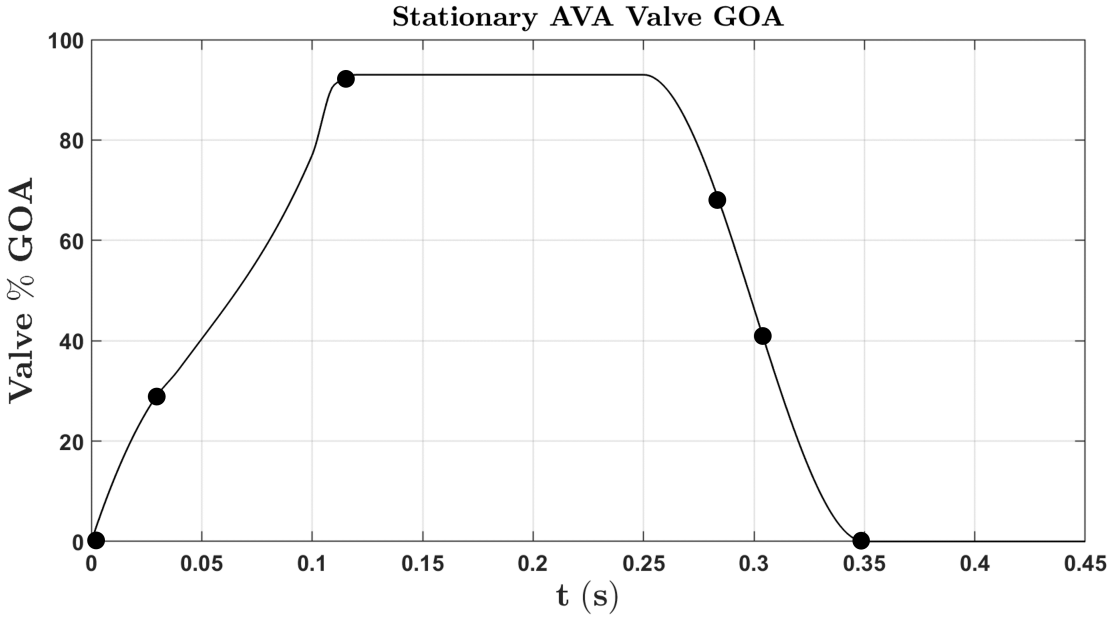


Figure 6.4: Temporal changes in the stationary AVA valve GOA. The black circles show the key time points used in Figure 6.3. Note there is a change in valve opening rate during early systole.

Figure 6.4 shows the temporal changes in GOA for the valve of the stationary AVA. The time to fully open is at $t = 0.11\ s$ while closure is at $t = 0.37\ s$. This figure confirms that the rate of opening is 10 % faster than the rate of closure. It also shows that the valve stays open over a time period during systole which was seen coinciding with a time where the valve leaflets were fluttering while open.

It is also important to note that the rate of opening during early systole changes at a time coinciding with the time of change in the concavity of the valve leaflets with respect to the inflow. In other words, the valve initially opening slows down then proceeds with a faster rate of opening. This local retardation in speed is when the leaflets change concavity. This may be seen particularly in Figure 6.3 in the maximum acceleration phase on the left coronary leaflet.

6.2.2 Vortex Coherent Structures

In order to get a better grasp of the flow field surrounding the valve leaflets, we started by looking for a method to visualise the vortex coherent structures in the AVA. Finding a unanimously accepted definition of a vortex is a very controversial topic in the field of fluid dynamics

and it is much more complicated than rotating flow fields [62]. Therefore, there is a pressing need for a mathematical technique to be able to identify regions of vortices. This is because vortices may yield crucial information about the pressure or velocity of a flow field [62].

Vortex coherent structures in a flow field are imaginary structures in areas of convected local pressure minima around which the flow would be swirling [62]. Jeong and Hussain presented a mathematical threshold method which is very simple and inclusive to detect vortex coherent structures in a flow field. Since we are looking for areas of pressure minima in the flow field, as with any mathematical function we would need the second derivative of the pressure field.

$$a_{i,j} = -\frac{1}{\rho}p_{,ij} + \mu u_{i,jkk,} \tag{6.1}$$

Equation 6.1 which is simply the first derivative of the Navier Stokes equations (comma notation denotes a tensor derivative) is the basis behind the method developed by Jeong and Hussain [62]. Taking the second derivative (the Hessian matrix) of the pressure field may be a complicated task so calculating the gradient of acceleration on the left hand side would be a much easier task since the acceleration gradient and strain matrices are much simpler to deal with [62]. This will yield three eigenvalues and since the second derivative of pressure is negative, two negative eigenvalues of the acceleration gradient will yield a vortex coherent structure with local pressure minima [62]. The lambda-2 (λ_2) method due to the two negative eigenvalues is available in most CFD post processing softwares and only requires a simple user input to detect the vortex coherent structures.

Figure 6.5 shows the vortex coherent structures in the AVA detected using the λ_2 method proposed by Jeong and Hussain. In the maxmium acceleration phase where the valve is at approximately 28 % GOA, a thin connected region having a triangular shape is formed. The reason it is triangular is due to the fact that the flow just started separating at the free edges of the valve leaflets forming very weak rotating regions connected by the triangular coherent structure. It is worthy to note that the triangular coherent structure is almost identical in shape to the open area of the valve leaflets.

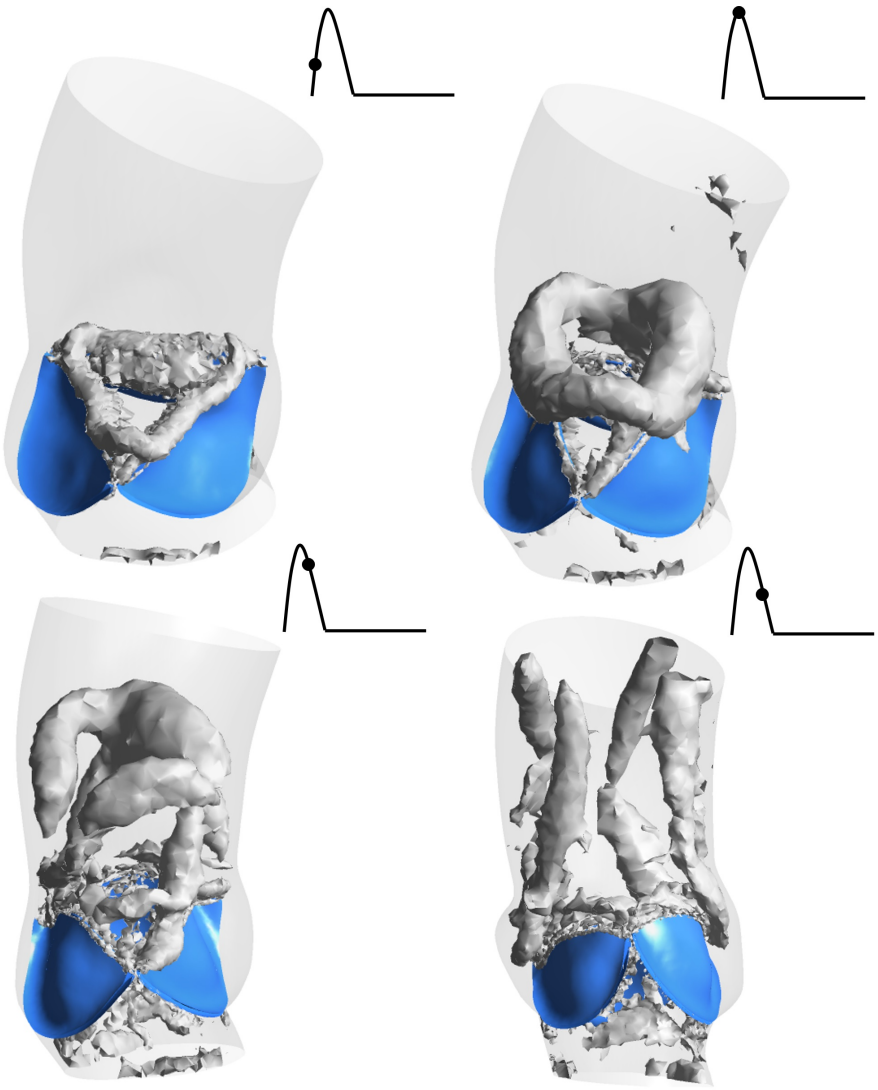


Figure 6.5: Vortex coherent structures in the AVA. Black inset curves show the cardiac cycle in terms of the prescribed inflow. The black dot shows the current time frame for each panel.

When the flow reaches maximum ejection, the triangular structure changes shape into a ring which has moved downstream due to convection. It is also important to note that the ring has three peaks coinciding with the commissures of the AVA while it is thicker along the free edges of the leaflets. This gives an idea that the vortices in the aortic sinuses have begun to form.

In the late systolic phases shown in the two bottom panels in the figure, the ring changed shape to a horse shoe shape followed by four broken vortex tubes. This is an important result as it implies the possible presence of helical flow in the ascending aorta. Helical flow has always been linked to aortic arch curvature as explained in the literature review; however, our results suggest a strong correlation between the dynamic behaviour of the valve and the vortex ring

which forms around it which evolves into a dual rotating helix in the late systolic phases of the cardiac cycle.

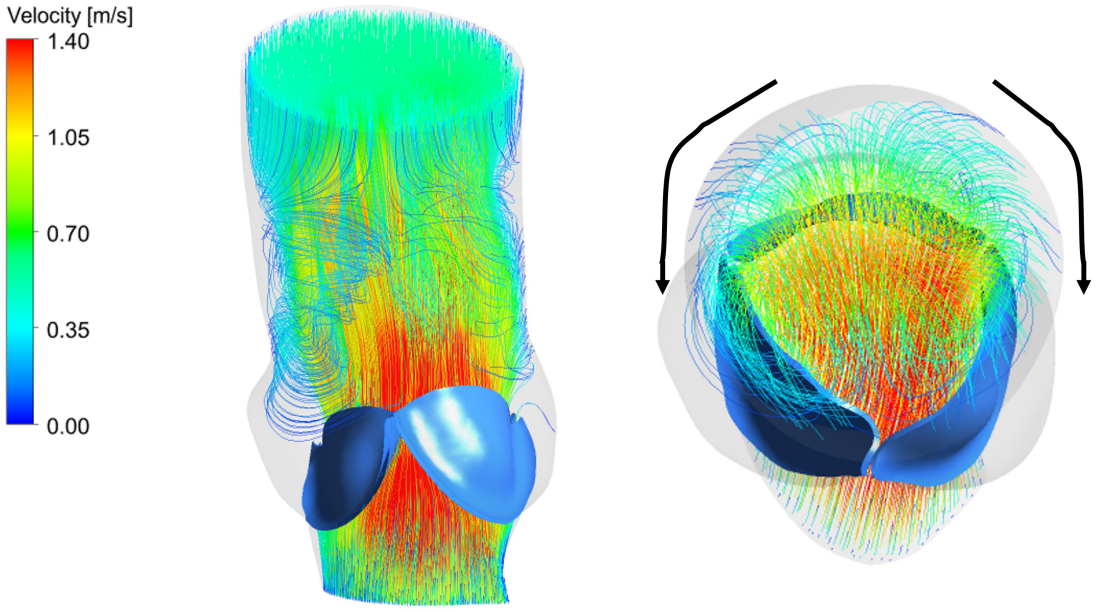


Figure 6.6: Velocity streamlines in the AVA at late systole. The arrows in the right panel show the direction of rotation from the anterior wall to the posterior wall of the aorta. The flow field ends up in a two dual rotating helices by conservation of mass.

Figure 6.6 shows the velocity streamlines in the AVA at late systole where the horse shoe structure changed shape to separate vortex tubes. Two dual rotating helices are clearly visible starting just downstream of the valve leaflets. This suggests that a dual rotating helix may be present not only in the aortic arch but starting from the leaflets of the valve. The right panel in the figure shows that the flow is moving from the anterior to the posterior wall of the aorta which can only happen due to higher pressures on the anterior side at this phase in the cardiac cycle. Although this finding disagrees with the findings from Kilner's work mentioned in Section 2.2.1, it is strongly supported by 4D flow data presented by Oechtering et al. showing similar flow patterns in young healthy volunteers [33],[37].

The aforementioned results from the FSI simulation of the non-accelerating AVA show that the coupling between the dynamic movement of the valve and the surrounding flow field is complex yet coordinated. We believe this coordination serves to redistribute or alleviate the large loads that could be incurred by the valve leaflets in the AVA. Hence, it is important at this stage to monitor the effects if any of an accelerating AVA on blood flow and valve loading.

6.3 Accelerating AVA

In order to study the effect of the acceleration of the AVA on blood flow, we used the analysis of the kinematics of the AVA explained in Chapter 4. We deduced the acceleration of the same patient used in this FSI analysis by the Fourier method. Since the data was only sampled at a frequency of 10 hz, we used the pchip algorithm in MATLAB.

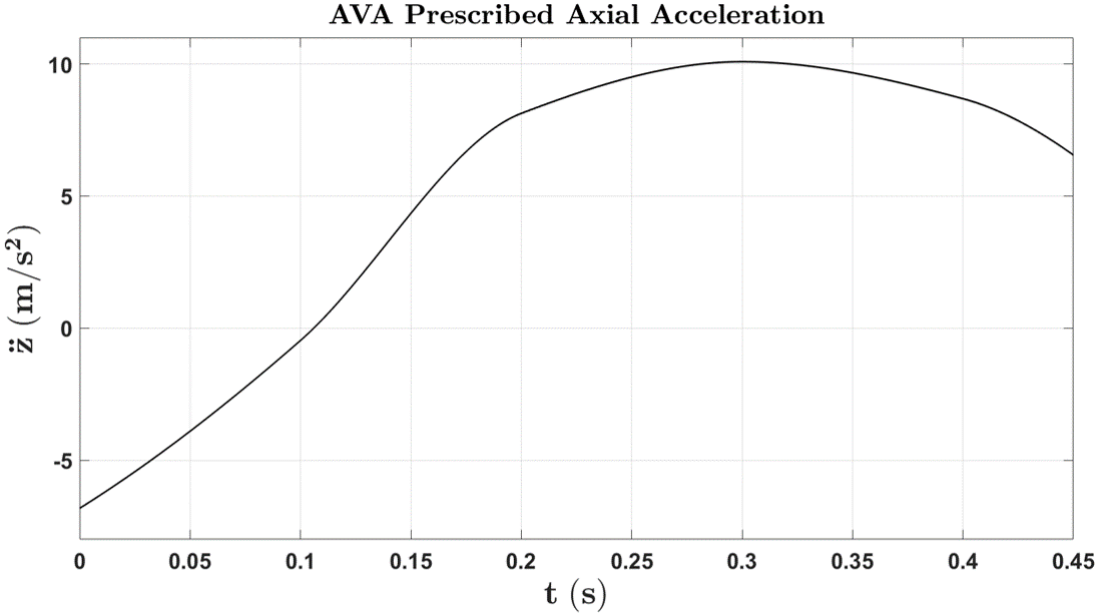


Figure 6.7: Prescribed AVA acceleration during systole as a boundary condition. This was interpolated using the pchip algorithm in MATLAB. The maximum acceleration around the time of valve closure is between $8 - 10\, m/s^2$.

Figure 6.7 shows the acceleration boundary condition after interpolation. This prescribed axial acceleration will enable the FSI process in the computation to include the movement of the AVA along its axis in addition to the deformable components of the AVA.

6.3.1 Valve Opening & Closure

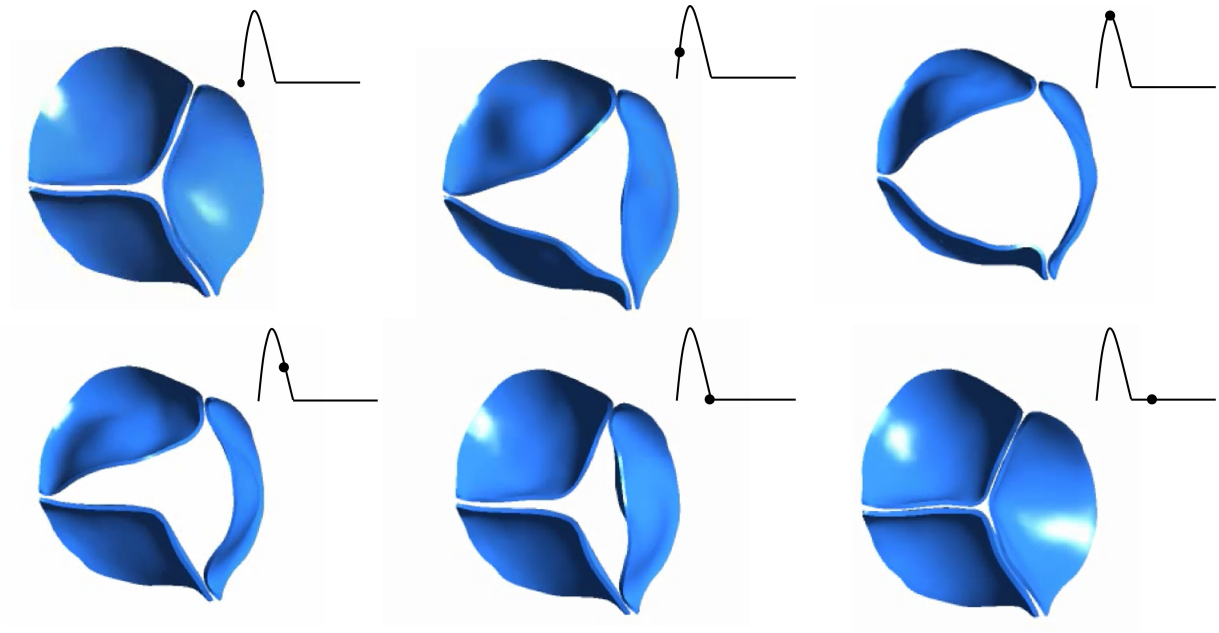


Figure 6.8: Temporal valvular motion for the accelerating AVA. Black inset curves show the cardiac cycle in terms of the prescribed inflow. The black dot shows the current time frame for each panel.

Figure 6.8 shows the temporal movement of the valve leaflets of the accelerating AVA for the same time points shown in Figure 6.3. The resultant valve opening and closure behaviour showed only two major differences compared to the stationary AVA case. At the time of maximum flow acceleration, the GOA was approximately 1.1 times the GOA at the same time point for the stationary AVA. This is because the maximum flow acceleration phase of the cardiac cycle coincides with the downward movement of the AVA towards the LV. This will cause an instantaneous rise in valve loading but will result in faster alleviation of the force on the valve as the valve achieves a larger GOA in a shorter time period.

When looking at the non-dimensional parameter ξ/β which represents the rate of valve opening and closure, the accelerating AVA valve reached a value of ξ/β equal to +1.65 during opening which is 1.1 times the value of the stationary AVA valve. This is because the opening of the accelerating AVA valve is 11 ms faster than the stationary AVA valve. In addition to this, the average leaflet velocity in the lateral directions of opening for the stationary AVA valve is 1 m/s compared to 1.3 m/s for the accelerating AVA valve. In summary, the accelerating AVA valve which is moving towards the inflow upstream causes a faster leaflet velocity and a

faster valve rate of opening. Although this movement of the AVA towards the LV may cause an instantaneous rise in the force on the valve initially, it will yield a faster reduction in the force on the valve throughout the opening phase due to the faster rate of opening.

Although the closing behaviour of the valve was similar for both the stationary and accelerating AVA, the second main difference was around the time of valve closure. The left coronary leaflet was still lagging in the accelerating AVA during closure; however, the mode shape of the closed valve showed a tighter coaptation and slight twist between the valve leaflets. ξ/β was slightly slower for the accelerating AVA valve compared to the stationary AVA valve with a value of -1.25 because the AVA stops briefly after reaching the maximum displacement towards the LV which slightly delays valve closure. The sudden acceleration away from the LV which changed the shape of the valve leaflets in the closed configuration means that there must be a difference in the load on the valve during closure due to the sudden positive acceleration.

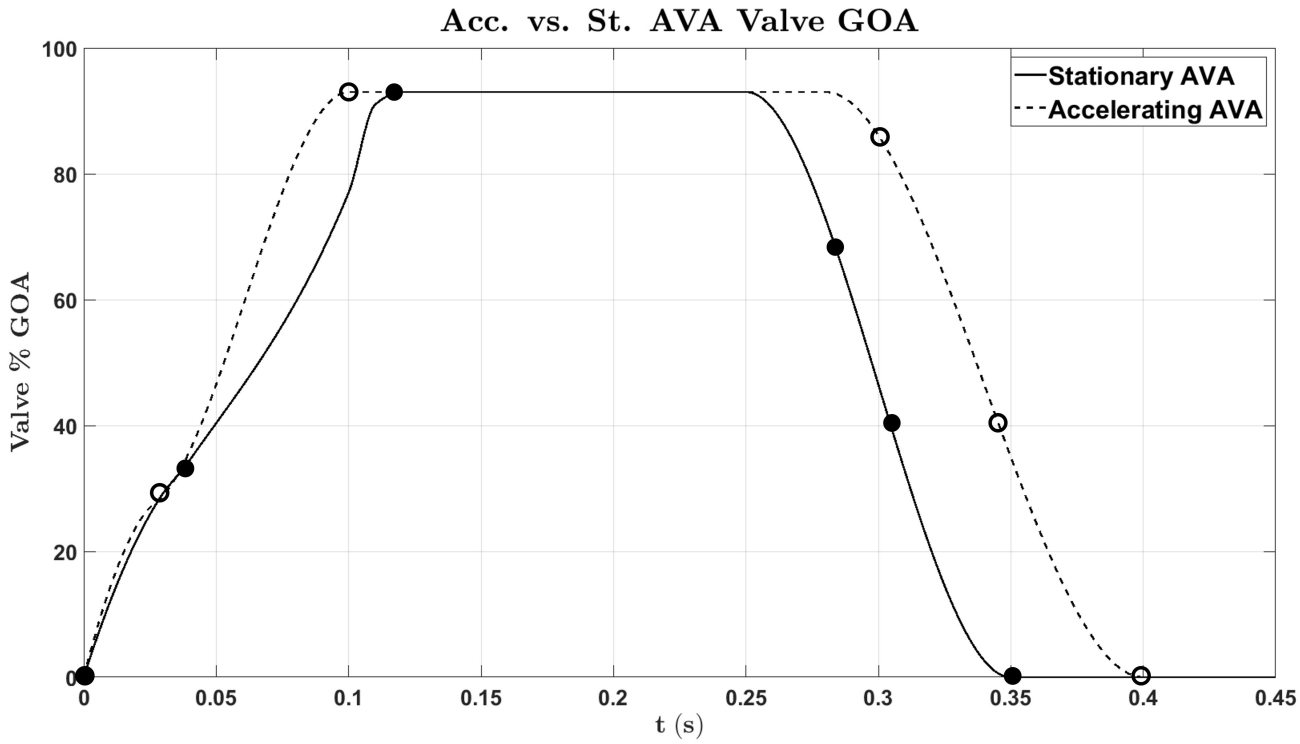


Figure 6.9: Temporal changes in the accelerating vs. stationary AVA valve GOA. The empty circles show the key time points used in Figure 6.8 and the solid circles show the time points used in Figure 6.3. A change in valve opening rate during early systole similar to that in the stationary AVA case is present. The main differences are a faster rate of opening and a slower rate of closure for the accelerating AVA valve.

Figure 6.9 shows the temporal changes in GOA for the valve of the accelerating and stationary

AVA's. For the accelerating AVA, the rate of opening was 30 % faster than the rate of closure which is a larger difference compared to that of the valve of the stationary AVA (10 %). Similar change in the rate of opening during systole was also observed which is due to the change in concavity of the leaflets; however, over a slightly shorter time period compared to the stationary AVA case. This suggests that the downward movement of the AVA during systole resulted in faster opening of the valve, sustained opening for a longer time period and slower rate of closure. The sudden positive acceleration of the AVA along its axis did not affect the rate of closure as it happened when the valve was fully closed.

6.3.2 Axial Movement of The AVA

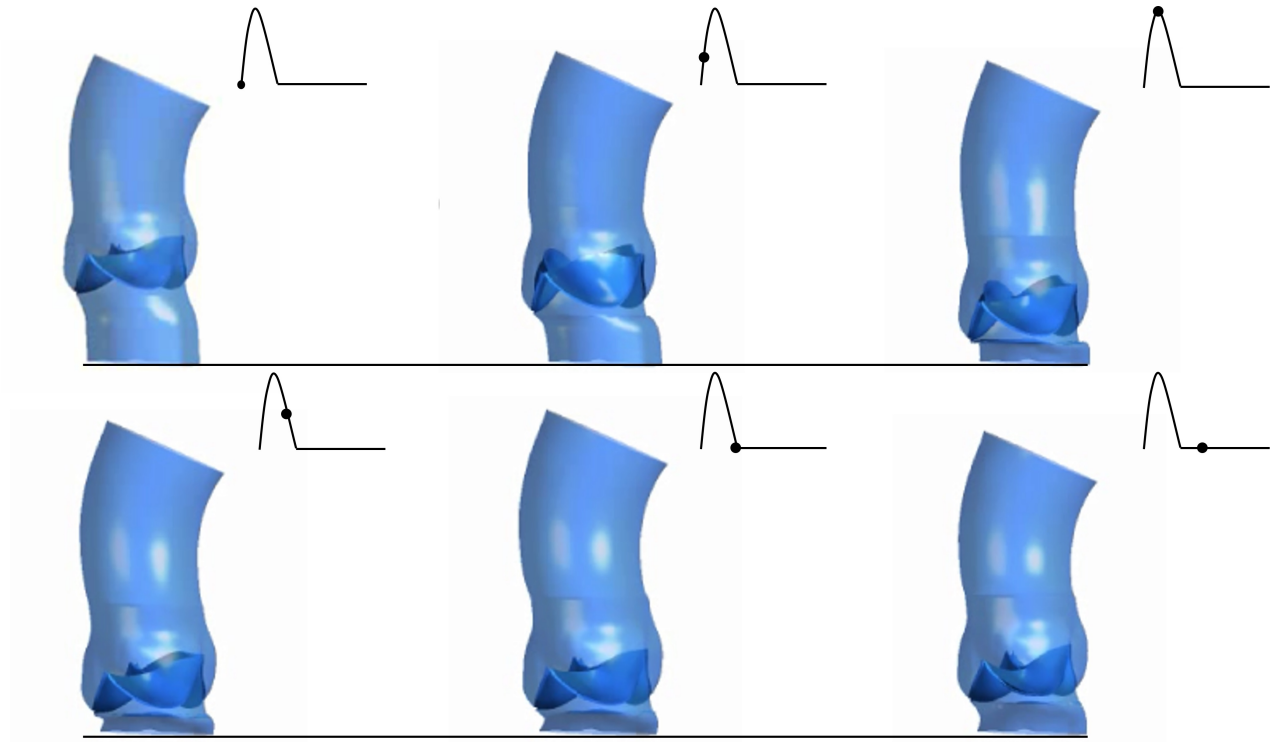


Figure 6.10: Temporal axial movement of the AVA. The reference position of the LVOT inflow is shown by the black lines. Black inset curves show the cardiac cycle in terms of the prescribed inflow. The black dot shows the current time frame for each panel.

Figure 6.10 shows the temporal position of the AVA along its axis at the same times defined in the previous sections. The initial downward movement of the AVA along its axis at the maximum flow acceleration phase caused a faster rate of valve opening. The time difference of 11 ms between the accelerating AVA valve and stationary AVA valve during opening manifests

as a rate of opening that is 30 % faster for the accelerating AVA valve. Although this is a substantial difference in the rate of opening, the velocity field showed no changes since there was almost no sudden acceleration of the AVA as discussed in Chapter 4 along its axis during systole. In other words, the AVA did move towards the LV during systole which altered the rate of valve opening; however, the movement is at a constant speed which in turn does not affect the flow field in the vicinity of the AVA.

It is also visible that the AVA lingers at its maximum downward displacement from the time of late systole until end systole. This retardation in the movement of the AVA may have delayed the closure of the valve leaflets by a very small time increment. When the AVA suddenly accelerates in the opposite direction away from the LV, it covers a distance of approximately 2 mm in 20 ms as shown in the early diastolic phase in the figure. This caused a visible change in the shape of the closed leaflets and may have an implication on the force on the valve.

It is worth noting that some crumpling of the LVOT section may be seen at the peak ejection panel (top right) of Figure 6.10. Although this may seem to be a motion artefact, it is magnified due to the angle of visualisation in the figure used to demonstrate the axial motion of the AVA. It would have been possible to avoid such crumpling had an artificial LVOT extension been used (a common practice in CFD simulations); however, for the purpose of this simulation this would have introduced uncertainties. This is because the flow at the LVOT inlet was known a priori and is never fully developed and the axial motion implemented in the AVA section is specifically no more than 20 mm as used in this simulation.

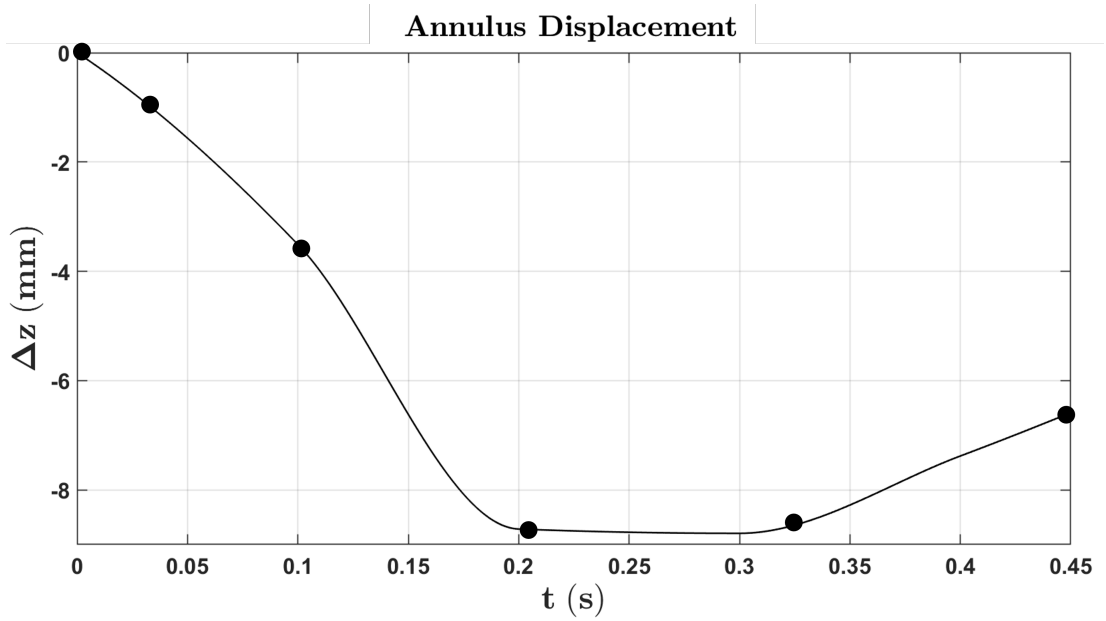


Figure 6.11: Temporal axial movement of annulus of the AVA. The displacement is calculated from the difference between the current position and initial position of the annulus. The black circles indicate the six chosen time points from Figure 6.10.

Figure 6.11 shows the displacement of the annulus of the AVA. At each time point the annulus' initial position was subtracted from its current position to give the displacement. The figure shows strong agreement with the observations from Figure 6.10. The annulus initially moves towards the LVOT inflow at a constant rate until the time of peak systole at $t = 0.1\ s$ where the movement accelerates until the time of late systole at approximately $t = 0.22\ s$. The annulus then exhibits no motion until the end of systole at $t = 0.33\ s$ where it suddenly accelerates upwards a distance of approximately 2 mm until the end of the computation run time.

This sudden acceleration of the AVA represented by the movement of the annulus will cause a sudden drop in the force on the valve as a reaction and is the reason behind the different mode shape of the closed valve in the accelerating AVA case.

6.4 Valve Force Response

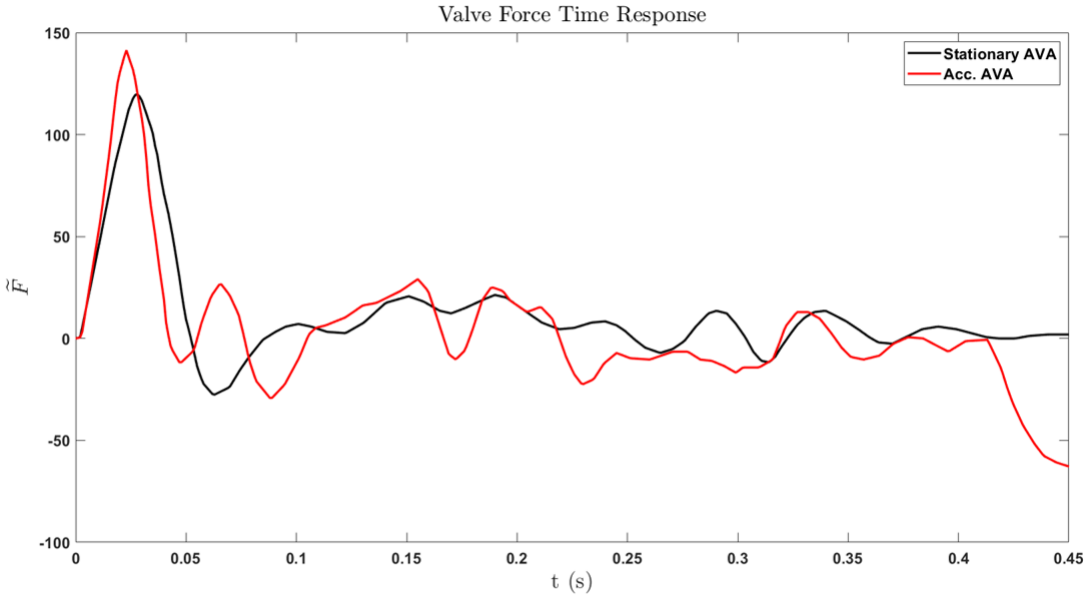


Figure 6.12: Valve force time response for the stationary and accelerating AVA's.

Figure 6.12 shows the time response of the non-dimensional force on the valve wetted area which is analogous to the force on the orifice discussed in Chapter 5. The wavy features in both responses in the above figure are due to flow detachment from the valve leaflets during opening and closure. The time response of the force on the valve shows similarities between the stationary and the accelerating AVA; however, with two main differences that were observed in the temporal movement of the valve leaflets.

The first difference is at the beginning of the cardiac cycle. After 0.02 s, the accelerating AVA has already moved downwards towards the LV which increases the relative velocity through the valve orifice. As a result, a sudden peak value of $\widetilde{F} = 147$ is reached but quickly falls to near zero due to the change in concavity of the valve leaflets with respect to the inflow. This change in concavity is due to the valve opening which reduces the force it incurs. On the other hand, the stationary AVA reaches a peak value of $\widetilde{F} = 123$ which falls to near zero with a delay of 11 ms compared to the accelerating AVA. Because the stationary AVA has a slower rate of opening compared to the accelerating AVA, it takes more time for the peak force on the valve to fall to near zero. The greater the valve GOA, the lower the value of $\widetilde{F}$.

The valve force fluctuates around zero for both the stationary and accelerating AVA for most of

the simulation up until the time of valve closure at 0.42 s. The accelerating AVA which suddenly accelerates upwards shows a sudden drop in the value of $\widetilde{F}$ equal to -60 or approximately -0.6 N. We have seen in Chapter 5 that a sudden movement of the orifice away from the inflow produces a sudden drop in $\widetilde{F}$ as a reaction to the sudden movement along the positive direction of the axis. When this happens, the positive movement of the orifice causes a change in direction of the retrograde flow adjacent to it.

The absence of this feature from the time response of $\widetilde{F}$ of the stationary AVA is important because this value of force along with the valve wetted area of approximately 0.0013 m^2 result in a pressure incurred by the valve of 3.5 $mmHg$. This pressure could be related to the pressure rise in the dicrotic notch transmitted by a wave due to the acceleration of the AVA. The mechanism behind this is a result of the movement of the AVA along its axis with the valve closed creating a boundary condition for a propagating wave along the aorta.

From Figures 6.3 and 6.8 there is a difference in the mode shape of the closed valve between the stationary and accelerating AVA. The valve of the accelerating AVA which is more coapted and shows a slight twist is affected by the acceleration of the AVA away from the inflow at the time of valve closure and in turn shows a different mode shape than the valve of the stationary AVA.

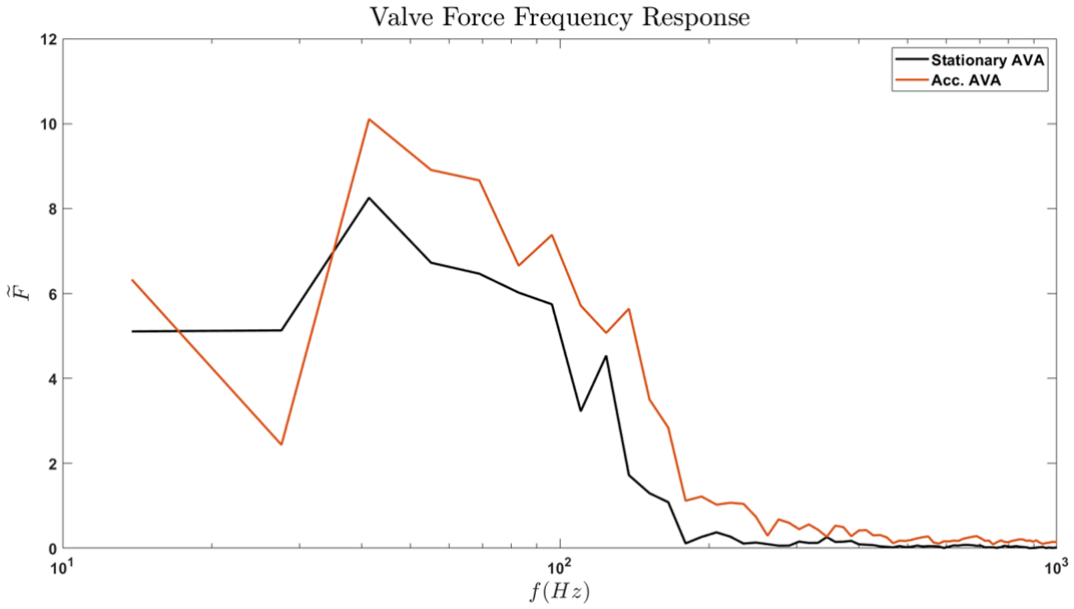


Figure 6.13: Valve force frequency response for the stationary and accelerating AVA's.

Figure 6.13 which shows the frequency response of $\widetilde{F}$ supports the analysis of the main difference between the stationary and accelerating AVA's. Since the acceleration of the AVA at the time of valve closure happens across a time interval $\Delta t = 25\ ms$, the dominant shedding frequency of 40 hz can be seen in the frequency response of the valve force of the accelerating AVA. It is also visible that the shedding frequency is always higher for the $\widetilde{F}$ of the accelerating AVA in the frequency range of $40 - 110\ hz$ which can only be due to the disturbance in the flow field caused by both the movement of the leaflets of the valve and the movement of the AVA along its axis. The valve force of the stationary AVA also shows a peak at the 40 hz frequency which is due to the peak of $\widetilde{F}$ at the beginning of the cycle which was reached over a period of approximately 25 ms.

In conclusion, including the acceleration of the AVA in FSI computations did not show major differences between a stationary and an accelerating AVA in terms of the flow field. However, the key differences were related to the rate of opening and closure of the valves especially the behaviour of the valve around the time of closure. This is due to the sudden acceleration of the AVA which may induce a boundary condition along with a closed valve that could cause the dicrotic notch rise in pressure.

Chapter 7

Conclusion

7.1 Summary of Investigation

The main purpose of this study was to investigate the effect of the acceleration of the aortic root on haemodynamics. We have seen from the literature that the aortic root is a highly dynamic organ thought to contain contractile elements. It is also thought by some to be actively dynamic. Regardless whether the aortic root is actively or passively dynamic, its motion across the cardiac cycle must have an impact on the surrounding blood flow. Due to the link between structure and function which was discussed in Section 2.1.3, we believe that considering the motion of the AVA in simulations related to cardiac surgery is necessary since it will have an effect on the surgical outcome. Valve sparing surgeries have shown positive postoperative outcomes due to basic consideration of the kinematics of the aortic root. We believe that augmenting simulation platforms to include the motion of the AVA will induce further improvement on surgical outcomes.

Prior to beginning the analysis in this study, we provided a new definition of the AVA as the definition of the aortic root may have been a source of confusion according to the abundant definitions mentioned in the literature. The AVA according to our definition is bounded by a section in the LVOT approximately 20 mm below the aortic annulus, the aortic sinuses of valsalva and the STJ in addition to the aortic valve.

The first step in the analysis was to study the kinematics of the AVA which will then be coupled with CFD in order to monitor their effect on blood flow. Four patients admitted to Aswan Heart Centre and then discharged for being normal underwent CT imaging. The CT images were used to reconstruct the anatomy of interest of the AVA and quantify its temporal motion using linear algebra techniques. The analysis revealed crucial observations mainly related to the local deformations of the AVA which causes a constant asymmetric change in shape across the cardiac cycle.

The dominant mode of motion we quantified was the axial acceleration of the AVA. The AVA in all patients reached an acceleration value of $8 - 10\ m/s^2$ in the direction away from the LV at the time of valve closure. Using this value of acceleration coupled with the water-hammer equation we predicted that this sudden acceleration at the time of valve closure may initiate a wave transmitted in the proximal aorta which correlates to the dicrotic notch pressure rise seen in arterial waveforms.

To investigate the effect of the acceleration of the AVA on haemodynamics, we started with an idealised model of the anatomy of the AVA as an intermediate step to decouple the complex physiological interactions between deformations and nature of the blood flow. Based on an idealised tube-orifice model, we deduced non-dimensional parameters to be used in our analysis and to economise the number of computations required to monitor the effect of acceleration of the AVA.

The first out of three different scenarios in this idealised problem was a stationary orifice with a steady inflow boundary condition. The results from this scenario gave us insights into the flow patterns downstream of an orifice immersed in fluid flow along with a relationship between the axial loading on the orifice and the Reynolds Number of flow through the orifice.

In the second scenario we studied the effect of a stationary orifice which was closing in a shutter-like mechanism. The two main non-dimensional parameters describing this problem were ξ which is a measure of the maximum rate of closure of the orifice and β which is a ratio between the maximum rate of closure and the time average rate of closure of the orifice.

The results showed a quasi-steady response of the axial force on the orifice where the quasi-steady value of force was dependent on the final GOA of the orifice. In this context quasi-steady means that the force response of the orifice started with varying values over time then reached a steady value. Moreover, the prominent effect was due to the parameter ξ/β which is the non-dimensional time average rate of closure of the orifice. We observed from the analysis of the second scenario that an orifice with a smaller GOA coupled with higher Reynolds Numbers at the inflow will incur higher axial loads. This is an important result because it highlights the benefit of rapid orifice opening and slow orifice closure to its structural endurance. This knowledge is transferable to the aortic valve since it is analogous to an orifice and many cardiac diseases are related to valvular malfunction.

In the final scenario we looked at the effect of an accelerating orifice with constant area coupled with a steady inflow. The acceleration of the orifice was prescribed as a displacement boundary condition in the CFD computations. The non-dimensional parameter of interest in this scenario was the Strouhal Number where the frequency of interest was that of the acceleration of the orifice. Starting with sinusoidal frequencies of 1 hz, 2 hz and 10 hz we observed that the peak axial load on the orifice increased with increasing frequency while the phase lag between the acceleration of the orifice and the flow field decreased. This is because an orifice accelerating at higher frequencies or with higher velocities compared to the inflow has the ability to overcome the inertia of the fluid adjacent to it by changing its direction.

In addition to this, studying an orifice accelerating with a subject specific waveform obtained from one of the patients showed that the dominant shedding frequency and negative force change occurred at the instant of peak positive acceleration at the time of valve closure. This suggests that when the orifice accelerates in the positive direction along its axis, there is a sudden negative change in its axial force as a reaction which will correspond to the initial condition of a pressure wave to be transmitted downstream.

The final step in this study was to analyse an accelerating physiological model of the AVA obtained from one of the patients. This was achieved by means of an FSI computation coupled with a moving wall boundary condition which to our knowledge is a novel technique in physio-

logical fluid dynamics. Using the CT images to derive realistic inflow conditions, we studied the difference between a stationary AVA and an accelerating AVA of the same patient. Although the flow field was similar in terms of flow patterns and velocities in both cases, the two main differences were related to the dynamic behaviour of the valve and the axial force response of the valve.

The accelerating AVA showed a faster valve opening and slower valve closure by 10 % compared to the stationary case. More importantly, the accelerating AVA showed a sudden negative change in force at the time of valve closure equal to $-0.6\ N$ which corresponds to a pressure of 3.5 $mmHg$. Comparing the frequency response of the axial force on the stationary and accelerating AVA's we saw that the stationary AVA exhibits no change in axial force during the time of valve closure unlike the accelerating AVA. The value of the axial force at that instant may correlate to the rise in pressure in the proximal aorta seen as the dicrotic notch due to wave transmission. This result suggests that the acceleration of the AVA during valve closure may be a key parameter in analysing aortic function.

7.1.1 Applications

The main outcomes in this thesis from studying the kinematics of the AVA to using an idealised parametric model and finally analysing a physiological model of the AVA led to a crucial hypothesis. Our hypothesis states that the sudden acceleration of the AVA away from the LV along its axis at the time of valve closure may initiate a boundary condition that transmits a pressure wave to the proximal aorta leading to the pressure rise seen as the dicrotic notch in arterial pressure waveforms. The rise in pressure is related to the acceleration of the AVA by the water hammer equation.

Working backwards, one may calculate the acceleration of the AVA and from that estimate the dicrotic notch pressure rise. This is important as the presence and magnitude of the dicrotic notch rise in pressure varies according to different cardiac diseases. This may lead to the use of the acceleration of the AVA as a non-invasive parameter to diagnose various cardiac diseases.

This is because the acceleration of the AVA deduced from the study of the kinematics may be easily obtained using non-invasive imaging techniques such as ultrasound.

Similar to our future aims, Reddy et al. demonstrated a strong correlation between LV contractility and the acceleration of flow through the aortic valve during systole in mice [63]. LV contractility is a key paramter in diagnosing LV disease and can only be obtained invasively where the derivative of the temporal LV pressure yields the contractility. They recommended based on their findings that the acceleration of flow during systole which can be deduced from non-invasive ultrasound imaging (Doppler) can be a diagnostic tool for LV malfunction [63]. The novelty in this technique is that instead of using an invasive technique to assess cardiac disease (LV contractility) a non-invasive technique deduced by simple Doppler measurements will be used.

7.2 Suggestions for Future Work

In order to enable us to present the acceleration of the AVA as a non-invasive diagnostic parameter we would first need to strengthen the hypothesis by showing a strong correlation between the acceleration and the dicrotic notch rise in pressure. To do this, we could further test the hypothesis using idealised computational models then use the new ultra fast ultrasound technique currently available for research purposes.

A study using an idealised computational model would involve setting up a controlled experiment using FSI with an intervention of approximately the same order of magnitude as we expect from the accelerating closed valve boundary condition that was presented in Chapter 4. The idealised model we would devise for this purpose would consist of an elastic tube fixed at both ends with a wall boundary condition at its origin. Applying external pressure on the surface of the tube at the closed end would induce a wavefront travelling through the elastic walls of the tube. This would enable us to assess the decoupled and simplified wave transmission phenomena before applying the same technique with an accelerating boundary condition. In the accelerating tube problem, a physiological *notchless* pressure wave would be applied as an outlet boundary condition. The hypothesis is that an accelerating orifice at closure would induce a notch in the fluid downstream that would correlate the acceleration boundary condition applied to the dicrotic notch rise in pressure.

As for the clincial trial relying on medical imaging, we would start by recruiting healthy volunteers following a normal probability distribution meaning that they would be of different gender, age and race. The sample size would depend on a statistical analysis before the study in order to quantify the number of subjects needed for statistical significance. The ultrasound can yield 2D temporal images in multiple views of the AVA which may be analysed using the developed code used in the analysis in Chapter 4 to calculate the acceleration of the AVA for each volunteer. Knowing the time period of valve closure for each patient we would be able to calculate values of the dicrotic notch rise in pressure using the water hammer equation.

Furthermore, the ultrasound would show the temporal changes in area of the proximal aorta

which may be correlated to pressure via a tube law equation. This would enable us to quantify the values of the dicrotic notch rise in pressure of each volunteer which may then be compared to our calculations using the water hammer equation. If a strong correlation is found meaning that the acceleration of the AVA could be the probable cause of the dicrotic notch rise in pressure, we could investigate a variety of cardiac diseases known to have indistinct or absent dicrotic notches. In the event of these diseases, if the acceleration of the AVA falls outside the range of values obtained from the healthy cohort, we could succeed in providing a non-invasive method to diagnose a wide range of heart disease. In addition to the benefit of being non-invasive, this method would be much faster and safer to the comfort of the patients and clinicians.

In this study, we would recruit a minimum of 50 volunteers as an initial cohort. This number would likely change throughout the study depending on the resultant statistics when calculating sensitivity and specificity. The same number of diseased patients should also be recruited if the hypothesis testing phase is successful. The metrics used to correlate the acceleration of the AVA calculated would involve a Bland-Altman plot comparing the dicrotic notch pressure calculated using the conventional ultrasound technique against the acceleration based dicrotic notch pressure from the water-hammer equation. In the following events of testing diseased cases, a more rigorous metric would then be used depending on the gold standard reference to be used at the time. For example, if the pressures in diseased patients would be measured invasively using a catheter then sensitivity and specificity may be calculated to quantify the efficacy of the acceleration based model.

7.3 Limitations

7.3.1 Chapter 4

Since the work in this thesis was focused on studying the impact of acceleration of the AVA on haemodynamics in the absence of cardiac disease, acquiring the data was a challenge. CT imaging was needed for this study in order to provide a means of 3D reconstruction for the anatomy of the AVA including the aortic valve which is not feasible using MRI. As a result, recruiting healthy patients for CT scans was not an option since it defies ethical guidelines; however, only four cases admitted to Aswan Heart Centre with chest pain and later discharged for being normal had CT imaging available during their diagnosis.

Some of the numerical data in Chapter 4 represented as temporal curves seems to contain noise. In order to quantify the noise in the data originating from the reconstructed CT images, one must analyse more than one temporal curve for the same data. This is not possible with CT imaging since the reconstructed images which are temporal over the cardiac cycle are chosen by the machine from many cardiac cycles. In other words, each reconstructed temporal phase is chosen as the phase with the best resolution from many heartbeats. In order to give some quantification of noise, an alternative approximation was used. Each temporal curve was analysed in terms of mean and standard deviation and the curve peaks and troughs were compared against the deduced values in order to check how many standard deviations are they away from the mean (Figure 4.10).

In the work of quantifying the acceleration of the AVA, only one of the four cases in this thesis was used. This is because obtaining higher frequency data around the time of valve closure for all cases was not possible. In the future it would be beneficial to collaborate with the radiology department in order to find cases with good quality CT scans and with mild cardiac disease that has no effect on the acceleration of the AVA so as to be able to obtain better statistics.

7.3.2 Chapter 5

The work in this chapter pivots around using an idealised geometrical model as a representation of the anatomy of the AVA. Three different scenarios were investigated using the moving wall method in CFD computations, i.e. steady orifice, closing orifice and an accelerating orifice. The aforementioned scenarios were coupled with a steady flow boundary condition at the domain inlet. A major limitation in this study is not repeating the scenarios coupled with a pulsatile flow boundary condition at the domain inlet. This was a challenge due to the limited computational resources and complex nature of the simulations. Instead we relied on our previous knowledge of pulsatile flow behaviour from Womersley flow and the fact that the full coupled scenario was carried out in Chapter 6.

Although Womersley flow presents the analytical solution for pulsatile flow in an infinitely rigid tube, we chose the length to diameter ratio of our idealised model to be 32 in order to approach the infinitely long tube model and to minimise errors due to domain truncation.

Another challenge was the need to run the CFD simulations in addition to the simulations in Chapter 6 for multiple cycles in order to overcome initial condition effects. Due to the expensive computations this was not feasible. In addition to this, initial condition effects are dominant when the flow conditions at the end of the first cycle are different from the domain initial conditions. For example, using Windkessel models as outlet boundary conditions requires multiple simulation cycles in order to allow the capacitance (compliance) component to charge and to allow the flow to reach the diastolic pressure values which are orders of magnitude higher than initial conditions. Based on previous experience and since we did not use boundary conditions that require multiple cycles, our simulations were run for only one cycle in order to save computational cost. While some fluctuations may be seen in the force response curves of the orifice, this is due to the use of a deforming mesh which has a normal occurrence in moving boundary problems.

7.3.3 Chapter 6

A major limitation in Chapter 6 and also in the computational work from Chapter 5 is the use of the force on the orifice as a parameter to correlate to the dicrotic notch rise in pressure. The hypothesis we presented in Chapter 4 relates the acceleration of the AVA at the time of valve of closure to the sudden rise in arterial pressure observed as the dicrotic notch. This hypothesis relies on the idea that the sudden acceleration of the closed valve of the AVA introduces a new boundary condition of a forward compression wave being transmitted downstream thus causing the rise in pressure of the decelerating fluid.

What would have been beneficial was if the correlation between the acceleration of the AVA and dicrotic notch was observed as a rise in the pressure of the fluid downstream. In order to achieve this, a physiological pressure boundary condition must be used along with a flexible wall for the artery or tube in the CFD model. Using a flexible (deformable) wall in the idealised model was not an option since we relied on the moving wall method rather than a full FSI simulation setting. Moreover, the material model to be used for the flexible wall needs to accurately capture the physics of deformation in order to show the correct wave transmission.

Although a flexible wall was used in the computational work in Chapter 6, we refrained from assessing the pressure of the fluid downstream due to uncertainties from the material model used. In addition to this, applying a physiological pressure boundary condition would have required either invasive pressure measurements available from the patient a priori or applying a Windkessel boundary condition relying on certain approximations. Invasive pressure measurements were not available from the patients in this thesis as they were discharged for being normal while Windkessel models impose a difficulty in convergence since they are a coupling between the 3D Navier-Stokes equations and 0D pressure flow rate equations derived from electrical circuit analogy. Taking into account the aforementioned factors in addition to the complexity of the FSI simulation carried out in Chapter 6, we used the force on the orifice as a parameter to test our hypothesis.

Appendix A

A.1 Chapter 4

Dominance of Rigid Translation in AVA Kinematics

In Chapter 4 we stated that after quantifying and decomposing the different modes of deformation of the AVA, we found that the rigid translation component was the dominant mode of deformation. This was the foundation of the hypothesis we introduced in this chapter and tested throughout the work of this thesis using computational techniques. Moreover, the rigid translational motion of the AVA showed a sudden acceleration in the axial direction away from the LV which we believe correlates to the dicrotic notch rise in pressure at the time of valve closure through the water-hammer effect.

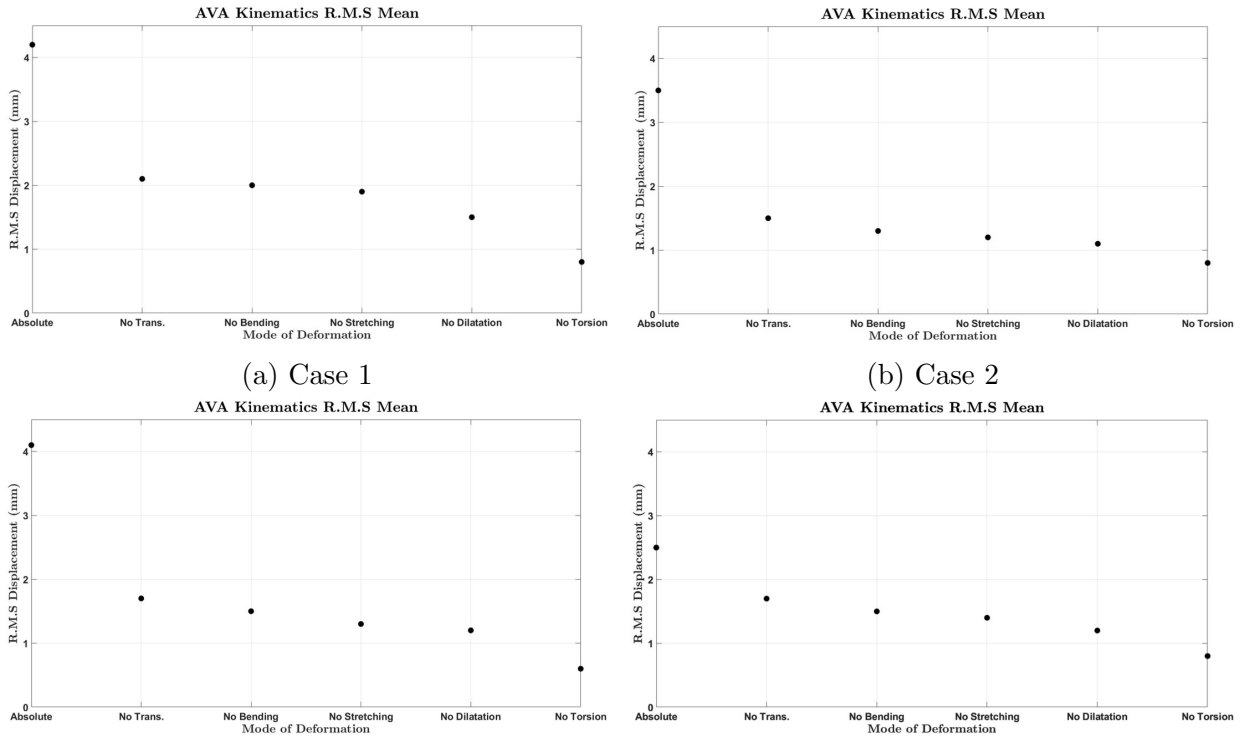
In order to assess the dominance of the rigid translation component of motion of the AVA in comparison to the other modes of deformation we used a simplified Root Mean Square (R.M.S) statistical approach. Equation 4.1 states that we represent the fiducial points of the AVA in a multidimensional matrix as follows:

$$[X] = X_{ijn}$$

In the above equation i (number of rows) is the index of the fiducial points ($i = 1-9$), j (number of columns) is the spatial coordinate of each point $[x, y, z]$ and n represents the temporal phases of the cardiac cycle ($n = 1 - 11$).

From that, a simple quantification of the R.M.S displacement of the AVA at each step of motion decomposition may be calculated using the following equation:

$$\Delta X_{RMS} = \sqrt{\frac{(\Delta X_{..n})^2}{9}}$$



(a) Case 1 (b) Case 2

(c) Case 3 (d) Case 4

Figure A.1: Quantification of the AVA modes of deformation by R.M.S mean. The R.M.S value after each mode of deformation is quantified.

Figure A.1 shows the resultant quantification of the R.M.S of every mode of deformation of the AVA for all cases. It can be seen that the highest R.M.S displacement is between the absolute movement of the AVA and the rigid translation after averaging. This result shows that the dominant mode of deformation for all cases was the rigid translation component which contains the acceleration of the AVA.

A.2 Chapter 5

A.2.1 Non-dimensional parameters derivation

Womersley Number α:

$$\Pi_3 \equiv \alpha = f(\rho, D, \mu, \omega)$$
$$\alpha = \rho^a D^b \mu^c \omega$$
$$\alpha = (ML^{-3})^a (L)^b (ML^{-1}T^{-1})^c (T^{-1})$$
$$\Rightarrow (M^0 L^0 T^0) = (ML^{-3})^a (L)^b (ML^{-1}T^{-1})^c (T^{-1})$$
$$\Rightarrow (M^0 L^0 T^0) = \left(M^{a+c} L^{-3a+b-c} T^{-c-1}\right)$$

$$a + c = 0$$
$$-3a + b - c = 0$$
$$-c - 1 = 0$$
$$\Rightarrow a = 1, b = 2, c = -1$$
$$\mapsto \Pi_3 \equiv \alpha = \frac{D^2 \rho \omega}{\mu}$$

Since α is a non-dimensional parameter it can be square rooted and multiplied by a factor of $1/2$ in order to represent it in the conventional form of Womersley Number. Hence, α becomes:

$$\alpha = \frac{D}{2}\sqrt{\frac{\omega\rho}{\mu}}$$

Rate of orifice opening and closure ξ:

$$\Pi_4 \equiv \xi = f(\rho, D, Q, \dot{A}_{max})$$
$$\xi = \rho^a D^b Q^c \dot{A}_{max}$$
$$\xi = (ML^{-3})^a (L)^b (L^{-3}T^{-1})^c (L^2T^{-1})$$
$$\Rightarrow (M^0L^0T^0) = (ML^{-3})^a (L)^b (L^{-3}T^{-1})^c (L^2T^{-1})$$
$$\Rightarrow (M^0L^0T^0) = \left(M^a L^{-3a+b+3c+2} T^{-c-1}\right)$$

$$a = 0$$
$$-3a + b + 3c + 2 = 0$$
$$-c - 1 = 0$$
$$\Rightarrow a = 0, b = 1, c = -1$$
$$\mapsto \Pi_4 \equiv \xi = \frac{\dot{A}_{max} D}{Q}$$

Strouhal Number St:

$$\Pi_6 \equiv St = f(\rho, D, Q, \omega_a)$$
$$St = \rho^a D^b Q^c \omega_a$$
$$St = (ML^{-3})^a (L)^b (L^3T^{-1})^c (T^{-1})$$
$$\Rightarrow (M^0L^0T^0) = (ML^{-3})^a (L)^b (L^{-3}T^{-1})^c (T^{-1})$$
$$\Rightarrow (M^0L^0T^0) = \left(M^a L^{-3a+b+3} T^{-c-1}\right)$$

$$a = 0$$

$$-3a + b + 3 = 0$$

$$-c - 1 = 0$$

$$\Rightarrow a = 0, b = 3, c = -1$$

$$\mapsto \Pi_6 \equiv St = \frac{\omega_a D^3}{Q}$$

A.2.2 Simulation parameters

The simulations carried out in Chapter 5 and 6 related in the sense that they involve dynamic meshes. We present the basic simulation parameters used in tabulated form in Section A.2.2 and A.3.1. Other than the simulation specific parameters in the tables, the following similar parameters were used:

- Spatial Discretisation Scheme: Least Squares Cell Based scheme with a quadratic interpolation for the staggered grid
- Temporal Discretisation Scheme: Second Order Implicit Time Scheme
- Residual Errors cut-off for the continuity equation: 1×10^{-3}
- Residual Errors cut-off for the momentum equations: 1×10^{-6}

Blood Viscosity μ	0.0034 $Pa \cdot s$
Blood Density ρ	1060 kg/m^3
Time Step ΔT	0.001 s

A.2.3 Modelling Blood as a Newtonian Fluid

Blood is known to be a Non-Newtonian fluid, meaning whose viscosity varies with shear strain rate. Specifically, blood is a shear thinning fluid where its viscosity is inversely proportional to the shear strain rate [55].

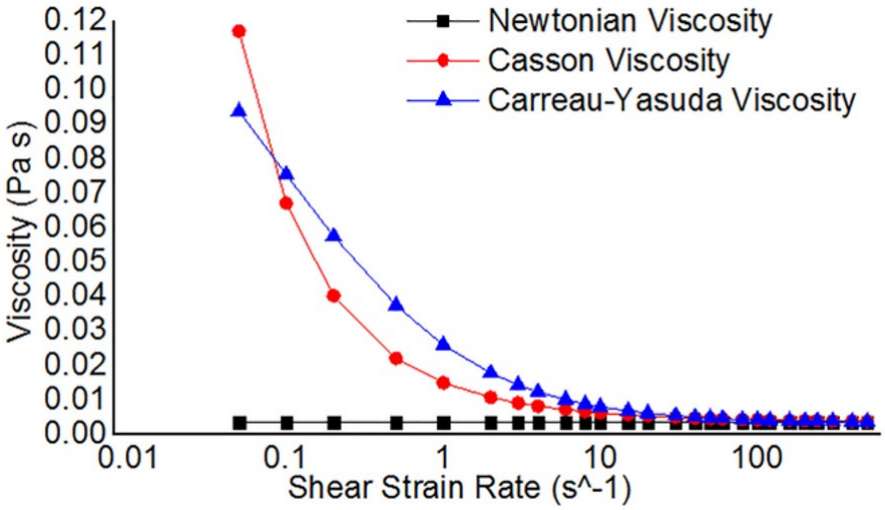


Figure A.2: Relationship between viscosity and shear strain rate. A Newtonian approximation shows a constant value of viscosity (black line). (Reproduced from [55])

Figure A.2 shows the difference between modelling blood as a Newtonian versus a Non-Newtonian fluid. For a Newtonian fluid, the blood is given a constant viscosity value that does not vary with shear strain rate. On the other hand, blood may be modelled as Non-Newtonian using an equation describing the variation of viscosity with shear strain rate. The most commonly used equations for a Non-Newtonian blood models are shown in the figure, i.e. the Casson Viscosity model and the Carreau-Yasuda model [55].

It can be seen from the figure that both Non-Newtonian blood models show an inverse proportionality between viscosity and shear strain rate while asymptotically reaching the constant value for Newtonian blood viscosity for a considerable range of shear strain rate values. From the above figure, it is noticeable that in regions of lower shear strain rate (low WSS) the difference between Newtonian and Non-Newtonian fluids would be amplified.

In a study by Liu et al., they investigated the use of the aforementioned blood viscosity models in three subject specific ICAS. Figure A.3 shows the CFD results for the three ICAS models using the Newtonian fluid assumption and the percentage differences in the pressure field between the Newtonian assumption versus the other two Non-Newtonian assumptions. The percentage difference in the pressure field was between $0 - 0.25$ % on average especially in the first model where the stenosis was clinically non-significant [55].

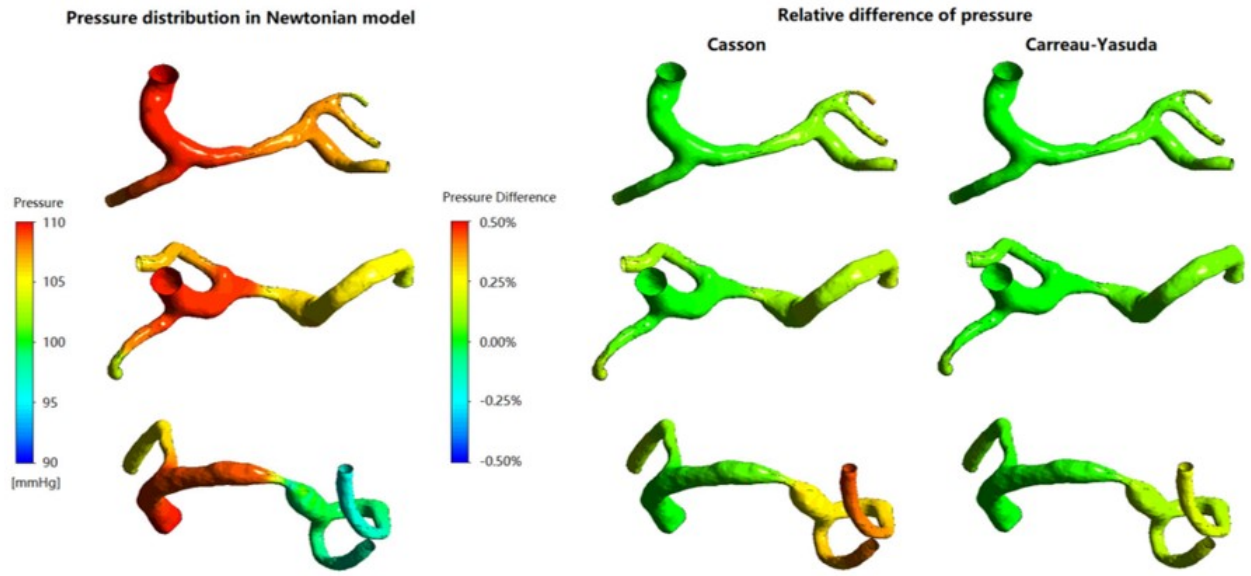


Figure A.3: CFD testing of Newtonian vs. Non-Newtonian blood models in subject specific Intracranial Atherosclerotic Stenosis (ICAS). Left panel shows the pressure field using a Newtonian fluid assumption. Right panel shows the percentage difference in the pressure field between the other two Non-Newtonian models with the Newtonian assumption. (Reproduced from [55])

Although they state that the in areas of low fluid WSS the percentage difference in values was as high as 7 %, this was mainly in the cases with clinically significant stenosis.

Another study by Vinoth et al. [64] investigated the effect of the Newtonian versus the Non-Newtonian assumption in a healthy aorta under subject-specific pulsatile conditions. Their conclusion differs from the conclusion from the study by Liu et al. where they stated that the use of Non-Newtonian models is necessary since it gives higher values of WSS especially in regions of arterial narrowing like the descending aorta [64]. In addition to this, they observed that in regions of low WSS (lower shear strain rate) the differences in WSS could be higher than 10% as predicted by the relationship shown in Figure A.2. In other words, blood flow under the Newtonian assumption would always give unfavourable results when WSS as a parameter is used in assessing the function of the aorta [64]. On the other hand, they discovered that the difference in the pressure field between a Newtonian and Non-Newtonian model showed differences as low as 100 Pa at peak systole which is less than 1 mmHg [64].

As a result of that analysis and in order to avoid computational expense by solving an extra equation for a Non-Newtonian blood model, we used the Newtonian viscosity assumption

throughout the work in this thesis. We also believe this is justified by the fact that our simulations were focused on an idealised model in the work in Chapter 5 and a reconstruction of a healthy AVA in Chapter 6. In addition to this, WSS as a parameter was not a focus in our quantitative analysis during testing the hypothesis we presented. However, the force on the orifice/valve which was continuously used as a parameter relies on the pressure field which shows negligible differences between using a Newtonian versus a Non-Newtonian model [55], [64].

A.2.4 Grid Dependence

In order to conserve computational cost, a mesh or grid dependence study was carried out to deduce the number of mesh elements at which the CFD results converge to a value independent of refining the mesh further. The idealised tube orifice model was discretised into 0.8, 1, 2 and 2.5 million elements. As explained in Section 5.4, a laminar flow solver was used to avoid uncertainties using turbulence models. However, refining the mesh while using a laminar solver will always result in resolving smaller scales of flow instabilities. As a result, we quantified $\widetilde{F}$ as the main parameter to assess grid dependence.

Figure A.4 shows the results of the grid dependence study. At an orifice GOA of 20 % and an inlet flow velocity of 0.1 m/s the value of $\widetilde{F}$ converged at 2 million elements. Another benefit of the grid dependence analysis is related to the concept of using a laminar flow solver.

We previously discussed in Section 5.4 (page 115) that we used a laminar flow solver to avoid uncertainties from using turbulence models. Since we are interested in events occurring at low Reynolds numbers the use of turbulence models would have been unnecessary. However, at some events in our simulations, the Reynolds numbers did reach values suggesting transitional flow. The grid dependence study shows that refining the mesh used with the laminar solver converges the quantity of interest at a particular value even when the flow was sometimes transitional. On the other hand, a benefit of using turbulence would have been to achieve an averaging of the fluctuations in the flow field. While we believe abstaining from using turbulence models would not have a major impact on the results in this thesis since our hypothesis depends on values

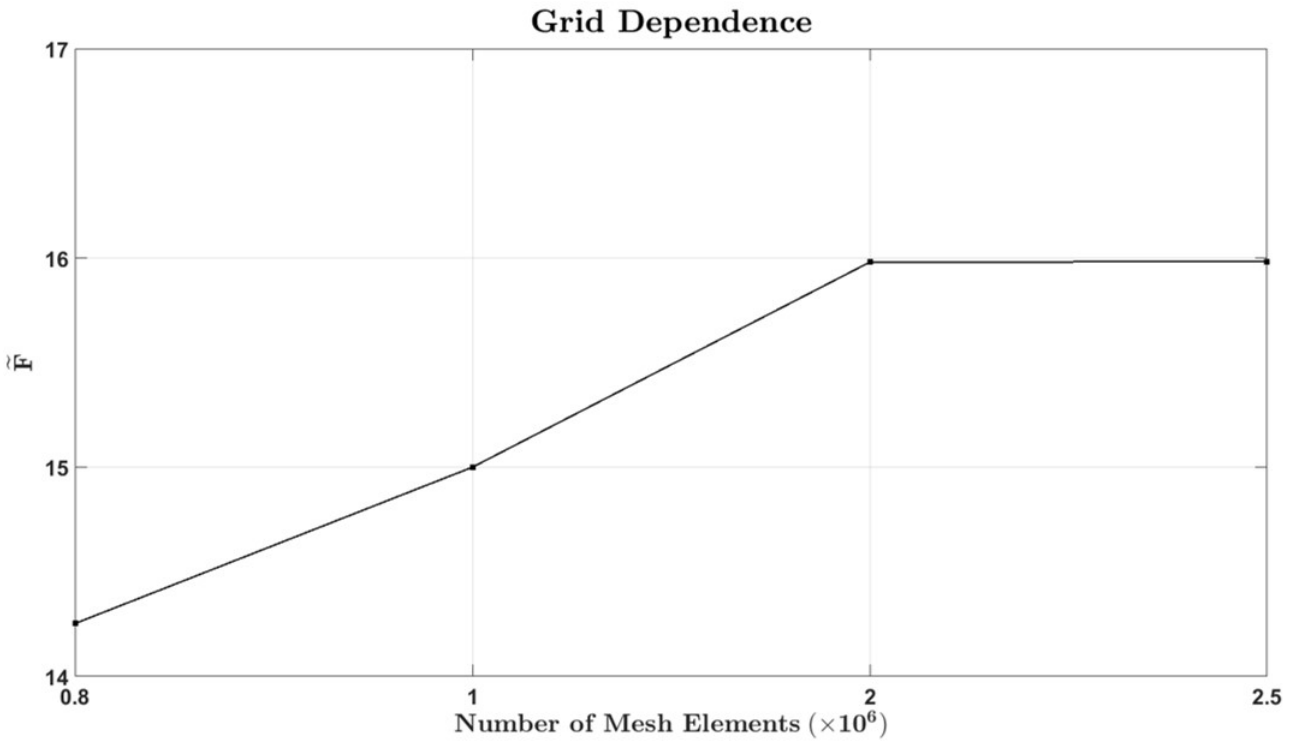


Figure A.4: Grid Dependence

of pressure and force on the orifice, we would perform an analysis comparing flow fields from turbulence solvers and laminar solvers to study their impact on the flow field in more detail.

A.3 Chapter 6

A.3.1 Simulation Parameters

The following parameters follow a study by Cao et al. with a similar application to the work in this thesis [8].

Blood Viscosity μ	0.0034 $Pa \cdot s$
Blood Density ρ	1060 kg/m^3
Fluid Time Step ΔT_f	0.001 s
Solid Time Step ΔT_s	0.001 s
Valve Material Model	Mooney-Rivlin 3 Parameter
Valve Material Parameters	$\rho = 1000\ kg/m^3$ $C_{10} = 32.823\ kPa$ $C_{01} = 2.955\ kPa$ $C_{11} = 585.79\ kPa$
Aortic Wall Material Model	Linear Elastic
Aortic Wall Material Parameters	$\rho = 1000\ kg/m^3$ $E = 1\ MPa$ $\nu = 0.49$

Bibliography

[1] M. H. Yacoub, "Valve-Conserving Operation for Aortic Root Aneurysm or Dissection," *Operative Techniques in Thoracic and Cardiovascular Surgery*, vol. 1, pp. 57–67, 1996, ISSN: 10855637. DOI: 10.1016/S1085-5637(07)70081-5.

[2] G. M. London and B. Pannier, "Arterial functions : how to interpret the complex physiology," no. October, pp. 3815–3823, 2010. DOI: 10.1093/ndt/gfq614.

[3] K. H. Parker, "An introduction to wave intensity analysis," pp. 175–188, 2009. DOI: 10.1007/s11517-009-0439-y.

[4] H. Aguib, R. Torii, S. Romeih, and M. Yacoub, *Characterisation of spatiotemporal aortic flow and aortic wall biomechanics in coarctation*, Sep. 2015. DOI: 10.5339/gcsp.2015.45.

[5] M. H. Yacoub, P. J. Kilner, E. J. Birks, and M. Misfield, "The aortic outflow and root: a tale of dynamism and crosstalk," *The Annals of Thoracic Surgery*, vol. 68, no. 3, 1999. [Online]. Available: http://www.sciencedirect.com/science/article/pii/S0003497599007456.

[6] D. Berdajs, S. Mosbahi, Z. Forro, C. Gerber, and E. Ferrari, "Numerical analysis of the 3-dimensional aortic root morphology during the cardiac cycle," pp. 1–9, 2015. DOI: 10.1093/ejcts/ezv295.

[7] A. Barker, P. Van Ooij, K. Bandi, J. Garcia, M. Albaghdadi, P. McCarthy, R. Bonow, J. Carr, J. Collins, C. Malaisrie, and M. Markl, "Viscous Energy Loss in the Presence of Abnormal Aortic Flow," vol. 72, no. 3, pp. 620–628, 2015. DOI: 10.1002/mrm.24962.Viscous.

[8] K. Cao and P. Sucosky, "Computational comparison of regional stress and deformation characteristics in tricuspid and bicuspid aortic valve leaflets," *International Journal for Numerical Methods in Biomedical Engineering*, vol. 33, no. 3, 2017, ISSN: 20407947. DOI: 10.1002/cnm.2798.

[9] S. Chandra, N. M. Rajamannan, and P. Sucosky, "Computational assessment of bicuspid aortic valve wall-shear stress: Implications for calcific aortic valve disease," *Biomechanics and Modeling in Mechanobiology*, vol. 11, no. 7, pp. 1085–1096, 2012, ISSN: 16177959. DOI: 10.1007/s10237-012-0375-x.

[10] M. Catanho, "Model of Aortic Blood Flow Using the Windkessel Effect," 2012.

[11] J. Lantz, J. Renner, and M. Karlsson, "Wall shear stress in a subject specific human aorta - Influence of fluid-structure interaction," no. 3, pp. 759–778, 2011.

[12] E. W. Lo, L. J. Menezes, and R. Torii, "Impact of inflow boundary conditions on the calculation of CT-based FFR," *Fluids*, vol. 4, no. 2, pp. 1–16, 2019, ISSN: 23115521. DOI: 10.3390/fluids4020060.

[13] S. Nijjer, C. Broyd, A. Ali, J. Keegan, D. P. Francis, C. D. Mario, and S. K. Prasad, "Mechanisms of Myocardial Ischemia in Hypertrophic Cardiomyopathy," *Journal of the American College of Cardiology*, vol. 68, no. 15, 2016. DOI: 10.1016/j.jacc.2016.07.751.

[14] M. R. Noor, C. H. Ho, K. H. Parker, A. R. Simon, N. R. Banner, and C. T. Bowles, "Investigation of the Characteristics of HeartWare HVAD and Thoratec HeartMate II Under Steady and Pulsatile Flow Conditions," *Artificial Organs*, vol. 40, no. 6, pp. 549–560, 2016. DOI: 10.1111/aor.12593.

[15] I. Ogobuiro, C. J. Wehrle, and F. Tuma, "Anatomy, Thorax, Heart Coronary Arteries," in, StatPearls Publishing, 2021. [Online]. Available: https://www.ncbi.nlm.nih.gov/books/NBK534790/.

[16] M. M. Bissell, E. Dall'Armellina, and R. P. Choudhury, "Flow vortices in the aortic root: In vivo 4D-MRI confirms predictions of Leonardo da Vinci," *European Heart Journal*, vol. 35, no. 20, p. 1344, 2014, ISSN: 15229645. DOI: 10.1093/eurheartj/ehu011.

[17] J. Keegan, C. E. Raphael, K. Parker, R. M. Simpson, S. Strain, R. De Silva, C. Di Mario, J. Collinson, R. H. Stables, R. Wage, P. Drivas, M. Sugathapala, S. K. Prasad, and D. N. Firmin, "Validation of high temporal resolution spiral phase velocity mapping of temporal patterns of left and right coronary artery blood flow against Doppler guidewire," *Journal of Cardiovascular Magnetic Resonance*, vol. 17, no. 1, pp. 1–13, 2015, ISSN: 1532429X. DOI: 10.1186/s12968-015-0189-y. [Online]. Available: http://dx.doi.org/10.1186/s12968-015-0189-y.

[18] A. Elfaramawy, M. Hassan, M. Nagy, A. ElGuindy, and M. F. Elmahdy, "Impact of fractional flow reserve on decision-making in daily clinical practice: A single center experience in Egypt," *Egyptian Heart Journal*, vol. 70, no. 3, pp. 161–165, 2018, ISSN: 2090911X. DOI: 10.1016/j.ehj.2017.12.007. [Online]. Available: https://doi.org/10.1016/j.ehj.2017.12.007.

[19] B. J. Bellhouse, F. H. Bellhouse, and K. G. Reid, "Fluid mechanics of the aortic root with application to coronary flow.," *Nature*, vol. 219, no. 5158, pp. 1059–1061, 1968, ISSN: 0028-0836. DOI: 10.1038/2191059a0.

[20] T. H. Oechtering, C. F. Hons, M. Sieren, P. Hunold, A. Hennemuth, M. Huellebrand, J. Drexl, M. Scharfschwerdt, D. Richardt, H.-H. Sievers, J. Barkhausen, and A. Frydrychowicz, "4D Flow-MRI analysis of hemodynamics in valve-sparing aortic root repair with an anatomically shaped sinus prosthesis," *The Journal of Thoracic and Cardiovascular Surgery*, 2016, ISSN: 00225223. DOI: 10.1016/j.jtcvs.2016.04.029. [Online]. Available: http://linkinghub.elsevier.com/retrieve/pii/S0022522316301180.

[21] S. Mirsadraee, "Imaging of aortic valve and transcatheter aortic valve implantation (TAVI) special issue," *Clinical Radiology*, vol. 76, no. 1, pp. 1–2, 2021, ISSN: 1365229X. DOI: 10.1016/j.crad.2020.08.037. [Online]. Available: https://doi.org/10.1016/j.crad.2020.08.037.

[22] E. I. Charitos and H.-H. Sievers, "Anatomy of the aortic root: implications for valve-sparing surgery.," *Annals of cardiothoracic surgery*, vol. 2, no. 1, pp. 53–6, 2013, ISSN: 2225-319X. DOI: 10.3978/j.issn.2225-319X.2012.11.18. [Online]. Available:

http://www.pubmedcentral.nih.gov/articlerender.fcgi?artid=3741810&tool=pmcentrez&rendertype=abstract.

[23] H. Dormand and R. H. Mohiaddin, "Cardiovascular Magnetic Resonance in Marfan syndrome," pp. 1–28, 2013.

[24] D. Berdajs, S. Mosbahi, F. Strano, Z. Forro, M. Burki, and L. K. von Segesser, "Impact of synthetic elements on aortic root haemodynamics: Computed fluid dynamics of aortic root reconstruction and valve reimplantation," *European Journal of Cardio-thoracic Surgery*, vol. 51, no. 3, pp. 432–441, 2017, ISSN: 1873734X. DOI: 10.1093/ejcts/ezw347.

[25] M. H. Yacoub, H. Aguib, M. A. Gamrah, N. Shehata, M. Nagy, M. Donia, Y. Aguib, H. Saad, S. Romeih, R. Torii, A. Afifi, and S. L. Lee, "Aortic root dynamism, geometry, and function after the remodeling operation: Clinical relevance," *Journal of Thoracic and Cardiovascular Surgery*, vol. 156, no. 3, pp. 951–962, 2018, ISSN: 1097685X. DOI: 10.1016/j.jtcvs.2018.03.157. [Online]. Available: https://doi.org/10.1016/j.jtcvs.2018.03.157.

[26] M. H. Yacoub, A. Afifi, H. Hosny, M. Nagy, N. Shehata, M. A. Gamrah, A. El Sawy, W. Simry, A. Mahgoub, N. Francis, H. El Nashar, Y. T. Tseng, S. Romeih, and H. Aguib, "A New Technique for Shaping the Aortic Sinuses and Conserving Dynamism in the Remodeling Operation," *Annals of Thoracic Surgery*, vol. 112, no. 4, pp. 1218–1226, 2021, ISSN: 15526259. DOI: 10.1016/j.athoracsur.2020.10.036. [Online]. Available: https://doi.org/10.1016/j.athoracsur.2020.10.036.

[27] P. Dagum, G. R. Green, F. J. Nistal, G. T. Daughters, T. a. Timek, L. E. Foppiano, a. F. Bolger, N. B. Ingels, and D. C. Miller, "Deformational dynamics of the aortic root: modes and physiologic determinants.," *Circulation*, vol. 100, no. 19 Suppl, pp. II54–I62, 1999, ISSN: 0009-7322. DOI: 10.1161/01.CIR.100.suppl{_}2.II-54.

[28] L. L. Benhassen, D. M. Ropcke, T. Lading, J. K. Skov, T. Bechsgaard, S. N. Skov, S. L. Nielsen, and J. M. Hasenkam, "Asymmetric Dynamics of the Native Aortic Annulus Evaluated by Force Transducer and Sonomicrometry in a Porcine Model," *Cardiovascular*

Engineering and Technology, vol. 10, no. 3, pp. 482–489, 2019, ISSN: 18694098. DOI: 10.1007/s13239-019-00418-1.

[29] J. E. Moore, N. Guggenheim, A. Delfino, P.-A. Doriot, P.-A. Dorsaz, W. Rutishauser, and J.-J. Meister, "Preliminary Analysis of the Effects of Blood Vessel Movement on Blood Flow Patterns in the Coronary Arteries," *Journal of Biomechanical Engineering*, no. September 1994, 1994. DOI: 10.1115/1.2895734.

[30] M. Abou Gamrah, J. Xu, A. El Sawy, H. Aguib, M. Yacoub, and K. H. Parker, "Mechanics of the dicrotic notch: An acceleration hypothesis," *Proceedings of the Institution of Mechanical Engineers, Part H: Journal of Engineering in Medicine*, vol. 234, no. 11, pp. 1253–1259, 2020, ISSN: 20413033. DOI: 10.1177/0954411920921628.

[31] C. J. Beller, M. R. Labrosse, M. J. Thubrikar, and F. Robicsek, "Role of Aortic Root Motion in the Pathogenesis of Aortic Dissection," *Circulation*, vol. 109, no. 6, pp. 763–769, 2004, ISSN: 00097322. DOI: 10.1161/01.CIR.0000112569.27151.F7.

[32] M. Moseley and G. Donnan, "Multimodality imaging: Introduction," *Stroke*, vol. 35, no. 11 SUPPL. 1, pp. 2632–2634, 2004, ISSN: 00392499. DOI: 10.1161/01.STR.0000143214.22567.cb.

[33] P. J. Kilner, G. Z. Yang, R. H. Mohiaddin, D. N. Firmin, and D. B. Longmore, "Helical and retrograde secondary flow patterns in the aortic arch studied by three-directional magnetic resonance velocity mapping.," *Circulation*, vol. 88, no. 5 Pt 1, pp. 2235–2247, 1993, ISSN: 0009-7322. DOI: 10.1161/01.CIR.88.5.2235.

[34] J. Chapron, H. Aguib, S. Theodoropoulos, and M. Kalantzi, "Quantitative assessment of right ventricular structure and flow dynamics in pulmonary homograft obstruction," *Global Cardiology Science and Practice*, 2014. DOI: dx.doi.org/10.5339/gcsp.2014.47.

[35] M. Markl, A. Frydrychowicz, S. Kozerke, M. Hope, and O. Wieben, "4D flow MRI," *Journal of Magnetic Resonance Imaging*, vol. 36, no. 5, pp. 1015–1036, 2012, ISSN: 10531807. DOI: 10.1002/jmri.23632.

[36] M. S. M. Elbaz, E. E. Calkoen, J. J. M. Westenberg, B. P. F. Lelieveldt, A. A. W. Roest, and R. J. V. D. Geest, "Vortex flow during early and late left ventricular filling in normal subjects : quantitative characterization using retrospectively-gated 4D flow cardiovascular magnetic resonance and three-dimensional vortex core analysis," *Journal of Cardiovascular Magnetic Resonance*, pp. 1–12, 2014.

[37] T. H. Oechtering, M. M. Sieren, P. Hunold, A. Hennemuth, M. Huellebrand, M. Scharfschwerdt, D. Richardt, H. H. Sievers, J. Barkhausen, and A. Frydrychowicz, "Time-resolved 3-dimensional magnetic resonance phase contrast imaging (4D Flow MRI) reveals altered blood flow patterns in the ascending aorta of patients with valve-sparing aortic root replacement," *Journal of Thoracic and Cardiovascular Surgery*, vol. 159, no. 3, pp. 798–810, 2020, ISSN: 1097685X. DOI: 10.1016/j.jtcvs.2019.02.127.

[38] N. Westerhof, J. W. Lankhaar, and B. E. Westerhof, "The arterial windkessel," *Medical and Biological Engineering and Computing*, vol. 47, no. 2, pp. 131–141, 2009, ISSN: 01400118. DOI: 10.1007/s11517-008-0359-2.

[39] M. Abdi, A. Karimi, M. Navidbaksh, G. Jahromi, and K. Hassani, "A lumped parameter mathematical model to analyze the effects of tachycardia and bradycardia on the cardiovascular system," *International Journal of Numerical Modelling*, no. 28, pp. 346–357, 2014, ISSN: 08943370. DOI: 10.1002/jnm.

[40] Y. Shi, P. Lawford, and R. Hose, "Review of Zero-D and 1-D Models of Blood Flow in the Cardiovascular System," *BioMedical Engineering Online*, vol. 10, 2011, ISSN: 1475925X. DOI: 10.1186/1475-925X-10-33.

[41] C. J. Broyd, F. Rigo, and J. Davies, "Non-invasive coronary wave intensity analysis," *The International Journal of Cardiovascular Imaging*, vol. 33, no. 7, pp. 1061–1068, 2017, ISSN: 1573-0743. DOI: 10.1007/s10554-017-1185-0.

[42] P. J. Blanco, C. A. Bulant, L. O. Müller, G. D. Talou, C. G. Bezerra, P. L. Lemos, and R. A. Feijóo, "Comparison of 1D and 3D Models for the Estimation of Fractional Flow Reserve," *Scientific Reports*, vol. 8, no. 1, pp. 1–12, 2018, ISSN: 20452322. DOI: 10.1038/s41598-018-35344-0.

[43] D. Doorly and S. Sherwin, "Geometry and flow," *Cardiovascular mathematics*, pp. 1–36, 2009, ISSN: 20375255. DOI: 10.1007/978-88-470-1152-6{_}5. [Online]. Available: http://link.springer.com/chapter/10.1007/978-88-470-1152-6_5.

[44] U. Morbiducci, R. Ponzini, D. Gallo, C. Bignardi, and G. Rizzo, "Inflow boundary conditions for image-based computational hemodynamics: Impact of idealized versus measured velocity profiles in the human aorta," *Journal of Biomechanics*, vol. 46, no. 1, pp. 102–109, 2013, ISSN: 00219290. DOI: 10.1016/j.jbiomech.2012.10.012. [Online]. Available: http://dx.doi.org/10.1016/j.jbiomech.2012.10.012.

[45] J. Lantz, P. Dyverfeldt, and T. Ebbers, "Improving Blood Flow Simulations by Incorporating Measured Subject-Specific Wall Motion," *Cardiovascular Engineering and Technology*, vol. 5, no. 3, pp. 261–269, 2014, ISSN: 18694098. DOI: 10.1007/s13239-014-0187-5.

[46] M. Haussmann, P. Reinshaus, S. Simonis, H. Nirschl, and M. J. Krause, "Fluid–structure interaction simulation of a coriolis mass flowmeter using a lattice boltzmann method," *Fluids*, vol. 6, no. 4, 2021, ISSN: 23115521. DOI: 10.3390/FLUIDS6040167.

[47] F. Sturla, E. Votta, M. Stevanella, C. A. Conti, and A. Redaelli, "Impact of modeling fluid-structure interaction in the computational analysis of aortic root biomechanics," *Medical Engineering and Physics*, vol. 35, no. 12, pp. 1721–1730, 2013, ISSN: 13504533. DOI: 10.1016/j.medengphy.2013.07.015.

[48] R. Toninato, J. Salmon, F. M. Susin, A. Ducci, and G. Burriesci, "Physiological vortices in the sinuses of Valsalva: An in vitro approach for bio-prosthetic valves," *Journal of Biomechanics*, vol. 49, no. 13, pp. 2635–2643, 2016, ISSN: 18732380. DOI: 10.1016/j.jbiomech.2016.05.027. [Online]. Available: http://dx.doi.org/10.1016/j.jbiomech.2016.05.027.

[49] M. Misfeld and H. H. Sievers, "Heart valve macro- and microstructure," *Philosophical Transactions of the Royal Society B: Biological Sciences*, vol. 362, no. 1484, pp. 1421–1436, 2007, ISSN: 09628436. DOI: 10.1098/rstb.2007.2125.

[50] V. M. Zatsiorsky, *Kinematics of Human Motion*. Illinois: Human Kinetics, 1998.

[51] D. Skillicorn, *Understanding Complex Datasets*. Chapman and Hall/CRC, 2007, pp. 71–112. DOI: 10.1201/9781584888338-8.

[52] J. P. Sutton III, S. Yen Ho, and R. H. Anderson, "The Forgotten Interleaflet Triangles: A Review of the Surgical Anatomy of the Aortic Valve," *Ann Thorac Surg*, vol. 59, pp. 419–427, 1995.

[53] E. D. Burman, J. Keegan, and P. J. Kilner, "Aortic Root Measurement by Cardiovascular Specification of Planes and Lines of Measurement and Corresponding Normal Values," 2016. DOI: 10.1161/CIRCIMAGING.108.768911.

[54] ANSYS Inc., *ANSYS Fluent Users Guide*, 2013.

[55] H. Liu, L. Lan, J. Abrigo, H. L. Ip, Y. Soo, D. Zheng, K. S. Wong, D. Wang, L. Shi, T. W. Leung, and X. Leng, "Comparison of Newtonian and Non-newtonian Fluid Models in Blood Flow Simulation in Patients With Intracranial Arterial Stenosis," *Frontiers in Physiology*, vol. 12, Sep. 2021, ISSN: 1664042X. DOI: 10.3389/fphys.2021.718540.

[56] I. Sadrehaghighi, *Mesh Generation in CFD*. Annapolis, MD: CFD Open Series, 2020, vol. Patch 1.86.7.

[57] ANSYS Inc., *ANSYS ICEM CFD User's Manual*, 2013.

[58] A. A. Sonin, "A generalization of the Π-theorem and dimensional analysis," *Proceedings of the National Academy of Sciences of the USA*, 2004. DOI: doi/10.1073/pnas.0402931101. [Online]. Available: www.pnas.org/cgi/doi10.1073/pnas.0402931101.

[59] W. Sun, W. Mao, and B. E. Griffith, "Computer modeling and simulation of heart valve function and intervention," in *Principles of Heart Valve Engineering*, Academic Press, 2019, ch. 7, pp. 177–211.

[60] W. Sun, C. Martin, and T. Pham, *Computational modeling of cardiac valve function and intervention*, 2014. DOI: 10.1146/annurev-bioeng-071813-104517.

[61] G. Luraghi, J. F. R. Matas, M. Beretta, N. Chiozzi, L. Iannetti, and F. Migliavacca, "The impact of calcification patterns in transcatheter aortic valve performance: a fluid-structure interaction analysis," *Computer Methods in Biomechanics and Biomedical Engineering*, vol. 24, no. 4, pp. 375–383, 2020, ISSN: 14768259. DOI: 10.1080/10255842.2020.1817409.

[62] J. Jeong and F. Hussain, "On the identification of a vortex," *Journal of Fluid Mechanics*, vol. 285, pp. 69–94, 1995, ISSN: 14697645. DOI: 10.1017/S0022112095000462.

[63] J. E. T. Perez, J. Ortiz-Urbina, C. P. Heredia, T. T. Pham, S. Madala, C. J. Hartley, M. L. Entman, G. E. Taffet, and A. K. Reddy, "Aortic acceleration as a noninvasive index of left ventricular contractility in the mouse," *Scientific Reports*, vol. 11, no. 1, Dec. 2021, ISSN: 20452322. DOI: 10.1038/s41598-020-79866-y.

[64] R. Vinoth, D. Kumar, R. Adhikari, and V. Shankar, "Non-Newtonian and Newtonian blood flow in human aorta: A transient analysis," *Biomedical Research*, vol. 28, no. 7, pp. 3194–3203, 2017. [Online]. Available: www.biomedres.info.